Università degli Studi di Udine
Dipartimento Politecnico di Ingegneria e Architettura
Dottorato di Ricerca in Ingegneria industriale e dell'informazione

Ph.D. Thesis

Time of Arrival and Angle of Arrival estimations of LTE Signals for Positioning Applications.

Candidate
Alessandro Pin

Supervisor
Prof. Roberto Rinaldo

Co-Supervisors
Prof. Andrea Tonello
Dott. Chris Marshall

Cycle XXXII — Year 2020

This thesis is in memory of my father.
I would like to dedicate this work to my mother, my family, my friends and to Chompoo who supported me during this last year of my PhD program.

Acknowledgements

This PhD thesis is part of a project, made in collaboration with u-blox, a company that creates wireless semiconductors and modules for consumer, automotive and industrial markets. It is a pleasure for me to thank Dr. Chris Marshall from u-blox UK, firstly for giving me the opportunity to start this PhD journey, and secondly for his patience and his ideas that helped me to reach the end of this challenging trip. My best thanks go to Andrea Dalla Torre and Alessandro Biason from u-blox Italia for their availability and their technical support, and also to Marco Driusso from u-blox UK who supported me technically in the first period of my PhD journey. A big part of this thesis would not have been possible without his cooperation. I also would like to thank prof. Gonzalo Seco-Granados, prof. José A. López-Salcedo and all the people of the SPCOMNAV team of the UAB in Barcelona, in particular Sergi, Dani, José del Peral, Ning, Vicente, Ruben Alejandro and Olivier, who welcomed me as one of them since the first day of my visit there. Finally a sincere "thank you so much!" goes to my supervisor Roberto Rinaldo, who has always been patient and understanding towards me, and also always helped me in achieving this goal.

Then, I want to thank my mum Laura for her patience, my brothers Andrea and Carlo, my sister Raffaella, all my nephews and nieces Niccolò, Alessia, Anna, Massimo and Matilde, my old friends "I fioi di san pae", Franci, Mazzo, Baz, Enry, Bise, Zan and Casta, all the new friends that I met after I moved to Udine, Matt, Mario, Gio, Giulio, Fiore, Alba, Isa, Roby and Anastasia, and finally Chompoo for her support during this last year.

Abstract

With the increase of services that need accurate location of the user, new techniques that cooperate with the Global Navigation Satellite System (GNSS) are necessary. Toward this objective, this thesis presents our research work about the estimation of the time of arrival (TOA) and of the angle of arrival (AOA) exploiting modern cellular signals. In particular, we focus on the Third Generation Partnership Project (3GPP) Long Term Evolution (LTE) standard, and in particular uplink and downlink reference signals are exploited to this purposes. The current release of the 3GPP LTE specification supports uplink time difference of arrival (UTDOA) localization technique based on the Sounding Reference Signal (SRS). In real environments, however, user equipments (UE) are rarely set up to transmit this particular signal.

The main original contribution of this thesis consists in a new TOA estimation method based on uplink transmission. In particular, we explore the possibility of performing radio localization exploiting the uplink Demodulation Reference Signal (DM-RS), which is always sent by UEs during data transmission. Real uplink transmissions are modeled in simulations and the performance of known algorithms like SAGE and IAA-APES are evaluated for TOA estimation. A new method to estimate the initial conditions of the SAGE algorithm is proposed and the estimation performance in uplink scenarios is evaluated. The analysis revealed that the proposed method outperforms the non-coherent initial conditions estimation proposed in the literature, when uplink transmission are used. Then, the benefits of our proposal are evaluated and the feasibility of TOA estimation exploiting the DM-RS is demonstrated by means of experiments using real DM-RS signals generated by an LTE module.

A second original contribution is given by AOA estimation. In particular, the independence of AOA estimation with respect to uplink and downlink transmission is verified. According to this result, the performance of IAA-APES and SAGE in real-world AOA experiments is evaluated in the downlink scenarios. Based on the overall results, we conclude that the proposed radio localization method, exploiting the uplink Demodulation Reference Signal (DM-RS), can be extended also to joint TOA, AOA using SAGE, for hybrid localization techniques. We can also conclude that the proposed method can be easily extended to downlink transmission exploiting the cell specific reference signal (CRS).

Publications

Conference Papers

- A. Pin, R. Rinaldo, A. Tonello, C. Marshall, M. Driusso and A. Biason, "LTE Uplink TOA Opportunistic Measurement Based on DM-RS," *WSA 2019; 23rd International ITG Workshop on Smart Antennas*, pp. 1-6, Apr. 2019.

- A. Pin, R. Rinaldo, A. Tonello, C. Marshall, M. Driusso, A. Biason and A. Dalla Torre "LTE Ranging Measurement Using Uplink Opportunistic Signals and the SAGE algorithm," *2019 27th European Signal Processing Conference (EUSIPCO)*, Sept. 2019.

- C. Marshall, A. Dalla Torre, M. Driusso, A. Pin, F. Pittino, R. Rinaldo, "Positioning Indoors with LTE Communications Signals of Different Bandwidth," *International Conference on Indoor Positioning and Indoor Navigation (IPIN)*, Sept. 2019.

Journal Paper (to be submitted)

- Joint AOA and TOA estimations exploiting LTE signals, for opportunistic positioning applications.

Table of contents

Abstract **vii**

Publications **ix**

List of figures **xv**

List of tables **xxiii**

List of Acronyms **xxv**

1 Introduction **1**

2 Fundamentals of Positioning **5**

2.1 Introduction 5
2.2 Radio Positioning System 5
2.3 Classification of Positioning System 7
2.4 Measurements 8
2.4.1 Time of Arrival 9
2.4.2 Time Difference of Arrival 11
2.4.3 Angle of Arrival (AOA) 12
2.4.4 Received Signal Strength (RSS) 12
2.4.5 Cell ID 14
2.4.6 Carrier Phase Measurement 14
2.4.7 Power Delay Profile (PDP) 15
2.5 Positioning Techniques 15
2.5.1 Lateration 15
2.5.2 Hyperbolic Positioning 18
2.5.3 Angulation 21
2.5.4 Hybrid Approaches 22

3 LTE Signals For Positioning **25**
3.1 Introduction . . . 25
3.2 Orthogonal Frequency Division Multiplexing (OFDM) . . . 26
3.2.1 OFDM Modulation . . . 26
3.2.2 OFDM Demodulation . . . 28
3.3 Single Carrier Frequency Division Multiple Access (SC-FDMA) . . . 32
3.3.1 Modulation . . . 32
3.3.2 Demodulation . . . 34
3.4 LTE Time and Frequency Structure . . . 37
3.5 Reference Signals for Positioning . . . 40
3.5.1 Downlink Reference Signals . . . 40
3.5.2 Uplink Reference Signals . . . 42

4 TOA and AOA Estimation Techniques **47**
4.1 Introduction . . . 47
4.2 TOA Estimation Techniques . . . 49
4.2.1 Correlation Based Techniques . . . 50
4.2.2 Deconvolution Method . . . 52
4.2.3 ML-Based Methods . . . 53
4.2.4 Subspace-Based Techniques . . . 54
4.3 AOA Estimation Techniques . . . 57
4.3.1 Wave Propagation Model . . . 58
4.3.2 Frequency Description . . . 59
4.3.3 Spatial Filtering . . . 62
4.3.4 Conventional Beamforming . . . 63
4.3.5 Minimum variance distortionless response beamformer . . . 65
4.3.6 Subspace Methods . . . 66
4.3.7 IAA-APES . . . 66
4.4 Joint ML Parameters Estimation . . . 69
4.4.1 SAGE Algorithm . . . 71
4.4.2 Detection of the number of paths . . . 73
4.5 Cramér Rao lower bound . . . 75

5 LTE Uplink TOA Estimation Results **79**
5.1 Introduction . . . 79
5.2 IAA-APES for delay estimation . . . 80
5.3 Uplink DM-RS transmission issues . . . 83

5.4 SAGE initial conditions for Uplink transmission. 84
5.5 Simulation Results With Different Initialization Procedures 87
5.6 Simulation Results with Different Channel Models 99
5.6.1 EPA Channel Simulations 100
5.6.2 EVA Channel Results 113
5.6.3 ETU Channel Results 127
5.7 Experimental Results in a Real Scenario 140
5.7.1 Set-up 140
5.7.2 Results 143
5.8 Conclusions 147

6 AOA and TOA estimation using LTE signals. 149
6.1 Introduction 149
6.2 Simulation set-up 150
6.3 Simulation Results 151
6.4 Experimental set up for the Anechoic Chamber 157
6.5 Results for the Anechoic Chamber Experiments 161
6.6 Conclusion 168

7 Conclusion 171

References 173

List of figures

2.1 Classification of positioning systems based on topology 7
2.2 Geometrical example of lateration with three anchors 16
2.3 Geometrical example of hyperbolic positioning with three anchors . . . 19
2.4 Geometrical example of angulation positioning with three anchors . . . 21

3.1 OFDM Transceiver Scheme 31
3.2 SC-FDMA Transceiver Scheme 36
3.3 LTE Radio frame structure 37
3.4 LTE slot structures 38
3.5 LTE resource grid 39
3.6 Mapping of the CRS with two antenna ports 41
3.7 DM-RS auto-correlation and cross-correlation 43
3.8 Uplink reference signal modulation 45

4.1 Correlation in a multipath scenario 50
4.2 Correlation with no resolvable paths 51
4.3 Block scheme of the deconvolution method 52
4.4 Coordinates system for DOA 59
4.5 Beam pattern with different look direction 63
4.6 Beam pattern with different number of antenna elements 64
4.7 Beam pattern with different distances between antenna elements 64
4.8 Flow chart of SAGE algorithm 74

5.1 Time-frequency pattern. 83
5.2 Time-frequency pattern of an uplink transmission. The transmission does not cover the overall available bandwidth but only a small portion of it. The figure shows the bandwidth occupied by a real uplink transmission corresponding to a “ping” message. 85
5.3 Block diagram of the simulation setup. 88

5.4 RMSEE of the delays. Comparison between SAGE 2D initialization and SAGE non-coherent initialization in the full band scenario. 91
5.5 RMSEE of the Doppler. Comparison between SAGE 2D initialization and SAGE non-coherent initialization in the full band scenario. 92
5.6 RMSEE of the delays. Comparison between SAGE 2D initialization and SAGE non-coherent initialization in the simulated ping scenario. 92
5.7 RMSEE of the Doppler. Comparison between SAGE 2D initialization and SAGE non-coherent initialization in the simulated ping scenario. . 93
5.8 RMSEE of the delays. Comparison between SAGE 2D initialization and SAGE non-coherent initialization in real ping scenario. 94
5.9 RMSEE of the Doppler. Comparison between SAGE 2D initialization and SAGE non-coherent initialization in real ping scenario. 94
5.10 RMSEE of the delays using IAA-APES in the full band scenario. 95
5.11 RMSEE of the first path delay. Comparison between different algorithms in the full band scenario. 96
5.12 RMSEE of the first path delay. Comparison between different algorithms in the simulated ping scenario. 97
5.13 RMSEE of the first path delay. Comparison between different algorithms in the real ping scenario. 97
5.14 First path delay RMSEE. Comparison between SAGE 2D initialization, SAGE non-coherent initialization and IAA-APES, in the three different simulated scenarios. 98
5.15 RMSEE of the delays. Comparison between different paths estimation obtained with SAGE, considering the EPA channel model in the full band scenario with fixed Doppler. 101
5.16 RMSEE of the Doppler. Comparison between different paths estimation obtained with SAGE, considering the EPA channel model in the full band scenario with fixed Doppler. 101
5.17 RMSEE of the delays. Comparison between different paths estimation obtained with IAA-APES, considering the EPA channel model in the full band scenario with fixed Doppler. 102
5.18 RMSEE of the delays. Comparison between different paths estimation obtained with SAGE, considering the EPA channel model in the simulated ping scenario with fixed Doppler. 103

5.19 RMSEE of the Doppler. Comparison between different paths estimation obtained with SAGE, considering the EPA channel model in the simulated ping scenario with fixed Doppler. 103
5.20 RMSEE of the delays. Comparison between different paths estimation obtained with SAGE, considering the EPA channel model in the real ping scenario with fixed Doppler. 104
5.21 RMSEE of the Doppler. Comparison between different paths estimation obtained with SAGE, considering the EPA channel model in the real ping scenario with fixed Doppler. 105
5.22 RMSEE of the first path delay. Comparison between SAGE, IAA-APES and the correlator peak detector, considering the EPA channel model in the three different scenarios with fixed Doppler. 105
5.23 RMSEE of the first path delay. Inset of the comparison between SAGE, IAA-APES and the correlator peak detector, considering the EPA channel model in the three different scenarios with fixed Doppler. 106
5.24 RMSEE of the delays. Comparison between different paths estimation obtained with SAGE, considering the EPA channel model in the full band scenario with random Doppler. 107
5.25 RMSEE of the Doppler. Comparison between different paths estimation obtained with SAGE, considering the EPA channel model in the full band scenario with random Doppler. 108
5.26 RMSEE of the delays. Comparison between different paths estimation obtained with IAA-APES considering the EPA channel model in the full band scenario with random Doppler. 108
5.27 RMSEE of the delays. Comparison between different paths estimation obtained with SAGE, considering the EPA channel model in the simulated ping scenario with random Doppler. 109
5.28 RMSEE of the Doppler. Comparison between different paths estimation obtained with SAGE, considering the EPA channel model in the simulated ping scenario with random Doppler. 110
5.29 RMSEE of the delays. Comparison between different paths estimation obtained with SAGE, considering the EPA channel model in the real ping scenario with random Doppler. 110
5.30 RMSEE of the Doppler. Comparison between different paths estimation obtained with SAGE, considering the EPA channel model in the real ping scenario with random Doppler. 111

5.31 RMSEE of the first path delay. Comparison between SAGE, IAA-APES and the correlator peak detector, considering the EPA channel model in the three different scenarios with random Doppler. 112
5.32 RMSEE of the first path delay. Inset of the comparison between SAGE, IAA-APES and the correlator peak detector, considering the EPA channel model the three different scenarios with random Doppler generation. 112
5.33 RMSEE of the delays. Comparison between different paths estimation obtained with SAGE, considering the EVA channel model in the full band scenario with fixed Doppler. 113
5.34 RMSEE of the Doppler. Comparison between different paths estimation obtained with SAGE, considering the EVA channel model in the full band scenario with fixed Doppler. 114
5.35 RMSEE of the delays. Comparison between different paths estimation obtained with IAA-APES, considering the EVA channel model in the full band scenario with fixed Doppler. 115
5.36 RMSEE of the delays. Comparison between different paths estimation obtained with SAGE, considering the EVA channel model in the simulated ping scenario with fixed Doppler. 115
5.37 RMSEE of the Doppler. Comparison between different paths estimation obtained with SAGE, considering the EVA channel model in the simulated ping scenario with fixed Doppler. 116
5.38 RMSEE of the delays. Comparison between different paths estimation obtained with SAGE, considering the EVA channel model in the real ping scenario with fixed Doppler. 117
5.39 RMSEE of the Doppler. Comparison between different paths estimation obtained with SAGE, considering the EVA channel model in the real ping scenario with fixed Doppler. 117
5.40 RMSEE of the first path delay. Comparison between SAGE, IAA-APES and the correlator peak detector, considering the EVA channel model in the three different scenarios fixed Doppler. 118
5.41 RMSEE of the first path delay. Inset of the comparison between SAGE, IAA-APES and the correlator peak detector, considering the EVA channel model in the three different scenarios fixed Doppler. 119
5.42 RMSEE of the delays. Comparison between different paths estimation obtained with SAGE, considering the EVA channel model in the full band scenario with random Doppler. 120

5.43 RMSEE of the Doppler. Comparison between different paths estimation obtained with SAGE, considering the EVA channel model in the full band scenario with random Doppler. 121
5.44 RMSEE of the delays. Comparison between different paths estimation obtained with IAA-APES, considering the EVA channel model in the full band scenario with random Doppler. 121
5.45 RMSEE of the delays. Comparison between different paths estimation obtained with SAGE, considering the EVA channel model in the simulated ping scenario with random Doppler. 122
5.46 RMSEE of the Doppler. Comparison between different paths estimation obtained with SAGE, considering the EVA channel model in the simulated ping scenario with random Doppler. 123
5.47 RMSEE of the delays. Comparison between different paths estimation obtained with SAGE, considering the EVA channel model in the real ping scenario with random Doppler. 123
5.48 RMSEE of the Doppler. Comparison between different paths estimation obtained with SAGE, considering the EVA channel model in the real ping scenario with random Doppler. 124
5.49 RMSEE of the first path delay. Comparison between SAGE, IAA-APES and the correlator peak detector, considering the EVA channel model in the three different scenarios with random Doppler. 125
5.50 RMSEE of the first path delay. Inset of the comparison between SAGE, IAA-APES and the correlator peak detector, considering the EVA channel model in the three different scenarios with random Doppler. 126
5.51 RMSEE of the delays. Comparison between different paths estimation obtained with SAGE, considering the ETU channel model in the full band scenario with fixed Doppler. 127
5.52 RMSEE of the Doppler. Comparison between different paths estimation obtained with SAGE, considering the ETU channel model in the full band scenario with fixed Doppler. 128
5.53 RMSEE of the delays. Comparison between different paths estimation obtained with IAA-APES, considering the ETU channel model in the full band scenario with fixed Doppler. 128
5.54 RMSEE of the delays. Comparison between different paths estimation obtained with SAGE, considering the ETU channel model in the simulated ping scenario with fixed Doppler. 129

5.55 RMSEE of the Doppler. Comparison between different paths estimation obtained with SAGE, considering the ETU channel model in the simulated ping scenario with fixed Doppler. 130
5.56 RMSEE of the delays. Comparison between different paths estimation obtained with SAGE, considering the ETU channel model in the real ping scenario with fixed Doppler. 130
5.57 RMSEE of the Doppler. Comparison between different paths estimation obtained with SAGE, considering the ETU channel model in the real ping scenario with fixed Doppler. 131
5.58 RMSEE of the first path delay. Comparison between SAGE, IAA-APES and the correlator peak detector, considering the ETU channel model in the three different scenarios with fixed Doppler. 132
5.59 RMSEE of the first path delay. Inset of the comparison between SAGE, IAA-APES and the correlator peak detector, considering the ETU channel model in the three different scenarios with fixed Doppler. . . . 132
5.60 RMSEE of the delays. Comparison between different paths estimation obtained with SAGE, considering the ETU channel model in the full band scenario with random Doppler. 133
5.61 RMSEE of the Doppler. Comparison between different paths estimation obtained with SAGE, considering the ETU channel model in the full band scenario with random Doppler. 134
5.62 RMSEE of the delays. Comparison between different paths estimation obtained with IAA-APES, considering the ETU channel model in the full band scenario with random Doppler. 135
5.63 RMSEE of the delays. Comparison between different paths estimation obtained with SAGE, considering the ETU channel model in the simulated ping scenario with random Doppler. 135
5.64 RMSEE of the Doppler. Comparison between different paths estimation obtained with SAGE, considering the ETU channel model in the simulated ping scenario with random Doppler. 136
5.65 RMSEE of the delays. Comparison between different paths estimation obtained with SAGE, considering the ETU channel model in the real ping scenario with random Doppler. 137
5.66 RMSEE of the Doppler. Comparison between different paths estimation obtained with SAGE, considering the ETU channel model in the real ping scenario with random Doppler. 137

5.67 RMSEE of the first path delay. Comparison between SAGE, IAA-APES and the correlator peak detector, considering the ETU channel model in the three different scenarios with random Doppler. 138
5.68 RMSEE of the first path delay. Inset of the comparison between SAGE, IAA-APES and the correlator peak detector, considering the ETU channel model in the three different scenarios with random Doppler. . . 139
5.69 Arrangement of the experimental setup. 142
5.70 Block diagram of the proposed system. 143
5.71 Distance estimates using SAGE and the correlator, for a 40 m distance between the two antennas. 145
5.72 Distance estimates using SAGE and the correlator, for a 35 m distance between the two antennas. 145
5.73 Distance estimates using SAGE and the correlator, for a 30 m distance between the two antennas. 146

6.1 RMSEE of the three path delays considering the full band, simulated ping and real ping scenarios, using SAGE with 3D initial conditions. . . 152
6.2 RMSEE of the three path Doppler considering the full band, simulated ping and real ping scenarios, using SAGE with 3D initial conditions. . . 153
6.3 RMSEE of the angle. Comparison between SAGE and IAA-APES in the full band scenario. 154
6.4 RMSEE of the angle. Comparison between SAGE and IAA-APES in the simulated ping scenario 154
6.5 RMSEE of the angle. Comparison between SAGE and IAA-APES in the real ping scenario 155
6.6 Sketch representing the set up of the first scenario in the anechoic chamber 158
6.7 Sketch representing the set up of the second scenario in the anechoic chamber 159
6.8 Sketch representing the set up of the third scenario in the anechoic chamber 159
6.9 Picture representing the set up of the second scenario in the Anechoic chamber 160
6.10 RMSEE of the angle of arrival. Comparison of the results obtained with SAGE and IAA-APES in the first scenario used in the anechoic chamber. 162
6.11 RMSEE of the delays difference. Results obtained with SAGE in the first scenario used in the anechoic chamber. 162

6.12 RMSEE of the angle of arrival. Comparison of the results obtained with SAGE and IAA-APES in the second scenario used in the anechoic chamber. 163
6.13 RMSEE of the angle of arrival. Inset of the comparison between SAGE and IAA-APES in the second scenario used in the anechoic chamber. . 164
6.14 RMSEE of the delays difference. Results obtained with SAGE in the second scenario used in the anechoic chamber. 164
6.15 RMSEE of the angle of arrival. Comparison of the results obtained with SAGE and IAA-APES in the third scenario used in the anechoic chamber. 165
6.16 RMSEE of the angle of arrival. Inset of the comparison between SAGE and IAA-APES in the second scenario used in the anechoic chamber. . 166
6.17 RMSEE of the delays difference. Results obtained with SAGE in the second scenario used in the anechoic chamber. 167

List of tables

2.1 Physical signal properties used for measurement in positioning 9
2.2 Typical values of the path loss exponent 13

3.1 List of possible bandwidth configuration 39

5.1 Channel model used in simulation 99
5.2 Necessary parameters for DM-RS TOA estimation 141

6.1 Parameter used in simulations for AOA estimation 151
6.2 Table of the parameters used in the anechoic chamber scenarios. 158

List of Acronyms

The following list describes several symbols that will be later used in this thesis

3GPP	*3rd Generation Partnership Project*
A-GNSS	*Assisted GNSS*
AOA	*Angle Of Arrival*
BS	*Base Station*
CFR	*Channel Frequency Response*
CID	*Cell ID*
CIR	*Channel Impulse Response*
CP	*Cyclic Prefix*
DFT	*Discrete Fourier Transform*
DOA	*Direction Of Arrival*
DRSS	*Differential Received Signal Strength*
E-CID	*Enhanced Cell ID*
E-CID	*Enhanced Cell Identity*
EKF	*Extended Kalman Filter*
EM	*Expectation-Maximization*
eNodeB	*Evolved Node B*
EPA	*Extended Pedestrian A model*

ESPRIT	*Estimation of Signal Parameters via Rotational Invariance Techniques*
ETU	*Extended Typical Urban model*
EVA	*Extended Vehicular A model*
FIM	*Fisher Information Matrix*
GLONASS	*Russian Global Navigation Satellite System*
GNSS	*Global Navigation Satellite System*
GPS	*Global Positioning System*
GSM	*Global System for Mobile Communications*
IDD	*Independent and Identically Distributed*
IIA-APES	*Iterative Adaptive Approach for Amplitude and Phase Estimation*
IRNSS	*Indian Regional Navigation Satellite System*
LMU	*Location Measurement Units*
LORAN	*Long Range Navigation*
LOS	*Line Of Sight*
LPS	*Local Positioning System*
LS	*Least Squares*
LSS	*Linear Least Squares*
LTE	*Long Term Evolution*
ML	*Maximum Likelihood*
MS	*Mobile Station*
MSEE	*Mean Square Estimation Error*
MUSIC	*MUltiple SIgnal Classification*
NLOS	*No Line Of Sight*
OFDM	*Orthogonal Frequency Division Multiplexing*

OFDMA	*Orthogonal Frequency Division Multiple Access*
OTDOA	*Observed Time Difference of Arrival*
PAPR	*Peak to Average Power Ratio*
PDP	*Power Delay Profile*
PRS	*Positioning Reference Signal*
QZZS	*Quasi-Zenith Satellite System*
RB	*Resource Block*
RE	*Resource Element*
RS	*Reference Signal*
RSS	*Received Signal Strength*
RV	*Random Variable*
SNR	*Signal to Noise Ratio*
SRS	*Sounding Reference Signal*
TA	*Time Advance*
TDOA	*Time Difference Of Arrival*
TOA	*Time Of Arrival*
UE	*User Equipment*
ULA	*Uniform Linear Array*
UMTS	*Universal Mobile Telecommunications System*
UTDOA	*Uplink Time Difference of Arrival*
WLAN	*Wireless Local Area Network*
WLPS	*Wireless Local Positioning System*
WLS	*Weighted Least Square*
WPAN	*Wireless Personal Area Network*
ZC	*Zadoff-Chu*

Chapter 1

Introduction

The contributions presented in this thesis are the results of a three year PhD study as a student at the University of Udine. This work has been developed with the technical support of u-blox, a company that creates wireless semiconductors and modules for consumer, automotive and industrial markets.

Nowadays, positioning and navigation technologies are commonly used in a large variety of contexts [1–5]. The most popular applications are in the transportation field, where positioning systems are used to guide the users. In the majority of the positioning applications, the localization task is performed by global navigation satellite systems (GNSSs), which are typically very precise and require a cheap end user receiver. However, in some scenarios, the GNSSs may not work effectively [6], for instance in urban canyons and indoor environments. Urban canyons correspond to locations where the sky view is covered by skyscrapers or by other buildings, whereas, in indoor environments, the sky view is obscured by the ceiling. All these scenarios are characterized by the fact that the available satellites signals are hindered by objects in the environment. The need to find new alternatives, that do not rely on GNSS, is made necessary by the previous issues, but also by other GNSS issues, such as the vulnerability to jamming and spoofing.

One alternative is represented by wireless terrestrial signals, which provide good coverage and which benefit from the fact that usually there is no need for further infrastructure deployment. In this context, localization by means of the cellular system looks a promising approach, also considering that the new incoming 5G technology will require the deployment of a large number of micro/pico-cells. Consequently, positioning using Third Generation Partnership Project (3GPP) Long Term Evolution (LTE) downlink signals has become a subject of research and industrial interest, also for possible evolution in the future standards. In general, LTE uplink signals have

generated little hype in the positioning research, and the support for uplink positioning was introduced only in the latest versions of of LTE standard. Positioning systems based on uplink signals rely on a particular reference signal, called the sounding reference signal (SRS). Unfortunately, in real scenarios, these signals are rarely transmitted, or never transmitted in some cases, making it impossible to exploit uplink transmission for positioning purposes.

In this thesis, we address the problem of estimating, for positioning purposes, the time of arrival (TOA) and the angle of arrival (AOA) of 3GPP LTE signals, using uplink and downlink signals, with more focus on uplink signals.

The main original contribution of this thesis consists in a new TOA estimation method based on uplink transmission, in particular exploiting the uplink Demodulation Reference Signal (DM-RS). We perform simulations in order to evaluate the performance of the well known SAGE and IAA-APES algorithms for the estimation of the signal parameters needed for localization. In particular, we found that the SAGE algorithm, in its original formulation, does not provide good estimates when using DM-RS signals, due to their particular characteristics. We propose a new method for the estimation of the initial conditions that alleviates the problem. The simulation results reveal that the proposed method outperforms the non coherent initial conditions estimation proposed in [7], when uplink transmission are used. Then, the feasibility of the proposed TOA estimation procedure is also evaluated by means of experiments exploiting real-world DM-RS transmissions generated by an LTE module.

A second original contribution of this work is given by AOA estimation. In particular, we demonstrate by means of simulations that using uplink or downlink signals, with their different characteristics, does not influence the estimation quality too much. According to this result, the performance of IAA-APES and SAGE in a real-world AOA and TOA estimation experiment is evaluated for downlink signals.

Based on our results, we can conclude that the proposed radio localization method, exploiting the uplink Demodulation Reference Signal (DM-RS), can be also extended to joint TOA and AOA estimation, using hybrid localization techniques. A similar procedure can be used to estimate TOA and AOA using downlink transmissions exploiting the cell specific reference signal (CRS).

This thesis is divided into two main parts. The first part includes the second, the third and the fourth chapters, where the background topics studied at the beginning of the Ph.D. program are introduced. The second part describes the original contributions and the conclusion.

In Chapter 2, the basic principles of a positioning system are presented, with particular attention to the positioning systems based on time based distance measurements. First, a classification of the positioning systems is briefly described. Then, the focus falls on the description of the physical quantities which are measured to obtain distance estimates or angle estimates.

In Chapter 3, the LTE downlink and uplink physical layer is briefly described. In the first part the focus is on the OFDM and SC-FDMA modulation techniques. The second part describes the time and frequency structure of the physical layer. The last part describes the uplink and downlink reference signals.

In Chapter 4, some common TOA and AOA estimation techniques are discussed. In the first part, some TOA estimation techniques, such as the correlation based approach, the deconvolution method, the Maximum Likelihood (ML) approach, and the subspace-based methods ere described. In the second part, some AOA techniques are introduced, such as Barlet estimation, the standard Capon beamformer and the IAA-APES algorithm. In the last part, the SAGE algorithm is presented, then the chapter ends with an introduction of the Cramer Rao lower bound (CRLB) in our application.

In Chapter 5 we present the first original contribution of our work. In particular, the Chapter focuses on how to perform TOA measurements using the uplink signal DM-RS. In the first part of this Chapter, we present the difficulties that we had to face when uplink transmission is used. We describe the proposed solution confirming its reliability by means of simulations. In the last part, the results obtained using real-world uplink transmission are showed, and we confirm that the DM-RS can be effectively used for positioning purposes using TDOA techniques.

In Chapter 6 we present the second original contribution of our work. In the first part of this Chapter, we present simulations comparing the AOA performance with SAGE and IAA-APES in the three different scenarios defined in the previous chapters. We verify that AOA estimation is not really influenced by the particular type of transmission used, downlink or uplink. Then, in the second part of the chapter, we perform real world experiments using downlink signals in an anechoic chamber.

Finally, Chapter 7 ends the thesis, summarizing the obtained original contribution.

Chapter 2

Fundamentals of Positioning

2.1 Introduction

In recent years there has been a rapid increase in the demand for services and systems based on accurate positioning of people and objects. Location-based services and emergency call positioning affects the development and enhancement of wireless positioning techniques. This chapter introduces the basic principles of localization. Firstly, radio positioning systems are introduced and some common classifications are presented, then some common measurements adopted for positioning are explained, with a particular focus on time and angle measurements. In the last part, some common algorithms used for localization are reviewed. This chapter focuses more on terrestrial wireless systems based on time and angle measurements, since these type of measurements are exploited throughout this thesis.

2.2 Radio Positioning System

Nowadays several positioning systems are based on wireless communications. A very famous and well-known positioning system is the Global Navigation Satellite System (GNSS). This technology is capable of determining the outdoor position in the range meters of accuracy. GNSSs include some advanced systems like GPS, the Russian GLONASS, the European Galileo, the Chinese BeiDou, the Indian IRNSS and the Japanese QZSS. In particular, to determine the position of the receiver, these systems exploit distance measurements between a constellation of satellites and the receiver.

With this technology the distance between one satellite and the receiver is estimated indirectly. Assuming knowledge of the speed of light in the atmosphere, the distance can be calculated using the time that a radio signal employs to travel from the satellite to the receiver. Moreover, the position of the satellites in their orbits are calculated and shared with the receiver, to allow the receiver to estimate its position. The precision of such systems is mostly due to the presence of high accuracy clocks in the satellites, which give a good time reference.

Some positioning systems do not rely on satellites. These are the so called terrestrial positioning systems. In the past decade, for instance, some terrestrial positioning systems were used for maritime and air navigation, like the LOng RAnge NAvigation (LORAN) system, the Decca Navigation System and the OMEGA radio navigation system, but nowadays these systems have been decommissioned. Recently, some new terrestrial wireless positioning systems have been introduced, which are used in several applications. These rising technologies have become very interesting because they represent a valid substitute to the GNSS in such environment where the GNSS performance falters or fails. Usually, GNSSs have bad performance in indoor and urban canyons, even though wireless communication systems like 4G LTE, UMTS and GSM, provide good coverage in these environment. Positioning systems based on cellular communications network are called cellular-based positioning systems. In particular, the 3GPP LTE protocol (3rd Generation Partnership Project Long Term Evolution) [8] introduced the support for positioning since its early releases, and improved it in the following stages. Currently, some positioning methods available in the LTE standards are: enhanced cell identity (E-CID), Assisted GNSS (A-GNSS), observed time difference of arrival (OTDOA) and uplink time difference of arrival (UTDOA).

Usually, a wireless terrestrial positioning system is composed of some devices called anchor nodes, which have a known position, and some devices called blind nodes whose position is unknown and has to be determined. Both types of nodes can be in a fixed position or in movement. In a cellular-based positioning system anchors are usually the base stations (BSs) of the communication system, which are in a fixed and known position, and the blind nodes are the mobile terminals, which are referred to as the mobile stations (MSs). The process of positioning consists of two main steps. The first step is the measurement phase, where some physical property of the signal is measured. The second step is the location phase, where the position of the blind node is determined using both the information coming from the measurements and the knowledge of the position of the anchors.

2.3 Classification of Positioning System

Positioning systems can be classified according to different criteria. According to the classification in [2, 9], if we consider the topology of the system, we can divide the positioning systems into global positioning systems and local positioning systems (LPS). For example, a global positioning system is the GNSS and a LPS is a cellular-based positioning system. Considering a LPS, we can divide the system according to where the measurements are made and where measurements are processed. A system is classified as a self-positioning system when the measurements are obtained and processed in the MS, and in order to operate correctly the BSs have to inform the MS of their positions. When measurements are obtained and processed at the network side (at one or more BSs) the system is called a remote positioning system. When measurements are obtained in a type of node and processed in the other, the systems are said to be indirect, which means that one type of indirect self-positioning system occurs when the BSs measure the signals and the MSs calculate the position, while in the opposite case the system is called an indirect remote positioning system. Remote positioning systems can be further classified as active remote positioning systems when the MS cooperates in the process of positioning, and as passive remote positioning systems when there is no cooperation by the MS. A wireless local positioning systems (WLPSs) is an example of active positioning system, while a tracking radar is an example of passive positioning system. Figure 2.1 summarizes the positioning systems classification based on topology.

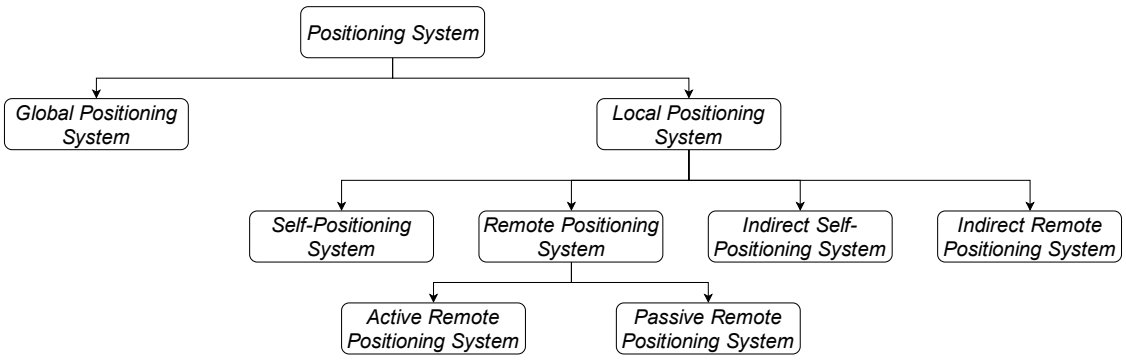

Fig. 2.1 Classification of positioning systems based on topology

Other classifications are suggested in [9]. A positioning system can be also classified taking into account the physical coverage range of the communication technology. This

classification generally distinguishes satellite, cellular and short-range systems. Satellite positioning systems provide position information, in principle, in every part of the world, so in this case position can be determined "almost" everywhere, the word "almost" being used because there are some limitations of the system (e.g., in indoor and in some urban environment where GNSS fails). In a cellular positioning system, the MS is positioned depending on the communication technologies (LTE, UMTS or GSM), which means that the range is restricted to the coverage areas of the cellular BSs. Typically, cellular systems are used in urban scenarios. Short-range positioning rely on WLAN/WPAN technologies and typically is used for indoor positioning, because the range of these technologies is limited to some tens of meters.

Another classification can be done according to how the positioning system is integrated into a communication technology. In this case, a system can be classified as integrated, opportunistic and hybrid. In integrated systems, the positioning system is integrated with the wireless communication technology, one example being the GPS receiver integrated in a smart phone. Opportunistic solutions exploit an existing communications protocol, usually not designed for positioning, in order to estimate a position. The results of this thesis are based on an opportunistic positioning systems, and indeed the basic idea is to exploit LTE reference signals designed for communication purposes and not for positioning. Generally, the price to pay with these solutions is the lower accuracy with respect to integrated solutions. Finally, hybrid systems use both solutions in cooperative or alternate ways.

2.4 Measurements

The first step for positioning estimation in a terrestrial positioning system is the measurement phase. During this phase, some physical parameters of the signals are measured. After the measurement phase, some positioning algorithms can be applied in order to estimate the position. In terrestrial positioning systems the signals used for measurement purposes are often reference signals. Some common position-dependent parameters measured from a reference signal are the time of arrival (TOA), the received signals strength (RSS), the angle of arrival (AOA) (also called direction of arrival (DOA)), some identifier of the particular transmitting node such as the cell identifier (cell ID or CID), the time difference of arrival (TDOA), the differential received signal strength (DRSS), the carrier phase of the signal and the power delay profile (PDP). Table 2.1 summarizes these physical parameters with a brief description. In the following subsections, these parameters are described in more detail.

Parameters	Physical quantity	Brief description
TOA	Time	Time instant in which the signal is received
TDOA	Time	Difference between two TOA measurements
RSS	Power	Received signals power
DRSS	Power	Difference between two RSS measurements
AOA	Angle	Incident angle with respect to a fixed orientation
CID	-	Identifier of the node that transmits the reference signals
Carrier Phase	Signal phase	Received phase of the signals
PDP	Power w.r.t delay	Shape of the multipath power delay profile

Table 2.1 Physical signal properties used for measurement in positioning

2.4.1 Time of Arrival

In a terrestrial positioning system, TOA represents the time when the signal arrives at the receiver. Once TOA is estimated, assuming knowledge of the time when the signal was transmitted, the distance between transmitter and receiver can be easily calculated, considering that the propagation velocity of the signal in air can be considered constant, and as a first approximation equal to the speed of light $c = 299792458 m/s$. There are different configurations for TOA measurements based on different approaches. In general, this kind of measurement suffers some drawbacks, like the necessity to have a good synchronization between anchor nodes and blind nodes in order to achieve a good TOA estimation.

A simplest case of TOA system assumes synchronization between transmitter and receiver, usually obtained by sharing the same reference clock. During transmission, a timestamp representing the transmission time t_{tx}, is sent to the receiver. In this case, the receiver estimates the TOA $\hat{t}_{rx}$ and the distance can be calculated according to:

$$\hat{d} = \left(\hat{t}_{rx} - t_{tx}\right) c. \tag{2.1}$$

Equation (2.1) assumes that the transmitter and the receiver are synchronized, but in general this is very difficult to achieve. Without a perfect synchronization, there remains a bias in the system which must be considered in Equation (2.1), otherwise the distance estimation error increase. Supposing that the receiver has a time clock offset t_{of} with respect to the transmitter's clock, when the receiver estimates the TOA, the $\hat{t}_{rx}$ value is based on its clock. In this case, the system is not estimating the distance

correctly, but is estimating a quantity $\hat{\rho} = \left(\hat{t}_{rx} - t_{tx}\right) c$, which is called pseudorange and contains a bias due to the clock offset. For evaluating correctly the distance, the clock offset has to be estimated with some techniques. Then the distance can be calculated as

$$\hat{d} = \left(\hat{t}_{rx} - t_{tx} - \hat{t}_{of}\right) c. \tag{2.2}$$

There are several techniques that allow to estimate the clock offset, e.g., in GPS, the clock offset is treated as an additional unknown in the positioning equations and is estimated together with the coordinates of the receiver [1].

A TOA solution that does not require a high cost in terms of synchronization between nodes, is the two-way TOA ranging. In this approach, the transmitter node sends a signal to the receiver node, which in turn sends back the signal to the transmitter after a defined time delay Δt_{rx}. When the transmitter receives the signal, it estimates the TOA $\hat{t}_{2d}$ relative to the two-way trip plus the receiver time delay. Assuming that the time Δt_{rx} is known, the distance in this case is calculated as

$$\hat{d} = \left(\hat{t}_{2d} - t_{tx} - \Delta t_{rx}\right) \frac{c}{2}. \tag{2.3}$$

The main benefit of this approach is that the receiver does not need to be synchronized with the transmitter. A potential problem occurs if the receiver's clock is not precise, since this can introduce an error about the knowledge of Δt_{rx}, which is unknown at the transmitter. Another drawback is that, with this approach, all the nodes of the network have an active role, and in particular all the nodes must be transceivers (i.e., devices that can both transmit and receive signals), which means that the cost of the system can increase.

Assuming a good propagation environment, one of the factors that most influences the error in TOA estimations is the granularity of the internal clock. Indeed, for every received signal that is within a clock period, the estimated TOA will be the same. Another potential problem is the propagation environment. In fact, if the signal propagates in a line of sight (LOS) condition, which means that there is a virtual line that connects the transmitter and the receiver, with no obstacle in between, the TOA measurement is related to the distance between the nodes. On the other hand, if the environment is characterized by a no line of sight (NOLOS) condition or by multipath were the strongest component is not represented by the direct path, the resulting distance estimation will be biased. To overcome these issues, appropriate signal processing techniques must be applied to the received signal in order to improve

the resolution and to separate the TOA component due to the direct path from the other components. This thesis tackles this problem and some algorithms will be presented in Chapter 4. The result of this thesis will show the behaviour of these algorithms through simulations and also in a real scenario experiments.

2.4.2 Time Difference of Arrival

The TDOA technique is based on the difference between two TOA measurements. This technique was proposed to avoid the need for synchronization between transmitters and receivers. With this approach, only the anchor nodes must be synchronized. Suppose that two synchronized anchor nodes transmit a reference signal at the same time and that the mobile receiver estimates the TOA coming from the two anchors according to its internal clock. Considering that there is a bias t_{of} between the receiver clock and the transmitters clock, and that the distances between the anchors and the receiver are d_1 and d_2 for the first and second anchors respectively, the time difference between the two TOAs ΔT is

$$\Delta T = t_{rx,1} - t_{rx,2} = t_{tx} + \frac{d_1}{c} + t_{of} - \left(t_{tx} + \frac{d_2}{c} + t_{of} \right) = \frac{d_1 - d_2}{c}. \tag{2.4}$$

It is clear that the contribution of the transmission time and of the offset is cancelled with this approach. Moreover, note that this is not a distance measurement, but that it provides a differential value that can be employed in hyperbolic localization techniques, explained in detail in Section 2.5.2. Similarly to TOA techniques, also TDOA suffers multipath and NOLOS propagation. Note that the synchronization between the anchors node is not such a strict requirement, as it is possible to see in [10] that the localization can be done with asynchronous anchors, taking one of the anchors as a reference for the others.

TDOA measurements constitute the basis for the observed time difference of arrival (OTDOA), which is a technique based on LTE downlink communication for positioning purposes using the positioning reference signal (PRS). The LTE standard also defines a technique for uplink communication called uplink time difference of arrival (UTDOA) based on the transmission of the sounding reference signal (SRS). Further details on positioning tools in the LTE standard can be found in [11–15].

2.4.3 Angle of Arrival (AOA)

In AOA techniques, the angle of the incident signal that arrives at the receiver is measured, with respect to a fixed orientation. In general, AOA is referred to some reference orientation and the angle is defined as the angle formed by this reference and the virtual line that connects the transmitter to the receiver. To measure the AOA, two elements are needed. First, an antenna array with two or more elements, and, second, a signal processing algorithm that permits to estimate the angle starting from the signals received at each element of the antenna array.

Assuming that the receiver is placed at position (x_{rx}, y_{rx}) and that the transmitter is at position (x_{tx}, y_{tx}), the relative AOA θ is:

$$\theta = \arctan\left(\frac{y_{tx} - y_{rx}}{x_{tx} - x_{rx}}\right). \tag{2.5}$$

One of the biggest problems related to AOA measurement is the shadowing effect present in the propagation channel. Since shadowing can decrease the signal magnitude of the direct path, the magnitude of the received signal can be mostly due to a path that has a different angle with respect to the angle that connects the transmitter and the receiver, and this can cause a bias in the measurements. The benefit of this type of measurements is that no synchronization between the transmitter and the receiver, or between transmitters, is necessary.

2.4.4 Received Signal Strength (RSS)

In RSS techniques, the relationship between the received power and the distance is exploited. Indeed, assuming that the transmission power is known and that it is possible to calculate the power at the receiver, the loss in terms of power, due to the propagation distance, can be calculated. A propagation model establishes the relation between distance and power loss, but also depends on other parameters. Taking into account a simple model like the one in [16], the instantaneous received power $P_{rx,dB}(t)$ in dB can be calculated as

$$P_{rx,dB}(t) = P_{tx,dB} - 10\,\alpha \log_{10}(d) - K - X_f(t) - X_s, \tag{2.6}$$

where $P_{tx,dB}$ is the transmission power, K is a gain factor depending on the antenna gain and the carrier frequency, $X_f(t)$ is a random variable (RV) that models the instantaneous small scale fading, X_s is the shadowing term corresponding to a large attenuation due to an obstacle in the propagation environment (usually modeled as

Environment	Range of α
Urban macrocells	3.7-6.5
Urban microcells	2.7-3.5
Office buildings (same floor)	1.6-3.5
Office buildings (multiple floors)	2-6
Store	1.8-2.2
Factory	1.6-3.3
Home	3

Table 2.2 Typical values of the path loss exponent

a log-normal RV), and $10\,\alpha\log_{10}(d)$ is the attenuation due to distance d according to the path loss exponent α, which represents the attenuation due to the particular propagation environment. Typical values for the path loss exponent are reported on Table 2.2 [16]. The fading term rapidly changes in time, so it can be easily removed by averaging a certain number of measurements, obtaining the average power $\overline{P}_{rx,dB}(t)$. Assuming we know the gain parameter K and the path loss exponent α, it is possible to estimate the distance from the mean power as

$$\hat{d} = 10^{\frac{\overline{P}_{rx,dB}(t) - P_{tx,dB} + K}{10\cdot\alpha}}. \tag{2.7}$$

The distance estimated with this method is strongly dependent on the path loss exponent. Usually, this value is obtained after some calibration measurement campaign, or determined dynamically according to some strategies.

Similar to TDOA-based localization, also with RSS it is possible to apply differential measurements. In this case the technique is called DRSS. This technique preserves all the advantages of RSS-based localization. One benefit is that the control overhead message between anchors and the blind node is minimized or even no longer required, which saves energy, bandwidth and throughput [17]. In this case the estimation is not related to the difference of the distances, but it is related to the ratio of the distances when the subtraction is calculated from values in dB.

Another benefit of this technique is that it does not need synchronization of the nodes and it is simple to implement. Indeed, the receiver needs only to be able to estimate the power of the received signals, which is typically a common function for the most used communications devices. The main drawback is that the error on distance estimation is highly dependent on how much the chosen models fit the real propagation

environment. Indeed, an incorrect path loss exponent can cause high errors in the final distance estimation.

2.4.5 Cell ID

Cell ID is a non ambiguous identifier signal that the BSs usually broadcast to all the MSs. In wireless CID positioning systems, the MS usually uses the CIDs transmitted by the BSs to estimate its position. Typically, the MS checks the CID of the BS to which it is connected, and also searches if other CIDs coming from other BSs can be detected. Once the MS has the information of the visible CIDs, it queries a database where information that relate visible CIDs with positions are stored. If just one BS is visible, the position of the MS is approximated to the position of the BS, with an error equal to the coverage range of the BS. To achieve a better position estimation, in LTE the CID method is enhanced by using other information. This technique is called enhanced cell ID (E-CID) and usually exploits four different sources: the CID and the corresponding geographical description of the serving cell, the time advance (TA) of the serving cell, which is a time offset calculated by the BS in order to maintain a time alignment in uplink transmission, the CIDs signals coming from the other cells, as well as the AOA of the CIDs. Typically, the TA measurement is a two-way measurement (section 2.4.2) so it gives a distance information, then combining this distance with the AOA and CIDs information, it is possible to improve the position estimate.

2.4.6 Carrier Phase Measurement

The phase of a received continuous-wave can be used to estimate distance. In this technique, an anchor transmits a tone and the receiver measures the phase of the received signal. Assuming that the phase of the transmitter is equal to zero, the total distance between transmitter and receiver can be written as

$$d = \lambda \left(\frac{\phi}{2\pi} + n \right), \tag{2.8}$$

where λ is the wavelength of the tone, ϕ is the phase, and n is an integer that represents the number of wavelengths intercurring between the transmitter and receiver for distances greater than λ. The n value represents an ambiguity that has to be solved.

The literature reports many techniques to solve these ambiguities and estimate d [18]. In one simple strategy, one can send two tones and measure the difference between the phase of the two received signals.

The benefit of this technique is that it is possible to reach very high precision in position estimation, also with cellular-based positioning systems in LOS conditions, as reported in [19]. On the other hand, one of the main drawback of carrier phase measurement is multipath propagation, because in such scenario the phase measurement is corrupted by the superposition of different replica of the signal, which cause an error in the position estimation.

2.4.7 Power Delay Profile (PDP)

Similar to CID techniques, PDP is used in positioning systems which adopt fingerprinting. This technique has a calibration phase in which the power received from BSs is measured at some particular positions, then the power/positions pairs are stored in a database. During the positioning phase, the receiver measures the received power and, after that, it queries the database in order to compare the measure with those present in the database. Then, the database answers with the position corresponding to the power most similar to the one measured.

2.5 Positioning Techniques

After the measurement phase, some positioning techniques must be applied to the collected measures in order to estimate the position. In this section, some common positioning techniques are presented. Usually, these techniques are strongly related to the type of measurement used. In the following, the concepts of lateration, hyperbolic positioning, angulation and hybrid approaches are presented. In particular, hybrid approaches estimate the position exploiting a combination of different types of measurements. More detail about positioning techniques can be found in [2, 9, 20–22].

2.5.1 Lateration

The lateration techniques exploit the distance estimates between the blind node and the anchors, in order to localize the blind node. Those distances can be calculated with TOA or RSS measurements. In a general case where there are M anchors, the geometric interpretation consists in finding the point of intersection of a set of M circumferences (spheres in the 3D case) centered at the anchor positions $\mathbf{p}_m \in \mathbb{R}^D$, $m = 1, \ldots, M$,

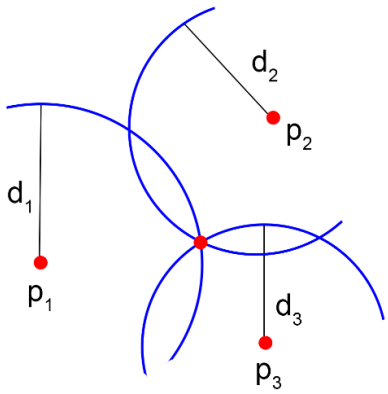

Fig. 2.2 Geometrical example of lateration with three anchors.

with radius equal to the measured distances $\hat{d}_m$, $m = 1, \ldots, M$, $D \in \{2, 3\}$. Indeed, if we consider the 2D case where the position of the m-th anchor is $\mathbf{p}_m = [x_m, y_m]^T$, the position of the blind node is $\mathbf{p} = [x, y]^T$ and $d_m = \tau_m c = (t_{rx,m} - t_{tx})c$, where τ_m is time that the signal takes to go from the m-th anchor to the blind node, it is possible to write

$$d_m = ||\mathbf{p}_m - \mathbf{p}|| = \sqrt{(x_m - x)^2 + (y_m - x)^2}. \tag{2.9}$$

Squaring and manipulating Equation (2.9), it is possible to obtain

$$(x_m - x)^2 + (y_m - x)^2 = (\tau_m c)^2 , \tag{2.10}$$

which is clearly an equation that defines a circle with radius d_m whose center lies in the position of the m-th anchor. Then, considering all the M anchors, the intersection of the circles give the position of the blind node, as depicted in Figure 2.2.

In the general case of M anchors, the position of the blind node is mathematically obtained by solving the system of equations

$$\begin{cases} ||\mathbf{p}_1 - \mathbf{p}|| = \hat{d}_1 \\ ||\mathbf{p}_2 - \mathbf{p}|| = \hat{d}_2 \\ \ldots \\ ||\mathbf{p}_M - \mathbf{p}|| = \hat{d}_M \end{cases} = \begin{cases} \sqrt{(x_1 - x)^2 + (y_1 - y)^2} = \hat{d}_1 \\ \sqrt{(x_2 - x)^2 + (y_2 - y)^2} = \hat{d}_2 \\ \ldots \\ \sqrt{(x_M - x)^2 + (y_M - y)^2} = \hat{d}_M \end{cases} , \tag{2.11}$$

which is a non linear system that has to be solved with respect to the unknown position $\mathbf{p} \in \mathbb{R}^D$. Since the system of Equation (2.11) is a system with D unknowns, the minimum number of equations that are required in order to find a finite number of solutions is D. This determines the constraint that at least D anchors are needed to find a finite number of solutions, usually with some remaining ambiguity in the position estimation (e.g., the intersection of two circles defines in general two points). The goal is to find a unique solution, so at least $D+1$ anchors are needed to remove the ambiguity. This implies that we must have at least $M = 3$ anchors and $M = 4$ anchors for 2D and 3D position estimation, respectively. In a real scenario the measurements are affected by noise, thus the distance estimate do not represent the correct distance values. In this case, it can happen that the system of equations (2.11) cannot be solved. To address this problem, several approaches are available, the most popular are the least squares (LS) algorithm [9], and Bayesian methods such as the extended Kalman filter (EKF) or particle filters.

Using a mathematical trick it is possible to linearize the system of equations (2.11) and use a linear least squares (LLS) algorithm to solve the problem. In the following, the 2D estimation case will be considered for simplicity, but it is easy to extend the procedure also to the 3D case. Without loss of generality, if we take the first anchor as a reference, it is possible to square Equation (2.9) and subtract the expression for the m-th anchors to the one of the first anchor. The result is

$$d_m^2 - d_1^2 = x_m^2 + y_m^2 - x_1^2 - y_1^2 - 2x\left(x_m - x_1\right) - 2y\left(y_m - y_1\right). \tag{2.12}$$

Doing the same for all the anchors and using a matrix notation the system of equations can be written as

$$\mathbf{Hp} = \mathbf{B}, \tag{2.13}$$

where $\mathbf{p}$ is the vector with the unknown coordinates, $\mathbf{H}$ is

$$\mathbf{H} = \begin{bmatrix} x_2 - x_1 & y_2 - y_1 \\ x_3 - x_1 & y_3 - y_1 \\ \vdots & \vdots \\ x_M - x_1 & y_M - y_1 \end{bmatrix}, \tag{2.14}$$

and $\mathbf{B}$ is

$$\mathbf{B} = \frac{1}{2}\begin{bmatrix} (d_1^2 - d_2^2) + (x_2^2 + y_2^2) - (x_1^2 + y_1^2) \\ (d_1^2 - d_3^2) + (x_3^2 + y_3^2) - (x_1^2 + y_1^2) \\ \vdots \\ (d_1^2 - d_M^2) + (x_M^2 + y_M^2) - (x_1^2 + y_1^2) \end{bmatrix}. \tag{2.15}$$

Then, the linear least square solution of Equation (2.13) can be obtained, as it is well known, by using the pseudo-inverse of $\mathbf{H}$

$$\mathbf{p} = \left(\mathbf{H^T H}\right)^{-1} \mathbf{H^T B}. \tag{2.16}$$

2.5.2 Hyperbolic Positioning

An alternative to the lateration technique is hyperbolic positioning. In this case, the position estimate is calculated using differential measurements, such as TDOA. Every TDOA measurement permits to evaluate the distance difference from the i-th and j-th anchor nodes

$$\Delta\hat{D}_{i,j} = \left(\hat{t}_{rx,i} - \hat{t}_{rx,j}\right) c = \hat{d}_{rx,i} - \hat{d}_{rx,j},\ i \neq j. \tag{2.17}$$

In the 2D case, it is well known that for any point on a hyperbola, the absolute difference of the distance to the two hyperbola foci has a constant value, and that the sign of the distance difference can identify one of the two hyperbola branches. Therefore, as depicted in Figure 2.3, the differential measurement obtained between two anchors describes an hyperbola, with the foci located at the positions of the two anchors. For a single TDOA measurement, the position of the blind node is ambiguous, and it can be located at any point along the hyperbolic curve, or hyperboloid surface in 3D space. With more than one TDOA measurements, the intersection of all the hyperbolas, or hyperboloids, allows to identufy the location of the blind node.

The generic mathematical description with M anchors, requires the solution of the following non linear system of $M-1$ equations

$$\begin{cases} ||\mathbf{p}_1 - \mathbf{p}|| - ||\mathbf{p}_2 - \mathbf{p}|| = \Delta\hat{D}_{1,2} \\ ||\mathbf{p}_1 - \mathbf{p}|| - ||\mathbf{p}_3 - \mathbf{p}|| = \Delta\hat{D}_{1,3} \\ \dots \\ ||\mathbf{p}_1 - \mathbf{p}|| - ||\mathbf{p}_M - \mathbf{p}|| = \Delta\hat{D}_{1,M} \end{cases}. \tag{2.18}$$

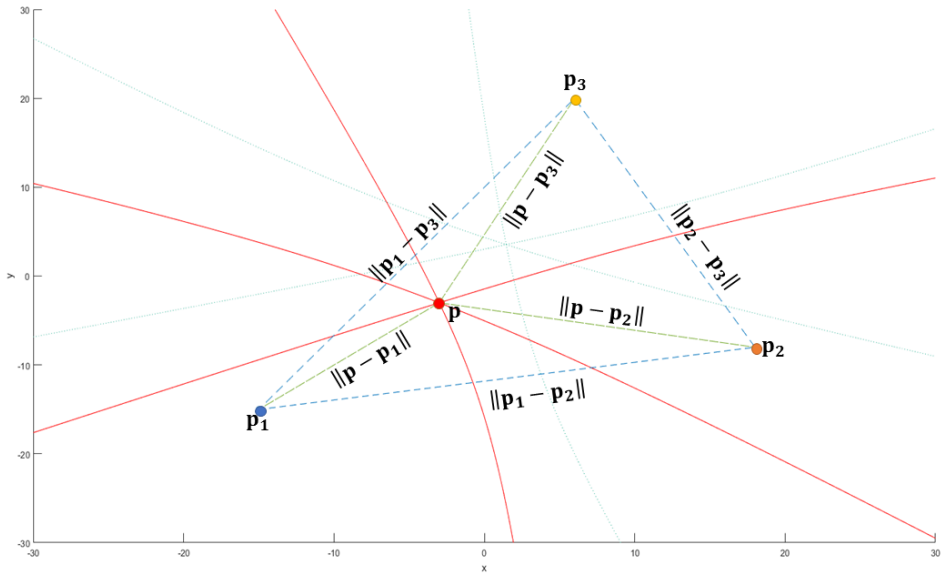

Fig. 2.3 Geometrical example of hyperbolic positioning with three anchors.

It should be noted that with M anchors there are $\frac{1}{2}M\,(M-1)$ possible distance difference equations, however only $M-1$ equations are useful for position estimation. This is because the additional equations are linear combinations of the set of $M-1$ equations. For example, with $M=3$, it is possible to calculate three different distances differences, $\Delta D_{1,2}$, $\Delta D_{1,3}$ and $\Delta D_{2,3}$, but $\Delta D_{2,3}$ is a linear combination of the first two equations, indeed

$$\Delta D_{2,3} = d_2 - d_3 = \Delta D_{1,3} - \Delta D_{1,2} = (d_1 - d_3) - (d_1 - d_2)\,. \tag{2.19}$$

The set of nonlinear equations (2.18) may not easy to solve, but it is possible to adopt a linearization similar to the one adopted for TOA measurements. Thus, considering the 2D case for simplicity, it is possible to take the first anchor as a reference and define the TDOA measurements $\Delta T_{i,1} = (t_{rx,i} - t_{rx,1})$ and the distance difference $\Delta D_{i,1}$ between the i-th anchor and the first anchor. With this assumption, the system of equations can be solved as follows. Consider

$$\Delta D_{i,1} = d_i - d_1, \tag{2.20}$$

then

$$(\Delta D_{i,1} + d_1)^2 = \Delta D_{i,1}^2 + 2\Delta D_{i,1} d_1 + d_1^2 = d_i^2. \tag{2.21}$$

Manipulating Equation (2.21), one obtains

$$\Delta D_{i,1}^2 + 2\Delta D_{i,1} d_1 = x_i^2 + y_i^2 - x_1^2 - y_1^2 - 2x\left(x_i - x_1\right) - 2y\left(y_i - y_1\right). \tag{2.22}$$

Now, writing Equation (2.22) for all the M anchors and using a matrix notation the system becomes

$$\mathbf{H}\mathbf{x} = \mathbf{B}, \tag{2.23}$$

where

$$\mathbf{x} = \left[x, y, d_1\right]^T, \tag{2.24}$$

$$\mathbf{H} = \begin{bmatrix} x_2 - x_1 & y_2 - y_1 & \Delta D_{2,1} \\ x_3 - x_1 & y_3 - y_1 & \Delta D_{3,1} \\ \vdots & \vdots & \vdots \\ x_M - x_1 & y_M - y_1 & \Delta D_{M,1} \end{bmatrix}, \tag{2.25}$$

$$\mathbf{B} = \frac{1}{2}\begin{bmatrix} (x_2^2 - y_2^2) - (x_1^2 - y_1^2) - \Delta D_{2,1}^2 \\ (x_3^2 - y_3^2) - (x_1^2 - y_1^2) - \Delta D_{3,1}^2 \\ \vdots \\ (x_M^2 - y_M^2) - (x_1^2 - y_1^2) - \Delta D_{M,1}^2 \end{bmatrix}. \tag{2.26}$$

Similarly to the lateration case, the solution is

$$\mathbf{x} = \left(\mathbf{H}^T\mathbf{H}\right)^{-1}\mathbf{H}^T\mathbf{B}. \tag{2.27}$$

In this case, it is important to notice that to solve the problem a further unknown is added to the system, which is the distance d_1 from the reference anchor. The estimation of this parameter is made together with the estimation of the coordinates of the blind node.

2.5.3 Angulation

Angulation is a technique that uses AOA measurements in order to locate the blind node. The algorithm can rely only on two anchors in a 2D scenario and on three anchors in a 3D scenario. The geometrical interpretation of angulation in 2D space is based on rays that start from the position of the anchors, and follow the direction of the angle. Thus, the intersection point of these rays identifies the position of the blind node. Figure 2.4 shows an example of angulation in 2D space with three anchors. It is easy to extend this concept to 3D space. Indeed, if there are at least 3 anchors, with at least one anchor measuring the zenith distance and one anchor measuring the azimuth, it is possible to locate a blind node in the 3D space. Also for the angulation

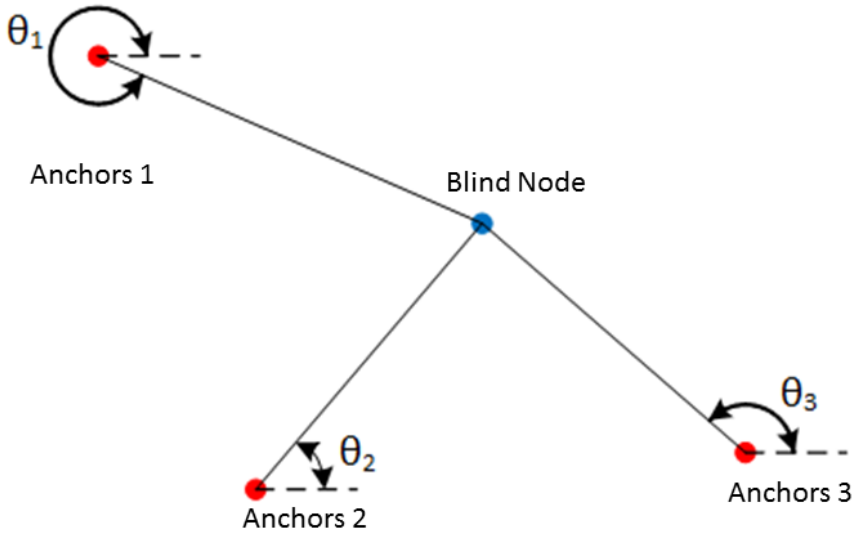

Fig. 2.4 Geometrical example of angulation positioning with three anchors.

technique, one can write a system of equations to calculate the position of the blind node. Assuming a 2D space and that there are M anchors, Equation (2.5) for the i-th anchor can be written as

$$(x_i - x)\sin\theta_i = (y_i - y)\cos\theta_i. \tag{2.28}$$

Then, in matrix notation, the system of equations can be written as

$$\mathbf{Hp} = \mathbf{B}, \tag{2.29}$$

where

$$\mathbf{p} = [x, y]^T, \tag{2.30}$$

$$\mathbf{H} = \begin{bmatrix} -\sin\theta_1 & \cos\theta_1 \\ -\sin\theta_2 & \cos\theta_2 \\ \vdots & \vdots \\ -\sin\theta_M & \cos\theta_M \end{bmatrix}, \tag{2.31}$$

$$\mathbf{B} = \frac{1}{2} \begin{bmatrix} y_1\cos\theta_1 - x_1\sin\theta_1 \\ y_2\cos\theta_1 - x_2\sin\theta_1 \\ \vdots \\ y_M\cos\theta_1 - x_M\sin\theta_1 \end{bmatrix}. \tag{2.32}$$

The solution is given by

$$\mathbf{p} = \left(\mathbf{H}^T\mathbf{H}\right)^{-1}\mathbf{H}^T\mathbf{B}. \tag{2.33}$$

2.5.4 Hybrid Approaches

In hybrid approaches, usually two or more different techniques are merged in order to improve the position estimates. Fingerprinting and other techniques can be used for hybrid localization. The biggest challenge of this approach is to combine properly the data coming from different techniques. In the following, using the same notation used before, two hybrid solutions will be considered. The first solution merges AOA and TOA measurements and is called hybrid angulation and lateration. The second solution, instead, merges AOA and TDOA measurements and is called hybrid angulation and hyperbolic positioning.

We assume M anchors and that the i-th anchor can measure the AOA θ_i and the distance related to the TOA from the anchor to the blind node d_i. The solution for hybrid angulation and lateration is the same described in Equation (2.16), where $\mathbf{p} = [x, y]^T = \left(\mathbf{H}^T\mathbf{H}\right)^{-1}\mathbf{H}^T\mathbf{B}$, with the only difference that the matrices $\mathbf{H}$ and $\mathbf{B}$ are defined as

$$\mathbf{H} = \begin{bmatrix} x_2 - x_1 & y_2 - y_1 \\ x_3 - x_1 & y_3 - y_1 \\ \vdots & \vdots \\ x_M - x_1 & y_M - y_1 \\ -\sin\theta_1 & \cos\theta_1 \\ -\sin\theta_2 & \cos\theta_2 \\ \vdots & \vdots \\ -\sin\theta_M & \cos\theta_M \end{bmatrix}, \tag{2.34}$$

$$\mathbf{B} = \frac{1}{2} \begin{bmatrix} (d_1^2 - d_2^2) + (x_2^2 + y_2^2) - (x_1^2 + y_1^2) \\ (d_1^2 - d_3^2) + (x_3^2 + y_3^2) - (x_1^2 + y_1^2) \\ \vdots \\ (d_1^2 - d_M^2) + (x_M^2 + y_M^2) - (x_1^2 + y_1^2) \\ y_1\cos\theta_1 - x_1\sin\theta_1 \\ y_2\cos\theta_1 - x_2\sin\theta_1 \\ \vdots \\ y_M\cos\theta_1 - x_M\sin\theta_1 \end{bmatrix}. \tag{2.35}$$

In hybrid angulation and hyperbolic positioning the solution is the same described in Equation (2.27). Thus, $\mathbf{x} = [x, y, d_1]^T = \left(\mathbf{H}^T\mathbf{H}\right)^{-1}\mathbf{H}^T\mathbf{B}$, with the only difference that the matrices $\mathbf{H}$ and $\mathbf{B}$ are defined as

$$\mathbf{H} = \begin{bmatrix} x_2 - x_1 & y_2 - y_1 & \Delta D_{2,1} \\ x_3 - x_1 & y_3 - y_1 & \Delta D_{3,1} \\ \vdots & \vdots & \vdots \\ x_M - x_1 & y_M - y_1 & \Delta D_{M,1} \\ -\sin\theta_1 & \cos\theta_1 & 0 \\ -\sin\theta_2 & \cos\theta_2 & 0 \\ \vdots & \vdots & \vdots \\ -\sin\theta_M & \cos\theta_M & 0 \end{bmatrix}, \tag{2.36}$$

$$\mathbf{B} = \frac{1}{2}\begin{bmatrix} (x_2^2 - y_2^2) - (x_1^2 - y_1^2) - \Delta D_{2,1}^2 \\ (x_3^2 - y_3^2) - (x_1^2 - y_1^2) - \Delta D_{3,1}^2 \\ \vdots \\ (x_M^2 - y_M^2) - (x_1^2 - y_1^2) - \Delta D_{M,1}^2 \\ y_1 \cos\theta_1 - x_1 \sin\theta_1 \\ y_2 \cos\theta_1 - x_2 \sin\theta_1 \\ \vdots \\ y_M \cos\theta_1 - x_M \sin\theta_1 \end{bmatrix}. \tag{2.37}$$

Chapter 3

LTE Signals For Positioning

3.1 Introduction

The 3GPP Long Term Evolution (LTE) provides the standard for the fourth generation of cellular mobile communications. The BS is usually defined as an Evolved Node B (eNodeB), which has a non-ambiguous cell ID in order to identify different BSs in the same environment. The mobile receiver meanwhile, is usually called user equipment (UE). The physical layer is the lowest protocol layer in telecommunications: it is at the interface between upper telecommunications layers and the physical media, such as the wireless channel. The LTE physical layer receives instructions from upper communications layers and processes them through functions such as channel coding, interleaving, baseband modulation, layer mapping for multi-antenna operation, precoding, antenna mapping functions and access scheme. The downlink communication, which occurs from the eNodeB to the UE, takes place through an orthogonal frequency division multiplexing (OFDM) modulation. The OFDM modulation is a special case of multi-carrier transmission, where the sub-carriers frequencies maintain spectral orthogonality. On the contrary, the uplink communication, that occurs from the UE to the eNodeB, takes place through a single carrier frequency division multiple access (SC-FDMA) modulation. The SC-FDMA is similar to OFDM with the main difference that it has a precoding stage obtained by applying a discrete Fourier transform (DFT). In the first part of this chapter a brief description of the LTE downlink and uplink physical layers is provided, with focus on OFDM modulation, SC-FDMA modulation and the radio frame structure. Then, common downlink and uplink reference signals (RSs) used for positioning purposes, are described.

3.2 Orthogonal Frequency Division Multiplexing (OFDM)

3.2.1 OFDM Modulation

OFDM modulation was designed in the LTE standard for being the modulation adopted in the downlink physical layer. The basic idea of this modulation scheme is to transmit different complex symbols using different sub-carriers. So, the overall transmitted signal is wideband, but the symbols carrying information are transmitted with parallel narrowband transmissions. In this way, OFDM is able to treat a frequency selective channel as a set of adjacent narrowband frequency non-selective channels.

OFDM modulation starts with a high-rate stream of data bits, which is first converted from serial to parallel. This procedure creates some blocks of data bits, which are subsequently converted into complex symbols using a quadrature amplitude modulation (QAM) or a phase-shift keying (PSK) modulation. The OFDM signal can be specified by defining the complex symbol transmitted on each subcarrier. Considering an OFDM system with a number N_{IDFT} of available sub-carriers, a signal in the frequency domain can be specified by the sequence

$$\mathbf{S} = \left[S_{-\frac{N_{IDFT}}{2}}, \ldots, S_{-1}, S_0, S_1, \ldots, S_{\frac{N_{IDFT}}{2}-1}\right]^T \in \mathbb{C}^{N_{IDFT}} \tag{3.1}$$

Each complex symbol obtained after QAM/PSK modulation is associated one by one to a subcarrier S_k according to some strategies. Usually, not all the N_{IDFT} available subcarriers are filled with some complex symbols; indeed the subcarriers at the edges of the band (i.e., those close to $S_{-\frac{N_{IDFT}}{2}}$ and $S_{\frac{N_{IDFT}}{2}}$) and the symbol corresponding to the center frequency, are set to zero, that is

$$S_k = \begin{cases} \text{some complex symbol,} & \text{if} \quad k \in \left[\frac{-N_{sc}}{2}, -1\right] \\ \text{some complex symbol,} & \text{if} \quad k \in \left[1, \frac{N_{sc}}{2}\right] \\ 0 & \text{otherwise,} \end{cases}, \tag{3.2}$$

where $N_{sc} < N_{IDFT}$ is the number of occupied subcarriers. The subcarriers at the edges of the available band are set to zero to avoid the interference with adjacent channels. The center frequency, instead, is set to zero to avoid the transmission of a symbol at the zero frequency, which corresponds to a DC voltage value in time domain. Once the complex symbols are mapped to the subcarriers in the frequency domain, it

is possible to apply an inverse Fourier transform in order to obtain the time domain signal, given by

$$s\left(t\right) = \sum_{k=-N_{sc}/2}^{N_{sc}/2} S_k \cdot e^{j2\pi k \Delta f t}, \quad t \in [0, T_{sym}[\,, \tag{3.3}$$

where T_{sym} is defined as the OFDM symbol duration, Δf is the subcarrier separation in frequency domain and an ideal interpolation is considered. If the subcarriers separation is $\Delta f = 1/T_{sym}$, orthogonality between the subcarriers is achieved. Sampling the continuous signal with a sampling period $T_s = T_{sym}/N_{IDFT}$ results in the discrete time signal,

$$\begin{aligned} s^{OFDM}\left[n\right] &= s\left(t\right)\big|_{t=n\frac{T_{sym}}{N_{IDFT}}} = \sum_{k=-N_{sc}/2}^{N_{sc}/2} S_k \cdot e^{j2\pi k \frac{1}{T_{sym}} \frac{nT_{sym}}{N_{IDFT}}} \\ &= \sum_{k=-N_{sc}/2}^{N_{sc}/2} S_k \cdot e^{j2\pi \frac{kn}{N_{IDFT}}} = \sum_{k=-N_{IDFT}/2}^{N_{IDFT}/2-1} S_k \cdot e^{j2\pi \frac{kn}{N_{IDFT}}} \\ &= \sum_{k=0}^{N_{IDFT}-1} \tilde{S}_k \cdot e^{j2\pi \frac{kn}{N_{IDFT}}} \\ &= N_{IDFT} \cdot IDFT\left\{\tilde{S}_k\right\}, \quad n = 0, \ldots, N_{IDFT} - 1, \end{aligned} \tag{3.4}$$

where $\tilde{S}_k$ is the sequence obtained applying the FFT-shift operation, corresponding to

$$\tilde{\mathbf{S}} = \left[S_0, S_1, \ldots, S_{\frac{N_{sc}}{2}}, \mathbf{0}^T_{N_{IDFT}-N_{sc}-1}, S_{\frac{N_{sc}}{2}}, \ldots, S_{-1}\right]^T \in \mathbb{C}^{N_{IDFT}} \tag{3.5}$$

Here, $\mathbf{0}^T_{N_{IDFT}-N_{sc}-1}$ is a column vector of zeros with length $N_{IDFT} - N_{sc} - 1$, corresponding to the zeros at the edge of the band, and $S_0 = 0$. Equation (3.4) shows that the discrete time signal $s^{OFDM}\left[n\right]$ is obtained applying an inverse-DFT (IDFT) with N_{IDFT} points, at the FFT-shifted version of sequence $\mathbf{S}$. Due to the definition of the IDFT, to obtain the correct amplitude, the signal has also to be multiplied by N_{IDFT}.

The OFDM scheme requires the addition of a cyclic prefix (CP) at the discrete time signal before DA conversion. The resulting signal, with CP, consists of a longer signal $s^{OFDM}_{cp}\left[n\right]$ that has at the beginning the last N_{cp} complex symbols of $s^{OFDM}\left[n\right]$, while the other N_{IDFT} complex symbols are equal to $s^{OFDM}\left[n\right]$. Thus, the total number of complex symbols that compose the discrete OFDM sequence is $N_{tot} = N_{IDFT} + N_{cp}$

and the sequence becomes

$$s_{cp}^{OFDM}[n] = \begin{cases} s^{OFDM}[N_{IDFT} - N_{cp} + n] & n = 0, \ldots, N_{cp} - 1, \\ s^{OFDM}[n - N_{cp}] & n = N_{cp}, \ldots, N_{tot}. \end{cases} \tag{3.6}$$

The time duration of the CP must be chosen greater than the maximum duration of the sampled baseband channel impulse response (CIR). Under this assumption the CP allows a simple frequency domain equalization thanks to the fact that, with the CP, the linear convolution with the channel becomes a circular convolution. The time interval occupied by the CP acts as a guard interval between subsequent OFDM symbols, and this permits to avoid inter-symbol interference, which is caused by the dispersivity of the channel [23].

The final continuous baseband OFDM signal is obtained after a DA conversion of $s_{cp}^{OFDM}[n]$. The resulting continuous signal $s_{cp}^{OFDM}(t)$, is

$$\begin{aligned} s_{cp}^{OFDM}(t) = & \sum_{k=-N_{IDFT}/2}^{-1} S_k \cdot e^{j2\pi k\Delta f(t-N_{cp}T_s)} + \\ & + \sum_{k=1}^{N_{IDFT}/2-1} S_k \cdot e^{j2\pi k\Delta f(t-N_{cp}T_s)}, \end{aligned} \tag{3.7}$$

where $t \in [0, N_{tot}T_s[$ and where we highlight the fact that there is no information in the subcarrier representing the central frequency, i.e., that $S_0 = 0$. After the DA conversion, the continuous baseband OFDM signal is up-converted to the carrier frequency f_C, resulting in the real transmitted continuous band-pass signal:

$$s_{tx}^{OFDM}(t) = \mathrm{Re}\left\{ s_{cp}^{OFDM}(t) \cdot e^{j2\pi f_C t} \right\} \tag{3.8}$$

3.2.2 OFDM Demodulation

The received signal is obtained by the convolution of the transmitted signal $s_{tx}^{OFDM}(t)$ with the continuous time CIR, plus noise. We assume that the signal is transmitted through a wireless multipath channel with L paths, with baseband impulse response

$$h(t) = \sum_{l=1}^{L} h_l \delta(t - \tau_l). \tag{3.9}$$

We also assume that the down-conversion from the band-pass signal to the baseband signal recovers it with no impairments due to frequency offset or carrier phase error.

The received baseband continuous time signal can be written as

$$r(t) = h(t) * s_{cp}^{OFDM}(t) + w(t) = \sum_{l=1}^{L} h_l s_{cp}^{OFDM}(t - \tau_l) + w(t). \tag{3.10}$$

Equation (3.10) assumes that the channel is constant during the duration of the OFDM symbol. In LTE, for example, with a standard cyclic prefix configuration (see Section 3.4), the duration of an OFDM symbol with CP is $T_{sym} + T_{cp,0} \approx 71.81\,\mu$s. According to [24], the coefficients h_l of the wireless CIR can be considered correlated inside the interval ΔT if its product with the maximum Doppler frequency f_D is smaller than 0.1, where the maximum Doppler frequency is $f_D = f_C v/c$, v is the relative velocity between transmitter and receiver and c is the speed of light. Considering that, in LTE, f_C is around 2 GHz, the maximum acceptable velocity is

$$f_d \cdot \Delta T \leq 0.1 \iff v \leq \frac{0.1c}{f_C \Delta T} \approx 208\,\frac{\text{m}}{\text{s}} \approx 748\,\frac{\text{km}}{\text{h}}, \tag{3.11}$$

which is very high compared with the usual speed in urban, indoor or pedestrian scenarios. Thus, the approximation of a constant channel is reasonable. Moreover, this approximation is crucial in OFDM system in order to work properly without performance loss.

Sampling the received signal $r(t)$ with and analog to digital (AD) converter and using the same sample period T_s used at the transmitter, the received discrete time signal is

$$r[n] = h[n] * s_{cp}^{OFDM}[n] + w[n] = \sum_{l=0}^{\tilde{L}-1} \tilde{h}_l s_{cp}^{OFDM}[n-l] + w[n], \quad n = 0, \ldots, N_{tot}, \tag{3.12}$$

where $h[n]$ is the discrete time channel equivalent to $h(t)$

$$h[n] = \sum_{l=0}^{\tilde{L}-1} \tilde{h}_l \delta[n-l]. \tag{3.13}$$

The values $\tilde{L}$ and $\tilde{h}_l$ represent the length of the CIR and the complex amplitude of the l-th sample of the CIR, respectively.

If L is smaller then the CP length, the discrete linear convolution between $h[n]$ and $s_{cp}^{OFDM}[n]$ is equal to the circular convolution between $h[n]$ and $s^{OFDM}[n]$. As demonstrated in [23], after discarding the first N_{cp} samples of the received signal $r[n]$,

the signal becomes

$$r[n] = h[n] \circledast_{N_{IDFT}} s^{OFDM}[n] + w[n], \quad n = 0, \ldots, N_{IDFT}, \tag{3.14}$$

where $\circledast_{N_{IDFT}}$ indicates the circular convolution calculated on N_{IDFT} samples. As a result of the circular convolution, the received signal $r[n]$ in the frequency domain corresponds to an element-wise multiplication between the channel frequency response (CFR) of the discrete channel, and the DFT values of the transmitted signal. Then

$$\begin{aligned}\mathbf{R} &= DFT\{r[n]\} = DFT\{h[n] \circledast_{N_{IDFT}} s^{OFDM}[n]\} + DFT\{w[n]\} = \mathbf{H} \odot \mathbf{S} + \mathbf{W} \\ &= [H_0 \cdot S_0 + W_0, \ldots, H_{N_{IDFT}-1} \cdot S_{N_{IDFT}-1} + W_{N_{IDFT}-1}]^T \in \mathbb{C}^{N_{IDFT}},\end{aligned} \tag{3.15}$$

where $\mathbf{H}$ is the sequence of CFR samples obtained by applying a DFT of length N_{IDFT} to the discrete sampled channel $h[n]$, and $\mathbf{W}$ is the sequence that represents the DFT of the noise. Equation (3.15) shows that the transmission of the signal over a frequency selective channel can be treated as the transmission over parallel flat-fading channels. As mentioned before, this result allows a simple single carrier equalization made by a complex multiplication for each subcarriers. The equalization process is used to recover the correct amplitude and phase of the transmitted subcarriers at the receiver. Indeed, the circular convolution property can be exploited to recover the H_k samples of $\mathbf{H}$. If $\mathbf{S}$ is known a priori at the receiver, dividing element-wise the $\mathbf{R}$ received samples by the $\mathbf{S}$ known samples, one can easily obtain the $\mathbf{H}$ samples.

In the LTE protocol, during a data transmission, some OFDM symbols are used to transmit Reference Signals. These signals are known in advance at the receiver and generally are used for coherent demodulation, channel estimation, determination of some indicator of the status of the network, and determination of resource allocation in case of multiple users connected to the same eNodeB. RSs sequences are constructed starting from particular complex sequences, such as Zadoff-Chu sequences or PSK sequences. Thus, the estimation of the k-th frequency sample of the channel can be obtained as

$$\hat{H}_k = \frac{R_k}{S_k} = H_k + \frac{W_k}{S_k}, \tag{3.16}$$

where S_k is known. As it will be shown in Chapter 4, the CFR samples are the input of the SAGE and IAA-APES algorithms. These algorithms exploit the CFR bins in order to estimate parameters like the TOA and the AOA of the received signal.

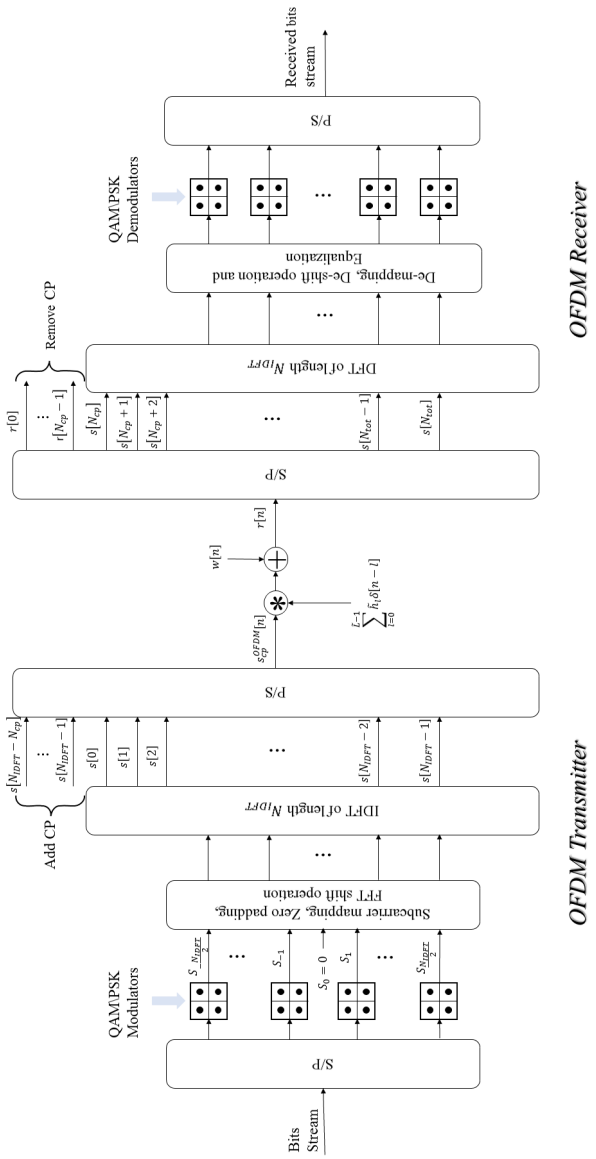

Fig. 3.1 Block scheme of an OFDM transceiver in discrete time domain, the representation of the system is in baseband. The left part represents the transmitter and the right part the receiver.

To summarize the whole procedure, an OFDM demodulator has to implement some steps in order to convert the received discrete baseband signal $r[n]$ into a data stream of bits. The first step consists in a serial to parallel conversion of the received samples and in the removal of the CP. Then, the resulting sequence is converted to the frequency domain through a DFT algorithm. After this, a subcarrier de-mapping is applied and the equalization is carried out exploiting the estimation of the taps H_k, obtained using RSs. Finally, a QAM\PSK demodulator takes as input the complex symbols and convert them to bits. Figure 3.1 summarizes the overall OFDM modulation and demodulation procedure in discrete time domain.

3.3 Single Carrier Frequency Division Multiple Access (SC-FDMA)

3.3.1 Modulation

The LTE uplink physical layer is similar to the downlink, but it poses some different challenges with respect to downlink. Some attributes that LTE uplink needs include orthogonal uplink transmission by different UEs to minimize intra-cell interference, and low peak to average power ratio (PAPR) to avoid excessive cost in terms of the UE power consumption[23]. The modulation used to satisfy these requirements is SC-FDMA, which combines the desirable OFDM characteristics with a small PAPR. Similar to OFDM, SC-FDMA divides the transmission bandwidth into multiple parallel sub-carriers, and prevents the inter-symbol interference by using the CP. As in OFDM, the CP converts the linear convolution into a cyclic convolution in order to make an easy equalization possible. The main difference between OFDM and SC-FDMA consists in a preliminary "spreading" operation of the complex symbols, performed after the QAM\PSK conversion of the data bits stream. This operation is carried out by calculating the DFT of blocks of N_{DFT} input symbols, where $N_{DFT} < N_{IDFT}$. Thus, one starts from the QAM\PSK sequence

$$\mathbf{x} = [x_1, x_2, \ldots, x_{N_{DFT}}]^T \in \mathbb{C}^{N_{DFT}}, \tag{3.17}$$

where x_m represents the m-th QAM\PSK complex value and N_{DFT} is the number of DFT points. Applying the DFT to $\mathbf{x}$, one obtains

$$X_k = \sum_{m=1}^{N_{DFT}} x_m e^{-j2\pi \frac{km}{N_{DFT}}}, \quad k = 1, \ldots, N_{DFT}, \tag{3.18}$$

and constructs the sequence $\mathbf{X}$

$$\mathbf{X} = [X_1, X_2, \ldots, X_{N_{DFT}}]^T \in \mathbb{C}^{N_{DFT}}. \tag{3.19}$$

After the DFT spreading operation, SC-FDMA modulation is similar to OFDM. Indeed, there are N_{IDFT} subcarriers available, but the subcarriers at the edges of the transmission band are used as guard bands. Only N_{sc} subcarriers can be used to transmit complex symbols. The N_{DFT} samples are mapped to some of the available N_{sc} subcarriers. When $N_{DFT} < N_{sc}$, the remaining $N_{sc} - N_{DFT}$ subcarrier values are set to 0. Considering the frequency domain sequence

$$\mathbf{S} = \left[S_{-\frac{N_{IDFT}}{2}}, \ldots, S_{-1}, S_0, S_1, \ldots, S_{\frac{N_{IDFT}}{2}}\right]^T \in \mathbb{C}^{N_{IDFT}} \tag{3.20}$$

the N_{DFT} complex symbols can be assigned to the sequence as:

$$S_k = \begin{cases} \text{some DFT complex symbol,} & \text{if} \quad k \in \left[\frac{-N_{sc}}{2}, \frac{N_{sc}}{2}\right] \\ 0 & \text{otherwise} \end{cases}, \tag{3.21}$$

where in this case the S_0 subcarrier can be assigned to some complex value. The discrete time SC-FDMA signal is obtained from S_k as:

$$\begin{aligned} s^{SCFDMA}[n] &= \sum_{k=-N_{sc}/2}^{N_{sc}/2-1} S_k \cdot e^{j2\pi\left(k+\frac{1}{2}\right)\Delta f \frac{nT_{sym}}{N_{IDFT}}} = \sum_{k=-N_{sc}/2}^{N_{sc}/2-1} S_k \cdot e^{j2\pi\frac{\left(k+\frac{1}{2}\right)n}{N_{IDFT}}} \\ &= \sum_{k=-N_{IDFT}/2}^{N_{IDFT}/2-1} S_k \cdot e^{j2\pi\frac{kn}{N_{IDFT}}} \cdot e^{j2\pi\frac{1}{2}\frac{n}{N_{IDFT}}} \\ &= \sum_{k=0}^{N_{IDFT}-1} \tilde{S}_k \cdot e^{j2\pi\frac{kn}{N_{IDFT}}} \cdot e^{j2\pi\frac{1}{2}\frac{n}{N_{IDFT}}} \\ &= N_{IDFT} \cdot IDFT\left\{\tilde{S}_k\right\} \cdot e^{j2\pi\frac{1}{2}\frac{n}{N_{IDFT}}}, \quad n = 0, \ldots, N_{IDFT} - 1, \end{aligned} \tag{3.22}$$

where $\tilde{S}_k$ is the sequence obtained applying the FFT-shift operation, so the left and right halves of the sequence $\mathbf{S}$ are swapped. Note that another difference with respect

to OFDM is the multiplication by $e^{\left(j2\pi\frac{1}{2}\frac{n}{N_{dft}}\right)}$. The multiplication by the exponential term in the time domain is equivalent to a shift of all the sub-carriers by one half of the sub-carrier spacing $\Delta f/2$ in the frequency domain. This approach is used to avoid the transmission of a DC component in time domain. As mentioned before, the SC-FDMA system scheme uses a CP that occupies N_{cp} samples, too. Similarly to OFDM, the CP consists of the final N_{cp} samples of $s^{SCFDMA}[n]$ inserted before the first sample of $s^{SCFDMA}[n]$, but in this case with a change of sign. The discrete time sequence becomes

$$s_{cp}^{SCFDMA}[n] = \begin{cases} s^{SCFDMA}[N_{IDFT} - N_{cp} + n] & n = 0, \ldots, N_{cp} - 1, \\ -s^{SCFDMA}[n - N_{cp}] & n = N_{cp}, \ldots, N_{tot}. \end{cases} \tag{3.23}$$

Similarly to OFDM, also in SC-FDMA we need that the CP is longer than the CIR to avoid intersymbol interference and exploit the circular convolution property for equalization. The final continuous baseband SC-FDMA signal is obtained after a DA conversion applied to $s_{cp}^{SCFDMA}[n]$. The resulting continuous signal $s_{cp}^{SCFDMA}(t)$, is

$$s_{cp}^{SCFDMA}(t) = \sum_{k=-N_{IDFT}/2}^{N_{IDFT}/2-1} S_k \cdot e^{j2\pi\left(k+\frac{1}{2}\right)\Delta f(t-N_{cp}T_s)} \tag{3.24}$$

where $t \in [0; N_{tot}T_s[$. As mentioned, in this case we can assign a complex symbol to the central frequency, because the DC component in the time domain is eliminated by the frequency shift. After DA conversion, the continuous baseband SC-FDMA signal is up-converted to the carrier frequency f_C, resulting in the real transmitted continuous band-pass signal

$$s_{tx}^{SCFDMA}(t) = \mathrm{Re}\left\{s_{cp}^{SCFDMA}(t) \cdot e^{j2\pi f_C t}\right\} \tag{3.25}$$

It is important to notice that, in standard OFDM, the complex QAM\PSK symbols are carried by individual subcarriers, but in SC-FDMA the QAM\PSK symbols, because of the preliminary spreading DFT, are actually carried by a group of subcarriers.

3.3.2 Demodulation

Under the same assumptions made for OFDM (Section 3.2) the received discrete time baseband signal can be written as

$$r[n] = h[n] \circledast_{N_{IDFT}} s^{SCFDMA}[n] + w[n], \quad n = 0, \ldots, N_{IDFT}. \tag{3.26}$$

Similarly to the OFDM receiver, the SC-FDMA receiver calculates the DFT and the subcarrier demapping. After demapping, equalization is performed. Then, the IDFT despreading operation recovers the QAM\PSK symbols. Finally, after the IDFT, the bit stream can be reconstructed applying a QAM\PSK demodulation and a parallel to serial conversion. Figure 3.2 shows the equivalent discrete time modulation and demodulation scheme.

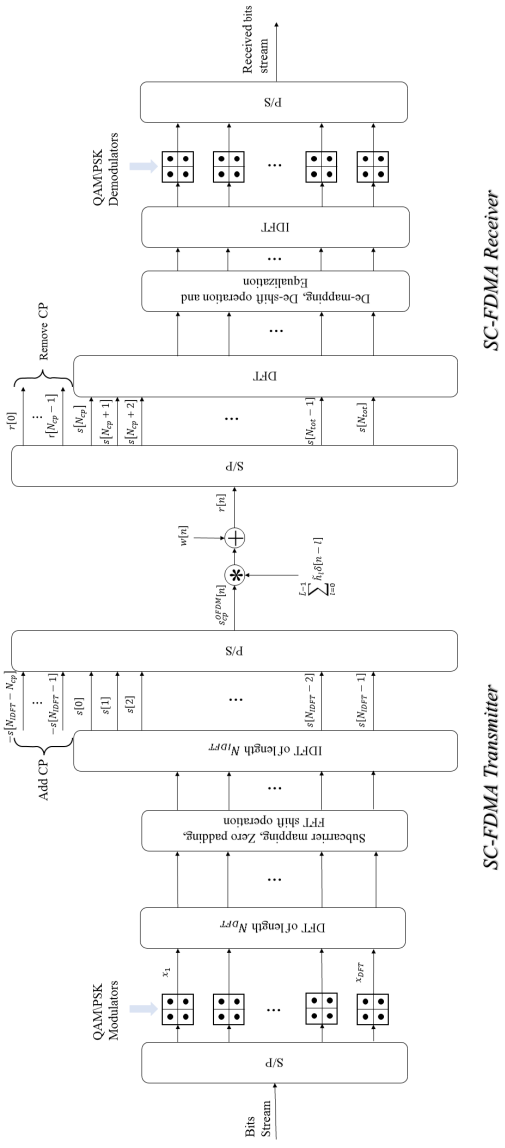

Fig. 3.2 Block scheme of an SC-FDMA transceiver in discrete time domain, the representation of the system is in baseband. The left part represents the transmitter and the right part the receiver.

3.4 LTE Time and Frequency Structure

The standard describes for downlink and uplink physical layers two possible duplex modes. The first is designed for frequency domain duplexing (FDD), and the second is designed for time division duplexing (TDD). In this thesis, only FDD is considered, because it is the most common duplexing mode used in real scenarios (at least in Europe). For more details about the TDD configuration refer to [15]. As depicted in Figure 3.3, the LTE FDD configuration is organized in radio frames with duration 10 ms. A radio frame is divided into ten subframes, each subframe has a duration of 1 ms and is in turn divided into two slots of 0.5 ms. Each OFDM (SC-FDMA) symbol inside

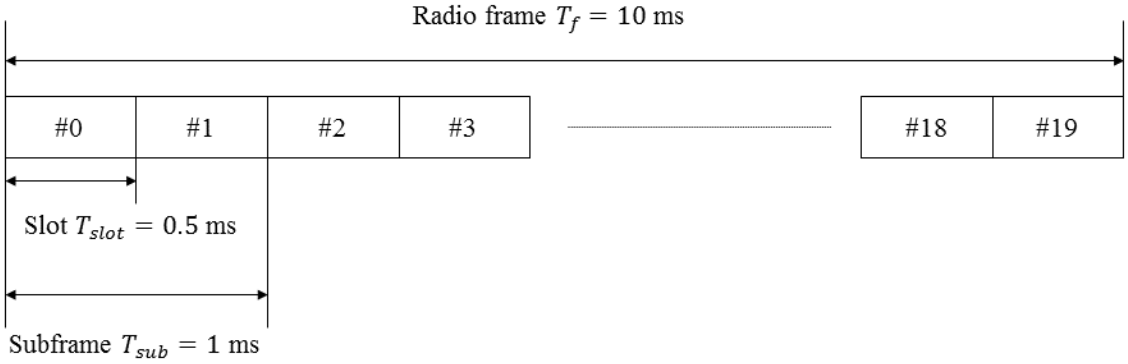

Fig. 3.3 LTE Radio frame structure.

a slot has a duration $T_{sym} = 1/\Delta f$, where Δf is the sub-carrier spacing usually equal to 15 kHz, which means that, without considering the CP, a symbol has a duration of $T_{sym} \approx 66.7\ \mu$s. Depending on the configuration, a slot can contain seven or six OFDM symbols (SC-FDMA symbols in uplink). The different configurations correspond to different cyclic prefix (CP) durations. In particular, as depicted in Figure 3.4, with the normal CP we have $N_{symb} = 7$ OFDM (SC-FDMA) symbols per slot, while with the extended CP the number of symbols is set to $N_{symb} = 6$. Downlink has also two other different configurations, where N_{symb} and the subcarrier spacing Δf take different values (for more detail refer to [15].) Usually, in urban scenarios with cells that have a small coverage range, a normal CP is used, but in case of large sub-urban and rural cells where a long coverage range is needed, the extended cyclic prefix is used. The CP duration is given by $N_{cp}T_s$, where $T_s = T_{sym}/2048 \approx 32.55$ ns is the basic time unit defined in the standard, which usually represents a sample period, and N_{cp} is the duration of the cyclic prefix in number of samples. In normal CP configuration, the first OFDM (SC-FDMA) symbol of the slot has $N_{cp} = 160$ while the other symbols

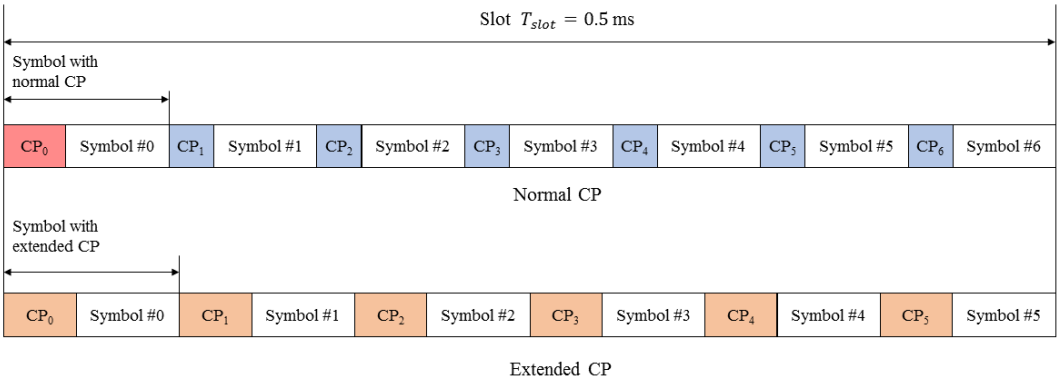

Fig. 3.4 LTE slot structure for normal and extended cyclic prefix. With normal CP mode, the first CP of the slot has a longer duration.

have $N_{cp} = 144$, in extended CP configuration all the OFDM (SC-FDMA) symbols have $N_{cp} = 512$.

An important concept defined in [15] is the so called resource grid, which is a grid used to define the transmission resources in both time and frequency. As depicted in Figure 3.5, the basic unit of the grid is the resource element (RE) that corresponds to the k-th subcarrier inside the l-th OFDM (SC-FDMA) symbol in the slot. REs are grouped in resource blocks (RBs), which correspond to 12 adjacent REs in the subcarrier domain, with a duration of one slot. Moreover, in the standard, the spatial domain is addressed with the concept of antenna ports. Each antenna port corresponds to a single physical antenna or to a set of antennas that are treated, from a communication point of view, as a single physical antenna (this is the case of beamforming). Also, the concept of resource grid is extended to the spatial domain, and in particular each antenna port refers to its own resource grid.

During a transmission, one OFDM (SC-FDMA) symbol can occupy $N_{sc} = N_{sc}^{RB} N_{RB}$ subcarriers, where N_{sc}^{RB} is the number of subcarriers in a resource block (i.e., 12) and N_{RB} is the number of resource blocks allocated for the transmission.

There are six different configurations for the maximum bandwidth available for an OFDM (SC-FDMA) transmission, which are summarized in Table 3.1. In particular, B is the total bandwidth occupation in MHz, N_{RB} is the total number of RBs available

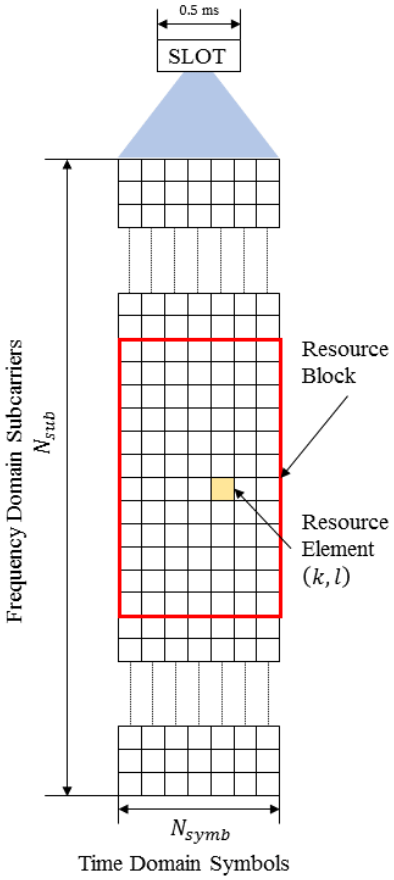

Fig. 3.5 Representation of the resource grid. One resource block (RB) is composed by 12 REs for the duration of one slot [15]. Each resource element is indicated by k-th index in frequency and l-th index in time

B [MHz]	N_{RB}	N_{sc}
1.4	6	72
3	15	180
5	25	300
10	50	600
15	75	900
20	100	1200

Table 3.1 List of possible bandwidth configuration

and N_{sc} is the total number of sub-carriers available (i.e., 12 N_{RB}). For example, one can notice that with $N_{sc} = 72$ and a frequency spacing of 15 kHz the total bandwidth occupation is 1.08 MHz and not 1.4 MHz. As described in Section 3.2, there is some extra band that does not contribute to symbol transmissions, and which is used as a guard band to avoid the interference with adjacent channels.

3.5 Reference Signals for Positioning

3.5.1 Downlink Reference Signals

In the LTE downlink, there are two RSs which are appropriate for range measurement. These are the positioning reference signal (PRS) and the cell specific reference signal (CRS). The PRS is specially designed for the acquisition of multiple simultaneous range measurements and is transmitted in dedicated time intervals [15]. The CRS, instead, is primarily designed for channel estimation and coherent data demodulation, but it may be opportunistically exploited for range measurements, in particular because it is always transmitted [25][26]. Both the CRS and PRS are cell specific: this means that the definition of the signal sequence and the mapping of this sequence on the resource grid changes with the cell ID. CRS and PRS are also defined as QPSK modulated lenght-31 Gold sequences, i.e., the complex reference QPSK symbols are obtained from a pseudorandom generator whose initialization depends on the CID.

The PRS pilot tones occupy one sub-carrier every six through all the available bandwidth (with a spacing of $\Delta f_{PRS} = 6\Delta f = 90$ kHz). The total number of transmitted pilot tones is $N_{PRS} = N_{sc}/6$ per OFDM symbol. The PRS is configured to be transmitted on specific positioning sub-frames, which are designed as low interference sub-frames, without transmission of data [11]. The mapping to the REs of the PRSs transmitted from different cells differs by a frequency shift of Δf depending on the cell ID. Considering that $\Delta f_{PRS} = 6\Delta f$, the frequency shift allows to have up to six orthogonal PRSs that can be detected from six different BSs, in order to estimate the position.

The CRSs are transmitted multiple times from a BS with a mapping to REs that depends on the antenna port configuration. For example, in a configuration with 2 antenna ports, the CRS transmission occurs twice per slot, and in particular it occupies the first and the fifth OFDM symbol in a slot (in case of normal CP), for all the antenna ports, see Figure 3.6. CRSs of different antenna ports are transmitted in non-overlapping subcarriers, as depicted in Figure 3.6. The different mapping

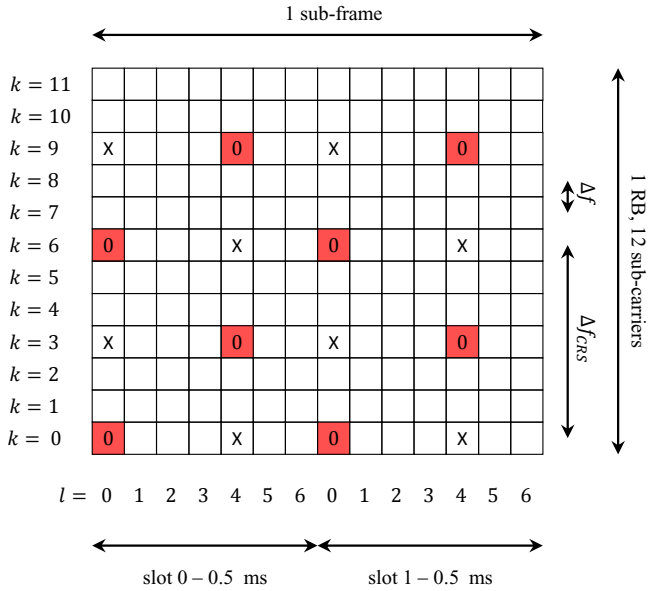

(a) Antenna port $p = 0$

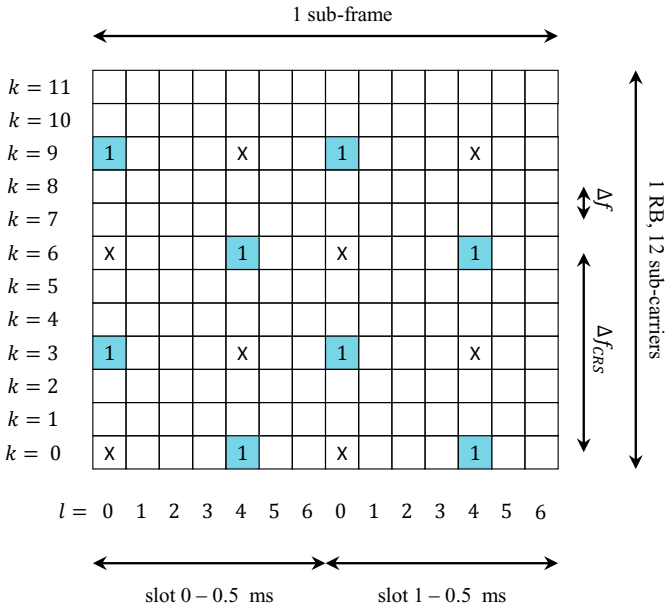

(b) Antenna port $p = 1$

Fig. 3.6 Mapping of the CRS with two antenna ports configuration. The empty REs can be filled by some data. The number in the colored REs identifies the antenna port. The $\times$ in the REs means that there is no transmission in that resource element for that antenna port.

configurations for different antenna ports can be found in [15]. Similarly to PRS, since the CRS pilot tones occupy one sub-carrier every six through all the available bandwidth (with a spacing of $f_{CRS} = 6\Delta f = 90$ kHz), the total number of transmitted pilot tones is $N_{CRS} = N_{sc}/6$ per antenna port per OFDM symbol. Because the CRS was designed for data demodulation and channel estimation, it is always transmitted. The user data allocated in a RB is then transmitted using the REs not allocated for CRS transmission. In particular the free REs of the first and fifth OFDM symbols may be used for data transmission. Similarly to PRS, the CRS transmitted from different BSs is mapped to REs using a frequency shift which depends on the cell ID. Using the previous example of two antenna ports, in this case there are up to three possible orthogonal CRS configurations. More detail about these two downlink RSs and their allocation in the resource grid can be found in [15].

3.5.2 Uplink Reference Signals

In the LTE uplink there are only two types of RSs, namely, the Demodulation Reference Signal (DM-RS) and the Sounding Reference Signal (SRS). The DM-RS is designed for coherent demodulation of the data and for channel estimation. In this thesis we demonstrate that even if the DM-RS is not designed for positioning, it is possible to exploit it opportunistically for this purpose. The SRS is designed to determine the channel quality in order to use a frequency selective scheduling in uplink transmissions [23].

The DM-RS is the reference signal associated to data or control transmissions. In the frequency domain, DM-RS occupies the same subcarriers occupied by the data or by the control data transmission, and in time it is located in some defined SC-FDMA symbols, using some defined REs. The SRS occupies the last SC-FDMA symbol in the subframe, but usually the SRS occupies different subcarriers with respect to the ones assigned to data transmission and in general the number of occupied subcarriers is larger. The main drawback of using SRS for uplink positioning is that the eNodeB can never instruct the UE to send it and makes it impossible to do TOA and AOA measurements exploiting SRS. This was actually observed in our experiments. This is the reason why in this thesis the use of DM-RS is proposed instead of the SRS for uplink positioning measurements. Moreover, one benefit is that each time there is some data (or control) transmission, there is an opportunity to make a measurement, since DM-RS is transmitted, too. The possible drawback of using the DM-RS is that it occupies only a portion of the bandwidth reserved for data (or control) transmission and not the whole bandwidth (like, for example, in downlink with the CRS and PRS

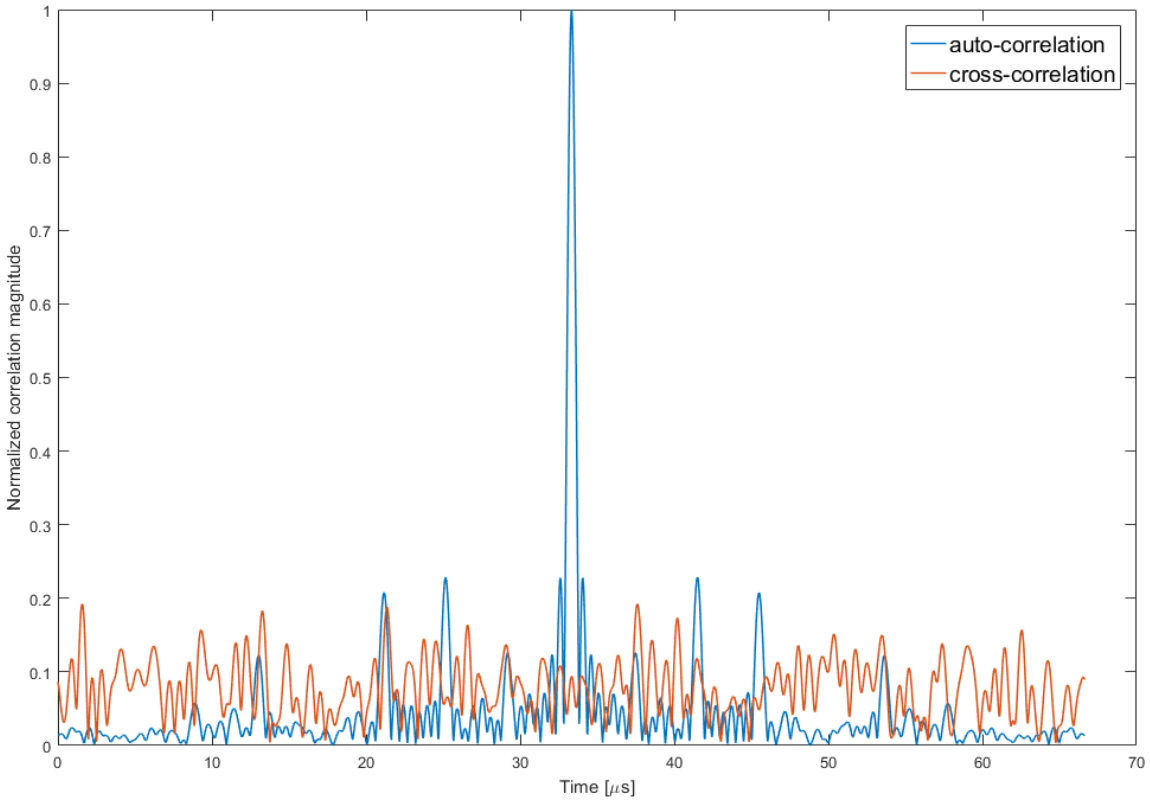

Fig. 3.7 Normalized DM-RS auto-correlation and cross-correlation of DM-RSs. The duration is $T_{symb} \approx 66.67\mu$s and the band occupied is ten RBs. The auto-correlation shows a sharp peak, while the cross-correlation is with DM-RSs with a different cell ID, with no evident peak.

signals, or with some configuration of SRS). This leads to a higher TOA variance in the measurements. To overcome this problem, this thesis proposes a method to combine multiple DM-RSs belonging to the same data transmission, in order to have a better estimation exploiting the SAGE algorithm.

The uplink RSs have several characteristics: a constant amplitude in the frequency domain in all the allocated subcarriers, good auto-correlation properties, and good cross-correlation properties between RSs transmitted by different UEs, in order to reduce the interference from RSs transmitted in the same RBs in other cells. Thus, as depicted in Figure 3.7, the auto-correlation gives a high and sharp peak with respect to the floor, and the cross-correlation between two different RSs does not return any apparent peak.

Both the DM-RS and the SRS are based on some particular reference sequences. These sequences have to satisfy the characteristics mentioned above. The length of a reference sequence, N_{rs}, is equal to the number of assigned subcarriers M_{sc}^{RB}, which is

always a multiple of the number of sub-carriers per RB, i.e., 12,

$$N_{rs} = M_{sc}^{RB} = m \cdot 12, \quad 1 \leq m \leq N_{RB}. \tag{3.27}$$

If the allocated RBs used for RS transmission are less or equal to two, the RS is based on special QPSK sequences. These special sequences are described in more detail in [15]. For RBs allocation greater than two the RS sequence is based on a Zadoff-Chu (ZC) sequence. The reference sequence is described as

$$\bar{r}_{u,v}[k] = x_q\left(k \mod N_{ZC}^{RS}\right), \quad k = 0, \ldots, N_{rs}, \tag{3.28}$$

where N_{ZC}^{RS} is the largest prime number smaller than N_{rs}, x_q is the Zadoff-Chu (ZC) sequence described as

$$x_q = e^{-j\pi q \frac{n(n+1)}{N_{ZC}^{RS}}}, \quad n = 0, \ldots, N_{ZC}^{RS}, \tag{3.29}$$

q is the root index of the ZC sequence that depends on the group index u and sequence index v according to:

$$q = \left\lfloor N_{ZC}^{RS} \frac{u+1}{31} + \frac{1}{2} \right\rfloor + v \cdot (-1)^{\left\lfloor 2N_{ZC}^{RS} \frac{u+1}{31} + \frac{1}{2} \right\rfloor}. \tag{3.30}$$

Then, $\bar{r}_{u,v}[n]$ is the cyclical extension of the ZC sequence x_q with length N_{ZC}^{RS}. The indices u and v are two indices that depend on some parameters configured by the upper layers. More details on this two indices can be found in [15, 23, 27]. In order to achieve orthogonality between different UEs transmitting in the same RBs, a cyclic time shift is added to the reference sequence [23]. This is equivalent to multiply the sequence by an exponential in frequency domain, thus the sequence becomes

$$\bar{r}_{u,v}^{(\alpha)}[k] = \bar{r}_{u,v}[k] \cdot e^{-i\alpha k}. \tag{3.31}$$

Once the sequence is generated, it is assigned to some subcarriers and after that an IFFT is applied to the sequence. This means that, for the uplink RSs, there is no DFT step, as showed in Figure 3.8. To reduce the inter-cell interference generated by uncoordinated uplink scheduling assignments across multiple neighboring cells, several randomization techniques of the reference signals are adopted. These randomization techniques include: group hopping, i.e., changing the group number u at each slot based on a pseudorandom 31 Gold sequence generator; sequence hopping, i.e., changing the

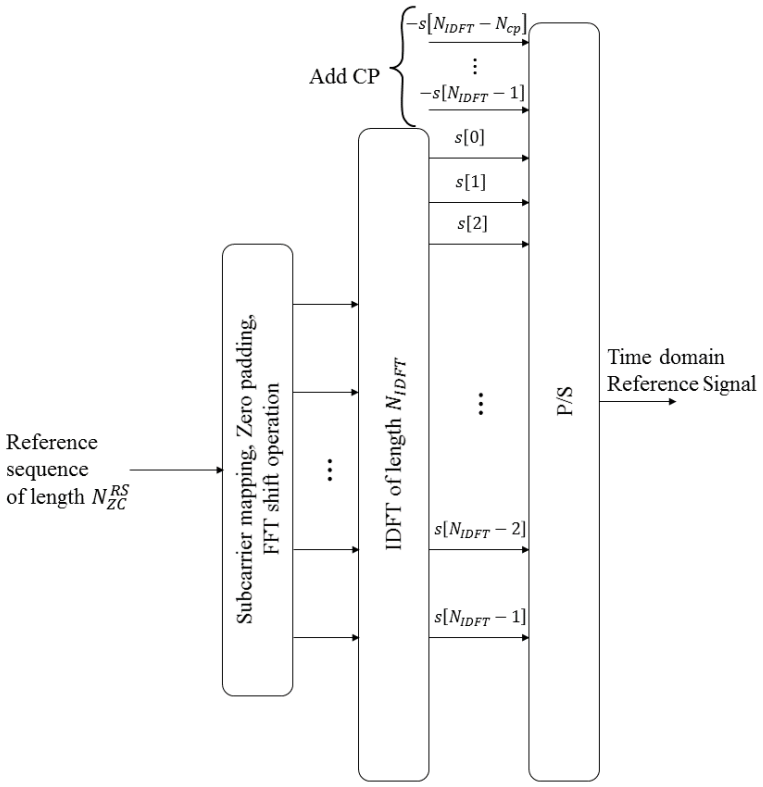

Fig. 3.8 Modulation applied to uplink reference signals. The only difference with respect to OFDM is the minus sign in the CP, such as in the SC-FDMA modulation.

sequence number v at each slot based on pseudorandom 31 Gold sequence generator; the usage of different cyclic shifts and frequency hopping. For more detail refer to [23, 27].

Chapter 4

TOA and AOA Estimation Techniques

4.1 Introduction

Estimating the arrival time of a signal is a crucial step for positioning systems based on TOA and TDOA measurements. The more accurate the arrival estimation is, the more precise is the final position estimation. TOA-based positioning systems measure the distance between a transmitter and a receiver using the estimated propagation delay of the signal. TDOA positioning systems are based on the differences between TOA estimates obtained by different receivers, and this overcomes the problem of synchronization between the transmitter and the receivers. The multipath is the major source of error in TOA estimation. Usually, a wireless environment presents many scatterers, and these scatterers reflect the transmitted signal, which arrives at the receiver through multiple paths. The overlap of different signals, due to the different paths, is a source of error when the interest is to estimate the TOA of the first arriving path, which is called the line of sight (LOS) signal. In particular, the TOA estimation error is a function of the signal bandwidth, as shown in Section 4.5. Indeed, if the signal bandwidth is small and multipath signals arrive close to the LOS signal, it becomes difficult to separate the LOS signal from the multipath signals. In some cases, the LOS component is not present in the received signal, and the estimation with only NOLOS component will necessarily give a bias in the measurement. All TOA estimation techniques presented in this chapter and used in this thesis assume that the LOS component is visible. However, even if the LOS component is present, there is

no certainty that it represents the dominant component, meaning that some NOLOS component can have a larger amplitude. Based on what has been reported already (Section 2.4), some signal processing techniques are necessary in order to estimate the LOS component and recognise it against the NOLOS components. Another source of error in TOA estimation is the additive noise. Even if multipath is not present, the accuracy of the time of arrival estimation can be limited by the noise. Indeed, for a given signal-to-noise-ratio (SNR) the variance of TOA estimation is lower bounded. Accordingly to this, the accuracy of a position time-based techniques is related to the ability of the receiver to accurately estimate the TOA of the LOS signal [2].

Direction of Arrival (DOA), also referred to as Angle of Arrival (AOA), estimation techniques have application in beamforming, detection, and localization. These techniques need to use antenna arrays, which are composed by a certain number of antennas that can be placed using different geometries. Each antenna element in the array has to be connected to a radio frequency demodulator. Compared to TOA techniques, these techniques have the benefit that just two receivers equipped with antenna arrays are sufficient to estimate a position. This makes DOA estimations more flexible than TOA estimations. In addition, TOA estimation methods suppose that the velocity of the wave is homogeneous in the physical medium. This is true for air and space, but not in sea water, for example. This makes AOA techniques more reliable in such environment were the propagation in the physical medium is not homogeneous.

Usually, in DOA estimation, a far field scenario is assumed, which means that the wave impinging the array can be considered a plane wave. In general, the antennas in the array are located at a constant distance d from each other, and d is usually selected to be half of the wavelength, in order to avoid ambiguity in the AOA estimation. Indeed, with $d > \lambda/2$, grating lobes appear in the beam pattern, which are lobes with the same amplitude of the main lobe and this creates an ambiguity in AOA estimation. This problem is similar to the problem of aliasing in time series analysis, which occurs when the time domain waveform is undersampled [28]. In DOA systems, the synchronization between the received signals at each antenna of the array is very critical, because DOA estimation is computed by exploiting the relative phase difference between signals received at different antennas. Calibration is also important in a DOA system, because usually the RF front end is not exactly the same in each antenna element, and this can add different phase offsets in the received signals.

In this chapter, some common TOA and AOA estimation techniques are discussed. These techniques include the correlation based approach, the deconvolution method, the Maximum Likelihood (ML) approach and the subspace based method for TOA

estimation. Then, some DOA techniques are introduced, such as Barlet estimation, the standard Capon beamformer and the IAA-APES algorithm. After that, the SAGE algorithm is presented, which is a technique to joint estimate the DOA, TOA and also Doppler spreading. At the end of the chapter, the Cramer Rao lower bound (CRLB) is introduced, which represents a universal lower bound on the variance of an estimate. Generally, all these methods can be applied either in the time domain, by exploiting the channel impulse response (CIR), or in the frequency domain by exploiting the channel frequency response (CFR).

4.2 TOA Estimation Techniques

In TOA estimation the baseband multipath wireless channel can be modeled via a CIR of the form

$$h\left(t\right)=\sum_{l=1}^{L}\alpha_{l}\delta\left(t-\tau_{l}\right) \tag{4.1}$$

where L represents the number of multipath components, α_l is the complex attenuation of the l-th path and τ_l is the propagation delay of the l-th path. In general, due to the motion of the transmitter, the receiver, or the scatters, the parameter α_l and τ_l are modeled as time varying random variables. However, as explained in Section 3.2, if the measurement is made in a sufficiently small time interval, these parameters can be considered constant. This approximation is fundamental in order to estimate properly the parameters of the channel. According with this channel model the CFR is equal to

$$H\left(f\right)=\sum_{l=1}^{L}\alpha_{l}e^{-j2\pi f\tau_{l}}, \tag{4.2}$$

and the received signal $y\left(t\right)$ in the presence of multipath and noise is

$$y\left(t\right)=\sum_{l=1}^{L}\alpha_{l}s\left(t-\tau_{l}\right)+n(t), \tag{4.3}$$

where $s\left(t\right)$ represents the known transmitted signal (for example the reference signal in the LTE case), with bandwidth B, center frequency f_c, duration T_0, $0\leq t<T_0$, and $n(t)$ is a zero-mean white Gaussian noise.

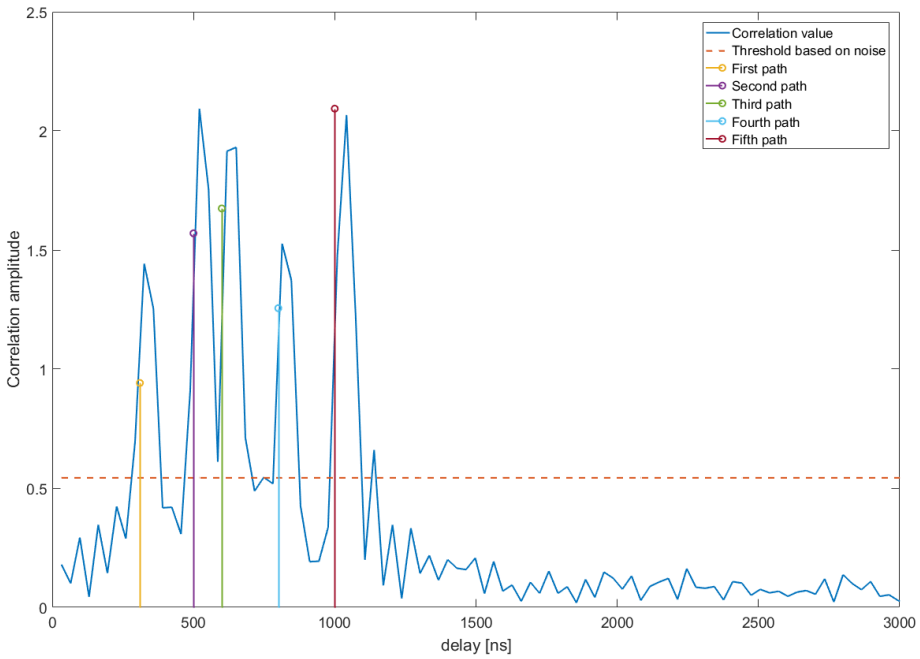

Fig. 4.1 Correlation of the DM-RS in a multipath scenario, where the number of paths is $L = 5$. The figure shows that the correlation magnitude of the first path is not the largest one. In order to estimate the first path, the first peak that exceeds the threshold is selected as the first arriving path.

4.2.1 Correlation Based Techniques

The TOA is the earliest arrival time that maximizes the cross correlation between the received signal and the known transmitted signal [29], where the cross correlation for a discrete time signal is defined as:

$$\mathbf{R}_{sy}[n] = \sum_{m=-\infty}^{+\infty} s^*[m]y[n+m], \tag{4.4}$$

where $s^*[n]$ represent the complex conjugate of $s[n]$. In general, an estimation of the TOA can be obtained using a correlator at the receiver that correlates the received signal with the known transmitted waveform, then the time shift that corresponds to the maximum correlation peak is chosen as the TOA. However, due to multipath, the maximum peak of the correlation could be located corresponding to a path that is not the first path. This situation is depicted in Figure 4.1, where the first path has a lower magnitude than the other paths. This is because there is no guarantee that the first path arriving at the receiver is the path with the maximum amplitude. So, the receiver must find the first arriving peak, that is estimated by comparing the absolute

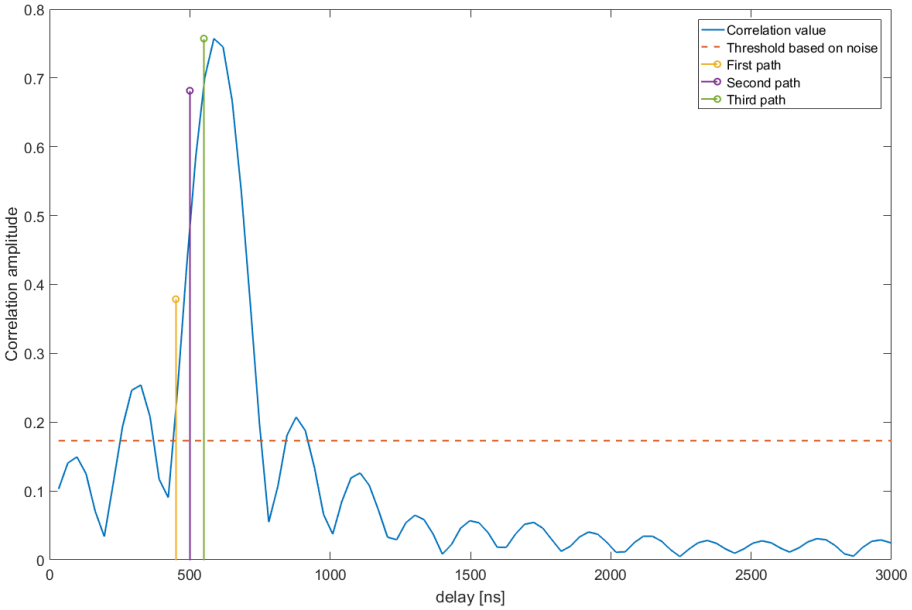

Fig. 4.2 Correlation of the DM-RS in a multipath scenario where the number of paths is $L = 3$. The figure shows that the correlation method is not able to distinguish the different paths because they are too close, and this causes a large error in the TOA estimation of the first path.

value of the cross correlation with a certain threshold, which is usually set based on the measured noise power as it is possible to see in Figure 4.1.

Generally, TOA-based range errors due to multipath are many times larger than those caused by the additive noise alone. The main benefit of this estimation technique is its low complexity. The main problem of this method is that the estimation is inaccurate in the presence of multipath. Indeed, close multipath signals can be resolved with this method only if the transmission bandwidth is increased. In Figure 4.2, a situation where the correlation method is not able to distinguish three close paths is depicted, and the first peak that exceeds the threshold is biased with respect to the first path. Another source of error of this method is given by the sample period. Indeed, also in an ideal case without noise and multipath, if the true TOA is in between two samples, the maximum of the correlation is in correspondence with the sample closest to the real TOA. This error can be reduced by averaging multiple measurements.

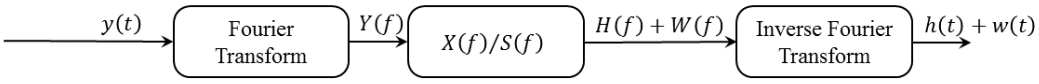

Fig. 4.3 Block scheme of the deconvolution method

4.2.2 Deconvolution Method

Based on Equation (4.3), the received signal $y(t)$ is the convolution of the transmitted signal with the CIR. Therefore, the relation results in

$$y(t) = s(t) * h(t) + n(t) \tag{4.5}$$

and, in the frequency domain,

$$Y(f) = S(f) H(f) + N(f) \tag{4.6}$$

where $Y(f)$, $S(f)$ and $N(f)$ are the Fourier transform of $y(t)$, $s(t)$ and $n(t)$, respectively, and $H(f)$ is the channel frequency response of Equation (4.2). Therefore, dividing $Y(f)$ by $S(f)$, the CFR can be estimated, and making an inverse Fourier transform we obtain the CIR. Based on the CIR, it is possible to estimate the TOA of the first path. The deconvolution method is essentially an inverse filter, and Figure 4.3 shows the scheme of this method. If the transmitted signal has a bandwidth B and a central frequency f_c, it is possible to sample in frequency the continuous frequency signals, i.e., $Y[k] = Y(f)|_{f=f_k}$, $S[k] = S(f)|_{f=f_k}$, $H[k] = H(f)|_{f=f_k}$, and $N[k] = N(f)|_{f=f_k}$, where $f_k = f_0 + k\Delta f$ with $k = \{0, 1, \ldots, K\}$. Moreover, $f_0 = f_c - B/2$ represents the lowest frequency component of the signal. Δf is the frequency sample spacing, which corresponds to the frequency resolution in the frequency domain, and $K = B/\Delta f$ is the number of samples. Considering LTE, $\Delta f = 15$ kHz and K depends on the bandwidth, as shown in Table 3.1. Based on the discrete notation, it is possible to write Equation (4.6) in vector notation as

$$\mathbf{Y} = \mathbf{SH} + \mathbf{N}, \tag{4.7}$$

where $\mathbf{Y} = [Y[f_0], Y[f_1], \ldots, Y[f_K]]^T \in \mathbb{C}^{1\times K}$ represents the vector of the transformed received signal, $\mathbf{S} = diag([S[f_0], S[f_1], \ldots, S[f_K]]) \in \mathbb{C}^{K\times K}$ is a diagonal matrix with the diagonal elements equal to the transmitted signal frequency samples, $\mathbf{H} = [H[f_0], H[f_1], \ldots, H[f_K]]^T \in \mathbb{C}^{1\times K}$ are the frequency samples of the channel and $\mathbf{N} = [N[f_0], N[f_1], \ldots, N[f_K]]^T \in \mathbb{C}^{1\times K}$ is the vector of the noise frequency samples.

So, calculating $\mathbf{X} = \mathbf{S}^{-1}\mathbf{Y}$ for the frequencies within bandwidth B, the transmitted signal $\mathbf{S}$ can be removed from $\mathbf{Y}$, obtaining

$$\mathbf{X} = \mathbf{H} + \mathbf{W}. \tag{4.8}$$

In the previous equation, $\mathbf{W} = \mathbf{S}^{-1}\mathbf{N}$ is the additive noise affecting vector $\mathbf{X}$. Applying an inverse Fourier transform to the vector $\mathbf{X}$, it is possible to obtain the CIR (affected by noise), whose magnitude typically presents a maximum in correspondence of the true time delay. The location of the maximum can be detected and used to estimate TOA by comparing the magnitude of the CIR with a threshold, usually calculated based on an estimate of the noise level. Using a threshold is similar to what is done in correlation techniques.

One of the drawbacks of the inverse filtering technique is possible noise enhancement, which occurs when the elements of matrix $\mathbf{S}^{-1}$ are small. This effect can be reduced by using the so-called constrained inverse filtering method [2].

In general, the deconvolution approach needs a coarse TOA estimation in order to set a proper window of data that will be later processed by the fast Fourier algorithm. This method can better resolve closely spaced multipath components compared to the correlation-based method, but the provided resolution is not enough for high-precision range measurement.

4.2.3 ML-Based Methods

ML-based algorithms estimate the multipath delays and the channel coefficients using a Maximum Likelihood estimator. The unknown channel coefficients, based on Equation (4.1), can be grouped into a real valued channel parameter vector as

$$\mathbf{\Omega} = [\mathrm{Re}\{\alpha_1\}, \mathrm{Im}\{\alpha_1\} \ldots, \mathrm{Re}\{\alpha_L\}, \mathrm{Im}\{\alpha_L\}, \tau_1, \ldots, \tau_L] \in \mathbb{R}^{3L\times 1}. \tag{4.9}$$

Under the assumption of Gaussian noise, the log-likelihood function with respect to the channel parameter vector $\mathbf{\Omega}$ is

$$\ln[\Lambda(\mathbf{\Omega})] = -\int_0^{T_0} \left| y(t) - \sum_{l=1}^{L} \alpha_l s(t-\tau_l) \right|^2 dt, \tag{4.10}$$

where $y(t)$ is the received signal and $s(t)$ is the transmitted signal. Therefore, the ML solution $\mathbf{\Omega}_{ML}$ is obtained by solving

$$\hat{\mathbf{\Omega}}_{ML} = \arg\max_{\mathbf{\Omega}} \{\ln[\Lambda(\mathbf{\Omega})]\} \tag{4.11}$$

It is important to notice that it is possible to find the ML solution in the frequency domain, i.e., by maximizing

$$\ln[\Lambda(\mathbf{\Omega})] = -\int_{-B/2}^{B/2} \left| Y(f) - \sum_{l=1}^{L} \alpha_l S(f) e^{-j2\pi f \tau_l} \right|^2 df. \tag{4.12}$$

As one can see in Equation (4.9), the length of the channel parameter vector is a function of the number of multipath components, and, in case of a large number of such components, the complexity of this approach becomes very high. This is because the maximization problem becomes a multidimensional (in this case $3L$ dimensional) maximization problem, whose solution requires a high computational burden. In order to solve the ML criterion, less complex algorithms have been proposed. For example, the SAGE algorithm described in Section 4.4, is a ML algorithm that jointly estimates TOA, Doppler frequency and the AOA of each path. The overall idea of this algorithm is to cancel the multipath interference by subtracting the previous estimated path to the CFR, separating the paths serially one by one. However, if the multipath component TOAs are very close, the algorithm start to become inefficient.

Usually, the variance of an ML estimator error is less than that obtained with other approaches, when only a single path is available in the received signal [2]. In addition, no prior information is needed for the implementation of ML-based methods, but, due to the search of a multidimensional solution of the optimization problem, the complexity of these methods is higher than that, for example, of the correlation and deconvolution approaches.

4.2.4 Subspace-Based Techniques

Subspace-based algorithms involve the decomposition of the space spanned by the observation vector into several sub-spaces, usually the noise subspace and the signal subspace. These algorithms use the orthogonality property between noise and signal subspaces to estimate the channel parameters. This approach uses the eigenvector decomposition of higher order matrices, so the level of complexity is high. The main advantage of this class of algorithms is the high resolution of the estimated parameter

estimation, i.e. the ability to discriminate close paths. Some super-resolution algorithms, such as estimation of signal parameters via rotational invariance techniques (ESPRIT) or multiple signal classification (MUSIC), are indeed based on the subspace approach. More detail about super-resolution algorithms used for TOA in wireless channels can be found in the literature, e.g., in [26, 30–34] and references therein. In general, super-resolution algorithms are also used also for other parameters estimation, such as AOA. The interested reader may refer to [2, 28, 35] for further details.

In the following, the sub-space approach on which super-resolution techniques rely is presented. Suppose that at the receiver a rough estimation of the CFR is available. This estimation may likely be a sampled and noisy version of the continuous CFR showed in Equation (4.2), where the frequency domain sampling interval is Δf:

$$H[k] = \sum_{l=1}^{L} \alpha_l e^{-j2\pi k \Delta f \tau_l} + w[k]. \tag{4.13}$$

Consider a set of $M > L$ adjacent samples of $H[k]$ collected in vector $\mathbf{H}_k$, which is referred to as a snapshot,

$$\mathbf{H}_k = [H[k], H[k+1], \ldots, H[k+M-1]]^T. \tag{4.14}$$

Each snapshot $\mathbf{H}_k$ can be written as

$$\begin{aligned} \mathbf{H}_k &= \sum_{l=1}^{L} \alpha_l e^{-j2\pi k \Delta f \tau_l} \left[1, e^{-j2\pi \Delta f \tau_l}, e^{-j2\pi 2 \Delta f \tau_l}, \ldots, e^{-j2\pi (M-1) \Delta f \tau_l}\right]^T + \mathbf{w}[k] \\ &= \sum_{l=1}^{L} \alpha_l e^{-j2\pi k \Delta f \tau_l} \mathbf{v}[\Delta f \tau_l] + \mathbf{w}[k] = \mathbf{V}\mathbf{h}[k] + \mathbf{w}[k] = \mathbf{S}[k] + \mathbf{w}[k] \end{aligned} \tag{4.15}$$

where

$$\mathbf{S}[k] = \sum_{l=1}^{L} \alpha_l e^{-j2\pi k \Delta f \tau_l} \mathbf{v}[\Delta f \tau_l] = \mathbf{V}\mathbf{h}[k] \in \mathbb{C}^M, \tag{4.16}$$

$$\mathbf{V} = [\mathbf{v}[\Delta f \tau_1], \mathbf{v}[\Delta f \tau_2], \ldots, \mathbf{v}[\Delta f \tau_L]] \in \mathbb{C}^{M \times L}, \tag{4.17}$$

$$\mathbf{v}[\Delta f \tau_l] = \left[1, e^{-j2\pi \Delta f \tau_l}, e^{-j2\pi 2 \Delta f \tau_l}, \ldots, e^{-j2\pi (M-1) \Delta f \tau_l}\right]^T \in \mathbb{C}^M, \tag{4.18}$$

$$\mathbf{w}[k] = [w[k], w[k+1], \ldots, w[k+M-1]]^T \in \mathbb{C}^M, \tag{4.19}$$

$$\mathbf{h}[k] = \left[\alpha_1 e^{-j2\pi k \Delta f \tau_1}, \alpha_2 e^{-j2\pi k \Delta f \tau_2}, \ldots, \alpha_L e^{-j2\pi k \Delta f \tau_L}\right]^T \in \mathbb{C}^L, \tag{4.20}$$

are respectively the signal vector, the time-window frequency matrix, the time-window frequency vector, the noise vector and the channel coefficients vector. Each element of $\mathbf{w}[k]$ is assumed to be a complex Gaussian random variable with zero mean, independent components with variance $\sigma_w^2/2$, and independent from all the other noise samples. Hence, the auto-correlation matrix of $\mathbf{w}[k]$ is $\mathbf{R}_{ww} = \mathbb{E}[\mathbf{w}[k]\,\mathbf{w}^H[k]] = \sigma_w^2\mathbf{I}_M$, where $\mathbf{I}_M$ is the identity matrix of $M \times M$ dimension. Moreover, the complex channel gains α_l are assumed to be random variables having independent identically distributed phases with a uniform distribution in the interval $[0; 2\pi[$, while the modulus is assumed to be independent with respect to the phase. Under these assumptions, it is possible to demonstrate [28, 35] that the auto-correlation matrix $\mathbf{R}_{H_kH_k}$ of $\mathbf{H}_k$, is a normal matrix (i.e., $\mathbf{R}_{H_kH_k}\mathbf{R}^H_{H_kH_k} = \mathbf{R}^H_{H_kH_k}\mathbf{R}_{H_kH_k}$), so there exists an eigendecomposition of $\mathbf{R}_{H_kH_k}$ with an orthonormal basis of eigenvectors. The eigendecomposition can be written as the sum of two terms, corresponding to the signal eigenvectors and to the noise eigenvectors. This leads to

$$\mathbf{R}_{H_kH_k} = \sum_{m=1}^{L} \lambda_m \mathbf{q}_m \mathbf{q}_m^H + \sum_{m=L+1}^{M} \sigma_w^2 \mathbf{q}_m \mathbf{q}_m^H = \mathbf{Q}_s \mathbf{\Lambda}_s \mathbf{Q}_s^H + \sigma_w^2 \mathbf{Q}_w \mathbf{Q}_w^H \tag{4.21}$$

where

$$\mathbf{Q}_s = [\mathbf{q}_1, \ldots, \mathbf{q}_L] \in \mathbb{C}^{M \times L} \tag{4.22}$$

$$\mathbf{Q}_w = [\mathbf{q}_{L+1}, \ldots, \mathbf{q}_M] \in \mathbb{C}^{M \times (M-L)} \tag{4.23}$$

$$\mathbf{\Lambda}_s = \mathrm{diag}\{[\lambda_1, \ldots, \lambda_L]\} \in \mathbb{C}^{L \times L} \tag{4.24}$$

and $\mathbf{q}_l \in \mathbb{C}^M$ is the eigenvector of $\mathbf{R}_{H_kH_k}$, with λ_l the corresponding eigenvalue. In particular, the L eigenvalues relative to the signal sub-space are $\lambda_l = M\mathbb{E}\left[|\alpha_l|^2\right] + \sigma_w^2,\ l = 1, \ldots, L$ and the $M - L$ eigenvalues of the noise are $\lambda_l = \sigma_w^2,\ l = L+1, \ldots, M$. Thus, an orthonormal basis of the signal subspace is given by $\mathbf{Q}_s$ and an orthonormal basis of the noise subspace is given by $\mathbf{Q}_w$. The main point of the of subspace method is that the signal and noise sub-spaces are orthogonal to each other. Since the time-window frequency vector $\mathbf{v}[\Delta f \tau_l]$ lies in the signal sub-space, then, for different τ_l values, the vector is orthogonal to the noise sub-space, that is

$$\mathbf{v}^H[\Delta f \tau_l]\,\mathbf{q}_{l'} = 0\ \forall l,\ \forall l' \geq L+1 \tag{4.25}$$

Equation (4.25) is exploited by super-resolution algorithms for understanding if a particular discrete time delay $\hat{\tau}$ is present in the signal $\mathbf{H}_k$. The MUSIC and the

ESPRIT algorithms are quite similar, and indeed they are based on the same signal model showed before. They differ in the method used to estimate the different delay values. In particular, MUSIC exploits a pseudospectrum where the peaks represent the different TOAs of the impinging wave due to multipath. The accuracy of MUSIC is related to the discretization interval adopted in the calculation of the pseudospectrum. ESPRIT instead, is based on the observation that the signal sub-space has a rotational invariance property. This property can be exploited to estimate a rotational matrix that is related to the multipath time delays. In this case, the resolution of the estimated delays does not depend on any discretization interval. Further details about ESPRIT and MUSIC can be found in [35] and [28].

4.3 AOA Estimation Techniques

Estimating the angle of arrival AOA (also referred as DOA), needs to use antenna arrays, and this led to the development of array processing techniques in order to estimate the parameters of the impinging electromagnetic wave. Array processing is based on signal processing, since the signals captured by an array of spatially separated sensors can be seen as a spatial sampling of the incoming waves. Other types of array sensors include microphones, ultrasound, and infrared sensors instead of antennas. An emerging technology over the past decade is sensor networks, where sensors are distributed over a wide area, and the purpose is generally to monitor the environment and/or to localize a certain signal source [3].

Usually, an array of antennas is used to focus the energy of a signal in the spatial domain. At the transmitter side, a simple technique consists of adding some time delays to the signals transmitted by the various elements of the array. This allows the waveform to add coherently in a desired direction, while it is attenuated in other directions. The same technique can be used at the receiver side, by first applying the same time delays at the sensor outputs, and then summing the result. The result can be interpreted as a matched filter applied to the assumed arriving direction of the signal. This kind of signal processing is referred to as beamforming, and it is the spatial equivalent of temporal Finite Impulse Response (FIR) filtering. Usually, the performance of this approach depends critically on the number of elements and on the physical size of the array, also called aperture. Some more elaborate filter functions will be presented in this section. The interested reader can refer to [36, 37] for some review article, or to the books [28, 38, 39] to have a deeper comprehension of the beamforming techniques.

4.3.1 Wave Propagation Model

In order to understand the basic aspects of AOA detection, it is important to introduce some fundamental concepts related to the antenna array and to its physical model. Generally, in array processing, a common problem is to determine some parameter of the impinging wave that comes from different sources. Considering a single source and an electromagnetic wave that propagates in a homogeneous and non-dispersive medium, the electromagnetic field $E(t, \mathbf{r})$ representing the signal is described by the equation

$$\frac{\partial E(t, \mathbf{r})}{\partial x^2} + \frac{\partial E(t, \mathbf{r})}{\partial y^2} + \frac{\partial E(t, \mathbf{r})}{\partial z^2} = \frac{1}{c^2} \frac{\partial E(t, \mathbf{r})}{\partial t^2} \tag{4.26}$$

where t represents time, $\mathbf{r} = [x, y, z]^T$ is the space location and c represents the propagation speed. Assuming that the source is a point source and that the antenna array is small compared to the distance between the source and the array, then the distance between each antenna and the source can be considered constant. This leads to a solution for E [38], corresponding to a mono-chromatic wave that assumes the complex exponential form

$$E(t, \mathbf{r}) = Ae^{j2\pi f(t - \mathbf{r}\cdot\mathbf{u}/c)} = Ae^{j(2\pi f t - \mathbf{r}\cdot\mathbf{k})} \tag{4.27}$$

where f is the temporal frequency, $\mathbf{u}$ is the unit vector pointing to the direction of propagation, $\mathbf{r}$ is the coordinate vector of the observation point, $\mathbf{k} = k\mathbf{u}$ is the wave vector, where $k = 2\pi f/c$ is the wavenumber. The temporal and spatial frequencies are related by the following equation

$$|\mathbf{k}|^2 = k_x^2 + k_y^2 + k_z^2 = \frac{(2\pi f)^2}{c^2}. \tag{4.28}$$

Considering that the propagation velocity is $c = f\lambda$ where λ is the wavelength, the magnitude of the wavevector is $|\mathbf{k}| = 2\pi/\lambda$. Moreover, the wavevector can be expressed as

$$\mathbf{k} = \begin{bmatrix} k_x \\ k_y \\ k_z \end{bmatrix} = -k \begin{bmatrix} \cos(\varphi)\cos(\phi) \\ \cos(\varphi)\sin(\phi) \\ \sin(\varphi) \end{bmatrix} \tag{4.29}$$

where ϕ and φ are the azimuth and elevation angle of the coordinate system, respectively, as depicted in Figure 4.4. Both parameters characterize the direction of propagation

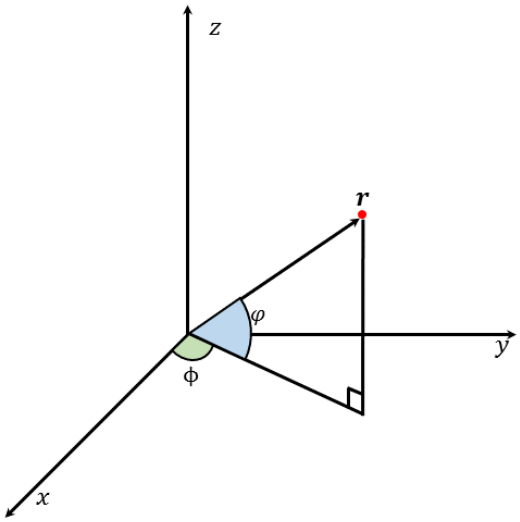

Fig. 4.4 Coordinates system considered for DOA estimation. The angle ϕ represents the azimuth angle and φ represents the elevation angle.

and are referred to as the direction of arrival (DOA or AOA). Note that for far-field sources, the distance between the source and the array of sensors is much larger than the aperture of the array, so the DOA value are approximately the same at each antenna. According to Equation (4.27), the wave is a plane wave, because the surface traced by a constant phase at time instant t is a plane perpendicular to the propagating direction given by $\mathbf{k} \cdot \mathbf{r} = constant$.

4.3.2 Frequency Description

Let us consider an array of sensors located at $\mathbf{p}_m,\ m = 1, \ldots, M \in \mathbb{R}^3$, that receive signals generated by L sources. Without loss of generality, we can consider the first sensor as the origin of the coordinate system. So, the l-th signal coming from the l-th source, received by the first sensor can be denoted as $s_l(t),\ l = 1, \ldots, L$. Based on this notation, the signal received at the m-th sensor will be the original signal with a time delay plus noise

$$y_m(t) = \sum_{l=1}^{L} s_l(t - \tau_{ml}) + n_m(t), \tag{4.30}$$

where τ_{ml} is the propagation time difference between the first sensor at the origin and the $m-th$ sensor. The time difference is given by $\mathbf{r}_m \cdot \mathbf{u}_l / c = \mathbf{r}_m \cdot \boldsymbol{\xi}_l$, where $\boldsymbol{\xi}_l$ is called the slowness vector and is related to the wave vector according to $\boldsymbol{\xi}_l = \mathbf{k}_l / (2\pi f)$. In

other words, the delay τ_{ml} is related to the DOA. If a Fourier transform is applied to the array output vector $\mathbf{y}(t) = [y_1(t), \ldots, y_M(t)]^T$, the time delays become phase shifts, so the output vector in the frequency domain is given by

$$\mathbf{Y}(f) = \begin{bmatrix} Y_1(f) \\ \vdots \\ Y_M(f) \end{bmatrix} = \sum_{l=1}^{L} \mathbf{a}(\phi_l, \varphi_l, f) S_l(f) + \mathbf{N}(f), \tag{4.31}$$

where $\mathbf{a}(\phi_l, \varphi_l, f)$ is called the steering vector and represents the spatial samples of the l-th incoming wave. In particular

$$\mathbf{a}(\phi_l, \varphi_l, f) = \begin{bmatrix} e^{-j\mathbf{r}_1 \cdot \mathbf{k}_l} \\ \vdots \\ e^{-j\mathbf{r}_M \cdot \mathbf{k}_l} \end{bmatrix} = \begin{bmatrix} e^{-j2\pi f \mathbf{r}_1 \cdot \boldsymbol{\xi}_l} \\ \vdots \\ e^{-j2\pi f \mathbf{r}_M \cdot \boldsymbol{\xi}_l} \end{bmatrix}. \tag{4.32}$$

From the steering vector it is possible to define the steering matrix for all the L sources as

$$\mathbf{A}(\boldsymbol{\phi}, \boldsymbol{\varphi}, f) = [\mathbf{a}(\phi_1, \varphi_1, f) \ldots \mathbf{a}(\phi_L, \varphi_L, f)], \tag{4.33}$$

Thus, in matrix notation, Equation (4.31) becomes

$$\mathbf{Y}(f) = \mathbf{A}(\boldsymbol{\phi}, \boldsymbol{\varphi}, f) \mathbf{S}(f) + \mathbf{N}(f), \tag{4.34}$$

where $\mathbf{S}(f) = [S_1(f), \ldots, S_L(f)]$.

Usually, for transmission, the signal is modulated by a carrier frequency f_c. At the receiver side, the radio frequency signals are demodulated to baseband for further processing. Let us assume that the signal is band limited with a bandwidth B, and that the maximum travel time between two sensors of the array is ΔT. It is possible to make a narrow band assumption if $B\Delta T \ll 1$, which means that the complex baseband signal waveform is approximately equal for all sensors, so the sensors outputs are all coherent and differ only by a phase shift. So, after baseband downconversion, the general expression in time becomes

$$\mathbf{y}(t) = \mathbf{A}(\boldsymbol{\phi}, \boldsymbol{\varphi}) \mathbf{s}(t) + \mathbf{n}(t), \tag{4.35}$$

where the steering matrix $\mathbf{A}(\boldsymbol{\phi}, \boldsymbol{\varphi})$ is calculated at the carrier frequency f_c, and $\mathbf{s}(t)$ represents the vector of baseband signals.

DOA estimation is typically based on sampled values of $\mathbf{y}(t)$ at time instants t_n, $n = 1, \ldots, N$, thus the snapshot discrete model is given by

$$\mathbf{y}[n] = \mathbf{A}(\boldsymbol{\phi}, \boldsymbol{\varphi})\,\mathbf{s}[n] + \mathbf{n}[n], \quad n = 1, \ldots, N. \tag{4.36}$$

In array processing methods, the second order statistics of the data is usually exploited. Let us assume that the signal and noise are independent, stationary random processes with zero mean, and with auto-correlation matrices $\mathbf{R}_{ss} = \mathbb{E}\left[\mathbf{s}[n]\,\mathbf{s}^H[n]\right]$ and $\mathbf{R}_{nn} = \mathbb{E}\left[\mathbf{n}[n]\,\mathbf{n}^H[n]\right]$. The noise process is typically assumed to be spatially white, i.e., $\mathbf{R}_{nn} = \sigma^2\mathbf{I}$ with $\mathbf{I}$ the identity matrix. Then, the auto-correlation matrix of the received signal is

$$\mathbf{R}_{yy} = \mathbb{E}\left[\mathbf{y}[n]\,\mathbf{y}^H[n]\right] = \mathbf{A}(\boldsymbol{\phi}, \boldsymbol{\varphi})\,\mathbf{R}_{ss}\mathbf{A}^H(\boldsymbol{\phi}, \boldsymbol{\varphi}) + \sigma^2\mathbf{I}. \tag{4.37}$$

The correlation matrix is not known at the receiver, but it can be estimated from the N observations as

$$\hat{\mathbf{R}}_{yy} = \frac{1}{N}\sum_{n=1}^{N}\mathbf{y}[n]\,\mathbf{y}^H[n]. \tag{4.38}$$

Note that, under weak assumptions $\hat{\mathbf{R}}_{yy}$ converges to the true $\mathbf{R}_{yy}$ for large N [40]. One of the most common antenna arrays is the uniform linear array (ULA). Considering the coordinates of Figure 4.4, the $m-$th array element of a ULA is placed along the y-axis at position $\mathbf{p}_m = [0, (m-1)\,d, 0]$, where d is the distance between sensors. In this case, the elevation angle φ is set to 90° and the steering vector is characterized by only the azimuthal angle ϕ. Then the ULA steering vector of an angle ϕ is

$$\mathbf{a}_{ULA}(\boldsymbol{\phi}) = \begin{bmatrix} 1 \\ e^{jkd\sin\phi} \\ e^{jk2d\sin\phi} \\ \vdots \\ e^{jk(M-1)d\sin\phi} \end{bmatrix} = \begin{bmatrix} 1 \\ e^{j2\pi\frac{d}{\lambda}\sin\phi} \\ e^{j2\pi\frac{2d}{\lambda}\sin\phi} \\ \vdots \\ e^{j2\pi\frac{(M-1)d}{\lambda}\sin\phi} \end{bmatrix}. \tag{4.39}$$

Typically, the distance d is taken half of the wavelength, i.e., $d = \lambda/2$.

4.3.3 Spatial Filtering

A linear spatial filter is simply obtained by weighting and summing the antennas outputs. Defining the weights as $\mathbf{w} = [w_1, \ldots, w_M]^T \in \mathbb{C}^M$. Considering only one source with DOA ϕ and a ULA, the output of the so called beamformer is given by

$$x[n] = \sum_{m=1}^{M} w_m^* y_m[n] = \mathbf{w}^H \boldsymbol{y}[n] = \mathbf{w}^H (\mathbf{a}(\phi) s[n] + \mathbf{n}[n]) \tag{4.40}$$

where $\mathbf{w}$ is called the beamforming vector or weight vector. Thus, $\mathbf{w}^H\mathbf{a}$ can be seen as the spatial transfer function from $s[n]$ to $x[n]$, at the direction ϕ and at the carrier frequency f_c . The magnitude of this transfer function $G(\phi) = \left|\mathbf{w}^H\mathbf{a}\right|$ is the gain of a spatial filter applied to a signal coming from the direction ϕ, and in case of ULA it is given by

$$G(\phi) = \left|\mathbf{w}_m^H\mathbf{a}\right| = \left|\sum_{m=1}^{M} w^* e^{j2\pi(m-1)\frac{d}{\lambda}\sin\phi}\right| \tag{4.41}$$

This magnitude is important to introduce the concept of beam pattern, which is the plot of the beamforming magnitude $G(\phi)$ when the weights are selected as $\mathbf{w} = \mathbf{a}(\phi_0)$, where ϕ_0 is called the look direction, which represents the DOA of the signal. The magnitude of the filter results to be

$$G(\phi, \phi_0) = \left|\mathbf{a}^H(\phi_0)\mathbf{a}(\phi)\right| = \left|\sum_{m=1}^{M} e^{j2\pi(m-1)\frac{d}{\lambda}(\sin\phi - \sin\phi_0)}\right| \tag{4.42}$$

Considering the Cauchy-Schwartz's inequality $\left|\mathbf{a}^H(\phi_0)\mathbf{a}(\phi)\right| \leq ||\mathbf{a}^H(\phi_0)||\,||\mathbf{a}(\phi)||$ so the gain $G(\phi, \phi_0)$ has a maximum for $\phi = \phi_0$. This type of filter is a matched filter; using this type of filtering in order to estimate the DOA, searching the angle that gives the maximum of the function G, is referred to as the conventional or Bartlett beamforming. Figure 4.5 shows the beam pattern for a 10 element ULA with respect to different look directions. Due to symmetry, the beam pattern is plotted only for $-90° \leq \phi < 90°$. It is shown that the function $G(\phi, \phi_0)$ has some zeros and that the location of the first null defines the beamwidth of the array. If the main lobe is narrow, there is better capability to discriminate between multiple sources at different positions, i.e., resolution [38]. Besides the main lobe, the beam pattern also displays sidelobes. It

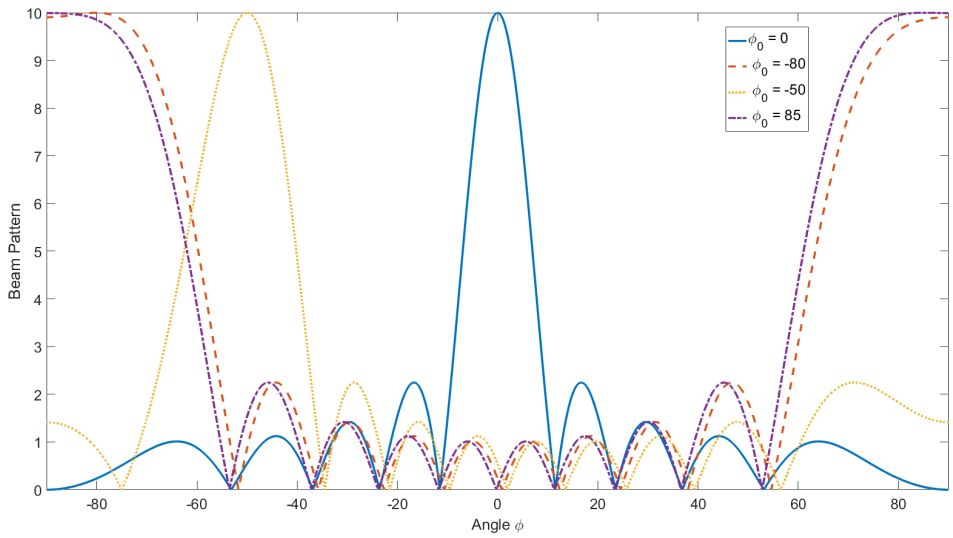

Fig. 4.5 Beam pattern obtained for different look directions ϕ_0, with $M = 10$ elements in the array and $d = \lambda/2$. When the angle approach $+90°$ or $-90°$, the width of the main beam is wider.

can be shown [38] that the width of the main lobe in angles can be calculated as

$$\phi_{BW} \approx \frac{\lambda}{Md\cos\phi_0} \tag{4.43}$$

This demonstrates clearly that the beamwidth is widened when $\cos\phi_0$ is close to zero. Indeed, looking at Figure 4.5, the beam pattern is wider when ϕ_0 approach 90° or -90°. Equation (4.43) shows also that the beamwidth is widened when the number of elements is increased, as depicted in Figure 4.6. The beamwidth becomes thinner also when the distance between the elements is increased. However, if the distance d is higher that half of the wavelength, the beam pattern exhibits the so called grating lobes, which means that the beam pattern has more than one maximum: this can create ambiguity in the DOA estimation. This effect is shown in Figure 4.7, and is the dual of the aliasing effect in time sampling.

4.3.4 Conventional Beamforming

The DOA estimation is made by looking in a spatial power spectrum the location where most power is concentrated. As showed in Section 4.3.3 beamforming methods are based on spatial filters that weight the sensors outputs. In particular, the weight vector is a function of the DOA, i.e., $\mathbf{w} = \mathbf{w}(\phi)$, and an estimation of the power spectrum at

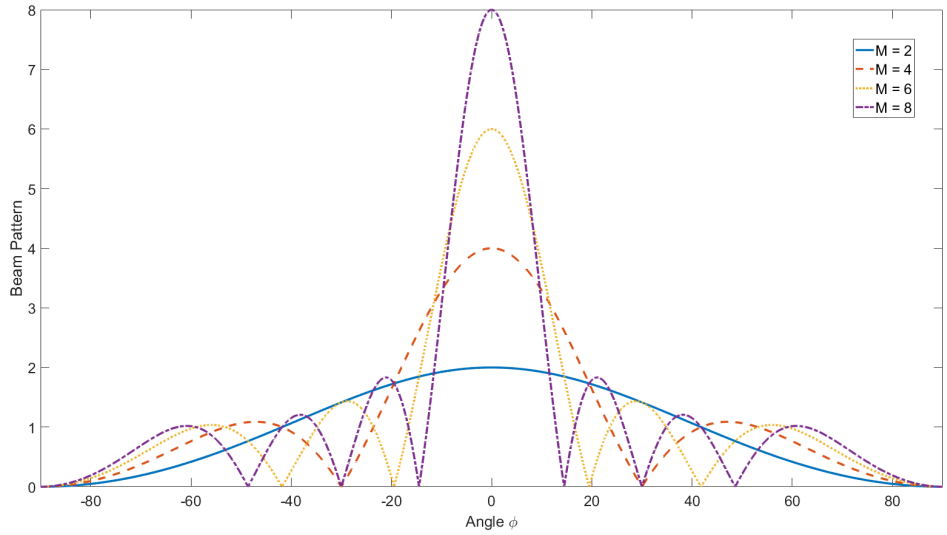

Fig. 4.6 Beam pattern obtained for different numbers of array elements M with $d = \lambda/2$ and look direction $\phi_0 = 0°$. Increasing the number of antenna elements makes the beamwidth narrower.

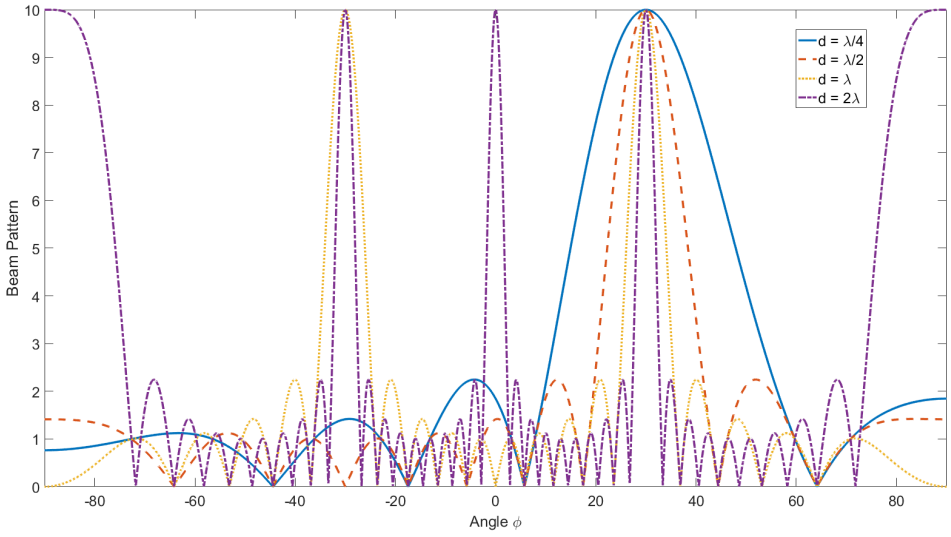

Fig. 4.7 Beam pattern obtained for different distances d between array elements, with $M = 10$ and the look direction $\phi_0 = 30°$. Increasing the distance between the elements of the array makes the beamwidth narrower, but if the distance becomes higher than $\lambda/2$ grating lobes appear due to spatial aliasing.

the direction ϕ is provided from the beamformer output as

$$P(\phi) = \frac{1}{N}\sum_{n=1}^{N} |x[n]|^2 = \mathbf{w}^H \hat{\mathbf{R}}_{yy}\mathbf{w} = \mathbf{w}^H \mathbf{y}\mathbf{y}^H \mathbf{w} \tag{4.44}$$

where $\mathbf{y} = \mathbf{a}(\phi)\, s[n] + \mathbf{n}[n]$. Here, $P(\phi)$ is called the spatial power spectrum and, considering only one source, the value of ϕ that gives the maximum of $P(\phi)$ is usually close to the true DOA. It is apparent that a good beam pattern, as a function of ϕ, has to be as much as possible close to a delta function. In practice, due to the finite array aperture, the beampattern has a main lobe and several sidelobes. The Conventional beamformer, coincides with the ML solution in case of a single source and white Gaussian noise. In case of multiple sources, the peaks tend to move due to leakage, and if two sources are too close, they merge in a single peak. It can also happen that a powerful source can cover with its sidelobes other sources with less power. To avoid this, windowing can be used at the price of less resolution.

4.3.5 Minimum variance distortionless response beamformer

The Minimum variance distortionless response (MVDR) beamformer, commonly also referred to as Capon beamformer [41], considers the following optimization problem

$$\min_{\mathbf{w}} \mathbf{w}^H \hat{\mathbf{R}}_{yy}\mathbf{w} \text{ subject to } \mathbf{w}^H \mathbf{a}(\phi) = 1. \tag{4.45}$$

The idea of the algorithm is to impose the constraint that the signal from the desired direction ϕ is not distorted (see Equation (4.40)), while minimizing the overall power due to noise and interference. The solution of this problem is well known [42], and is given by

$$\mathbf{w}_{MVDR} = \frac{\hat{\mathbf{R}}_{yy}^{-1}\mathbf{a}(\phi)}{\mathbf{a}^H(\phi)\,\hat{\mathbf{R}}_{yy}^{-1}\mathbf{a}(\phi)}. \tag{4.46}$$

Substituting Equation (4.46) in Equation (4.45) the power function becomes

$$P_{MVDR}(\phi) = \frac{1}{\mathbf{a}^H(\phi)\,\hat{\mathbf{R}}_{yy}^{-1}\mathbf{a}(\phi)}. \tag{4.47}$$

Because of the inversion of the matrix $\hat{\mathbf{R}}_{yy}$, this beamformer puts a constraint to the rank of the matrix, which needs to be full. In other words, this means that the number of snapshots N has to be greater or equal to the number of sensors M, i.e.,

$N \geq M$. The performance of the MVDR beamformer depends on the number of snapshots, array aperture, and SNR. In the presence of coherent or strongly correlated interference, the performance of the MVDR beamformer degrades dramatically. Due to the distortionless response constraint, the MVDR beamformer is sensitive to errors in array imperfection.

4.3.6 Subspace Methods

Similarly to that presented in Section 4.2.4 for TOA estimation, also for DOA estimation it is possible to exploit the orthogonality between the signal subspace and the noise subspace. In particular, considering the correlation matrix of Equation (4.37) for a ULA

$$\mathbf{R}_{yy} = \mathbf{A}\left(\boldsymbol{\phi_0}\right)\mathbf{R}_{ss}\mathbf{A}^H\left(\boldsymbol{\phi_0}\right) + \sigma^2\mathbf{I}, \tag{4.48}$$

it is apparent that $\mathbf{R}_{yy}$ depends on the true DOA parameter vector. Under the assumption that $L < M$, i.e., that the number of sources is less than the number of elements in the array, and assuming also that $\mathbf{R}_{ss}$ is full rank, matrix $\mathbf{A}\left(\boldsymbol{\phi_0}\right)\mathbf{R}_{ss}\mathbf{A}^H\left(\boldsymbol{\phi_0}\right)$ has rank L [38]. Then, there exists a basis of $M - L$ vectors that are orthogonal to $\mathbf{A}\left(\boldsymbol{\phi_0}\right)$ [38]. Similarly to TOA estimation, the correlation matrix $\mathbf{R}_{yy}$ can be decomposed in eigenvectors and their corresponding eigenvalues. Algorithms like ESPRIT or MUSIC can be exploited to estimate which eigenvectors lie in the signal subspace and which eigenvectors lie in the noise subspace. In general, if computational burden is not a concern and if the sensors are expensive, i.e., only few sensors are available, MUSIC is preferred. On the contrary, if the computational power is limited and if there are many sensors available compared to the number of sources to detect, ESPRIT is preferred.

4.3.7 IAA-APES

As seen, the beamforming methods localize the signal sources by estimating the power associated with various DOAs. Since the number of different AOAs is usually small, the AOA estimation can be viewed as a sparse data reconstruction where AOAs are associated to those directions that have non-zero amplitudes. In this approach, the first step is to find a sparse representation of the array output data. The beamforming output of the array observation of Equation (4.36) can be used to construct a sparse

data representation. Then the optimization problem will become to find nonzero AOA components that represent the direction of the sources.

We assume that there are L sources that arrive at the array with angles $\boldsymbol{\phi} = [\phi_1, \ldots, \phi_L]$. In the presence of additive noise the output of an antenna array with M elements is

$$\mathbf{y}[n] = \mathbf{A}(\boldsymbol{\phi})\,\mathbf{s}[n] + \mathbf{n}[n] \quad n = 1, \ldots, N \tag{4.49}$$

where N is the number of snapshots, $\mathbf{A}(\boldsymbol{\phi})$ is the $M \times L$ steering matrix defined as $\mathbf{A}(\boldsymbol{\phi}) = [\mathbf{a}(\phi_1), \ldots, \mathbf{a}(\phi_L)]$ and $\mathbf{s}[n] = [s_1[n], \ldots, s_L[n]]$ is the source vector signal at time n. Considering a ULA, the steering vector of the l-th source is given in Equation (4.39), with ϕ_p substituting the generic ϕ. It is important to note that if the geometry of the array changes, only the expression of the steering vector has to be modified. Usually, the number L of sources is unknown, and in order to estimate the DOAs of the different sources, a K point grid with $K \gg L$ is considered. In other words, the considered region of the angles of interest is subdivided into a grid $\tilde{\boldsymbol{\phi}} = \left[\tilde{\phi}_1, \ldots, \tilde{\phi}_K\right]$ of K points and for each point the power is estimated. Indeed, assuming that the set $\tilde{\boldsymbol{\phi}}$ contains all the values ϕ_p, vector $\mathbf{s}[n]$ in Equation (4.49) has only a few significant components, and is therefore "sparse."

The iterative adaptive approach for amplitude and phase estimation (IAA-APES) is a data-dependent, non parametric approach based on the weighted least square (WLS) algorithm [43]. Assume that $\mathbf{P} \in \mathbb{R}^{K \times K}$ is the diagonal matrix whose elements are the power at each angle of the scanning grid. Then the element on the diagonal can be expressed as

$$P_k = \frac{1}{N} \sum_{n=1}^{N} |s_k[n]|^2, \quad k = 1, \ldots, K, \tag{4.50}$$

where $s_k[n]$ has to be estimated. Considering that ϕ_k is the current angle of interest, it is possible to define the interference plus noise covariance matrix as

$$\mathbf{Q}(\phi_k) = \mathbf{R} - P_k \mathbf{a}(\phi_k)\,\mathbf{a}^H(\phi_k) \tag{4.51}$$

where the correlation matrix is $\mathbf{R} = \mathbf{A}(\boldsymbol{\phi})\,\mathbf{P}\mathbf{A}^H(\boldsymbol{\phi})$. Then it is possible to define the WLS cost function as [39, 43]:

$$\sum_{n=1}^{N} \|\mathbf{y}[n] - s_k[n]\,\mathbf{a}(\phi_k)\|^2_{\mathbf{Q}^{-1}(\phi_k)} \tag{4.52}$$

where

$$\|\mathbf{x}\|^2_{\mathbf{Q}^{-1}(\phi_k)} = \mathbf{x}^H \mathbf{Q}^{-1}(\phi_k)\,\mathbf{x}. \tag{4.53}$$

Minimizing the cost function with respect to $s_k[n]$, which is considered deterministic and unknown, it is possible to obtain the estimate

$$\hat{s}_k[n] = \frac{\mathbf{a}^H(\phi_k)\,\mathbf{Q}^{-1}(\phi_k)\,\mathbf{y}[n]}{\mathbf{a}^H(\phi_k)\,\mathbf{Q}^{-1}(\phi_k)\,\mathbf{a}^H(\phi_k)}, \quad n = 1, \ldots, N \tag{4.54}$$

using the matrix inversion lemma and the definition of $\mathbf{Q}(\phi_k)$ (Equation (4.51)). Equation (4.54) can be written as [43]

$$\hat{s}_k[n] = \frac{\mathbf{a}^H(\phi_k)\,\mathbf{R}^{-1}\mathbf{y}[n]}{\mathbf{a}^H(\phi_k)\,\mathbf{R}^{-1}\mathbf{a}(\phi_k)}, \quad n = 1, \ldots, N \tag{4.55}$$

This avoids the calculation of $\mathbf{Q}^{-1}$ for each of the k-th scan points. Furthermore, the calculation of $\hat{s}_k[n]$ may be done in parallel. Since IAA-APES requires the correlation matrix $\mathbf{R}$, which depends on the unknown signal powers, it has to be implemented iteratively, and usually the initialization is made with a conventional beamformer. In IAA-APES, the estimation of $\mathbf{P}$ and $\mathbf{R}$, are calculated using the signal estimation obtained in the previous iteration, differently from the Capon beamformer, where the snapshots are considered. This makes the IAA-APES algorithm more robust to coherent or high correlated sources. It also can have good performance using only few snapshots [44]. In page 68 the pseudocode of the algorithm is presented. It is

IAA-APES pseudocode algorithm

$P_k = \frac{1}{N}\sum_{n=1}^{N} \frac{\left|\mathbf{a}^H(\phi_k)\mathbf{y}[n]\right|^2}{\mathbf{a}^H(\phi_k)\mathbf{a}(\phi_k)} \quad k = 1, \ldots, K$

repeat
  $\mathbf{R} = \mathbf{A}(\boldsymbol{\phi})\,\hat{\mathbf{P}}\mathbf{A}^H(\boldsymbol{\phi})$
  for $k = 1, \ldots, K$ **do**

    $\hat{s}_k[n] = \frac{\mathbf{a}^H(\phi_k)\mathbf{R}^{-1}\mathbf{y}[n]}{\mathbf{a}^H(\phi_k)\mathbf{R}^{-1}\mathbf{a}(\phi_k)}, \quad n = 1, \ldots, N$

    $P_k = \frac{1}{N}\sum_{n=1}^{N} |s_k[n]|^2$

  end for
until convergence

important to notice that the algorithm is described in the time domain. However, it

can be also be implemented in the frequency domain, since the formulation remains the same.

4.4 Joint ML Parameters Estimation

For joint estimation, a propagation scenario with a transmitter equipped with a single antenna and a receiver equipped with an antenna array composed of M antenna elements is considered. As showed in Section 4.3, the antenna array steering vector is $\mathbf{a}(\phi) \in \mathbb{C}^M$, where ϕ is the azimuth angle. This type of channel is referred to as a single-input multiple-output (SIMO) channel. In the special case of a single omni-directional antenna receiver, the channel will be referred to as a single-input single-output (SISO) channel. In this case $M = 1$ and $\mathbf{a}(\phi) = 1, \forall\phi$.

Let us assume that the receiver is equipped with an antenna array of M elements and that the elements are located at positions $\mathbf{p}_1, \ldots, \mathbf{p}_m,\ \mathbf{p}_i \in \mathbb{R}^2$, with respect to an arbitrary origin. Assuming that the channel presents a finite number of paths L, it is possible to describe the received baseband signal, in vector notation, as

$$\mathbf{y}(t, \boldsymbol{\theta}) = [y_1(t, \boldsymbol{\theta}), \ldots, y_M(t, \boldsymbol{\theta})]^T = \sum_{l=1}^{L} \alpha_l s(t - \tau_l) e^{j2\pi\nu_l t} \mathbf{a}(\phi_l). \tag{4.56}$$

where $\boldsymbol{\theta} = [\boldsymbol{\theta_1}, \ldots, \boldsymbol{\theta_L}]^T$ represents the channel parameter vector of the $l-$path, namely $\boldsymbol{\theta_l} = [\mathrm{Re}\{\alpha_l\}, \mathrm{Im}\{\alpha_l\}, \tau_l, \nu_l, \phi_l]$. Considering the l-th impinging wave, the signal is indeed characterized by the complex amplitude α_l, the delay τ_l, the incident angle ϕ_l, while ν_l represents the frequency shift, which takes into account the Doppler frequency and the frequency offset between the transmitter and receiver. The steering vector is $\mathbf{a}(\phi) = [a_1(\phi), \ldots, a_M(\phi)]^T$ and its m-th component are described by the adopted geometry according to Equation (4.32). Assuming a ULA, the steering vector is described by Equation (4.39). Then, the corresponding CIR and CFR are respectively given by

$$\mathbf{h}(t; \tau; \boldsymbol{\theta}) = \sum_{l=1}^{L} \alpha_l \delta(\tau - \tau_l) e^{j2\pi\nu_l t} \cdot \mathbf{a}(\phi_l) \tag{4.57}$$

$$\mathbf{H}(t; f; \boldsymbol{\theta}) = \sum_{l=1}^{L} \alpha_l e^{j2\pi(\nu_l t - f\tau_l)} \cdot \mathbf{a}(\phi_l) \tag{4.58}$$

Let us assume that the CFR is observed through N_{sc} samples in frequency domain, at frequencies f_k separated by Δf (e.g., each sample can represent the channel estimate

obtained at different subcarriers from an LTE reference signal). Different N_t CFR snapshots are then estimated at each t_n, and separated by Δt (e.g., each CFR can be estimated in each LTE slot exploiting different RSs). Thus, the m-th antenna element of the array detects the channel sample

$$\hat{H}_m\left(t_n; f_k\right) = \sum_{l=1}^{L} \alpha_l e^{j2\pi(\nu_l t_n - f_k \tau_l)} \cdot a_m\left(\phi_l\right) + n(t_n; f_k). \tag{4.59}$$

Then, at the receiver, $N_t N_{sc} M$ complex valued observations are available, i.e.,

$$\hat{\mathbf{H}}\left(t_n; f_k\right) = \begin{bmatrix} \hat{H}_1\left(t_n; f_k\right) \\ \vdots \\ \hat{H}_M\left(t_n; f_k\right) \end{bmatrix} \in \mathbb{C}^M, \quad n = 1, \ldots, N_t; \quad k = 1, \ldots, N_{sc}. \tag{4.60}$$

We will refer to the complete set of channel observation as $\hat{\mathbf{H}}\left(\boldsymbol{t}; \boldsymbol{f}\right)$, which are the sum of the true channel samples plus complex Gaussian noise $\mathbf{n}(\boldsymbol{t}; \boldsymbol{f}) \in \mathbb{C}^M$, with $\sigma^2 = N_0/2$ variance per dimension, it is possible to write

$$\hat{\mathbf{H}}\left(\boldsymbol{t}; \boldsymbol{f}\right) = \mathbf{H}\left(\boldsymbol{t}; \boldsymbol{f}; \boldsymbol{\theta}\right) + \mathbf{n}\left(\boldsymbol{t}; \boldsymbol{f}\right), \tag{4.61}$$

where the noise samples are assumed independent and identically distributed (IDD) for each $t_n \in \boldsymbol{t}$ and $f_k \in \boldsymbol{f}$. Now the problem to solve is the estimation of the unknown channel parameter vector $\boldsymbol{\gamma} = [\sigma^2; \boldsymbol{\theta}] \in \mathbb{C}^{5L+1}$ starting from the channel observations $\hat{\mathbf{H}}\left(\boldsymbol{t}; \boldsymbol{f}\right)$. Under the Gaussian additive noise assumption, the likelihood function becomes

$$\Lambda\left(\boldsymbol{\gamma}\right) = \frac{1}{\left(2\pi\sigma^2\right)^{N_t N_{sc} M}} \exp\left\{-\frac{1}{2\sigma^2} \sum_{n=1}^{N_t} \sum_{k=1}^{N_{sc}} \|\hat{\mathbf{H}}\left(t_n; f_k\right) - \mathbf{H}\left(t_n; f_k; \boldsymbol{\theta}\right)\|^2\right\} \tag{4.62}$$

so the log-likelihood function is:

$$\ln\left[\Lambda\left(\boldsymbol{\gamma}\right)\right] = -N_t N_{sc} M \ln\left(2\pi\sigma^2\right) - \frac{1}{2\sigma^2} \sum_{n=1}^{N_t} \sum_{k=1}^{N_{sc}} \|\hat{\mathbf{H}}\left(t_n; f_k\right) - \mathbf{H}\left(t_n; f_k; \boldsymbol{\theta}\right)\|^2. \tag{4.63}$$

Then the ML solution is obtained by finding the vector parameters $\hat{\boldsymbol{\gamma}}_{ML}$ that maximize the log-likelihood function, i.e.,

$$\begin{aligned}\hat{\boldsymbol{\gamma}}_{ML} &= \arg\max_{\boldsymbol{\gamma}} \left\{\ln\left[\Lambda\left(\boldsymbol{\gamma}\right)\right]\right\} \\ &= \arg\min_{\boldsymbol{\gamma}} \left\{2N_t N_{sc} M \ln\left(2\pi\sigma^2\right) + \frac{1}{\sigma^2}\sum_{n=1}^{N_t}\sum_{k=1}^{N_{sc}}\left\|\hat{\mathbf{H}}\left(t_n, f_k\right) - \mathbf{H}\left(t_n; f_k; \boldsymbol{\theta}\right)\right\|^2\right\}\end{aligned} \tag{4.64}$$

From Equation (4.64), the estimation of noise variance σ^2 can be separated from the other parameters estimation, leading to the final ML estimates

$$\hat{\boldsymbol{\theta}}_{ML} = \arg\min_{\boldsymbol{\theta}} \left\{\sum_{n=1}^{N_t}\sum_{k=1}^{N_{sc}}\left\|\hat{\mathbf{H}}\left(t_n, f_k\right) - \mathbf{H}\left(t_n; f_k; \boldsymbol{\theta}\right)\right\|^2\right\}, \tag{4.65}$$

$$\hat{\sigma}^2_{ML} = \frac{1}{2N_t N_{sc} M}\left\{\sum_{n=1}^{N_t}\sum_{k=1}^{N_{sc}}\left\|\hat{\mathbf{H}}\left(t_n, f_k\right) - \mathbf{H}\left(t_n; f_k; \boldsymbol{\theta}_{ML}\right)\right\|^2\right\}. \tag{4.66}$$

It is important to point out that the estimation of $\hat{\boldsymbol{\theta}}_{ML}$ is a very high complex problem because it needs the estimation of $5L$ parameters, which means that the problem is a $5L-$dimensional minimization problem. In order to decrease the complexity of the problem the Space-Alternating Generalized Expectation-Maximization (SAGE) algorithm [7, 45–47] can be used to evaluate the ML estimation of $\hat{\boldsymbol{\theta}}_{ML}$. The SAGE algorithm breaks the $5L$ maximization problems into a sequence of $5L$ iterative mono dimensional problems[7, 45–47]. The algorithm is presented and explained in the next subsection.

4.4.1 SAGE Algorithm

Assuming that the number of multipath components L is known, starting from the channel observations $\hat{\mathbf{H}}\left(\boldsymbol{t}; \boldsymbol{f}\right)$, one can isolate the l-th term relating to the l-th path. This term can be calculated by canceling the interference caused by the other paths. Thus, having one previous estimate of the channel parameter vector $\hat{\boldsymbol{\theta}}'$, the term relating to the l-th path can be isolated as

$$\hat{\mathbf{H}}_l\left(t_n; f_k\right) = \hat{\mathbf{H}}\left(t_n, f_k\right) - \sum_{l'=1, l'\neq l}^{L}\mathbf{H}\left(t_n; f_k; \hat{\boldsymbol{\theta}'}_l\right), \tag{4.67}$$

This interference cancellation step is called the expectation step. After isolating the CFR relative to the single path l, its channel parameter vector $\boldsymbol{\theta}_l$ can be estimated by solving Equation (4.65), for a single path, namely

$$\hat{\boldsymbol{\theta}}_{l,ML} = \arg\min_{\boldsymbol{\theta_l}} \left\{ \sum_{n=1}^{N_t} \sum_{k=1}^{N_{sc}} \|\hat{\mathbf{H}}_l(t_n; f_k) - \mathbf{H}(t_n; f_k; \boldsymbol{\theta}_l)\|^2 \right\}. \tag{4.68}$$

Now the $5L$ dimensional maximization problem of Equation (4.65) has been turned into L five-dimensional minimization problems. The value of α_l can be determined in closed form assuming that the values τ_l, ν_l and ϕ_l, have been specified. The problem becomes

$$\alpha_{l,ML}(\tau_l, \phi_l, \nu_l) = \arg\min_{\alpha_l} \left\{ \sum_{n=1}^{N_t} \sum_{k=1}^{N_{sc}} \|\hat{\mathbf{H}}_l(t_n; f_k) - \alpha_l e^{i2\pi(\nu_l t_n - f_k \tau_l)} \mathbf{a}(\phi_l)\|^2 \right\}. \tag{4.69}$$

It is possible to arrange the values $\hat{\mathbf{H}}_l(t_n; f_k)$ and $e^{i2\pi(\nu_l t_n - f_k \tau_l)}\mathbf{a}(\phi_l)$ in the complex vectors $\boldsymbol{H}_l$ and $\boldsymbol{W}_l$, respectively, so that the minimization problem can be written as

$$\alpha_{l,ML}(\tau_l, \phi_l, \nu_l) = \min_{\alpha_l} \left\{ \|\boldsymbol{H}_l - \alpha_l \boldsymbol{W}_l\|^2 \right\} \tag{4.70}$$

It is well known that the vector $\alpha_l \boldsymbol{W}_l$ minimizing (4.70), is the orthogonal projection $\boldsymbol{U}_l$ of $\boldsymbol{H}_l$ onto $\boldsymbol{W}_l / \|\boldsymbol{W}_l\|$, namely

$$\boldsymbol{U}_l = \frac{\boldsymbol{H}_l \cdot \boldsymbol{W}_l}{\|\boldsymbol{W}_l\|^2} \boldsymbol{W}_l \qquad \alpha_{l,ML}(\tau_l, \phi_l, \nu_l) = \frac{\boldsymbol{H}_l \cdot \boldsymbol{W}_l}{\|\boldsymbol{W}_l\|^2}. \tag{4.71}$$

The inner product can be written as

$$\boldsymbol{H}_l \cdot \boldsymbol{W}_l = z\left(\tau, \phi, \nu, \hat{\mathbf{H}}_l\right) = \sum_{n=1}^{N_t} \sum_{k=1}^{N_{sc}} e^{-i2\pi(\nu_l t_n - f_k \tau_l)} \mathbf{a}^H(\phi_l) \hat{\mathbf{H}}_l(t_n; f_k), \tag{4.72}$$

and, furthermore, $\|\boldsymbol{W}_l\|^2 = N_t N_{sc} M$, and the $z\left(\tau, \phi, \nu, \hat{\mathbf{H}}_l\right)$ function can be interpreted as a three-dimensional correlation function. It can be shown [7] that the values τ_l, ϕ_l and ν_l can be obtained by solving the problem

$$\left(\hat{\tau}_l, \hat{\phi}_l, \hat{\nu}_l\right)_{ML} = \arg\max_{[\tau,\phi,\nu]} \left\{ \left| z\left(\tau, \phi, \nu, \hat{\mathbf{H}}_l\right) \right| \right\} \tag{4.73}$$

so that the overall problem now becomes finding the maximum of a three-dimensional correlation function. The procedure explained so far is an expectation-maximization (EM) algorithm. The EM algorithm proceeds iteratively by considering one multipath

component at a time, cancelling all the other components from the observations based on the previous parameter estimates $\hat{\boldsymbol{\theta}}'$ (E step), and updating the current parameters by maximizing the three-dimensional correlation function (M step). This results in the new parameters $\hat{\boldsymbol{\theta}}''$, which will be used in the next iteration. The iterations can be stopped when convergence is reached. The vector parameters obtained at the μ iteration is called $\hat{\boldsymbol{\theta}}(\mu)$. The sequence of likelihood values at each iteration is called $\Lambda(\hat{\boldsymbol{\theta}}(\mu))$ and has the property that it is always monotonically non decreasing through the successive iterations [7].

The SAGE algorithm further simplifies the EM algorithm, decomposing the 3D correlation maximization problem for each path into a sequence of 3 successive one dimensional maximization problems. In other words, the SAGE algorithm uses alternate optimization over the four parameters τ_l, ϕ_l ν_l and α_l, starting from an initial guess of their values. It optimizes only one variable at a time, keeping the others fixed. The process is then repeated until the variables have converged. Indeed, it is possible to obtain the new parameters $\hat{\boldsymbol{\theta}}_l'' = \left[\hat{\tau}_l'', \hat{\phi}_l'', \hat{\nu}_l'', \alpha_l''\right]$ from the previous estimated parameters $\hat{\boldsymbol{\theta}}_l' = \left[\hat{\tau}_l', \hat{\phi}_l', \hat{\nu}_l', \alpha_l'\right]$ as

$$\hat{\tau}_l'' = \arg\max_{\tau} \left\{ \left| z\left(\tau, \hat{\phi}_l', \hat{\nu}_l', \hat{\mathbf{H}}_l\right) \right| \right\} \tag{4.74}$$

$$\hat{\phi}_l'' = \arg\max_{\phi} \left\{ \left| z\left(\hat{\tau}_l'', \phi, \hat{\nu}_l', \hat{\mathbf{H}}_l\right) \right| \right\} \tag{4.75}$$

$$\hat{\nu}_l'' = \arg\max_{\nu} \left\{ \left| z\left(\hat{\tau}_l'', \hat{\phi}_l'', \nu, \hat{\mathbf{H}}_l\right) \right| \right\} \tag{4.76}$$

$$\hat{\alpha}_l'' = \frac{z\left(\hat{\tau}_l'', \hat{\phi}_l'', \hat{\nu}_l'', \hat{\mathbf{H}}_l\right)}{N_t N_{sc} M} \tag{4.77}$$

Also in the SAGE algorithm, the channel vector parameter obtained at the μ iteration $\hat{\boldsymbol{\theta}}(\mu)$ determines likelihood values which are always monotonically non decreasing thought successive iterations. The signal flow graph of the algorithm is depicted in Figure 4.8. The initialization of SAGE is addressed in Chapter 5, i.e., the calculation of the vector $\hat{\boldsymbol{\theta}}(0)$, because it is a problematic aspect of the algorithm, especially in the case of real uplink LTE signals.

4.4.2 Detection of the number of paths

The SAGE algorithm does not provide itself a method for the estimation of the number L of multipath components. In the previous subsection, the number of paths L is indeed assumed to be known a priori. Conventional information criteria [48] can be used to estimate L. The general idea under these criteria is to minimize a penalized

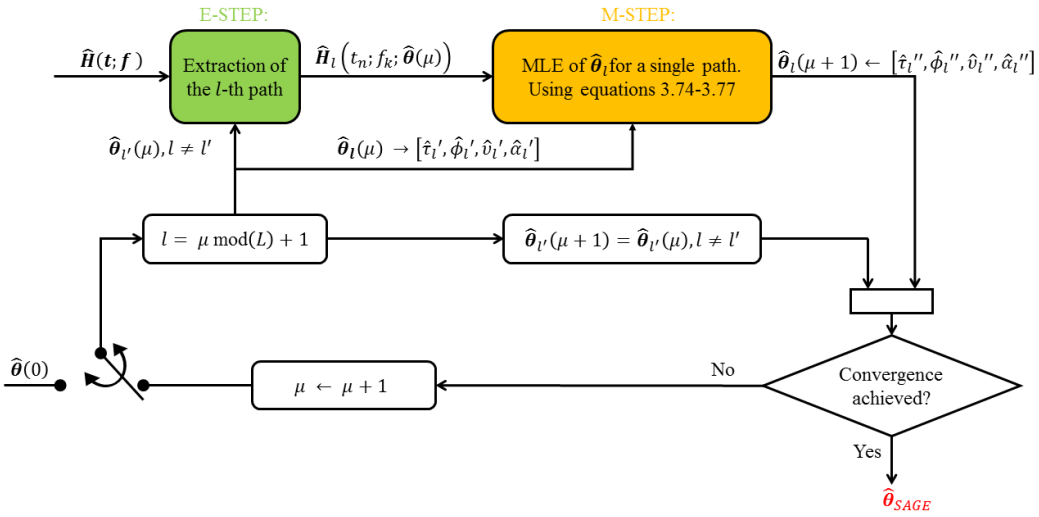

Fig. 4.8 Flow chart of SAGE algorithm

log-likelihood function, as

$$\hat{L} = \arg\min_{l} \left\{ -2 \ln \left[\Lambda \left(\boldsymbol{\gamma}_{ML} \right) \right] + lk \mathscr{P} \left(N_{tot}, lk \right) \right\} \tag{4.78}$$

where $\mathscr{P}\left(N_{tot}, lk\right)$ is the penalty function that depends on the particular criterion adopted, k is the number of real valued parameters to be estimated for each of the l paths, and N_{tot} is the total number of real valued observations available (i.e. $N_t N_{sc} M$). It can be shown that the above is equivalent to

$$\hat{L} = \arg\min_{l} \left\{ N_{tot} \ln \left[\sigma_{ML}^2 \right] + lk \mathscr{P} \left(N_{tot}, lk \right) \right\}. \tag{4.79}$$

As suggested in [49], to contrast the natural tendency of these estimators to overestimate the model order in case of high SNR and large observation sets (i.e., large N_{tot}), it is convenient to not equally weight the k parameters, depending on the specific underlying model. According to [49], in our problem, the τ_l, ϕ_l and ν_l parameters should be weighted three times with respect to the amplitude. This results in having a global weight $k = 2 + 3 \times 3 = 11$, hence

$$\hat{L} = \arg\min_{l} \left\{ N_{tot} \ln \left[\sigma_{ML}^2 \right] + 11 l \mathscr{P} \left(N_{tot}, 11l \right) \right\}. \tag{4.80}$$

In this thesis, the Minimum Description Length (MDL) criterion, also referred to as Bayesian Information Criterion (BIC), is adopted to estimate L. According to this

criterion, the penalty term is given by $\mathscr{P}(N_{tot}, lk) = \ln[N_{tot}]$. Hence, the model order selection metric that is adopted in this work is

$$\hat{L} = \arg\min_{l} \left\{ N_{tot} \ln\left[\sigma^2_{ML}\right] + 11l \ln[N_{tot}] \right\}. \tag{4.81}$$

4.5 Cramér Rao lower bound

In this section a theoretical performance bound used for assessing the effectiveness of the estimators used in this thesis will be presented. The bound used is the Cramér Rao bound.

Estimators that are usually considered have the property to yield on average the correct value. These estimators are referred to as unbiased estimators. In the case we are interested in, the goal is to estimate the $5L$-dimensional real vector

$$\begin{aligned} \mathbf{\Omega} = [&\mathrm{Re}\{\alpha_1\}, \ldots, \mathrm{Re}\{\alpha_L\}, \mathrm{Im}\{\alpha_1\}, \ldots, \mathrm{Im}\{\alpha_L\}, \\ &\tau_1, \ldots, \tau_L, \phi_1, \ldots, \phi_L, \mu_1, \ldots, \mu_L] \end{aligned} \tag{4.82}$$

and we suppose that our estimate $\hat{\mathbf{\Omega}}$ is unbiased, i.e., that

$$\mathbb{E}\left[\hat{\mathbf{\Omega}}\right] = \mathbf{\Omega} \tag{4.83}$$

Another optimality criterion which is frequently adopted for searching for good unbiased estimators, is the minimum variance criterion. According to this criterion, an unbiased estimator performance is quantified by its variance $\mathrm{VAR}\left(\hat{\mathbf{\Omega}}\right)$. This criterion is derived from a more general one, which can be applied also to biased estimators, and aims to minimising the overall mean square estimation error (MSEE).

Considering an unbiased estimator $\hat{\mathbf{\Omega}}$, it can be shown that its covariance matrix satisfies the inequality [50]

$$\mathbb{E}\left[\left(\hat{\mathbf{\Omega}} - \mathbf{\Omega}\right)^T \left(\hat{\mathbf{\Omega}} - \mathbf{\Omega}\right)\right] \geq F^{-1}(\mathbf{\Omega}) \tag{4.84}$$

where the $5L \times 5L$ real matrix $F(\mathbf{\Omega})$ is the so called Fisher information matrix (FIM), which is positive definite. The inequality sign in (4.84) means that the difference of the matrices in the left and right terms is positive definite. Considering the k-th element of $\hat{\mathbf{\Omega}}$, i.e., $\hat{\Omega}_k$, we have

$$\mathrm{MSSE}(\Omega_k) = \mathbf{E}\left[\left(\hat{\Omega}_k - \Omega_k\right)^2\right] \geq \left[F^{-1}(\mathbf{\Omega})\right]_{kk} \triangleq \mathrm{CRLB}(\Omega_k) \tag{4.85}$$

where $[F^{-1}(\mathbf{\Omega})]_{kk}$ represents the diagonal element in row and column k of the inverse of the FIM. CRLB (Ω_k) is called the Cramér Rao lower bound of the estimated parameter $\hat{\Omega}_k$. It is also possible to define the root MSEE as the square root of the MSEE, in other words RMSSE $(\Omega_k) \triangleq \sqrt{\text{MSSE}(\Omega_k)}$. In general an expression of the MSEE bound exists also if the estimator is biased.

In order to calculate $[F^{-1}(\mathbf{\Omega})]_{kk}$ we can proceed as follows. Let us denote with $\boldsymbol{s}(t, \mathbf{\Omega})$ a general a complex signal vector, which can have a strong non-linear dependence on the parameter vector $\mathbf{\Omega}$. In our problem of interest, we suppose that the noise $\mathbf{w}(t)$ is modeled as a white zero-mean complex Gaussian random process with independent real and imaginary parts, each with variance $\sigma_w^2/2$. We can write

$$\mathbf{y}(t) = \mathbf{s}(t, \mathbf{\Omega}) + \mathbf{w}(t) = \sum_{l=1}^{L} \alpha_l s(t - \tau_l) e^{j2\pi\nu_l t} \cdot \mathbf{a}(\phi_l) + \mathbf{w}(t) \in \mathbb{C}^M \tag{4.86}$$

where M is the number of antenna elements in the array. Let us suppose that $\mathbf{y}(t)$ has duration $[0; T_0[$. It can be shown [51] that the log-likelihood function of $\mathbf{\Omega}$ is

$$\Lambda(\mathbf{\Omega}; \mathbf{y}) = \frac{2}{\sigma_w^2} \int_0^{T_0} \text{Re}\left\{\mathbf{s}^H(t, \mathbf{\Omega})\, \mathbf{y}(t)\right\} dt + \frac{1}{\sigma_w^2} \int_0^{T_0} ||\mathbf{s}(t, \mathbf{\Omega})||^2 dt \tag{4.87}$$

Then the element (k, j) of the FIM, can be calculated as [50]

$$[F(\mathbf{\Omega})]_{kj} = -\mathbb{E}\left[\frac{\partial}{\partial\Omega_k}\frac{\partial}{\partial\Omega_j}\Lambda(\mathbf{\Omega}; y)\right]. \tag{4.88}$$

From the expression above, one can calculate the CRLBs, which are the elements in the diagonal of the inverse of the FIM, and, as demonstrated in [7] in case of a single path, i.e., $L = 1$, the CRLBs for the different parameters are

$$\begin{aligned}
\text{CRLB}(\tau) &= \frac{1}{\gamma_0}\frac{1}{8\pi^2\beta_g^2} \\
\text{CRLB}(\phi) &= \frac{1}{\gamma_0}\frac{6}{\pi^2\cos^2\phi\,(M^2-1)} \\
\text{CRLB}(\nu) &= \frac{1}{\gamma_0}\frac{3}{2\pi^2 t_n^2\,(N_t^2-1)} \\
\text{CRLB}\left(\frac{\alpha}{|\alpha|}\right) &= \text{CRLB}\left(\text{Re}\left\{\frac{\alpha}{|\alpha|}\right\}\right) + \text{CRLB}\left(\text{Im}\left\{\frac{\alpha}{|\alpha|}\right\}\right) = \frac{1}{\gamma_0}
\end{aligned} \tag{4.89}$$

In the expression above, β_g^2 is the Gabor bandwidth of the signal $s(t)$, which is the root mean square value of the spectral content of the signal $s(t)$ and is calculated as

$$\beta_g^2 = \frac{1}{\varepsilon_s} \int_0^{T_0} \left| \frac{ds(t)}{dt} \right|^2 dt \tag{4.90}$$

with ε_s the energy of the signal

$$\varepsilon_s = \int_0^{T_0} |s(t)|^2 \, dt. \tag{4.91}$$

In Equation (4.89), we have $\gamma_0 = N_t N_{sc} M \gamma_m$, where γ_m can be seen as the signal to noise ratio of the wave at the input of each antenna branch. In other words, γ_0 is the number of total observations times the SNR at the input of each antenna. The CRLBs calculated for $L > 1$ are lower bounded by the corresponding CRLB calculated for $L = 1$ [50]. Furthermore, the CRLBs for small L are close to those for $L = 1$ if the paths are well separable. This means that the CRLBs calculated in the case $L = 1$ can be used as a benchmark in order to assess the performance of a given estimator.

Chapter 5

LTE Uplink TOA Estimation Results

5.1 Introduction

The 3GPP LTE protocol (3rd Generation Partnership Project Long Term Evolution) introduced the support for positioning and, indeed, 4G LTE can provide good coverage in those scenarios where the GNSS fails. The network usually measures the Time of Arrival (TOA), the Time Difference of Arrival (TDOA), the Received Signal-Strength (RSS), or the Angle of Arrival (AOA) [2]. These measurements are used to perform positioning, using techniques like Enhanced Cell Identity (E-CID), Assisted GNSS (A-GNSS), Observed Time Difference of Arrival (OTDOA) and Uplink Time Difference of Arrival (UTDOA) [2]. 3GPP introduces two stand-alone network-based TDOA measures, i.e., OTDOA and UTDOA, which exploit downlink and uplink transmissions, respectively. In OTDOA, the UE measures the TDOA of neighbour eNodeBs with respect to a reference eNodeB, exploiting the Positioning Reference Signal (PRS). The UTDOA positioning method in LTE is similar to OTDOA, except that it uses the uplink Sounding Reference Signal (SRS). In this case, UE signals are measured at some eNodeBs or at some Location Measurement Units (LMUs), which are standalone units integrated in the eNodeBs or, alternatively, located in some known strategic locations.

In many cases, however, the eNodeB does not set up the UE to transmit the SRS, thus making it impossible to provide positioning information. The main contribution of this chapter is to define a new opportunistic method to estimate the TOA using the uplink demodulation reference signal (DM-RS) instead of the SRS. As a matter of fact,

the DM-RS signal is transmitted in every slot during UE data transmission, e.g., in the transmission of a simple “ping" signal. In the assumed scenario multiple eNodeBs, or alternatively multiple LMUs instructed by the reference eNodeB, can measure the DM-RS and estimate a time of arrival, then using a TDOA positioning techniques like hyperbolic positioning the position of the UE can be detected. A possible drawback of the use of DM-RS with this strategy, however, is that data transmission could occupy a smaller bandwidth than SRS, thus making TOA estimation less precise. In particular this Chapter focuses on the time of arrival measurement and how to perform this measurement also in a real scenario. In the first part of this Chapter we show some problems that we had to face when uplink transmission is used. We present our solution confirming its reliability by means of simulations. Then, in the second part of the Chapter, we show the performance results of the proposed algorithms. In particular we did extensive simulations using three different channel realizations and we test the algorithms in the extended pedestrian A channel model (EPA), extended vehicular A model (EVA) and extended typical urban model (ETU), which are channel models defined in the standard [52, 53]. In these simulations we compare the performance between SAGE algorithm, IAA-APES algorithm and correlation peak detector in three different scenarios. The first scenario represent a lower bound, while the other two scenarios simulate an uplink transmission. In the last part, we show the results obtained using uplink transmission, and we confirm that the DM-RS can be effectively used for positioning purposes using TDOA techniques. Then the Chapter ends with the conclusions.

5.2 IAA-APES for delay estimation

In Section 4.3.7, the IAA-APES algorithm for angle of arrival (AOA or DOA) estimation was presented. The algorithm can be also extended to TOA estimation. If we consider, without loss of generality, one receiving antenna and L paths, the k-th bin of the CFR at time t_n, can be written as

$$\hat{H}\left(t_n, f_k\right) = \sum_{l=0}^{L} \alpha_l e^{-j2\pi(\nu_l t_n - f_k \tau_l)} + n\left(t_n, f_k\right) \tag{5.1}$$

So the CFR can be written in matrix notation as

$$\hat{\boldsymbol{H}}\left(t_n\right) = \begin{bmatrix} \hat{H}\left(t_n, f_1\right) \\ \hat{H}\left(t_n, f_2\right) \\ \vdots \\ \hat{H}\left(t_n, f_K\right) \end{bmatrix} = \mathbf{A}\left(\boldsymbol{\tau}\right)\boldsymbol{\alpha}\left(t_n\right) + \mathbf{n}. \tag{5.2}$$

Using a notation similar to the one of Section 4.3.7, t_n represents the $n-$th snapshot, $\boldsymbol{\alpha}\left(t_n\right) = \left[\alpha\left(t_n\right), \ldots, \alpha_L\left(t_n\right)\right]^T$ has the same role of $\mathbf{s}\left[n\right]$ in Equation (4.49), with the l-th element $\alpha_l\left(t_n\right) = \alpha_l e^{-j2\pi\nu_l t_n}$, and finally the matrix $\mathbf{A}$ is similar to the steering matrix but is defined as $\mathbf{A}\left(\boldsymbol{\tau}\right) = \left[\mathbf{a}\left(\tau_1\right), \ldots, \mathbf{a}\left(\tau_L\right)\right]$ where the l-th column is $\mathbf{a}\left(\tau_l\right) = \left[e^{j2\pi f_1 \tau_l}, \ldots, e^{j2\pi f_K \tau_l}\right]^T$. The difference between Equation (5.2) and Equation (4.49) consists of different parameters in the matrix $\mathbf{A}$, because we want to estimate the TOAs τ_l instead of the AOAs ϕ_l. So, similarly to the AOA case, if we can construct a grid with $I \gg L$ elements, the problem can be represented as a sparse problem and the IAA-APES algorithm can be used to estimate the delays τ_l. In other words, it is possible to construct a grid with the τ_i values, where the τ_i that gives peaks in the power estimations represent the TOAs of the different paths. The TOA of the first path will be represented by the minimum τ_l. For completeness, we note that the same sparse representation can be obtained also if the number of antenna is M, simply using the M values coming from each antenna as additional snapshots.

Similarly, it is possible to use the IAA-APES algorithm for Doppler estimation, just replacing matrix $\mathbf{A}\left(\boldsymbol{\tau}\right)$ with matrix $\mathbf{A}\left(\boldsymbol{\nu}\right) = \left[\mathbf{a}\left(\nu_1\right), \ldots, \mathbf{a}\left(\nu_L\right)\right]$ where the l-th column is $\mathbf{a}\left(\nu_l\right) = \left[e^{-j2\pi t_1 \nu_l}, \ldots, e^{-j2\pi t_N \nu_l}\right]^T$. We can also perform joint estimations. For example a joint AOA, TOA estimation can be obtained by considering the following matrix

$$\mathbf{A}\left(\boldsymbol{\tau}, \boldsymbol{\phi}\right) = \left[\mathbf{a}\left(\tau_1, \phi_1\right), \mathbf{a}\left(\tau_2, \phi_1\right), \ldots, \mathbf{a}\left(\tau_I, \phi_1\right), \mathbf{a}\left(\tau_1, \phi_2\right), \ldots, \mathbf{a}\left(\tau_I, \phi_P\right)\right] \tag{5.3}$$

where, in case of uniform linear array (ULA), the vector $\mathbf{a}$ can be written as

$$\mathbf{a}\left(\tau_i, \phi_p\right) = \begin{bmatrix} e^{j2\pi f_1 \tau_i} \\ \vdots \\ e^{j2\pi f_K \tau_i} \\ e^{j2\pi\left(f_1\tau_i + \frac{d}{\lambda}\sin\phi_p\right)} \\ \vdots \\ e^{j2\pi\left(f_1\tau_i + \frac{2d}{\lambda}\sin\phi\right)} \\ \vdots \\ e^{j2\pi\left(f_K\tau_i + (M-1)\frac{d}{\lambda}\sin\phi_p\right)} \end{bmatrix}. \tag{5.4}$$

Also in this case, the parameters estimations are obtained from the pairs $\left(\hat{\tau}_i, \hat{\phi}_p\right)$ that maximize the power.

Let us denote with I the number of grid points for the delay, P the number of grid points for the angle, M the number of antennas and K the number of channel frequency bins. We can notice that one issue of the IAA-APES implementation is related to the inversion of the correlation matrix $\mathbf{R}$, which has a dimension $MK \times MK$. Indeed, for an $n \times n$ matrix, the calculation of the inverse has a complexity higher than $O\left(n^2\right)$ when optimized algorithms are used. This leads to a high computational burden and high time consumption in case of joint estimation. On the other hand, another problem is that, to achieve a proper resolution, I and P have to be selected large, so the matrix $\mathbf{A}\left(\boldsymbol{\tau}, \boldsymbol{\phi}\right)$ has a dimension equal to $MK \times PI$. Furthermore, the power has to be calculated for all the PI pairs. For example, considering a scenario with $M = 4$ antennas, a transmission bandwidth of $N_{sc} = 1200$ subcarriers (the highest transmission bandwidth in Table 3.1), a grid with a resolution $Ts \approx 32,55$ ns in delay domain (i.e., around 10 m in pseudorange) and a resolution $\Delta\phi = 2°$ in the angle domain, matrix $\mathbf{A}\left(\boldsymbol{\tau}, \boldsymbol{\phi}\right)$ occupies approximately 14 Gbytes and it becomes impossible to use this approach in a practical scenario. We can conclude that memory consumption is also a limitation of the IAA-APES algorithm in a practical implementation. The previously mentioned issues are the main reasons why we decided not to use the IAA-APES algorithm for joint estimation of TOA or AOA, while we can use it, in our application to LTE signals, to estimate them separately.

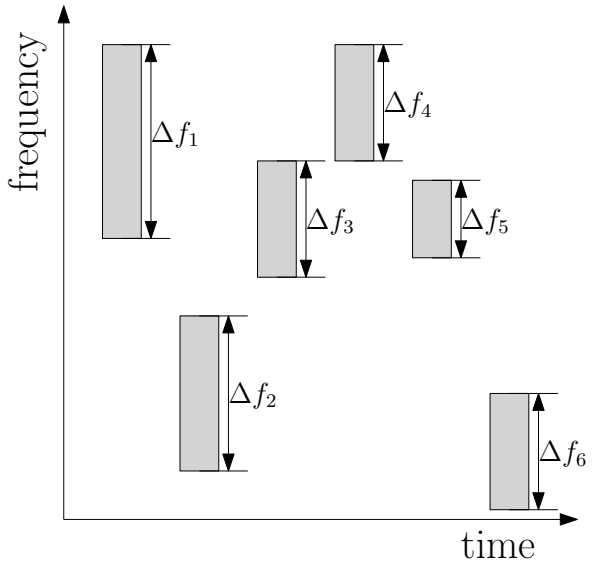

Fig. 5.1 Time-frequency pattern.

5.3 Uplink DM-RS transmission issues

Since the DM-RS is transmitted inside an uplink data transmission, the band occupied by the data is scheduled by the eNodeB. Therefore, in correspondence with a bandlimited DM-RS input, the CFRs can be estimated only in those portions of the band where the data transmission is scheduled. The typical resulting available time-frequency pattern $\hat{\boldsymbol{H}}(\boldsymbol{t};\boldsymbol{f})$ is depicted in Fig. 5.1. Due to this particular pattern, one can expect a performance degradation caused by the relatively small bandwidth available for TOA estimation in each subframe. It is possible to show that the correct approach to calculate Equations (4.73) - (4.77) in this case, is to set to zero the values $\hat{\boldsymbol{H}}(\boldsymbol{t};\boldsymbol{f})$ when no information is available.

Suppose therefore that the channel is observed at different subcarriers $f_k = k\Delta f$, and at different time snapshots $t_n = n\Delta t$, (corresponding to different measurements of the CFR) and through M different antennas. This defines a uniform grid of coordinates $I = \{(n,k,m)\}$. If we consider an uplink transmission where the observation in correspondence of some pairs (n,k) is not known, and the whole M antennas receive the same time and frequency pattern, it is possible to consider a nonuniform grid in time and frequency domain for each antenna. Considering the m-th antenna, we denote as $N_{tot,m} = |I_m|$ the cardinality of the set I_m of available channel observations in time and frequency. Moreover, since all antennas receive the same time and frequency pattern, i.e. $I_m = I_{m'}\ \forall\ m, m'$, $N_{tot,m}$ complex valued observations will be available at each antenna. The channel vector parameter $\boldsymbol{\theta}$, can be considered equal for each antenna

under far field and narrowband assumptions. Considering the m-th antenna, these channel measurements can be described as $\hat{\boldsymbol{H}}_m(\boldsymbol{t};\boldsymbol{f}) = \{\hat{H}_m(t_n; f_k) \in \mathbb{C},\ (n,k) \in I_m\}$. Under the assumption that the noise is independent among antennas, and considering independent complex Gaussian noise samples $n_m(t_n; f_k) \in \mathbb{C}$ at each antenna, with variance $\sigma_m^2 = \sigma^2,\ \forall\ m$, we can write $\hat{H}_m\left(t_n; f_k\right) = H_m(t_n; f_k; \boldsymbol{\theta}) + n_m(t_n; f_k)$. This is a $5L+1$ minimization problem with the vector of parameter $\boldsymbol{\Omega} = [\sigma^2, \boldsymbol{\theta}] \in \mathbb{R}^{5L+1}$, very similar to the one faced in Section 4.4. Then, the ML estimation consists of minimizing the log-likelihood function of $\hat{\boldsymbol{H}}(\boldsymbol{t};\boldsymbol{f})$, which under the Gaussian assumption is equal to

$$\begin{aligned}\boldsymbol{\Omega}_{ML} = \min_{\boldsymbol{\Omega}} \Big\{ & 2N_{tot,m} M \log\left(2\pi\sigma^2\right) + \\ & + \frac{1}{\sigma^2} \sum_{m=1}^{M} \sum_{(n,k)\in I_m} \left| \hat{H}_m(t_n; f_k) - H_m(t_n; f_k; \boldsymbol{\theta}) \right|^2 \Big\}. \end{aligned} \tag{5.5}$$

One can notice that Equation (5.5) is similar to Equation (4.64), with the only difference that $N_t N_{sc}$ is replaced by the total number of observations $N_{tot,m}$ available at each antenna. Furthermore, the summation is over the set of available observations, which are not located on a uniform grid, due to the holes in the time-frequency domain. It is important to notice that if zeros are added at the (n,k) locations where channel observations are not available, the log-likelihood minimization problem does not change. Therefore, we can consider a uniform grid with zeros substituting the non-available observations. Instead of using the product $N_t N_{sc}$ we have to use the cardinality of the set I_m, i.e., $N_{tot,m}$. In a uniform grid, Equations (4.74) - (4.77) can be easily computed via FFT algorithms. Therefore, also with uplink signals, where the grid is not uniform, we can formulate the problem in a uniform grid and compute the estimates efficiently via FFT, by setting to zero all the missing values.

5.4 SAGE initial conditions for Uplink transmission.

During the $\mu-$th iteration, SAGE estimates the parameters vector $\hat{\boldsymbol{\theta}}\left(\mu\right)$ using the parameters estimated in the previous iteration $\hat{\boldsymbol{\theta}}\left(\mu-1\right)$, as shown in Equations (4.74)-(4.77) and in Figure 4.8 in Section 4.4. So, during the first iteration (i.e., $\mu = 1$) SAGE needs a previous estimation of the parameters vector, i.e., it needs the vector $\hat{\boldsymbol{\theta}}\left(0\right)$. This vector can be estimated in different ways and represents the initial conditions that SAGE uses.

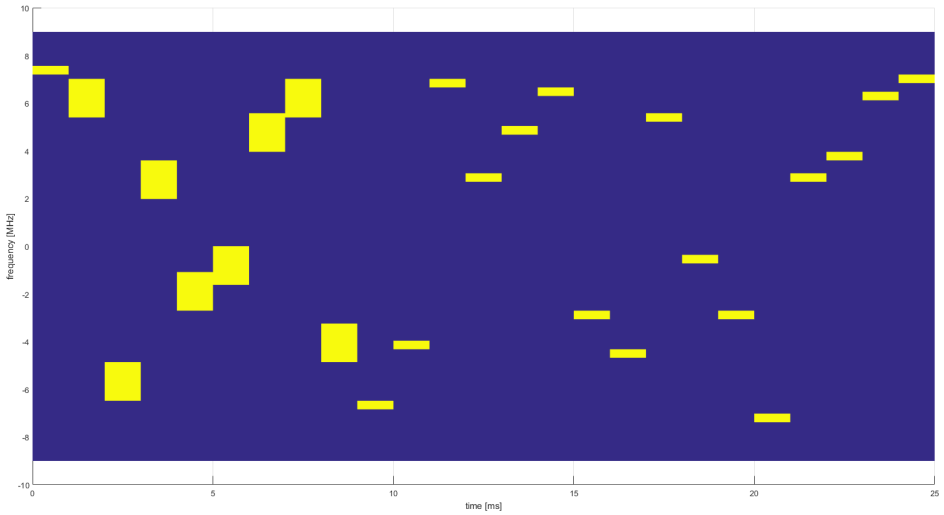

Fig. 5.2 Time-frequency pattern of an uplink transmission. The transmission does not cover the overall available bandwidth but only a small portion of it. The figure shows the bandwidth occupied by a real uplink transmission corresponding to a "ping" message.

In [7], the initial conditions are calculated using a non-coherent accumulation during the M-step, while a successive cancellation is used during the E-step. This means that, assuming that we want to estimate the initial conditions of the parameters $\left(\hat{\tau}_l, \hat{\phi}_l, \hat{\nu}_l, \hat{\alpha}_l\right)$, these are calculated as

$$\hat{\tau}_l = \arg\max_{\tau} \left\{ \sum_{m=1}^{M} \sum_{n=1}^{N} \left| \sum_{k=1}^{N_{sc}} e^{j2\pi f_k \tau} \hat{H}_{m,l}\left(t_n; f_k\right) \right|^2 \right\} \tag{5.6}$$

$$\hat{\phi}_l = \arg\max_{\phi} \left\{ \sum_{n=1}^{N} \left| \sum_{k=1}^{N_{sc}} e^{j2\pi f_k \hat{\tau}_l} \mathbf{a}^H\left(\phi\right) \hat{\mathbf{H}}_l\left(t_n; f_k\right) \right|^2 \right\}. \tag{5.7}$$

where $\hat{\nu}_l$ and $\hat{\alpha}_l$ are calculated as in Equation (4.76) and Equation (4.77), respectively. This procedure is called non coherent accumulation because, in contrast to what we saw in Equation (4.74) and Equation (4.75), in this case the summations are calculated outside the modulus, then the phase of the complex samples is not considered. The successive interference cancellation during the M-step is performed as

$$\hat{\mathbf{H}}_l\left(\boldsymbol{t}, \boldsymbol{f}\right) = \hat{\mathbf{H}}\left(\boldsymbol{t}; \boldsymbol{f}\right) - \sum_{l'=1}^{l-1} \mathbf{H}_{l'}\left(\boldsymbol{t}; \boldsymbol{f}; \hat{\boldsymbol{\theta}}_{l'}\right). \tag{5.8}$$

The procedure starts by estimating the initial condition of the first path. From Equation (5.8) one can notice that when the initial condition of the first path has to be estimated, no cancellation is performed and the non-coherent accumulation procedure is applied directly to the full observation matrix $\hat{\mathbf{H}}(\boldsymbol{t};\boldsymbol{f})$. Then, in the next step, the parameters concerning the second path have to be estimated. So, the first path estimation is cancelled and another non-coherent accumulation procedure is performed. This process continues until the last path initial conditions are estimated. In the following, we refer to this procedure as the non-coherent initialization of SAGE.

In general the correlation function $z(\tau_l, \phi_l, \nu_l)$ of Equation (4.72), can be calculated through DFFT and IDFT algorithms. One can notice that the correlation function corresponds to a periodogram in the delay-angle-Doppler domain. For convenience, we consider a joint delay Doppler estimation, so the relative delay-Doppler periodogram will have some maximum at the pairs $(\tau_l;\nu_l)$ that correspond to the parameters of the path. Based on this, we propose a new method to estimate the initial conditions of SAGE. In particular, the initial conditions of the first path is made by searching the pairs $(\tau;\nu)$ corresponding to a maximum of the periodogram calculated using the full observation matrix $\hat{\mathbf{H}}(\boldsymbol{t};\boldsymbol{f})$. Then we perform a cancellation as in Equation 5.8 and we calculate the second path parameters using again the periodogram. This procedure is repeated until the last path initial conditions are estimated.

The importance of the initial conditions is not to be underestimated. The SAGE algorithm, in particular, can give erroneous estimations when the values $\hat{\boldsymbol{\theta}}_l(0)$, relative to the l-th path, are close to some local maximum of $|z(\tau_l, \nu_l)|$. In this situation, it can happen that the SAGE algorithm converges to a local maximum which is not related to an existing path. Furthermore, during the E-step, SAGE will cancel a path that is not related to a real path and this adds further errors in the estimation. Indeed, this erroneous cancellation can add other local maximum to the correlation function and this has an impact also in the estimation of the others paths. This problem is particularly critical with uplink transmissions. Indeed, when no information about the CFR is available, we complete with zeros the unknown CFR bins (Section 5.3). An uplink transmission pattern similar to the one in Figure 5.2 can be seen as a time-frequency window that multiplies the overall observation matrix. In particular, without applying any window, if the bandwidth and the number of snapshots are sufficiently large, the correlation function will present a narrow main lobe in correspondence of the path values and some sidelobes nearby. Then, the multiplication of 2D window by the full band CFR corresponds to a convolution in the delay-Doppler domain, i.e., to a convolution between the peaks of the correlation function (which are ideally

Dirac's delta) and the shape of the 2D window in the delay-Doppler domain. The window's shape determines therefore the characteristics of the main and side lobes in the delay-Doppler domain. When there is multipath, and in particular with close paths, the 2D window can create some local maximum in the correlation function that are not related to a real multipath component.

Using the non-coherent initialization method proposed in [7], in uplink transmission, we noticed that the initial conditions tend to identify local maximum which are not related to a real path, and that the SAGE algorithm provides estimations with higher error.

The method that we propose directly computes the maximum of the correlation function. This technique can be extended also to the more general case where the angle ϕ has to be estimated. Indeed, it is necessary to perform a maximum search in the 3D correlation function to have a first estimate of the triad (τ, ϕ, ν). In general, this method requires more computational effort with respect to the simplest non-coherent accumulation, because it performs the search of the maximum in a 2D or 3D function, but the search for the maximum has to be done only once to estimate the initial conditions. However, as we will see, this method outperforms the non-coherent method when the CFR is estimated in an uplink transmission with a limited number of CFR sample estimates. Furthermore, we will also see that the two initialization methods have similar performance when all the available bandwidth is used. In the following part of the thesis, we refer to the proposed method as 2D initialization (or 3D initialization), and to non-coherent initialization when the method proposed in [7] is used.

5.5 Simulation Results With Different Initialization Procedures

This section presents some simulation results that show the performance of the 2D SAGE initialization and the non-coherent initialization, in different scenarios. For completeness, we compare the results obtained with these two initialization procedures with other techniques in order to give an idea of the overall performance. We test the ability of the algorithms to discriminate close paths in delay domain.

The SAGE algorithm uses as input the CFRs calculated at different time snapshots. Note that in each subframe two DM-RSs are transmitted, which occupy the same transmission bandwidth. A realistic transmission scenario consists of a number of consecutive transmitted subframes. In this way, one can calculate $2N_{sub}$ consecutive CFR estimates, where N_{sub} is the number of transmitted consecutive subframes.

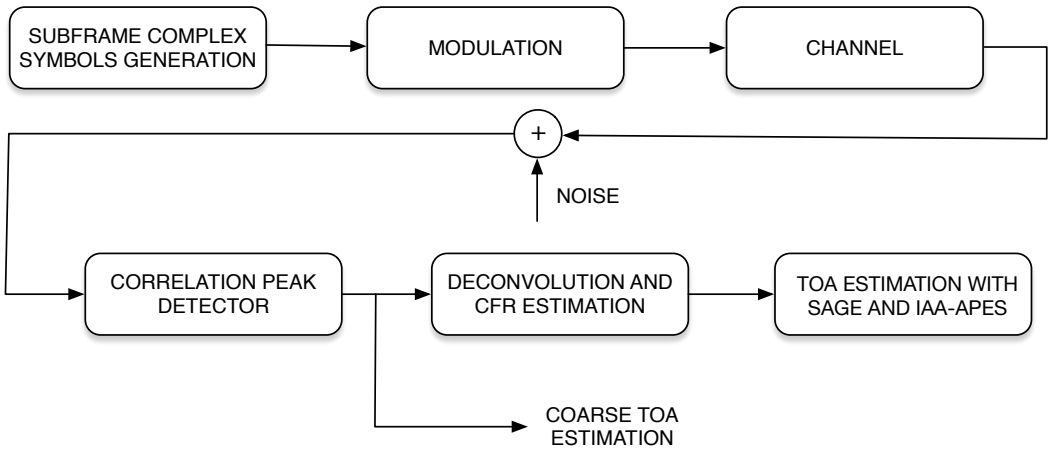

Fig. 5.3 Block diagram of the simulation setup.

In our simulations, we generate a random sequence of bits that are converted to complex symbols for each subframe according to the SC-FDMA modulation scheme showed in Section 3.3. We also include the DM-RSs, according to the specifications in [15]. Then, the channel is simulated using the model in Equation 4.57, and the convolution with the generated input is calculated. The channel is updated at every slot by taking Doppler into account.

Complex white Gaussian noise is added to the signal based on the SNR value, which is a simulation parameter. The variance of the noise is calculated based on the SNR, determined by the actual signal power (i.e., the DM-RS power). In this way, the other transmitted random data do not contribute to the calculation of the noise variance, since only the DM-RS is used to perform estimations. The resulting complex signal plus noise represents the received signal. The peak position obtained correlating the received signal with the known DM-RS sequence provides a first TOA estimation, which is usually not precise. Using the TOA correlation information and discarding the Cyclic Prefix, we are able to find the DM-RS location in the received signal and perform deconvolution in frequency. Since the time distance between a DM-RS and the following one is fixed and equal to $\Delta t = 0.5$ ms, once we have the position of the first DM-RS, we can easily find the position of the other DM-RS in the received signal. This provides an estimate of the CFR for each slot. This collected information constitutes the input of the SAGE and IAA-APES algorithm. These steps are summarized in the block diagram of Figure 5.3.

In the simulation we now describe, only one antenna is considered, so we are not considering the effect of different angles of arrival. In particular we consider three different scenarios:

1. We simulate a transmission that occupies the whole available LTE uplink bandwidth, and in particular we select the bandwidth with $N_{sc} = 1200$ subcarriers showed in Table 3.1. This case provides a lower bound for TOA estimation in LTE uplink. Indeed, considering the CRLB described in Section 4.5, the delay estimation is proportional to the occupied bandwidth, so in this case we have the maximum bandwidth occupation. This scenario can be used as a benchmark for the others, and in the following we refer to this scenario as the *full band scenario*.

2. The second scenario simulates a data transmission using the same $N_{sc} = 1200$ subcarriers of the first scenario, but in this case the occupied bandwidth is limited. In particular, we try to simulate an uplink transmission where the allocated band changes every two slots. Moreover, in this scenario, the allocated band occupies a minimum of 4 RBs and a maximum of 18 RBs. For each subframe two uniform random values are generated, we call them r_{NRB} and r_{start}. Value r_{NRB} represents the number of occupied RBs, so it is uniformly generated between 4 and 18. Value r_{start} represents the starting RB and is uniformly generated from 1 to $100 - r_{NRB}$. In other words, the band allocated for the uplink transmission in one subframe occupies the RBs from r_{start} to $r_{start} + r_{NRB}$. In general, this band occupation is slightly higher than in a real ping transmission. This can represent a situation where a large amount of data is transmitted. In the following, we refer to this scenario as the *simulated ping scenario*.

3. In the third scenario, we use the real ping transmission pattern showed in Figure 5.2, where the scheduled frequencies are obtained from a ping uplink transmission obtained from the commercial u-blox LTE module Toby L20 [54]. In the following this scenario is referred as the *real ping scenario*.

For each scenario we set the SNR to 10 dB and we simulate 3 paths with fixed Doppler frequencies $\nu_1 = \nu_2 = \nu_3 = 10$ Hz. Then, the delay is selected as

$$\begin{aligned} \tau_1 &= 15 \text{ ns} \\ \tau_2 &= \tau_1 + \Delta\tau \\ \tau_3 &= \tau_1 + 2\Delta\tau \end{aligned} \tag{5.9}$$

In the simulations, we evaluate the delay root mean square error (RMSEE), according to different $\Delta\tau$ values. We variate $\Delta\tau$ from 4 to 100 ns with steps of 4 ns. In particular, the simulated transmission has a duration in time of 25 subframes, i.e., 50 CFRs snapshots are available in each scenario. This duration is selected because a ping

transmission has approximately this duration. Then, we iterate the simulation for 100 times using different seeds for the random number generator. Thus, in the simulated ping scenario, the bandwidth allocation changes at every iteration, while in the real ping scenario and in the full band scenario the allocation is fixed and only the noise changes during each iteration. Furthermore, we assume that the number of paths is known, in order to have a better perspective on the algorithms performance.

The two choices of using one antenna and a ping transmission pattern in the simulations, are due to two reasons. First, we want to evaluate the performance in TOA estimation without adding the complexity related to AOA estimation, second, in the experimental results showed in Section 5.6, we estimate the TOA at two antennas placed at different positions, using uplink ping signals.

In particular we compare the following TOA estimation algorithms

- the first path TOA estimated with a correlation peak detector with threshold, where the transmitted DM-RS of each slot is correlated with the received signal
- the first path TOA estimated with a correlation peak detector with threshold, where in this case two contiguous DM-RSs belonging to the same subframe are correlated with the received signal, and the samples between the two DM-RS are filled with zeros
- IAA-APES
- the SAGE algorithm with 2D initialization
- the SAGE algorithm with non-coherent initialization

For completeness, since SAGE is set to estimate also the Doppler, we compare Doppler estimation using the two initializations procedure.

In Figure 5.4 we show the RMSEE of the delay obtained in the full band scenario. In the figure non-coherent initialization and the 2D initialization are compared. In particular, the figure shows that when the separation $\Delta\tau$ is below 30 ns, the RMSEE is between 10 and 20 ns for the three estimated paths (in pseudorange this is approximately an error between 3 and 6 m). This suggests that in this scenario SAGE is able to distinguish paths that are very close. With $\Delta\tau$ between 30 ns and 60 ns, it is possible to see that the 2D initialization algorithm has a slightly better RMSEE with respect to the non-coherent initialization, and that in general the RMSEE decreases. After 60 ns, the two initialization methods have almost the same performance and the error falls below 1 ns for the three estimated paths, corresponding to a pseudorange RMSEE below 1

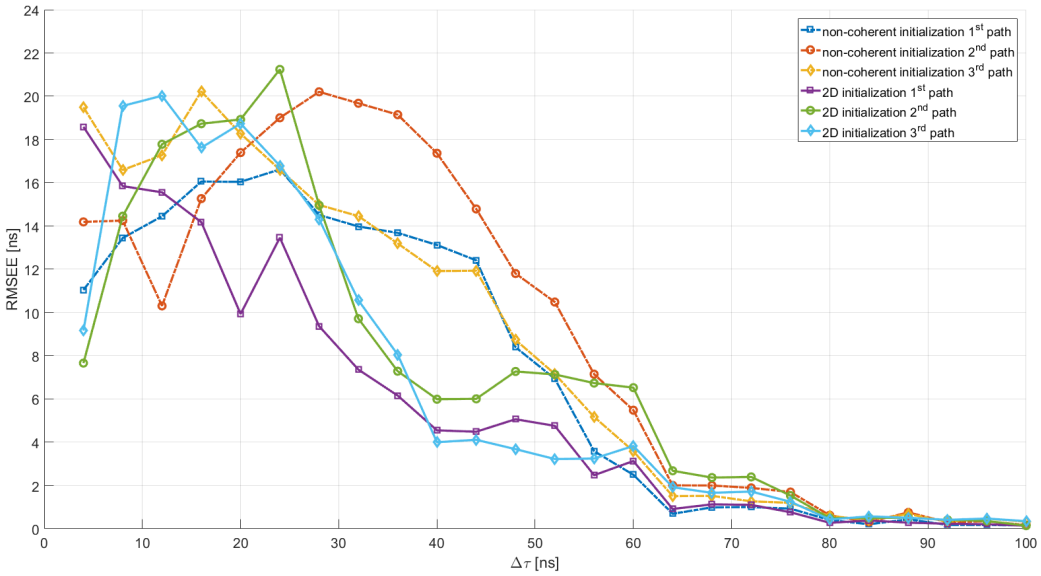

Fig. 5.4 RMSEE of the delays. Comparison between SAGE 2D initialization and SAGE non-coherent initialization in the full band scenario.

m. In Figure 5.5, the RMSEE of the Doppler estimation is showed. In particular, the Doppler RMSEE is very low and is below 1 Hz for both initialization methods. In general, we can say that the two initialization methods have the same performance in the full band scenario, both for delay and Doppler estimation.

In Figure 5.6 we plot the RMSEE of the delay obtained with the two initializations of SAGE, in the simulated ping scenario. In this case we can see that when $\Delta\tau$ is below 25 ns, the two methods have similar performance, with an error that is between 10 and 30 ns for the three estimated paths, i.e., between 3 and 10 m in pseudorange, respectively. When $\Delta\tau$ approaches and exceeds 25 ns, the error with the non-coherent initialization increases, and with $\Delta\tau = 100$ ns this approach has a delay RMSEE of 79 ns, which is around 25 m in pseudorange. Instead, the delay RMSEE with 2D initialization decreases when $\Delta\tau$ is above 25 ns, while the first path estimation is below 10 ns. A large error for the non-coherent initialization is evident also in the Doppler estimation. Indeed, from Figure 5.7, we see that the RMSEE of the Doppler exceeds 150 Hz for the non-coherent initialization while the 2D initialization has an error always below 5 Hz, apart from some cases where it approaches 20 Hz.

Figure 5.8 shows the RMSEE of the delays obtained with the two SAGE initializations in the real ping scenario. In this case, the SAGE 2D initialization performs better then the SAGE non-coherent initialization, similarly to the simulated ping scenario. Indeed, when $\Delta\tau$ is above 20 ns the RMSEE of the 2D initialization decreases and

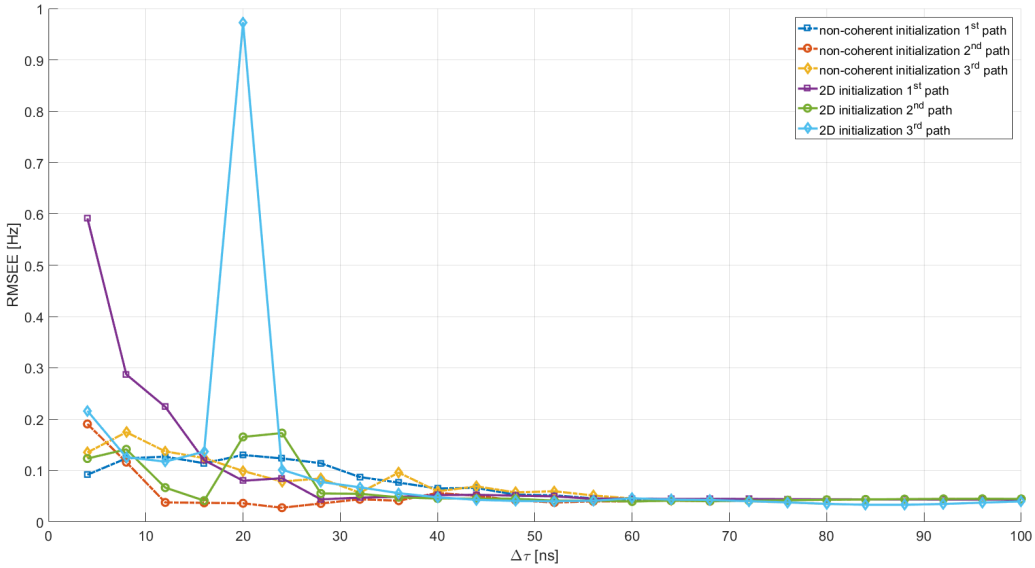

Fig. 5.5 RMSEE of the Doppler. Comparison between SAGE 2D initialization and SAGE non-coherent initialization in the full band scenario.

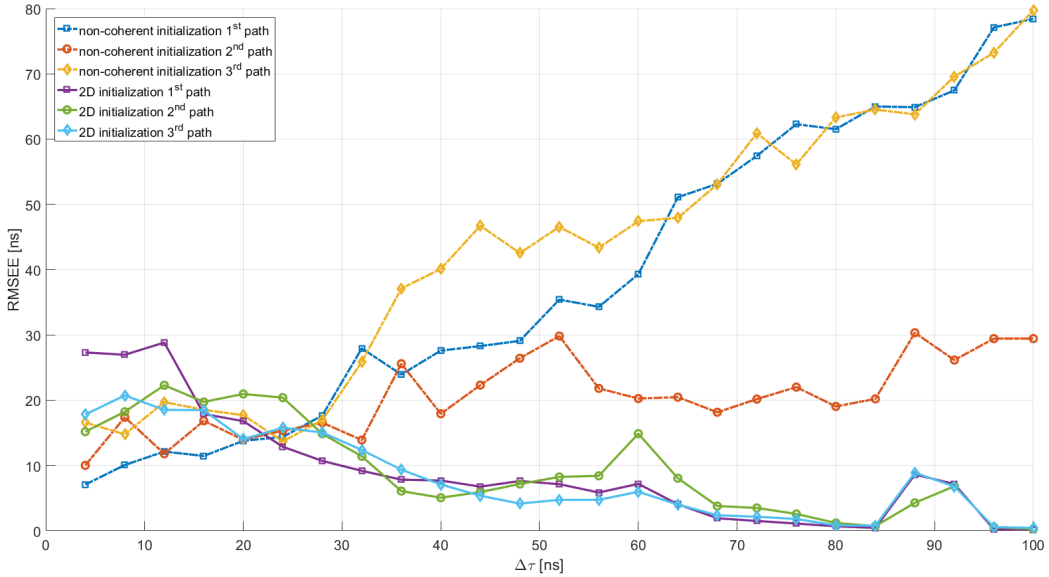

Fig. 5.6 RMSEE of the delays. Comparison between SAGE 2D initialization and SAGE non-coherent initialization in the simulated ping scenario.

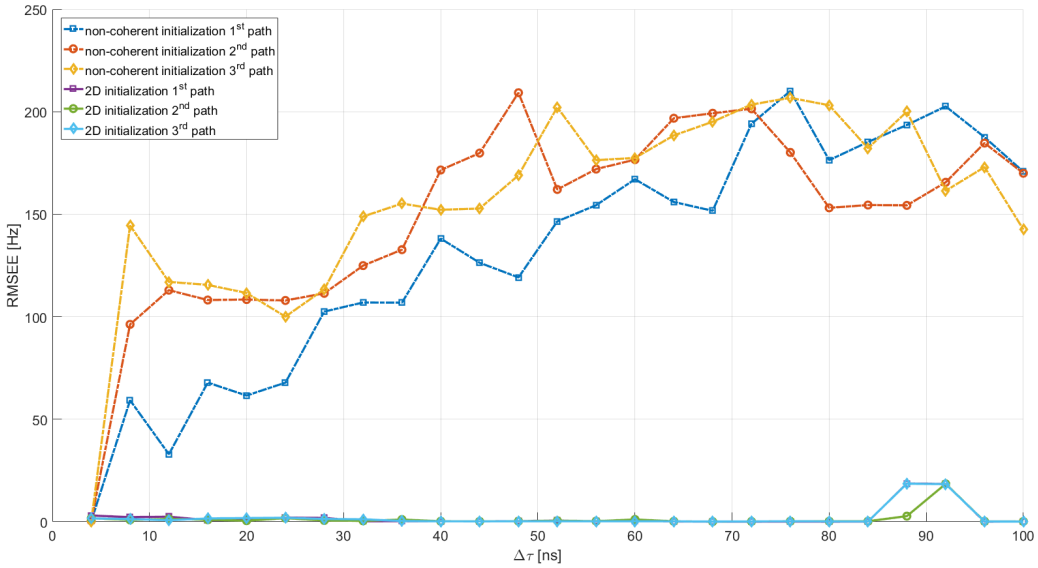

Fig. 5.7 RMSEE of the Doppler. Comparison between SAGE 2D initialization and SAGE non-coherent initialization in the simulated ping scenario.

is always below 20 ns, apart when $\Delta\tau$ is between 90 and 100 ns where the error is around 40 ns. In this case, the non-coherent initialization presents an error always higher than 25 ns and the first path estimation reaches 80 ns when $\Delta\tau$ is 100 ns. For $\Delta\tau$ around 95 ns, the relative high error of the 2D initialization is probably due to the particular pattern and band occupation of the ping message. We can see an increase of the RMSEE also in the Doppler estimation as depicted in Figure 5.9. From this figure, we note that in the real ping scenario the non-coherent initialization shows bad performance compared with the 2D initialization. Indeed, the RMSEE of the Doppler with non-coherent initialization exceeds 200 Hz for large $\Delta\tau$, while the 2D initialization is always below 2 Hz. When $\Delta\tau$ approaches the range 68 ns to 76ns and 86 ns to 100 ns, however, the error is around 20 Hz and 50 Hz respectively.

In Figure 5.10 the IAA-APES RMSEE of the delays is depicted for the full band scenario. When $\Delta\tau$ is between 4 and 12 ns, the three paths are too close and the algorithm is not able to separate them, so only one path is estimated and we see an increase of the error. When $\Delta\tau$ is between 12 and 24 ns, the algorithm is able to recognise only two paths and when $\Delta\tau$ exceeds 24 ns, the algorithm separates the three paths. When $\Delta\tau$ exceeds 48 ns, the RMSEE of the first path delay does not change anymore. Note that, as presented in Section 4.3.7, the IAA-APES algorithm explores a grid of possible delays, and that the true 1-st path delay, equal to 15 ns, does not belong to the used grid. So, even if the paths are well separated, there is a systematic

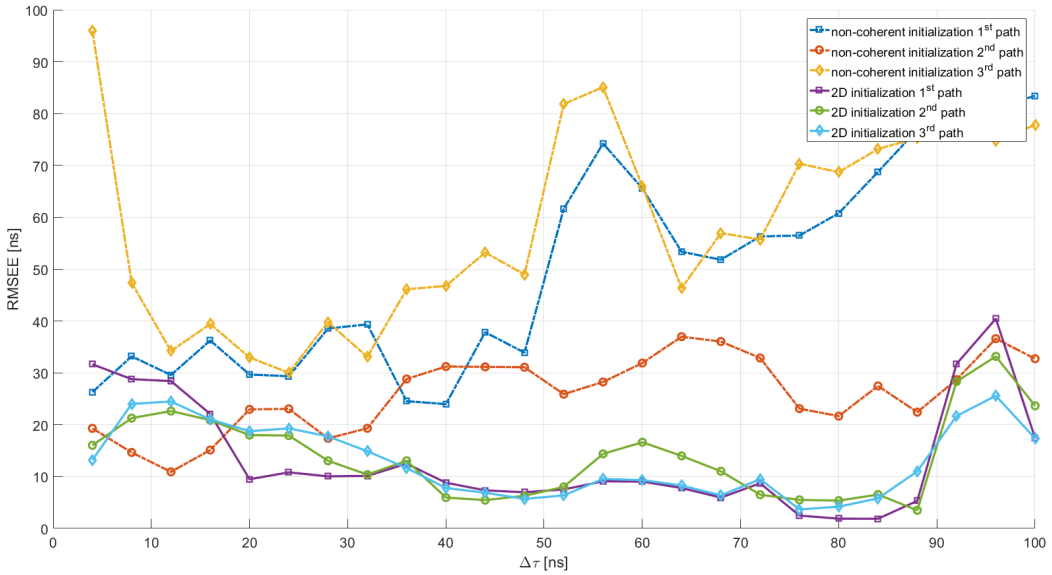

Fig. 5.8 RMSEE of the delays. Comparison between SAGE 2D initialization and SAGE non-coherent initialization in real ping scenario.

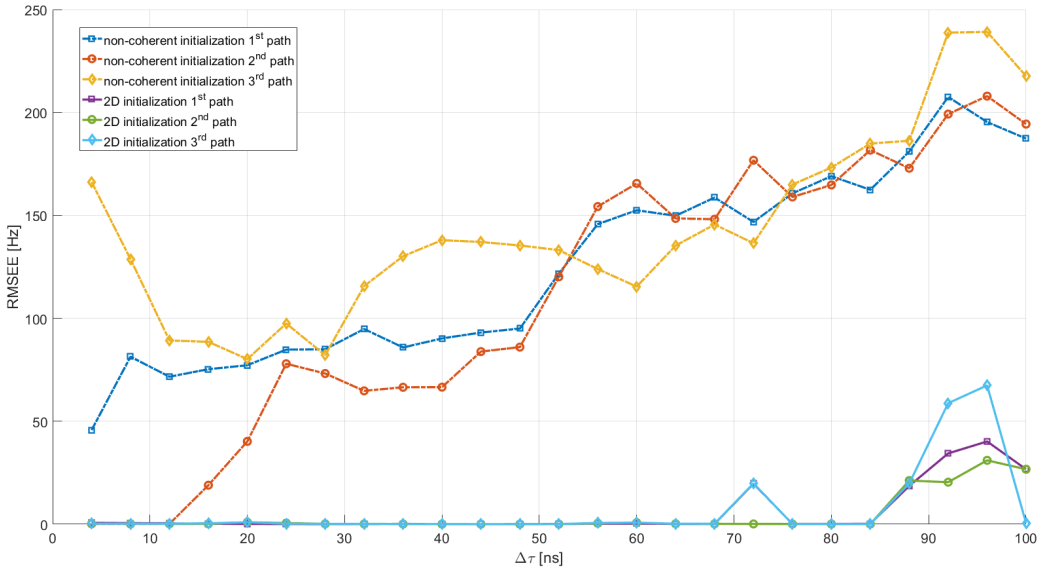

Fig. 5.9 RMSEE of the Doppler. Comparison between SAGE 2D initialization and SAGE non-coherent initialization in real ping scenario.

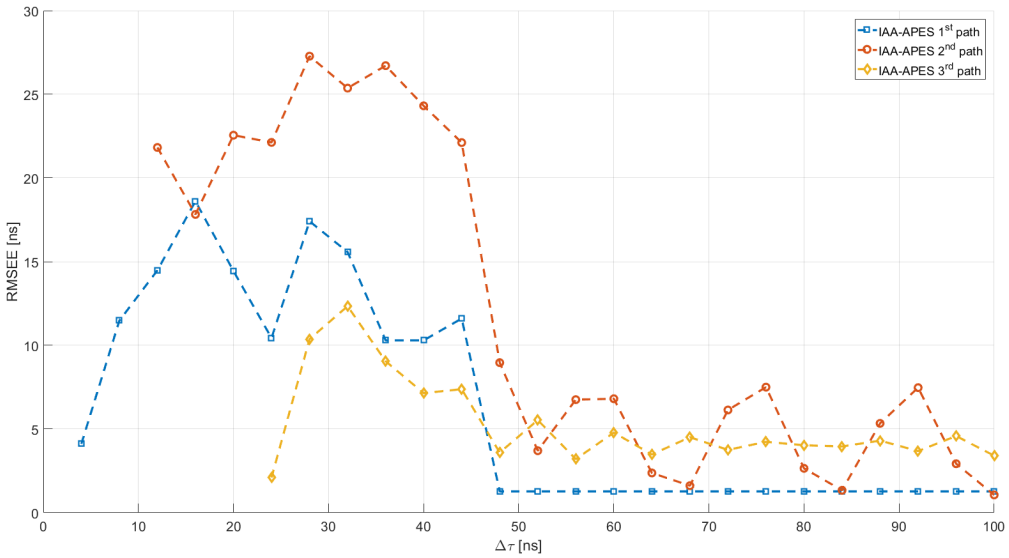

Fig. 5.10 RMSEE of the delays using IAA-APES in the full band scenario.

error for the first path. This also explains the oscillation of the error for the second and third paths, since, as $\Delta\tau$ varies, the values 15 ns $+\Delta\tau$ and 15 ns $+2\Delta\tau$ are not in the grid, and the true path delays may be near or far from a grid point. The RMSEE of the delays in the simulated ping and real ping scenarios are not showed because the IAA-APES algorithm could distinguish only one path in these two scenarios. Anyway, the RMSEE of the first path delay will be showed in the following, when we compare the RMSEE of the first path delay for the different algorithms.

Figure 5.11, Figure 5.12 and Figure 5.13 show the RMSEE of the first path delay using the two correlation method mentioned above, the SAGE 2D initialization procedure, the SAGE non-coherent initialization and IAA-APES. Figure 5.11 shows the RMSEE of the first path delay in the full band scenario. We can notice that the two correlation methods are less precise then the other algorithms. When $\Delta\tau$ is above 50 ns, the IAA-APES, SAGE 2D and SAGE non-coherent algorithms have almost the same performance, with an error below 2 ns.

Figure 5.12 shows the RMSEE of the first path delay in the simulated ping scenario. In this case, the SAGE 2D initialization outperforms all the other methods. As expected, with less band available, the correlation methods perform badly with a very large error. Note that SAGE, with non-coherent initialization, has an error that increases even with increasing $\Delta\tau$. This is due to the erroneous initialization, which is not correct when the bandwidth is small. Also IAA-APES exhibits an increasing error with increasing $\Delta\tau$. This happens because IAA-APES in this case is not able to

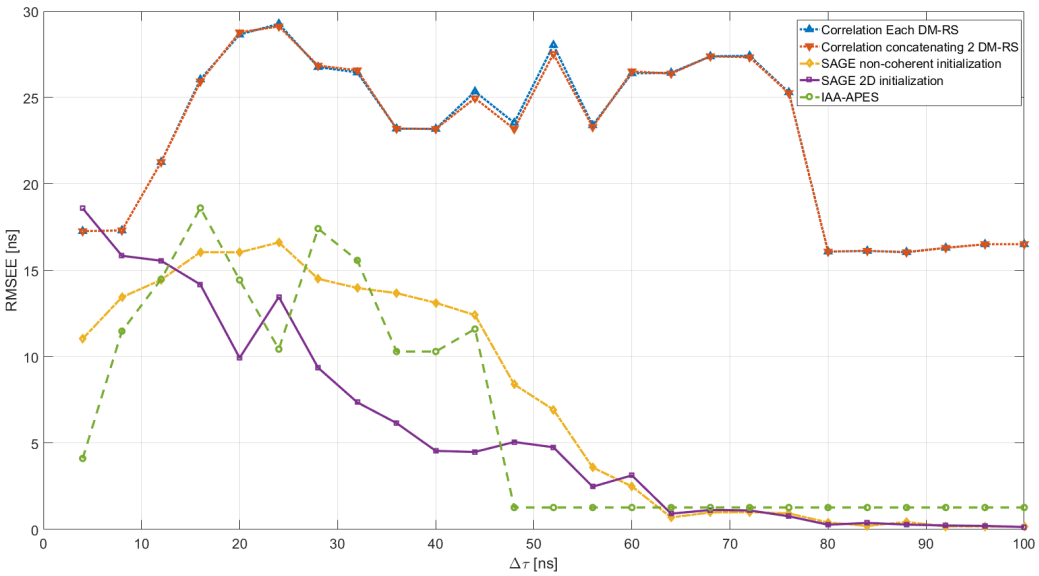

Fig. 5.11 RMSEE of the first path delay. Comparison between different algorithms in the full band scenario.

separate the three paths and only one path, with erroneous delay, is estimated. Finally, Figure 5.13 shows the RMSEE of the first path delay in the real ping scenario. Also in this case, we can see that the SAGE 2D algorithm outperforms the other algorithms. The behaviour is similar to that of the simulated ping scenario.

Figure 5.14 summarizes the RMSEE of the first path delay considering all the scenarios. The performance of SAGE 2D, SAGE non-coherent and IAA-APES are showed. From the figure we can point out that the 2D initialization of SAGE in case of the simulated ping and real ping scenarios ha performance comparable to the other algorithms in the full band scenario. Indeed, apart from the case of a real ping transmission with $\Delta\tau$ around 95 ns, 2D SAGE initialization in the two ping scenarios gives results very close to the full band scenario, with estimation errors below 10 ns when $\Delta\tau$ is higher than 40 ns. This suggest that when an estimation with missing data has to be performed (i.e., the two ping scenario represent a situation with missing data) the 2D initialization of the SAGE algorithm is a good choice. So in the following sections we will refer to SAGE always with this 2D initialization, in particular in the next section we compare the SAGE with 2D initialization with other algorithms suing different and more sophisticated channel models.

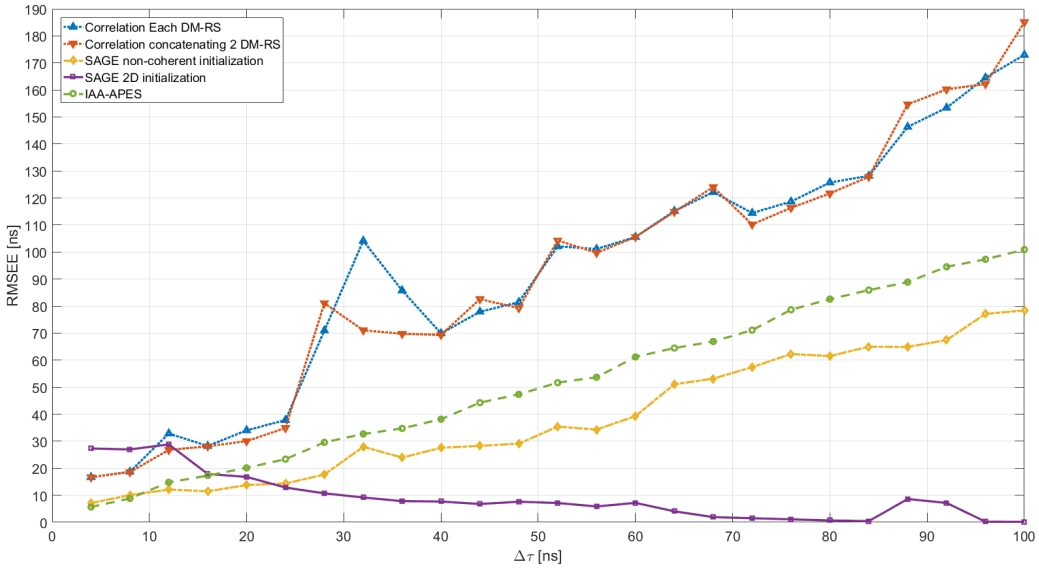

Fig. 5.12 RMSEE of the first path delay. Comparison between different algorithms in the simulated ping scenario.

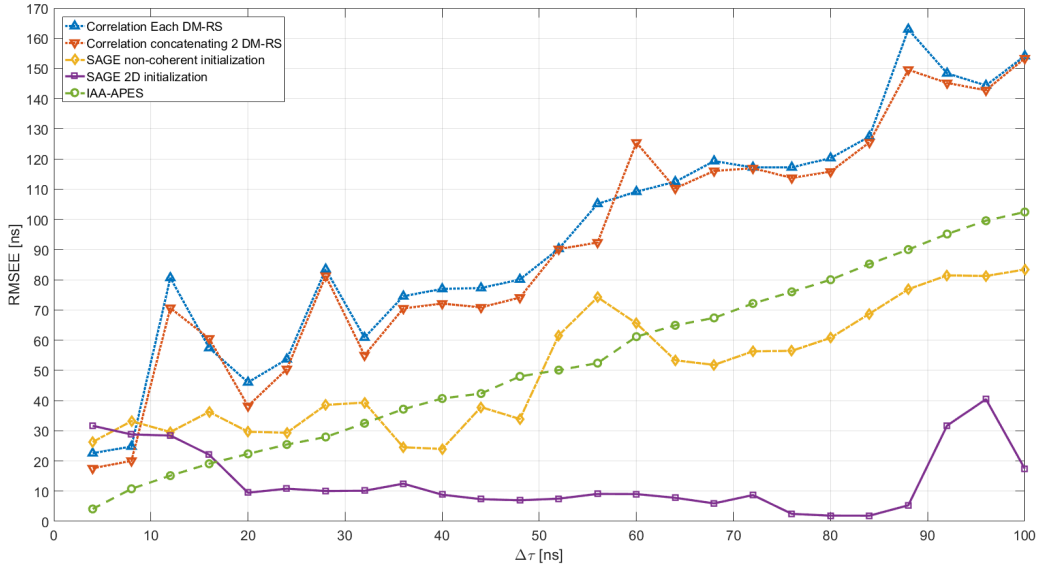

Fig. 5.13 RMSEE of the first path delay. Comparison between different algorithms in the real ping scenario.

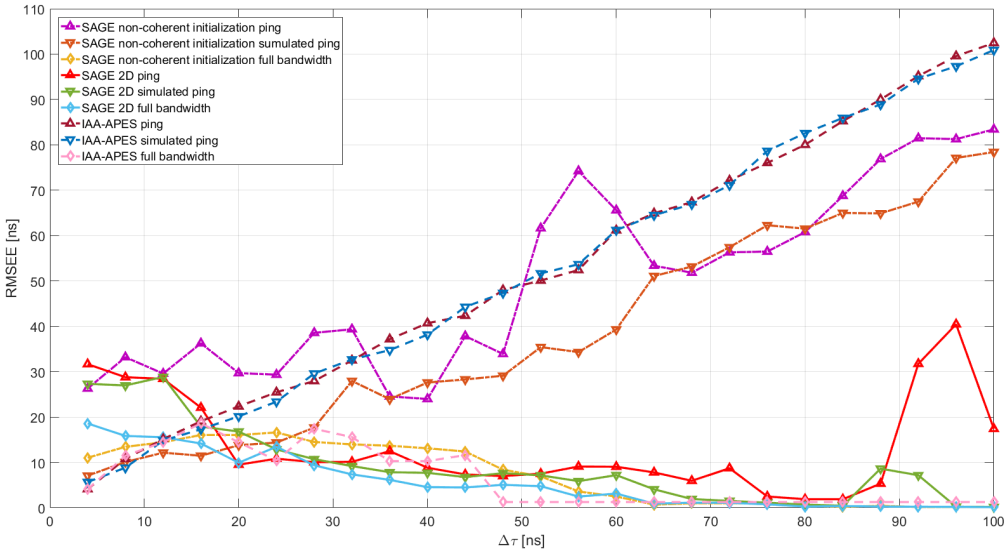

Fig. 5.14 First path delay RMSEE. Comparison between SAGE 2D initialization, SAGE non-coherent initialization and IAA-APES, in the three different simulated scenarios.

Paths	**1**	**2**	**3**	**4**	**5**	**6**	**7**	**8**	**9**
					EPA				
τ_l [ns]	0	30	70	90	110	190	410		
$f_{l,max}$ [Hz]	5	5	5	5	5	5	5		
$\lvert\alpha_l\rvert^2$ [dB]	0	-1	-2	-3	-8	-17.2	-20.8		
					EVA				
τ_l [ns]	0	30	150	310	370	710	1090	1730	2510
$\nu_{l,max}$ [Hz]	70	70	70	70	70	70	70	70	70
$\lvert\alpha_l\rvert^2$ [dB]	0	-1.5	-1.4	-3.6	-0.6	-9.1	-7	-12	-16.9
					ETU				
τ_l [ns]	0	50	120	200	230	500	1600	2300	5000
$\nu_{l,max}$ [Hz]	300	300	300	300	300	300	300	300	300
$\lvert\alpha_l\rvert^2$ [dB]	-1	-1	-1	0	0	0	-3	-5	-7

Table 5.1 Channel models used in simulation

5.6 Simulation Results with Different Channel Models

In this section we show the simulation results for more realistic channel realizations. We assume to know the number of paths L, which in a real implementation may be estimated iteratively minimizing Equation (4.81). In particular, we consider the RMSEEs in the three scenarios described in the previous section, i.e., the full band scenario, the simulated ping scenario and the real ping scenarios. However, in this case the channel is derived from three different models, based on the EPA, EVA and ETU channel models described in the LTE standard [52, 53], whose parameters are reported in Table 5.1.

In particular, the phase of the complex channel gain α_l for each path is generated randomly, i.e., $\alpha_l = |\alpha_l| e^{j\phi}$ with ϕ uniform in $[0, 2\pi]$. We simulate the transmission of 25 consecutive subframes, which are approximately the number of subframes occupied by a ping. We generate 50 different channel realizations for each SNR value, that ranges from -15 to 20 dB with 5 dB steps. Moreover, we used two different set-ups for the generation of the Doppler frequencies. The first set-up generates the Doppler of each path randomly with uniform values between $-\nu_{l,max}$ and $\nu_{l,max}$. The second set-up uses a fixed Doppler frequency equal to $\nu_{l,max}$ for each path. In the following, we refer

to these two situation as random Doppler simulations and fixed Doppler simulations, respectively.

5.6.1 EPA Channel Simulations

EPA Fixed Doppler Results

Figure 5.15 shows the RMSEE of the delays obtained with SAGE, considering the EPA channel model in the full band scenario with fixed Doppler. The RMSEE of the seventh path is not showed because the error exceeds 250 ns. This is mainly due to the non perfect estimation of the other paths. Indeed, during the E-step, SAGE performs a cancellation of the interference using the previously estimated paths. If the estimation is not precise, during the E-step some peaks that are not related to a real paths can pop up in the correlation function. So, in general, with a high number of paths, all the non correct cancellation effects will sum up, and the RMSEE of the paths with lower amplitude α_l will be usually higher compared to paths with a larger amplitude. Because of this, in the following we will show and comment only the estimates for paths with a relatively small error. Note that our interest is in the first path estimation, and we show the results for the other paths for completeness and to give an idea of the general performance.

From Figure 5.15, we can notice that for low SNR, the RMSEE of the delays is very high and some paths are estimated with errors that exceed 1 μs. We can conclude, in this case, that SAGE is not reliable with SNR values below -10 dB, considering the EPA channel model in the full band scenario.

In general, apart from the seventh path, the RMSEE of the remaining six paths is between 40 to 60 ns, i.e., between 12 and 18 m in pseudorange, when the SNR is between -10 and 20 dB. In particular, the first path estimate has a RMSEE below 40 ns when the SNR is high. This general level of error is due to the high proximity of the paths in the EPA channel model, and also to the high number of paths. Indeed, in Section 5.5 we saw that, when the paths are close to each other, the RMSEE increase. For completeness, Figure 5.16 shows the RMSEE of the Doppler. At low SNR, the performance drops, but at high SNR the RMSEE of all the paths is below 5 Hz.

Figure 5.17 shows the RMSEE of the delays obtained with IAA-APES , considering the EPA channel model in the full band scenario with fixed Doppler. In particular, with this algorithm only three paths can be resolved, and in general the error for these three paths is lower than the one obtained with SAGE. Furthermore, we can see that IAA-APES has good performance also for low SNR level. In particular, the first path

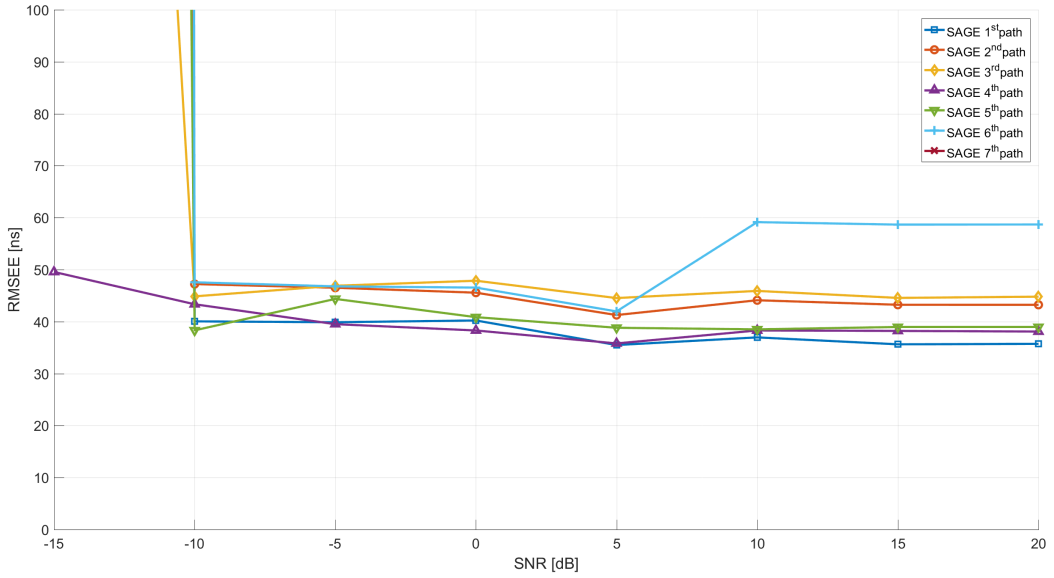

Fig. 5.15 RMSEE of the delays. Comparison between different paths estimation obtained with SAGE, considering the EPA channel model in the full band scenario with fixed Doppler.

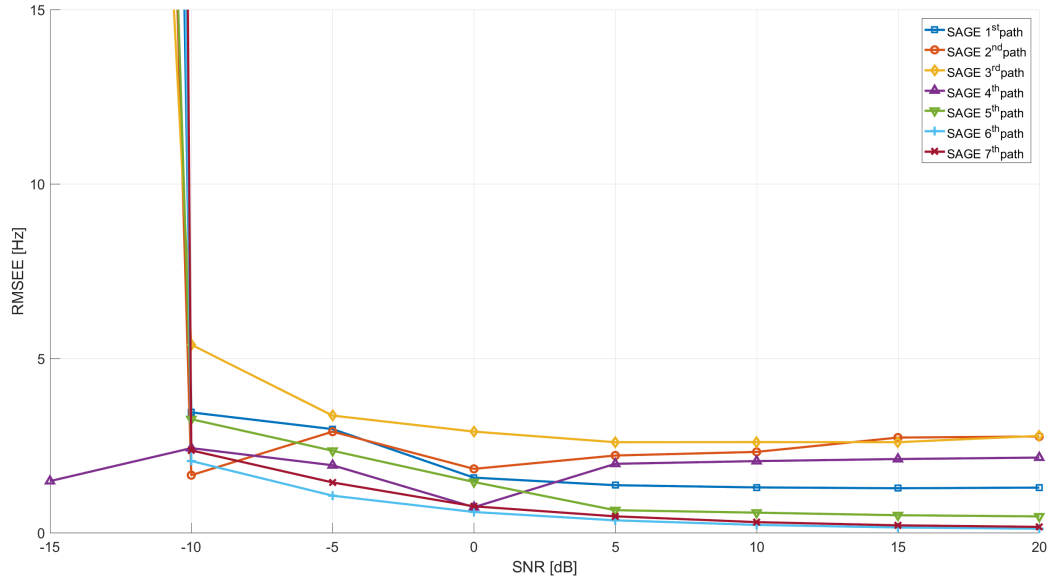

Fig. 5.16 RMSEE of the Doppler. Comparison between different paths estimation obtained with SAGE, considering the EPA channel model in the full band scenario with fixed Doppler.

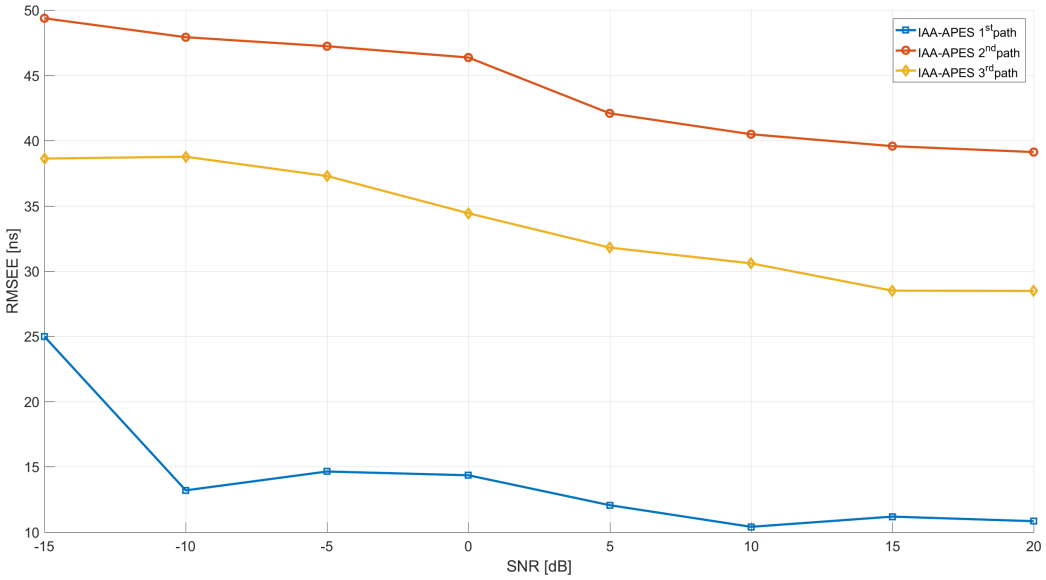

Fig. 5.17 RMSEE of the delays. Comparison between different paths estimation obtained with IAA-APES, considering the EPA channel model in the full band scenario with fixed Doppler.

estimation error is around 25 ns for low SNR and close to 10 ns for high SNR, which are respectively 7.5 m and 3 m in pseudorange.

Figure 5.18 and Figure 5.19 show respectively the RMSEE of the delays and the Doppler obtained with SAGE, considering the EPA channel in the simulated ping scenario with fixed Doppler. One can notice that the RMSEE in this case is similar to the full band one, indeed SAGE is not influenced too much by the characteristics of this scenario. The errors are between 70 and 25 ns. The Doppler estimation is less precise compared with the full band scenario, and for the first path the RMSEE of the Doppler is around 15 Hz.

In the two ping scenarios the IAA-APES algorithm is able to distinguish only one path. The RMSEE of the delay will be shown later, when we compare the RMSEE of the first path delay obtained with different algorithms.

Figure 5.20 and Figure 5.21 show, respectively, the RMSEE of the delays and of the Doppler obtained with SAGE, considering the EPA channel model in the real ping scenario with fixed Doppler. In this case, similarly to the full band and simulated ping scenarios, the RMSEEs are poor with low SNR level, but with SNR larger than -10 dB the RMSEE is approximately between 40 and 70 ns. In this case, the Doppler estimation error is below 5 Hz with SNR level higher that -5 dB, for all the paths. Comparing the different SAGE delay estimation in the EPA channel with fixed Doppler,

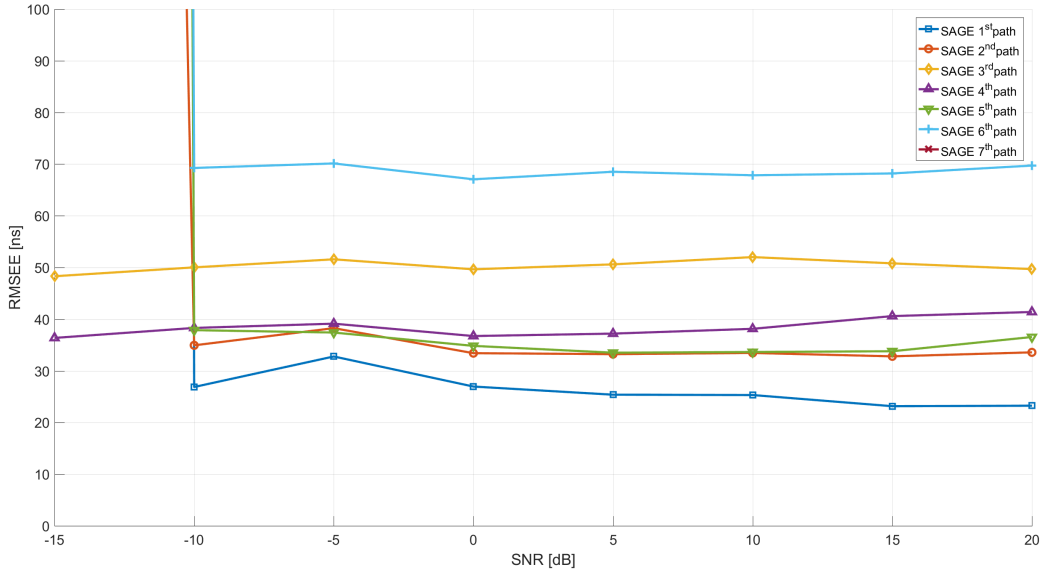

Fig. 5.18 RMSEE of the delays. Comparison between different paths estimation obtained with SAGE, considering the EPA channel model in the simulated ping scenario with fixed Doppler.

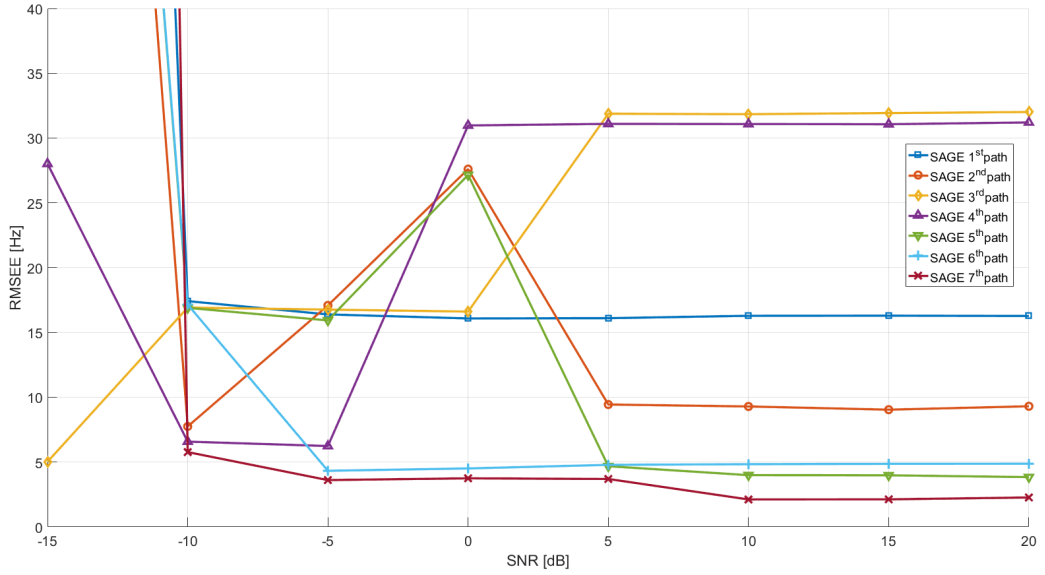

Fig. 5.19 RMSEE of the Doppler. Comparison between different paths estimation obtained with SAGE, considering the EPA channel model in the simulated ping scenario with fixed Doppler.

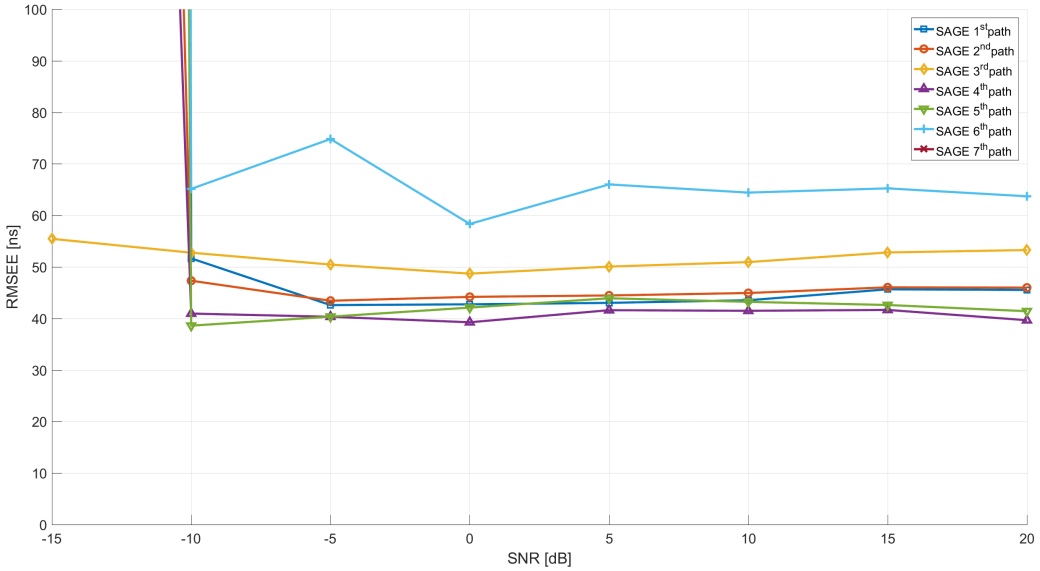

Fig. 5.20 RMSEE of the delays. Comparison between different paths estimation obtained with SAGE, considering the EPA channel model in the real ping scenario with fixed Doppler.

we can conclude that the estimates are not too much influenced by the considered scenario.

In Figures 5.22 and 5.23, the RMSEEs of the first path delay is showed. In particular, we compare the results obtained with SAGE, IAA-APES and the correlation peak detector, considering the EPA channel model in the three different scenarios with fixed Doppler. Figure 5.23 shows the detail of Figure 5.22. From these figures, we can see that the delay RMSEE of the correlation peak detector is high for low SNR levels and in the two ping scenarios. With high SNR, the RMSEE obtained with the correlation peak detector is comparable to the other algorithms only in the full band scenario. However, IAA-APES has the best performance in case of full band transmission, and gives the best performance also when the SNR is below -10 dB in all the scenarios. For low SNR, in the two ping scenario the error in pseudorange is around 15 m. On the contrary, in the real ping and simulated ping scenario with SNR higher than -10 dB, the SAGE algorithm has a slightly better performance, with errors in pseudorange around 13 m and below 10 m in the real ping and simulated ping scenarios, respectively.

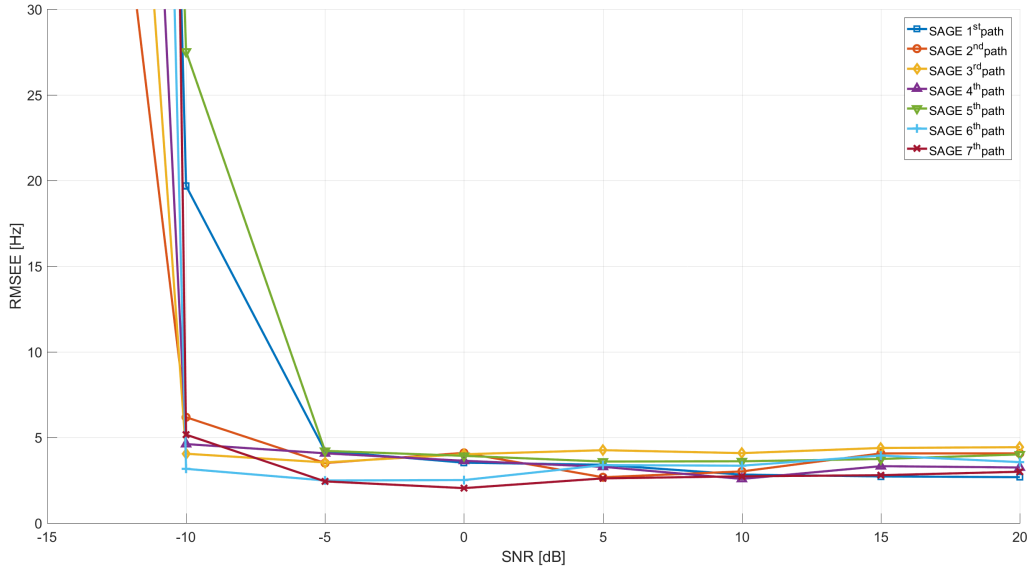

Fig. 5.21 RMSEE of the Doppler. Comparison between different paths estimation obtained with SAGE, considering the EPA channel model in the real ping scenario with fixed Doppler.

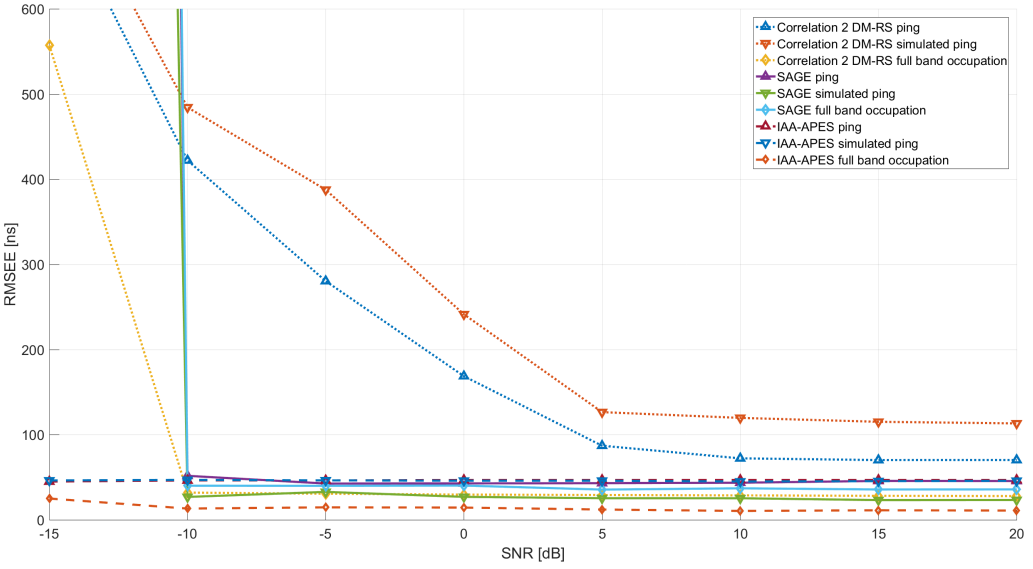

Fig. 5.22 RMSEE of the first path delay. Comparison between SAGE, IAA-APES and the correlator peak detector, considering the EPA channel model in the three different scenarios with fixed Doppler.

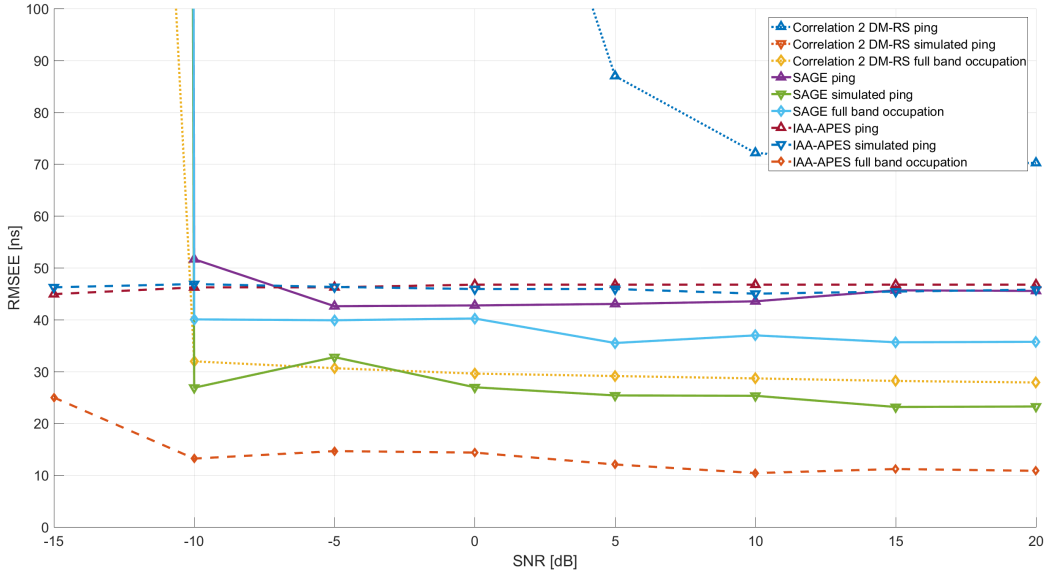

Fig. 5.23 RMSEE of the first path delay. Inset of the comparison between SAGE, IAA-APES and the correlator peak detector, considering the EPA channel model in the three different scenarios with fixed Doppler.

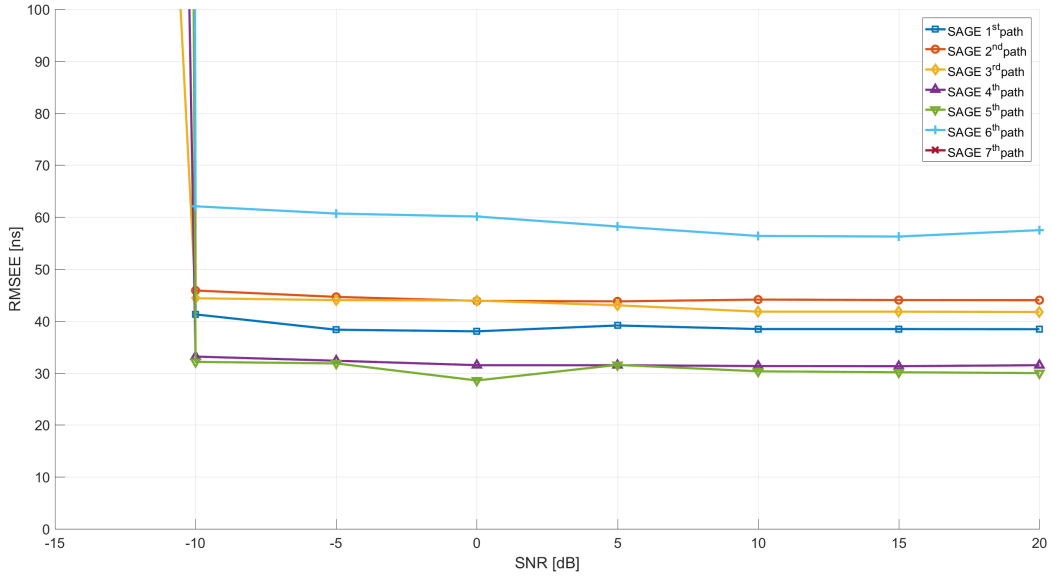

Fig. 5.24 RMSEE of the delays. Comparison between different paths estimation obtained with SAGE, considering the EPA channel model in the full band scenario with random Doppler.

EPA Random Doppler Results

Figure 5.24 and Figure 5.25 show respectively the RMSEE of the delays and the Doppler obtained with SAGE, considering the EPA channel model in the full band scenario with random Doppler. The RMSEE of the first six paths is approximately between 30 and 60 ns in the SNR range from -10 to 20 dB. With lower SNR, the algorithm is not reliable and the delay RMSEE is high. The first path RMSEE is around 40 ns, which corresponds to an error in pseudorange of approximately 12 m. Also in this case we can assume that the relatively high error is due to the proximity of the paths. In this case, the Doppler estimation error is below 10 Hz for all the paths when the SNR is higher that -10 dB, while for lower SNR the RMSEE exceeds 200 Hz for some paths.

Figure 5.26 shows the RMSEE of the delays obtained with IAA-APES, considering the EPA channel model in the full band scenario with random Doppler. With this algorithm only three paths can be solved and in general the error is lower compared with the error given by SAGE. Furthermore IAA-APES maintains good performance when the SNR level falls below -10 dB. The first path estimation is around 23 ns for low SNR and close to 10 ns for high SNR, which are respectively 7 m and 3 m in pseudorange.

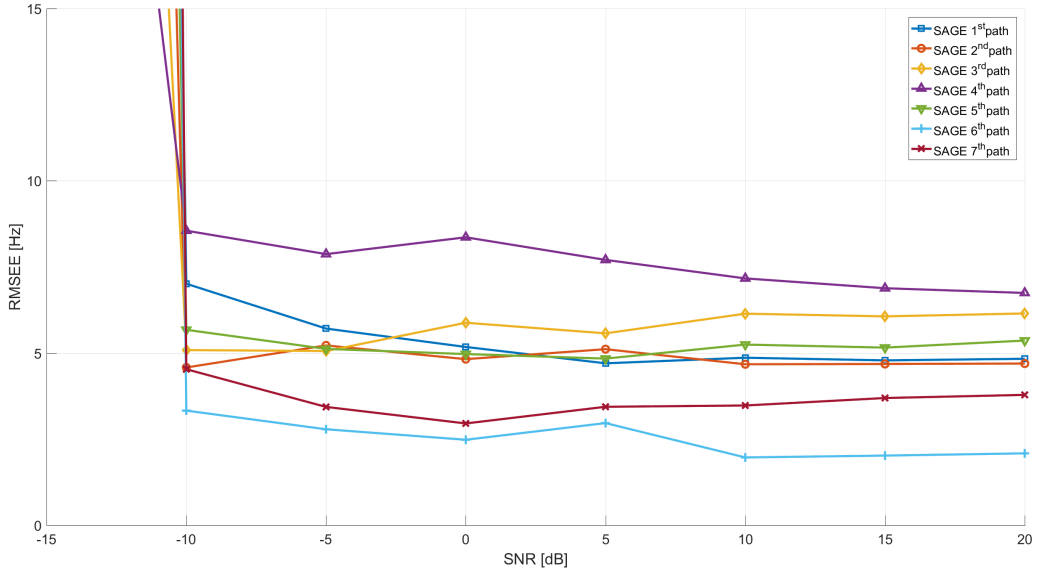

Fig. 5.25 RMSEE of the Doppler. Comparison between different paths estimation obtained with SAGE, considering the EPA channel model in the full band scenario with random Doppler.

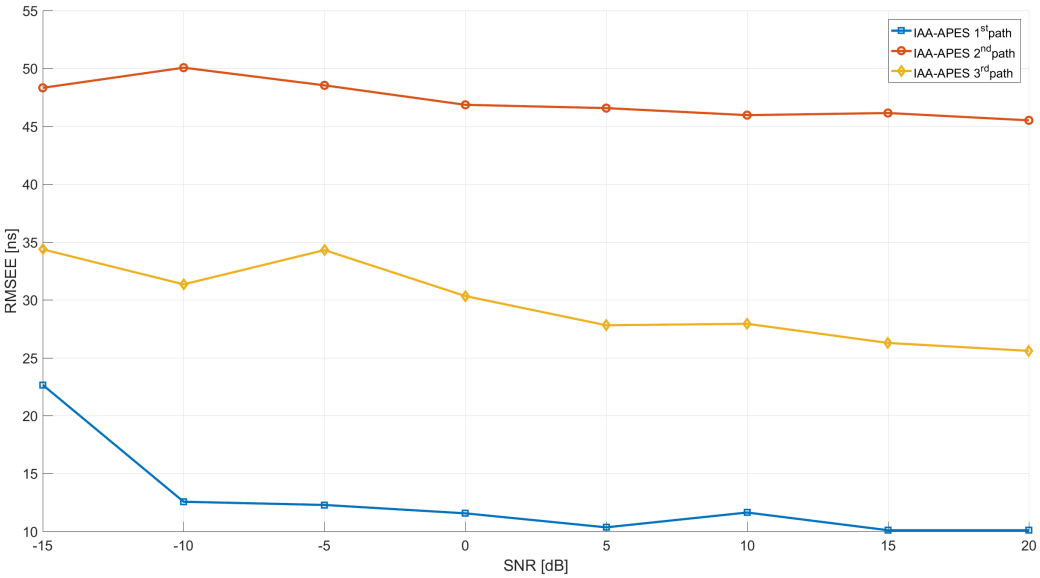

Fig. 5.26 RMSEE of the delays. Comparison between different paths estimation obtained with IAA-APES considering the EPA channel model in the full band scenario with random Doppler.

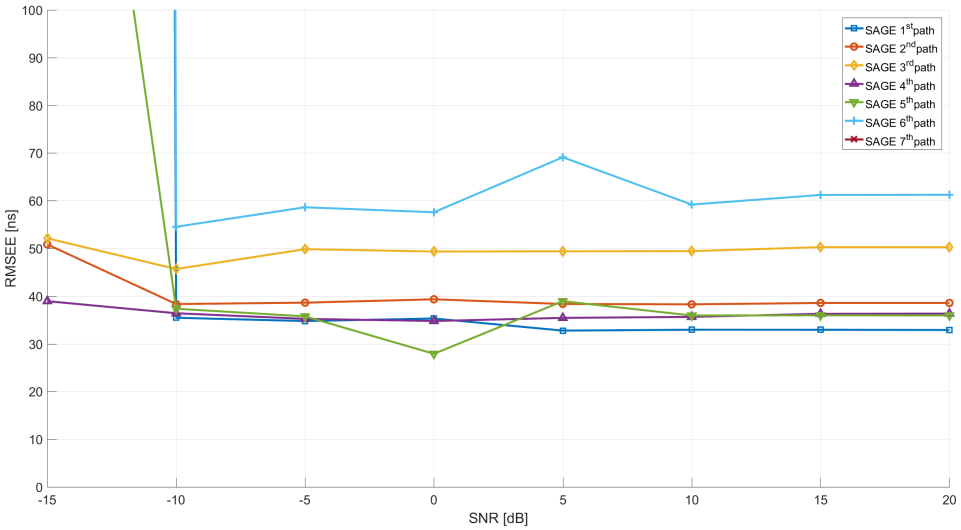

Fig. 5.27 RMSEE of the delays. Comparison between different paths estimation obtained with SAGE, considering the EPA channel model in the simulated ping scenario with random Doppler.

Figure 5.27 and Figure 5.28 show, respectively, the RMSEE of the delays and the Doppler obtained with SAGE, considering the EPA channel model in the simulated ping scenario with random Doppler. We can notice that the RMSEE in this case is in between 70 and 30 ns for SNR that exceeds -10 dB. The Doppler estimation is in general slightly less precise compared to the full band scenario and for the first path the RMSEE is around 5 Hz.

The IAA-APES algorithm is not able to distinguish more than one path in the simulated ping and real ping scenarios.

Figure 5.29 and Figure 5.30 show respectively the RMSEE of the delays and the Doppler obtained with SAGE, considering the EPA channel model in the real ping scenario with random Doppler. The RMSEE in this case is close to the full band and simulated ping scenarios. In general, the RMSEE of the paths delay is poor at low SNR, but with SNR above -10 dB the RMSEE reaches values approximately between 30 and 70 ns, for each path. In this case, the Doppler estimation error is below 10 Hz, at least for SNR values larger than -5 dB. The sixth path is estimated with an error of about 28 Hz, which decreases to 5 Hz when the SNR falls below 5 dB.

In Figure 5.31 and Figure 5.32, the RMSEEs of the first path delay is showed. In particular, we compare the results obtained with SAGE, IAA-APES and the correlation peak detector, considering the EPA channel model in the three different scenarios with

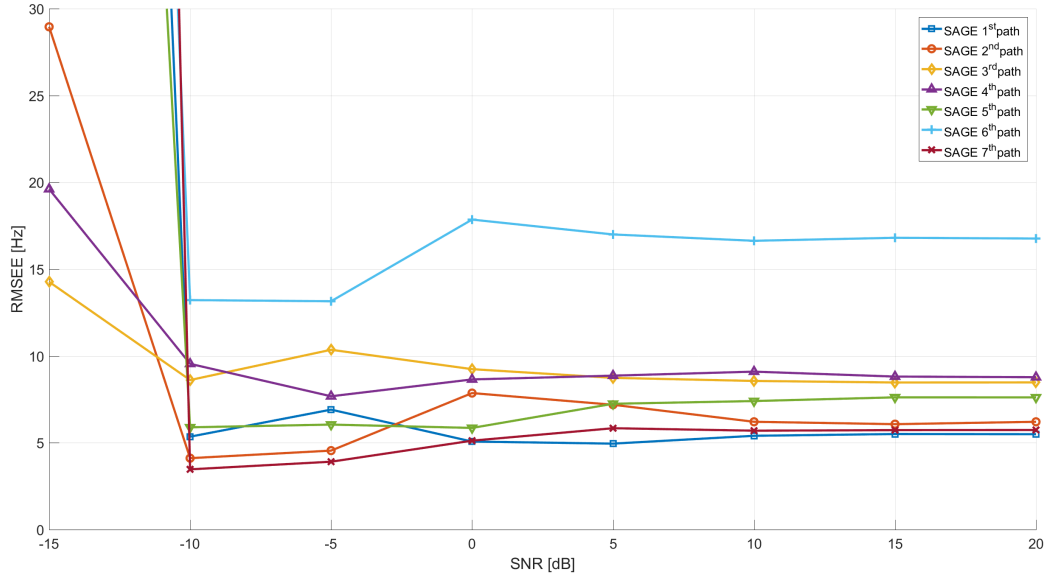

Fig. 5.28 RMSEE of the Doppler. Comparison between different paths estimation obtained with SAGE, considering the EPA channel model in the simulated ping scenario with random Doppler.

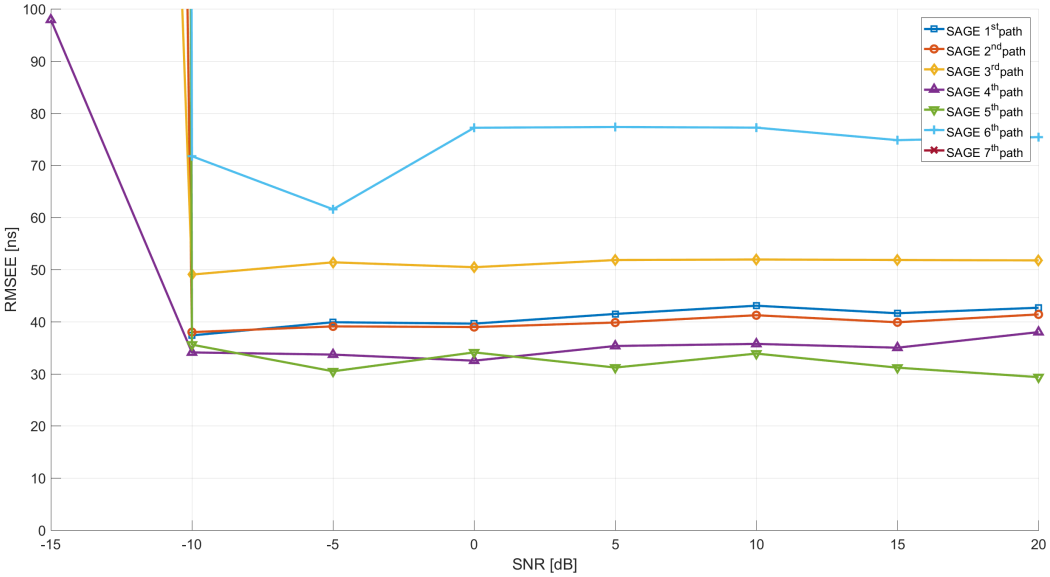

Fig. 5.29 RMSEE of the delays. Comparison between different paths estimation obtained with SAGE, considering the EPA channel model in the real ping scenario with random Doppler.

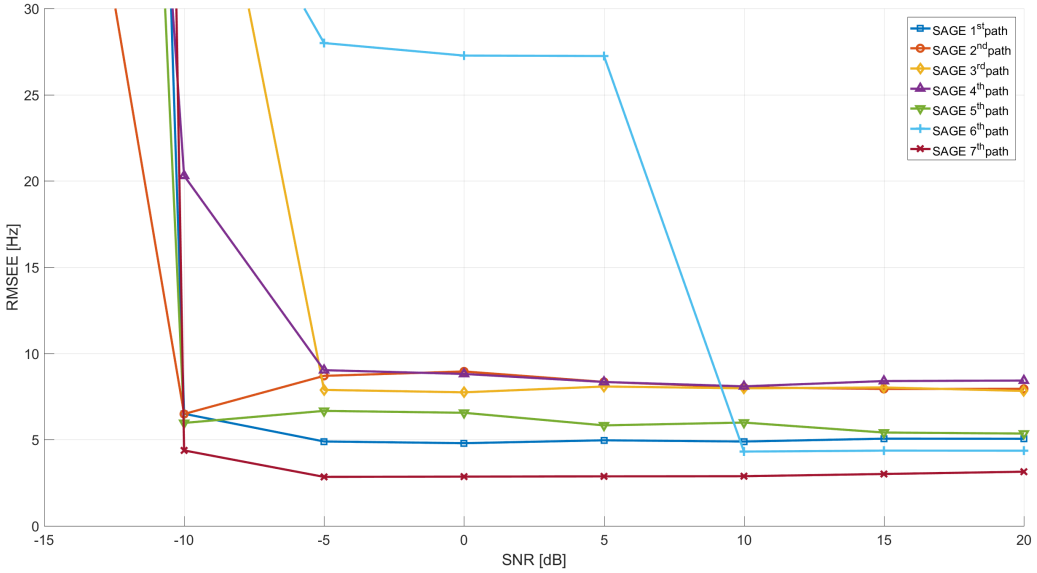

Fig. 5.30 RMSEE of the Doppler. Comparison between different paths estimation obtained with SAGE, considering the EPA channel model in the real ping scenario with random Doppler.

random Doppler. Figure 5.32 shows a detail of Figure 5.31. From these figures we can observe that the correlation based estimation has a high error with low SNR and in the two ping scenarios. In the full band case, the correlation RMSEE is comparable with the other methods. In particular, IAA-APES has the best performance in the full band scenario and gives the best performance also when the SNR is low in all the scenarios evaluated. For low SNR, in the two ping scenarios, the error in pseudorange is around 15 m. On the contrary, in the real ping and simulated ping scenarios with SNR higher than -10 dB, the SAGE algorithm gives a slightly better estimation, with errors in pseudorange around 13 m. So, SAGE has a slightly better performance compared to IAA-APES, while IAA-APES appears to be the best choice in the full band case with EPA channel.

Summarizing the results obtained with the EPA channel, IAA-APES appears to be the best choice when the SNR is lower than -10 dB in all scenarios with both fixed and random Doppler. IAA-APES shows also the best performance in the full band scenario in the evaluated SNR range, with RMSEE in pseudorange below 7.5 m. SAGE, indeed, appears to be preferable to IAA-APES with SNR level above -10 dB in the two ping scenarios. In particular, when simulated ping and real ping scenarios are considered, the RMSEE is similar to the one obtained with SAGE in the full band scenario and the RMSEE in pseudorange is around 13 m.

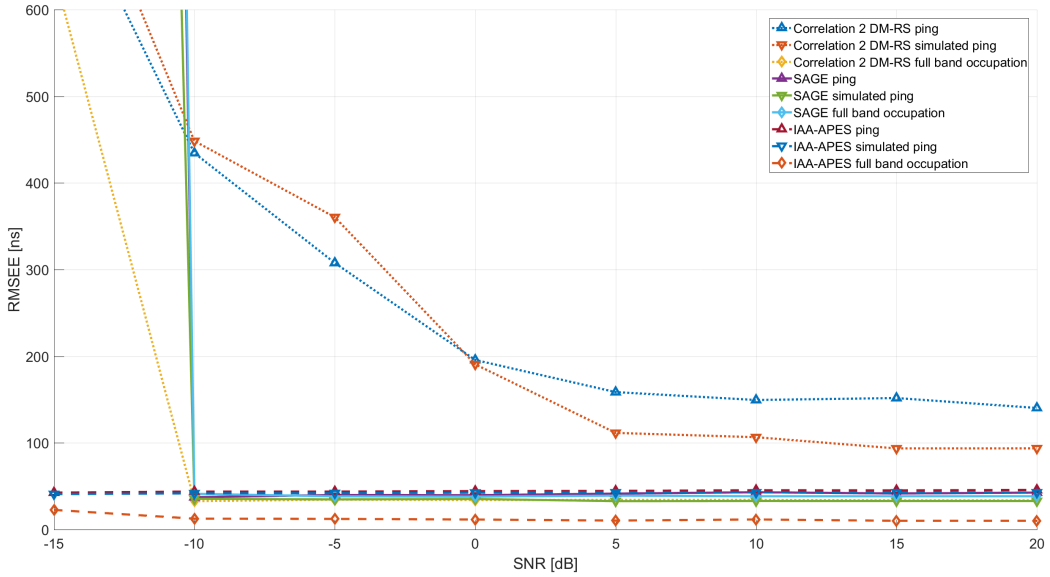

Fig. 5.31 RMSEE of the first path delay. Comparison between SAGE, IAA-APES and the correlator peak detector, considering the EPA channel model in the three different scenarios with random Doppler.

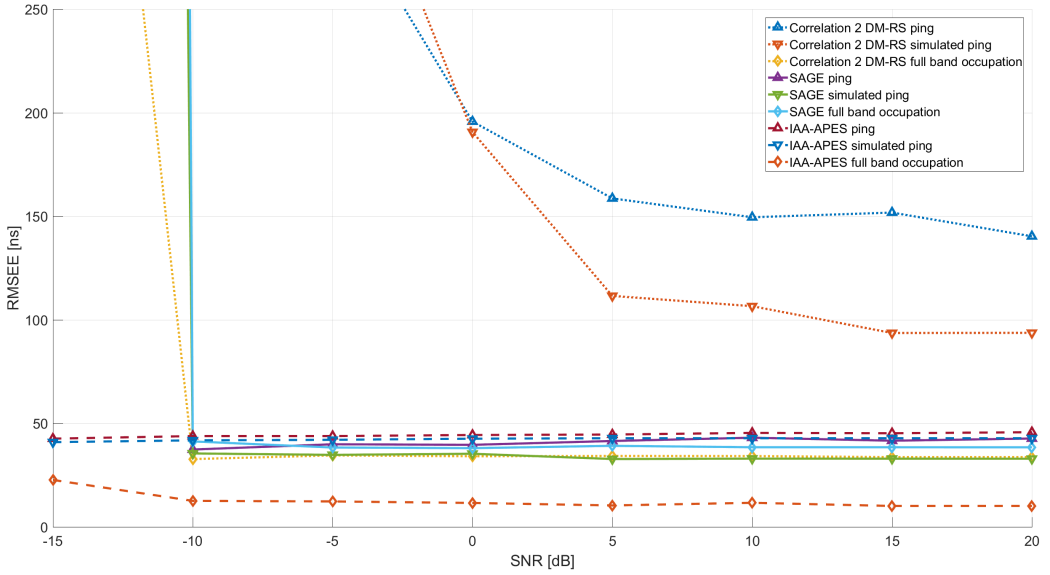

Fig. 5.32 RMSEE of the first path delay. Inset of the comparison between SAGE, IAA-APES and the correlator peak detector, considering the EPA channel model the three different scenarios with random Doppler generation.

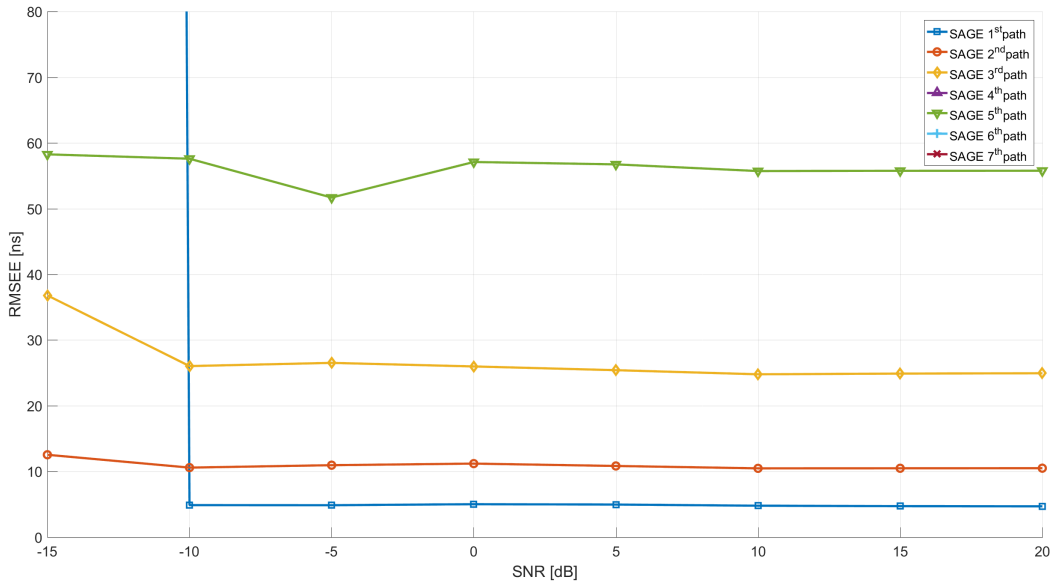

Fig. 5.33 RMSEE of the delays. Comparison between different paths estimation obtained with SAGE, considering the EVA channel model in the full band scenario with fixed Doppler.

5.6.2 EVA Channel Results

EVA Fixed Doppler Results

Figure 5.33 and Figure 5.34 show respectively the RMSEE of the delays and the Doppler obtained with SAGE, considering the EVA channel model in the full band scenario with fixed Doppler. In this case, the RMSEE of the first three paths is below 40 ns. This is probably due to the reduced proximity of the path delays in the EVA channel compared to the EPA channel. The RMSEE of the fifth path is below 60 ns, which is better than the estimate for the fourth path. This is because the magnitude of the fifth path is larger than the magnitude of the fourth path and because the two path delays are quite close. The fourth path has an error of about 150 ns. The other paths have a higher error that we do not show in the figures. The Doppler error is always below 5 Hz, also at low SNR. The first path delay RMSEE is around 5 ns for SNR higher than -10 dB, whereas for lower SNR the estimation is not reliable.

Figure 5.35 shows the RMSEE of the delays obtained with IAA-APES, considering the EVA channel model in the full band scenario with fixed Doppler. In this case, only three paths can be resolved, and in general the first path RMSEE is slightly higher than the one obtained by SAGE, even if the first path estimation for SNR below -10 dB is better than the one obtained with SAGE. The second and third path delay

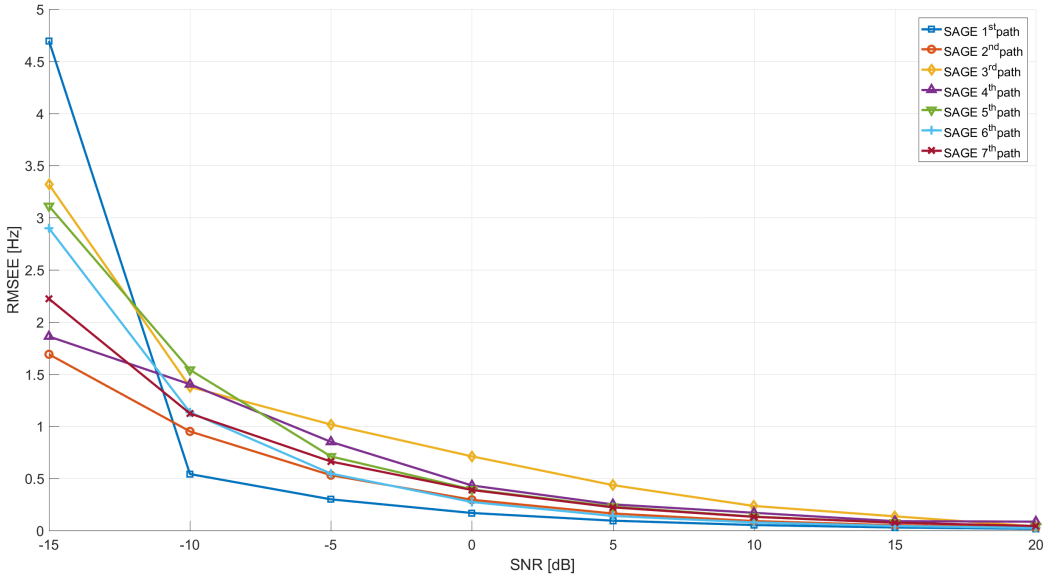

Fig. 5.34 RMSEE of the Doppler. Comparison between different paths estimation obtained with SAGE, considering the EVA channel model in the full band scenario with fixed Doppler.

estimates have a RMSEE approximately between 75 to 110 ns and between 100 to 155 respectively. The first path estimation error is around 15 ns at low SNR and close to 8 ns at high SNR, which are respectively 4.5 m and 2.4 m in pseudorange.

Figure 5.36 and Figure 5.37 show, respectively, the RMSEE of the delays and of the Doppler obtained with SAGE, considering the EVA channel model in the simulated ping scenario with fixed Doppler. We can notice that the RMSEE in this case is similar to the full band scenario for the first two paths. In particular the first path RMSEE is around 5 ns, which is approximately 1.5 m. The error from the third to the fifth path is around 60 ns, 130 ns and 80 ns, respectively. The error in the first path estimation at low SNR is high, and the estimation is not reliable. The Doppler estimation is in general similar to the full band scenario, and in particular the error is always below 5 Hz.

The RMSEE of the delays obtained with IAA-APES, considering the EVA channel model in the simulated ping and real ping scenarios with fixed Doppler and random Doppler, is omitted. This is because, in the simulated ping scenario, the error in the second and third path estimation is around 1 μs. This is similar to what happens in the real ping scenario, where only the second path is estimated and the delay RMSEE for the second path is above 1.1 μs. Indeed, this is due to the inability of the algorithm to distinguish close paths when the available bandwidth is reduced. This behavior is

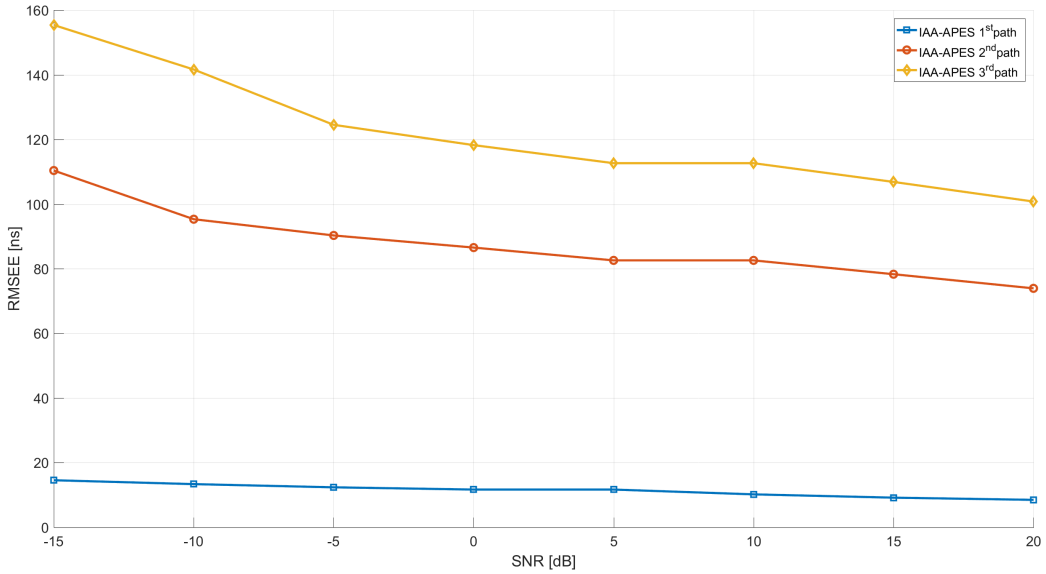

Fig. 5.35 RMSEE of the delays. Comparison between different paths estimation obtained with IAA-APES, considering the EVA channel model in the full band scenario with fixed Doppler.

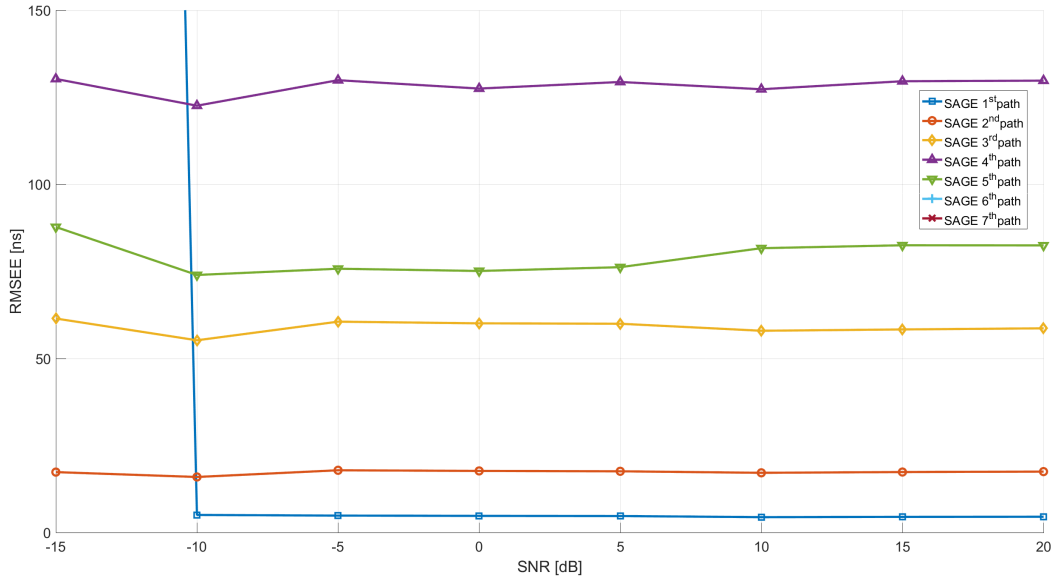

Fig. 5.36 RMSEE of the delays. Comparison between different paths estimation obtained with SAGE, considering the EVA channel model in the simulated ping scenario with fixed Doppler.

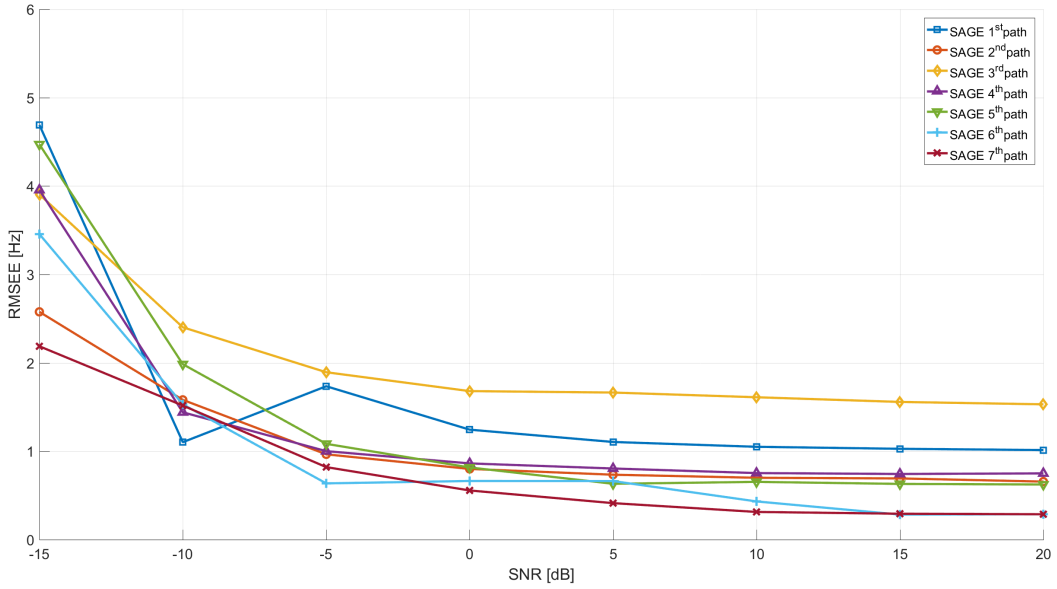

Fig. 5.37 RMSEE of the Doppler. Comparison between different paths estimation obtained with SAGE, considering the EVA channel model in the simulated ping scenario with fixed Doppler.

consistent with what shown in Figure 5.14 for the two ping scenarios. For this reason, we do not show these results and we will limit to show the first path RMSEE obtained with IAA-APES in the following plots.

Figure 5.38 and Figure 5.39 show, respectively, the RMSEE of the delays and of the Doppler obtained with SAGE, considering the EVA channel model in the real ping scenario with fixed Doppler. The delay RMSEE in this case is similar to the one obtained in the simulated ping scenario. The error for the first three paths delay estimation is approximately 13 ns, 20 ns and 50 ns, respectively. The RMSEE of the Doppler is higher than in the previous two scenarios. In this case, all the paths have an RMSEE between 30 and 60 Hz for high SNR, apart from the first path that has an error below 4 Hz.

In Figure 5.40 and Figure 5.41, the RMSEE of the first path delay is showed. In particular, we compare the results obtained with SAGE, IAA-APES and the correlation peak detector, considering the EVA channel model in the three different scenarios with fixed Doppler. Figure 5.41 shows a detail of Figure 5.40. From these figures, we can observe that the correlation based estimation has a high error at low SNR and for the two ping scenarios, while in the full band scenario the correlation RMSEE is comparable with the other methods. However, IAA-APES performs better then the correlation method in the full band scenario. Also, IAA-APES performs better than

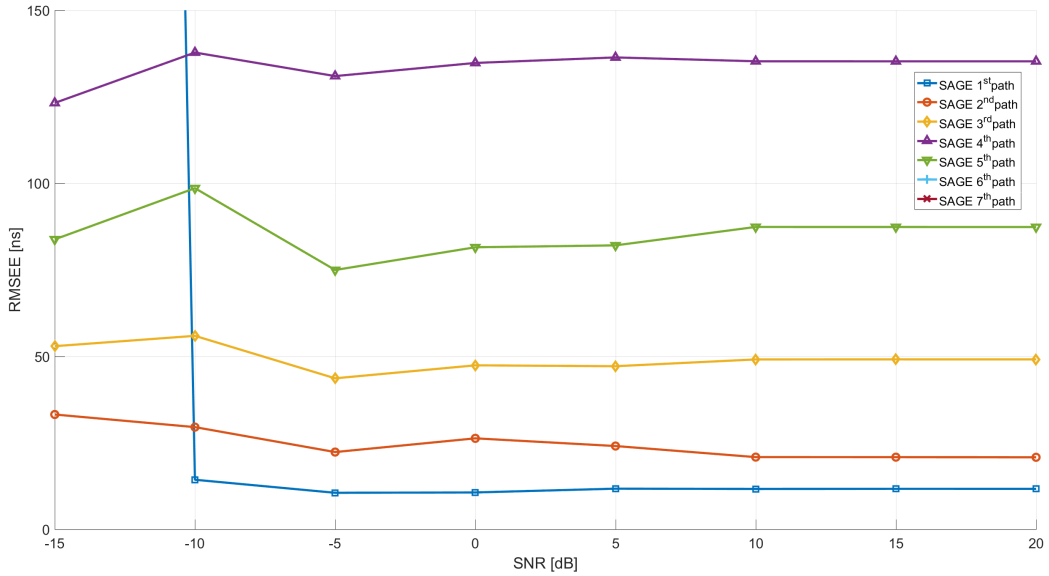

Fig. 5.38 RMSEE of the delays. Comparison between different paths estimation obtained with SAGE, considering the EVA channel model in the real ping scenario with fixed Doppler.

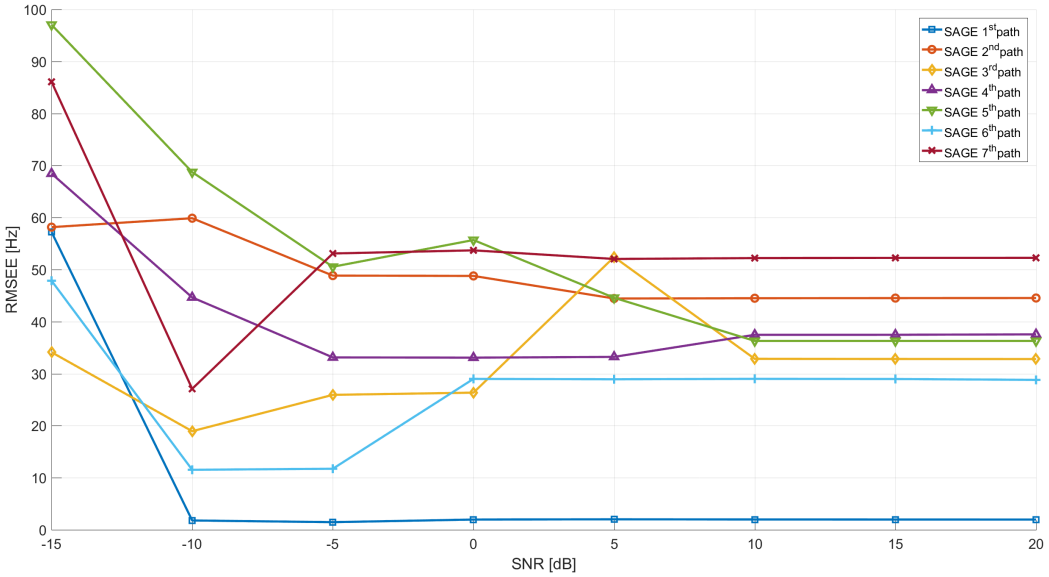

Fig. 5.39 RMSEE of the Doppler. Comparison between different paths estimation obtained with SAGE, considering the EVA channel model in the real ping scenario with fixed Doppler.

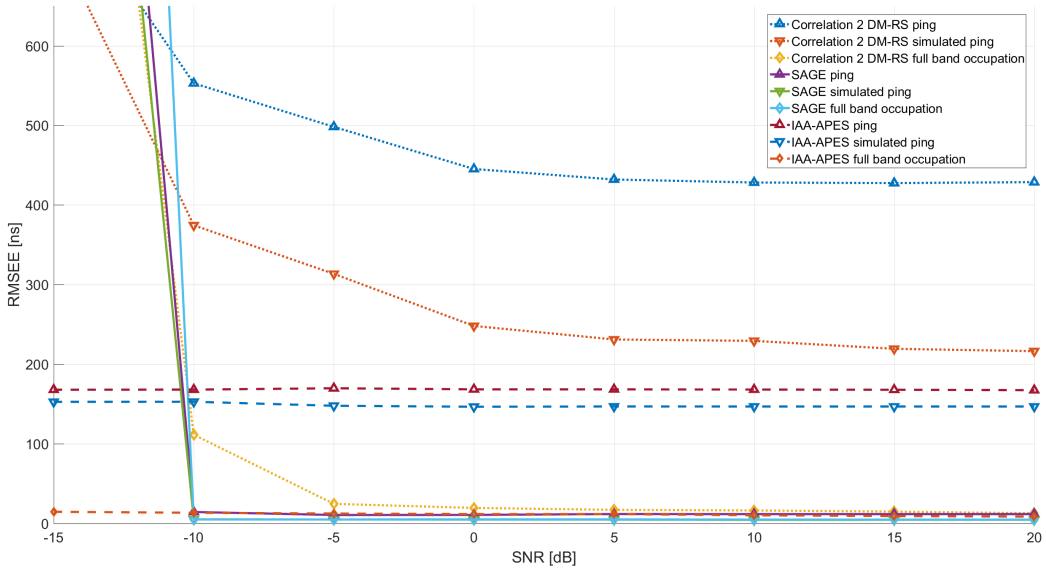

Fig. 5.40 RMSEE of the first path delay. Comparison between SAGE, IAA-APES and the correlator peak detector, considering the EVA channel model in the three different scenarios fixed Doppler.

the other techniques when the SNR level falls below -10 dB. In the full band scenario, IAA-APES has an error in pseudorange approximately between 4.5 m to 2.5 m for low and high SNR, respectively. The SAGE algorithm in this case outperforms the other algorithms, in particular when the two ping scenarios are used. Indeed, the RMSEE of SAGE in the simulated ping scenario are close to the RMSEE obtained with SAGE in the full band scenario. The RMSEE in pseudorange is close to 1.5 m. In the real ping scenario, SAGE has performance close to IAA-APES in the full band scenario, i.e., the RMSEE in pseudorange is around 3.5 m.

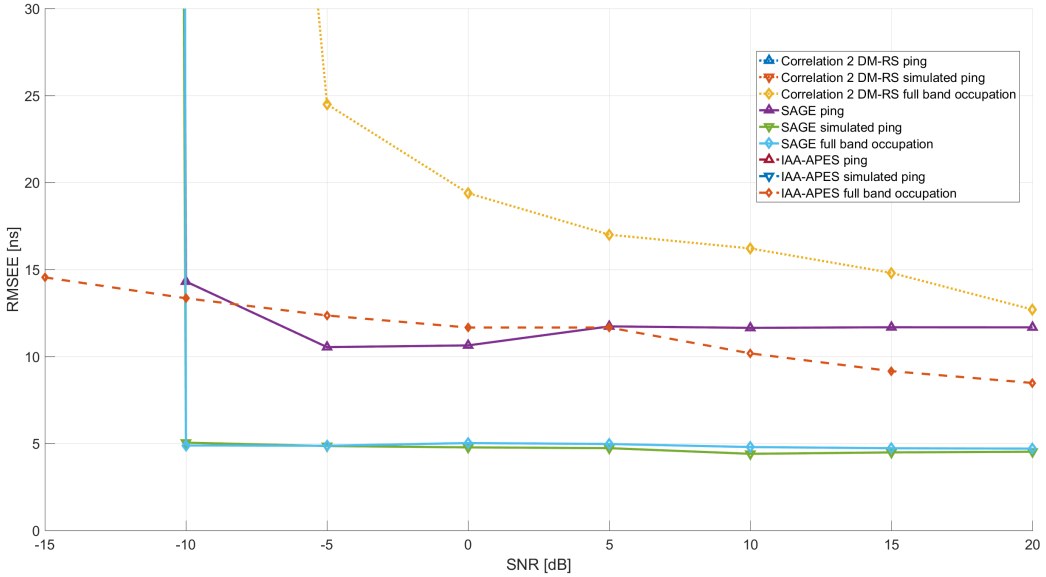

Fig. 5.41 RMSEE of the first path delay. Inset of the comparison between SAGE, IAA-APES and the correlator peak detector, considering the EVA channel model in the three different scenarios fixed Doppler.

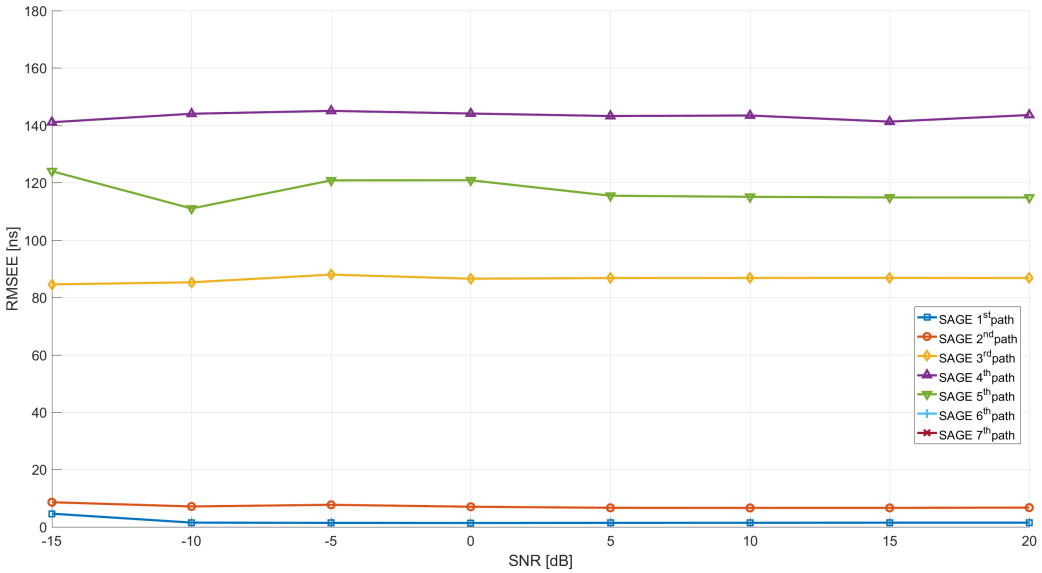

Fig. 5.42 RMSEE of the delays. Comparison between different paths estimation obtained with SAGE, considering the EVA channel model in the full band scenario with random Doppler.

EVA Random Doppler Results

Figure 5.42 and Figure 5.43 show, respectively, the RMSEE of the delays and of the Doppler obtained with SAGE, considering the EVA channel model in the full band scenario with random Doppler. In this case, the RMSEE of the first and second path is below 10 ns. For the third, the fourth and the fifth path, the RMSEE is around 80 ns, 140 ns and 110 ns respectively. The RMSEE of the Doppler follows a similar behaviour, and indeed the RMSEE of the first two paths is below 5 Hz, whereas the errors for the third, fourth and fifth path are between 40 Hz and 50 Hz. The RMSEE of the first path delay is around 5 ns, that corresponds to an error in pseudorange of approximately 1.5 m, while the RMSEE of the Doppler is below 3 Hz.

Figure 5.44 shows the RMSEE of the delays obtained with IAA-APES, considering the EVA channel model in the full band scenario with random Doppler. With this technique, only three paths can be resolved. The first path RMSEE in this case is slightly higher than the one given by SAGE. The RMSEE of the delay relative to the second and third paths is approximately between 120 ns to 45 ns and between 185 ns to 60 ns, for low and high SNR, respectively. The first path delay RMSEE is around 13 ns for low SNR and close to 6 ns for high SNR, which are respectively about 4 m and 2 m in pseudorange.

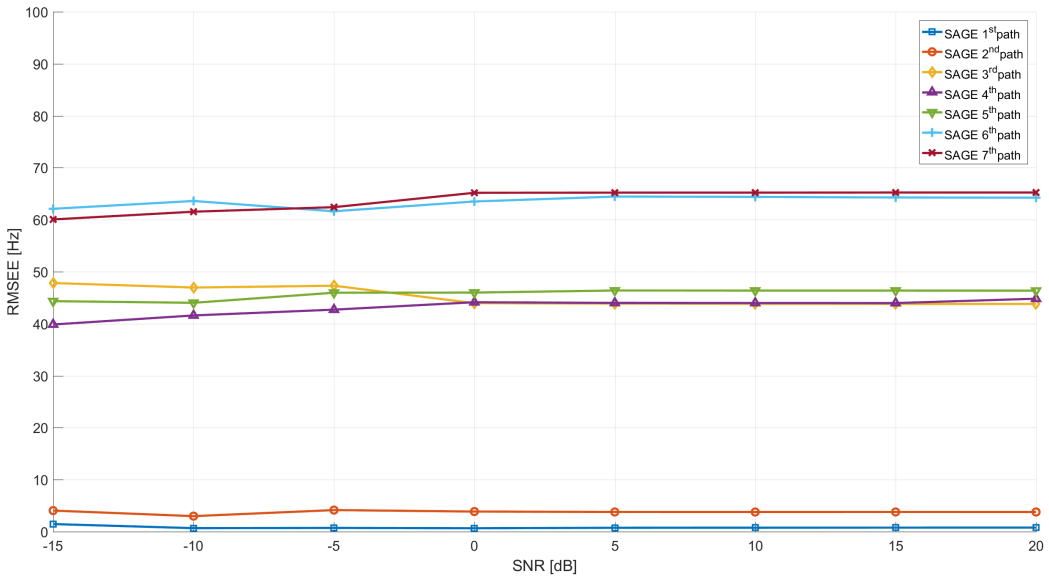

Fig. 5.43 RMSEE of the Doppler. Comparison between different paths estimation obtained with SAGE, considering the EVA channel model in the full band scenario with random Doppler.

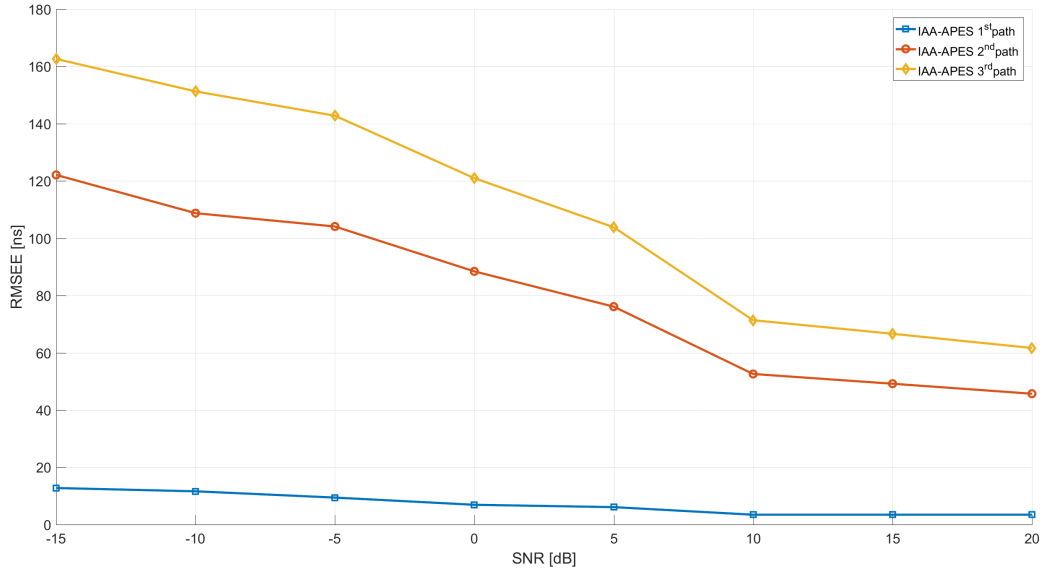

Fig. 5.44 RMSEE of the delays. Comparison between different paths estimation obtained with IAA-APES, considering the EVA channel model in the full band scenario with random Doppler.

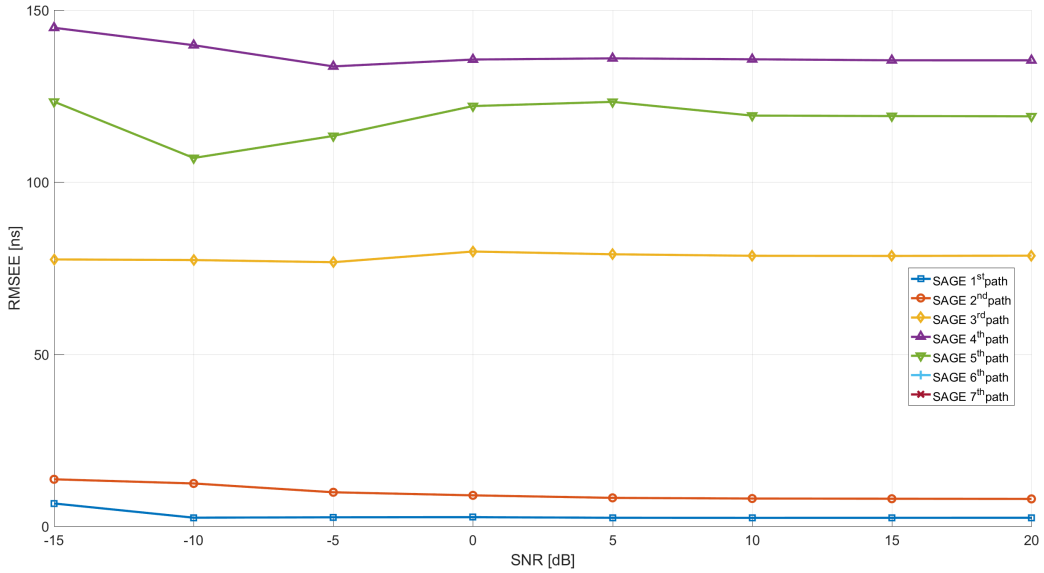

Fig. 5.45 RMSEE of the delays. Comparison between different paths estimation obtained with SAGE, considering the EVA channel model in the simulated ping scenario with random Doppler.

Figure 5.45 and Figure 5.46 show, respectively, the RMSEE of the delays and of the Doppler obtained with SAGE, considering the EVA channel model in the simulated ping scenario with random Doppler. We can notice that the RMSEE of the delays in this case is similar to the full band scenario considering all the paths. The Doppler estimation is in general similar to the full band scenario, and in particular the error of the first two paths is below 10 Hz with SNR above -10 dB.

As mentioned above, the IAA-APES algorithm does not provide proper estimation of the paths other than the first one. The RMSEE of the first path delay obtained with IAA-APES in the two ping scenarios will be shown in the following.

Figure 5.47 and Figure 5.48 show, respectively, the RMSEE of the delays and of the Doppler obtained with SAGE, considering the EVA channel model in the real ping scenario with random Doppler. The RMSEE in this case is higher compared to the simulated ping scenarios. The RMSEE is about 70 ns, 40 ns and 80 ns for the first, the second and the third paths, respectively. This relatively high errors also characterize the Doppler estimation, and indeed the Doppler RMSEE for the first path is between 100 and 40 Hz at low and high SNR, respectively. These relatively high RMSEE values are due to the small band occupation of this scenario and to the characteristics of the channel.

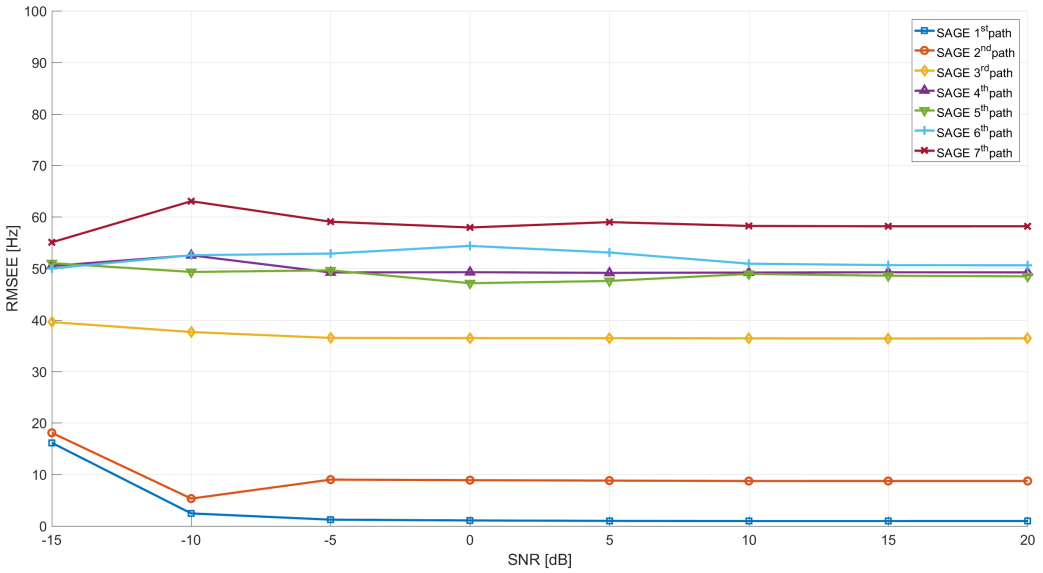

Fig. 5.46 RMSEE of the Doppler. Comparison between different paths estimation obtained with SAGE, considering the EVA channel model in the simulated ping scenario with random Doppler.

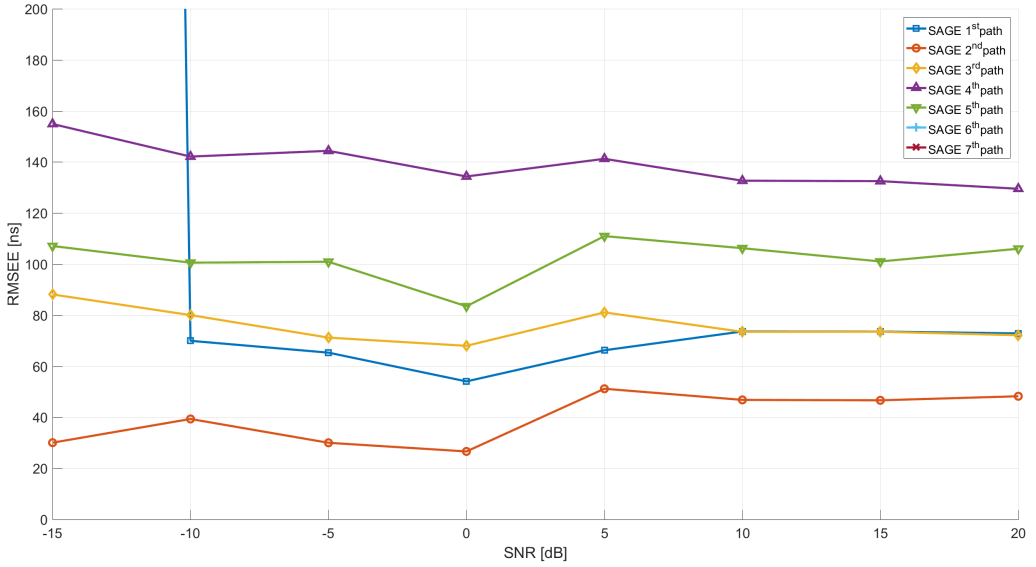

Fig. 5.47 RMSEE of the delays. Comparison between different paths estimation obtained with SAGE, considering the EVA channel model in the real ping scenario with random Doppler.

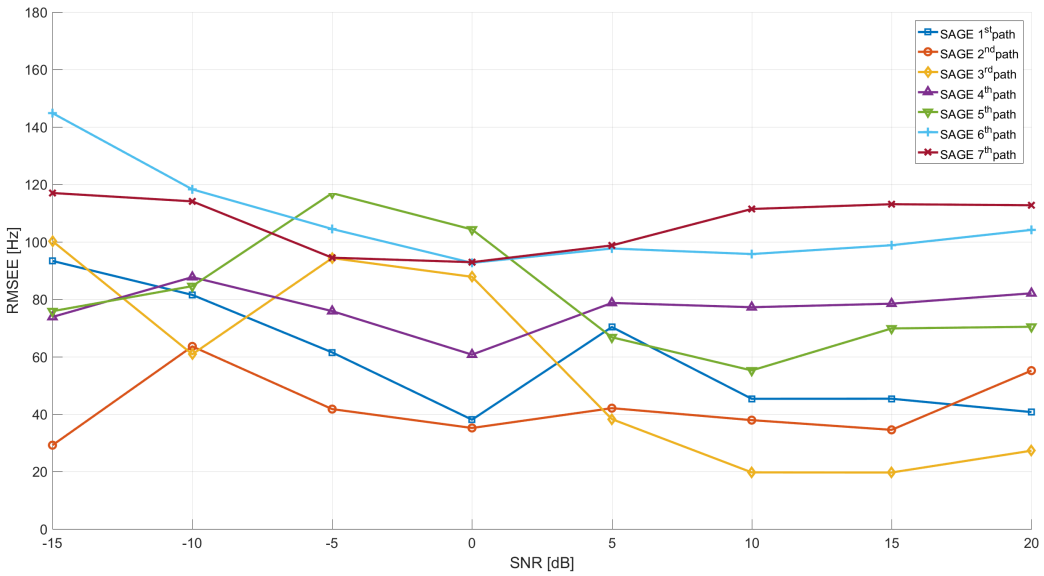

Fig. 5.48 RMSEE of the Doppler. Comparison between different paths estimation obtained with SAGE, considering the EVA channel model in the real ping scenario with random Doppler.

In Figure 5.49 and Figure 5.50 we show the RMSEE of the first path delay. In particular, we compare the results obtained with SAGE, IAA-APES and the correlation peak detector, considering the EVA channel model in the three different scenarios with random Doppler. Figure 5.49 shows a detail of Figure 5.50. From this figures, we can observe that the correlation based estimation has a high error at low SNR and in the two ping scenarios. In the full band case, the correlation RMSEE is comparable with the other methods. However, IAA-APES performs better then the correlation in the full band scenario. Moreover, IAA-APES performs better than SAGE only at SRN below -10 dB in the real ping scenario. In the full band scenario, IAA-APES has an RMSEE in pseudorange approximately between 4 m and 2 m at low and high SNR, respectively. The RMSEE obtained with IAA-APES in the simulated ping and real ping scenarios is around 150 ns and 160 ns, respectively, i.e. around 45 and 48 m in pseudorange. SAGE outperforms in this case the other algorithms, in particular when the two ping scenarios is considered, while in the full band scenario SAGE is only slightly better than IAA-APES. The RMSEE of SAGE in the simulated ping scenario is close to the SAGE RMSEE in the full band scenario, with an RMSEE in pseudorange equal to about to 1.5 m. SAGE, in the real ping scenario, reaches an RMSEE of about 20 m in pseudorange. This value is rather large, but considerably smaller compared to the RMSEE of IAA-APES in the real ping scenario.

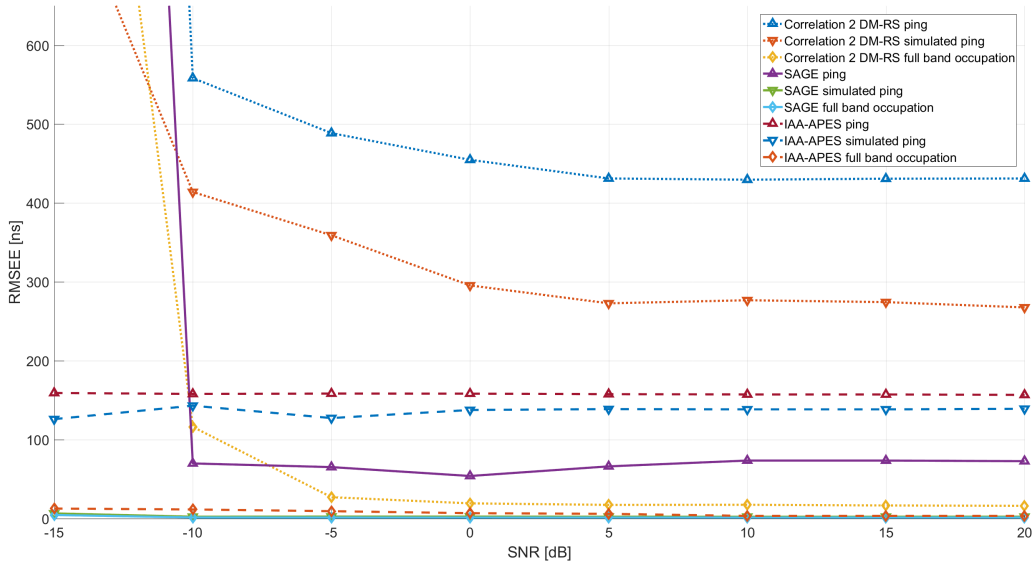

Fig. 5.49 RMSEE of the first path delay. Comparison between SAGE, IAA-APES and the correlator peak detector, considering the EVA channel model in the three different scenarios with random Doppler.

Summarizing the results for the EVA channel, IAA-APES seems to have better performance then SAGE only in some scenarios when the SNR is lower than -10 dB. SAGE, instead, has the best performance in the full band scenario for SNR higher than -10 dB giving a delay RMSEE in pseudorange of about 1.5 m. SAGE shows also the best performance in the simulated ping and real ping scenarios for SNR above -10 dB, giving estimation errors close to the full band case in the simulated ping scenario. In the real ping scenario, the errors in pseudorange are about 3.5 m with fixed Doppler and about 20 m with random Doppler. These values, although not small, are in any case much better than those obtained with the other algorithms.

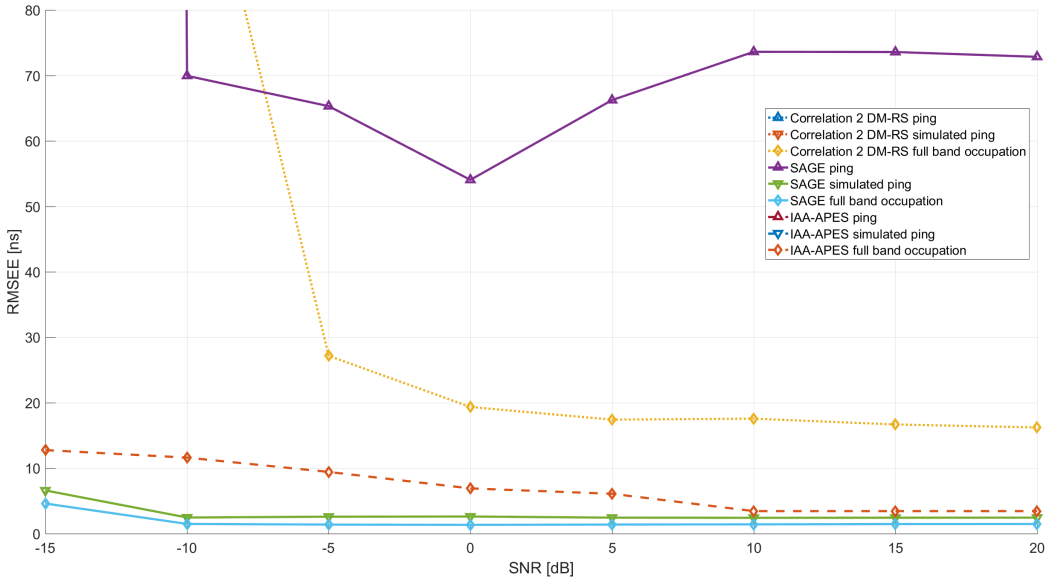

Fig. 5.50 RMSEE of the first path delay. Inset of the comparison between SAGE, IAA-APES and the correlator peak detector, considering the EVA channel model in the three different scenarios with random Doppler.

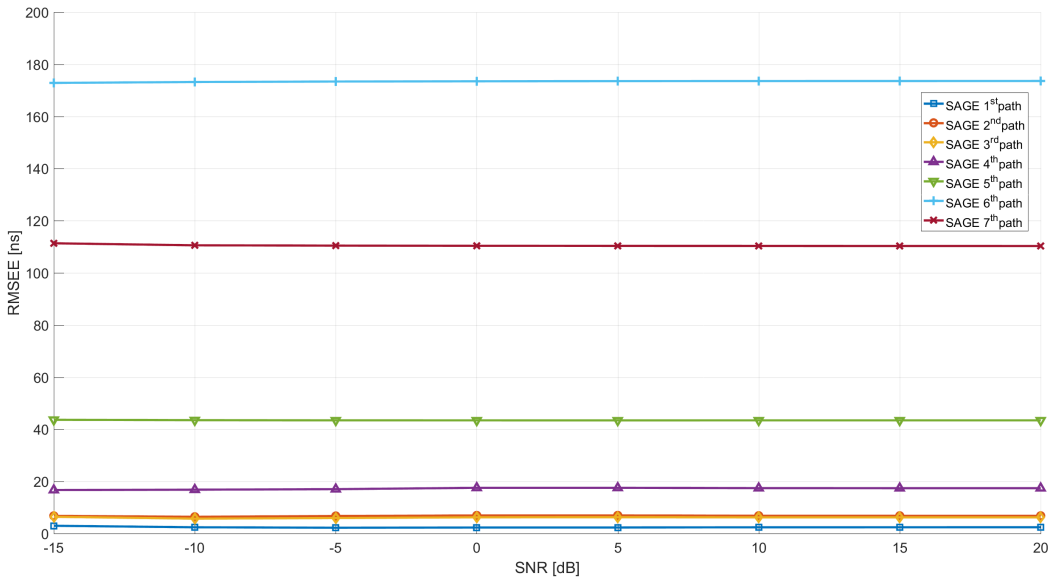

Fig. 5.51 RMSEE of the delays. Comparison between different paths estimation obtained with SAGE, considering the ETU channel model in the full band scenario with fixed Doppler.

5.6.3 ETU Channel Results

ETU Fixed Doppler Results

Figure 5.51 and Figure 5.52 show, respectively, the RMSEE of the delays and of the Doppler obtained with SAGE, considering the ETU channel model in the full band scenario with fixed Doppler. In this case, the delay RMSEE of the first four paths is below 20 ns. From the fifth to the seventh path, the errors are below 50 ns, 180 ns and 110 ns, respectively. With the ETU channel model, the RMSEE for the considered paths is in general lower then the one obtained with EPA and EVA channels. This is because, in the ETU channel model, the paths are more separated in the delay domain. Low RMSEE values are obtained also for Doppler estimation, which is below 2 Hz for all the paths. The first path delay RMSEE is below 5 ns, which corresponds to an error in pseudorange below 1.5 m.

Figure 5.53 shows the RMSEE of the delays obtained with IAA-APES, considering the ETU channel model in the full band in the fixed Doppler scenario. With this algorithm, only three paths can be resolved, and in general the first path delay RMSEE is slightly higher than the one given by SAGE. The RMSEE of the first path is about 22 ns at low SNR and below 10 ns at high SNR. The RMSEEs of the second and the third paths are approximately between 70 ns and 20 ns, and between 140 ns and 30 ns, respectively, for increasing SNR values.

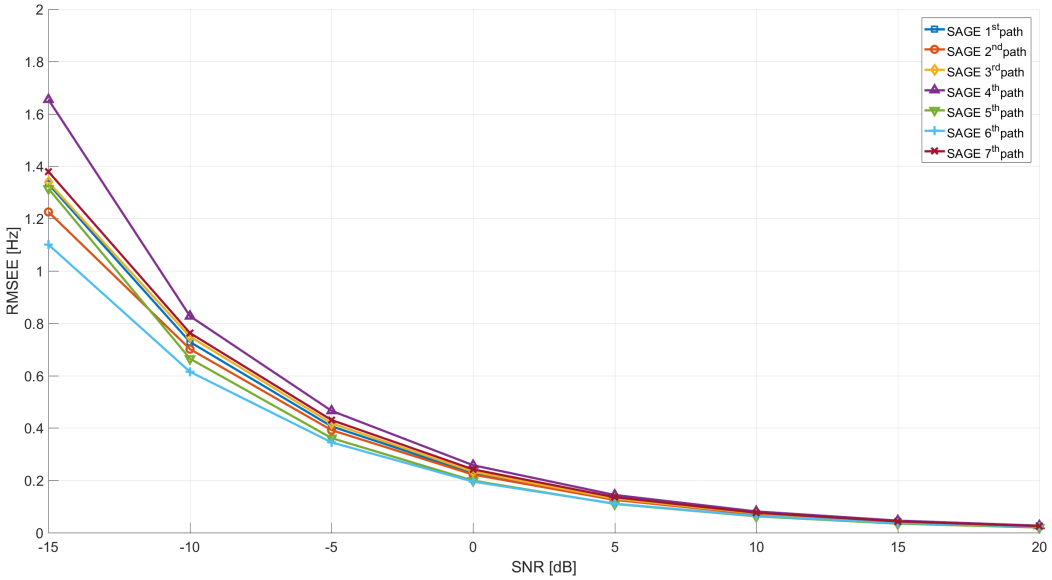

Fig. 5.52 RMSEE of the Doppler. Comparison between different paths estimation obtained with SAGE, considering the ETU channel model in the full band scenario with fixed Doppler.

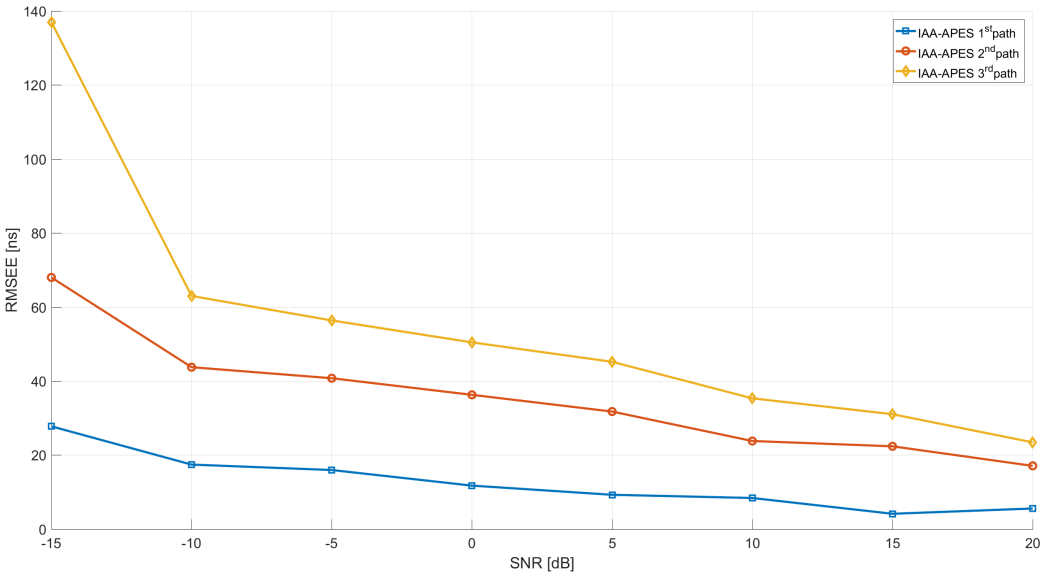

Fig. 5.53 RMSEE of the delays. Comparison between different paths estimation obtained with IAA-APES, considering the ETU channel model in the full band scenario with fixed Doppler.

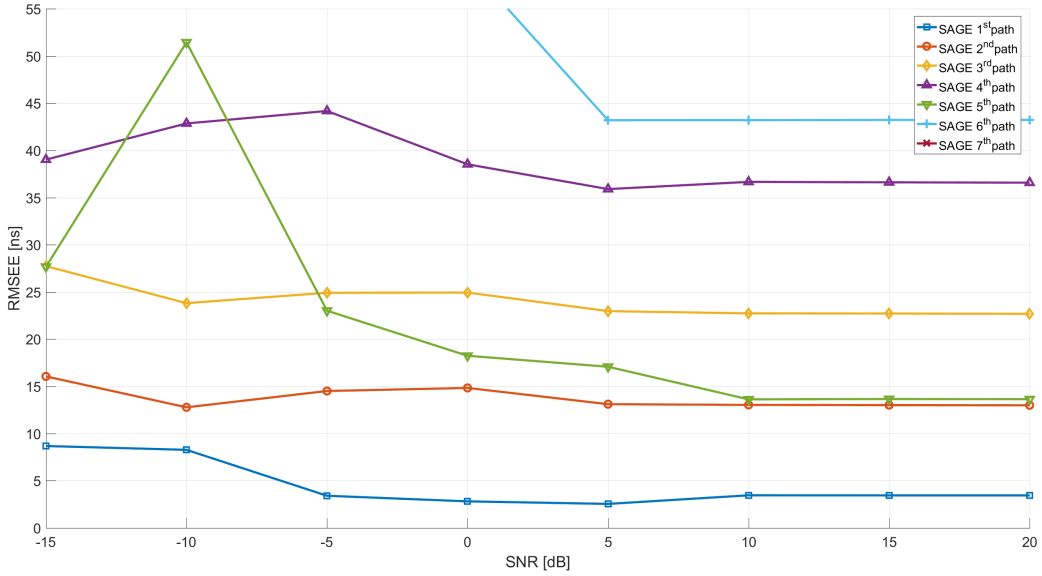

Fig. 5.54 RMSEE of the delays. Comparison between different paths estimation obtained with SAGE, considering the ETU channel model in the simulated ping scenario with fixed Doppler.

Figure 5.54 and Figure 5.55 show, respectively, the RMSEE of the delays and of the Doppler obtained with SAGE, considering the ETU channel model in the simulated ping scenario with fixed Doppler. We can notice that the RMSEE in this case is similar to the full band scenario, for the first five paths, and that in general the errors are below 50 ns. The first path RMSEE is always below 10 ns, and in particular, at high SNR, it is below 5 ns. The Doppler estimation is in general similar to the full band scenario for high SNR but for low SNR some paths have an RMSEEs that exceeds 10 Hz. For the fifth condidered path the maximum error is always below 55 Hz.

The first path delay RMSEE of IAA-APES for the two ping scenarios will be shown later. This for the same reasons explained in the previous EVA and EPA sections.

Figure 5.56 and Figure 5.57 show, respectively, the RMSEE of the delays and of the Doppler obtained with SAGE, considering the ETU channel model in the real ping scenario with fixed Doppler. The RMSEE in this case is higher then the simulated ping scenario, and indeed the first five path delays RMSEE is between 90 and 20 ns. The first path RMSEE is about 35 ns at high SNR, while at SNR lower than 10 dB, the RMSEE is very high. The RMSEE of the Doppler for the first path is about 3 Hz at high SNR and around 60 Hz at low SNR. The other paths exhibit an error between 25 Hz and 100 Hz in the whole SNR range, apart from the sixth and seventh path, with an RMSEE around 3 Hz at high SNR.

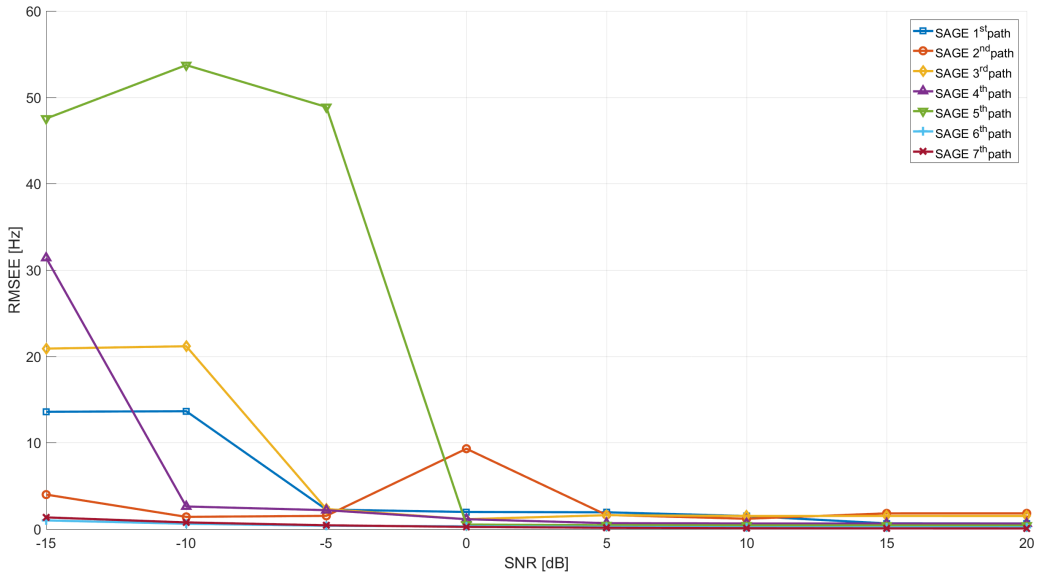

Fig. 5.55 RMSEE of the Doppler. Comparison between different paths estimation obtained with SAGE, considering the ETU channel model in the simulated ping scenario with fixed Doppler.

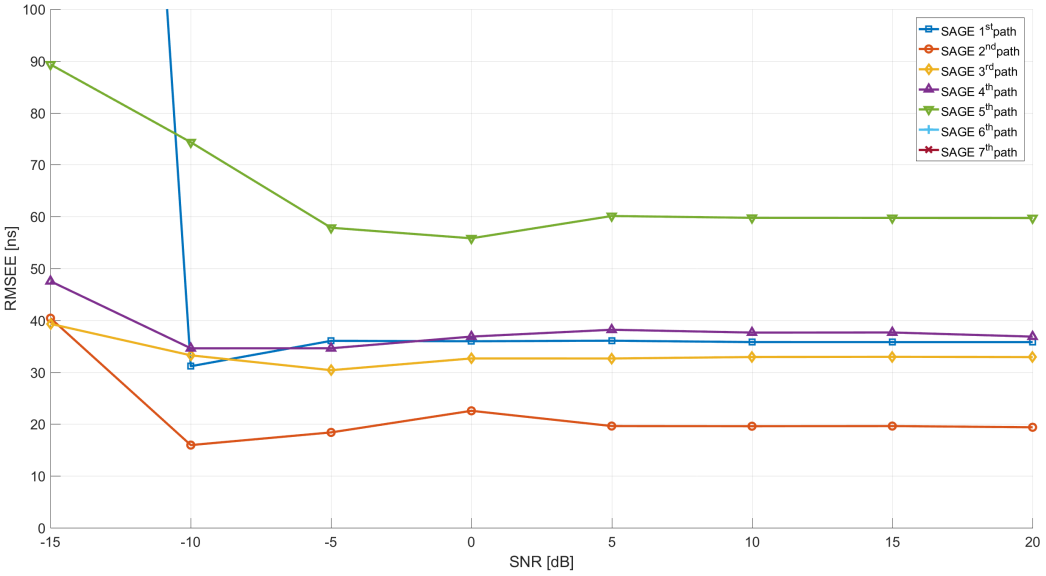

Fig. 5.56 RMSEE of the delays. Comparison between different paths estimation obtained with SAGE, considering the ETU channel model in the real ping scenario with fixed Doppler.

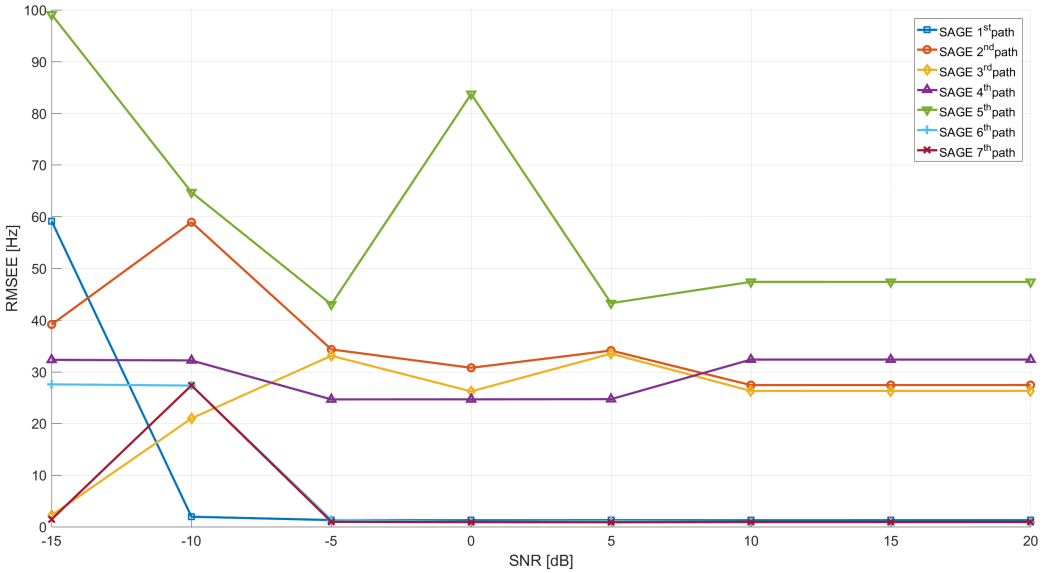

Fig. 5.57 RMSEE of the Doppler. Comparison between different paths estimation obtained with SAGE, considering the ETU channel model in the real ping scenario with fixed Doppler.

Figure 5.58 and Figure 5.59 show the RMSEE of the first path. In particular, we compare the results obtained with SAGE, IAA-APES and the correlation peak detector, considering the ETU channel model in the three different scenarios with fixed Doppler. Figure 5.58 shows a detail of Figure 5.59. From these figures, we can observe that the correlation based estimation has a high error at low SNR and in the two ping scenarios. In the full band case, the correlation RMSEE is comparable with the other methods. However, considering the full band case, IAA-APES performs better then the correlation. IAA-APES and SAGE have approximately the same performance at high SNR, while IAA-APES is slightly worse then SAGE at low SNR. In the full band scenario, IAA-APES has a RMSEE in pseudorange approximately between 7.5 m and 3 m, at low and high SNR, respectively. In the two ping scenario, IAA-APES has a high error equal to around 150 ns for the simulated ping and 170 ns for the real ping, and performs better than SAGE only at SNR below -10 dB in the real ping scenario. The SAGE algorithm, in this case, outperforms the other algorithms, in particular when the two ping scenarios are used. Indeed, the performance of SAGE in the simulated ping scenario are close to the performance of SAGE in the full band scenario and the RMSEE in pseudorange is close to 2.5 m. In the real ping scenario, SAGE has an RMSEE around 10 m in pseudorange, which is considerably lower than the RMSEE obtained with IAA-APES for the real ping scenario, which is around 45 m.

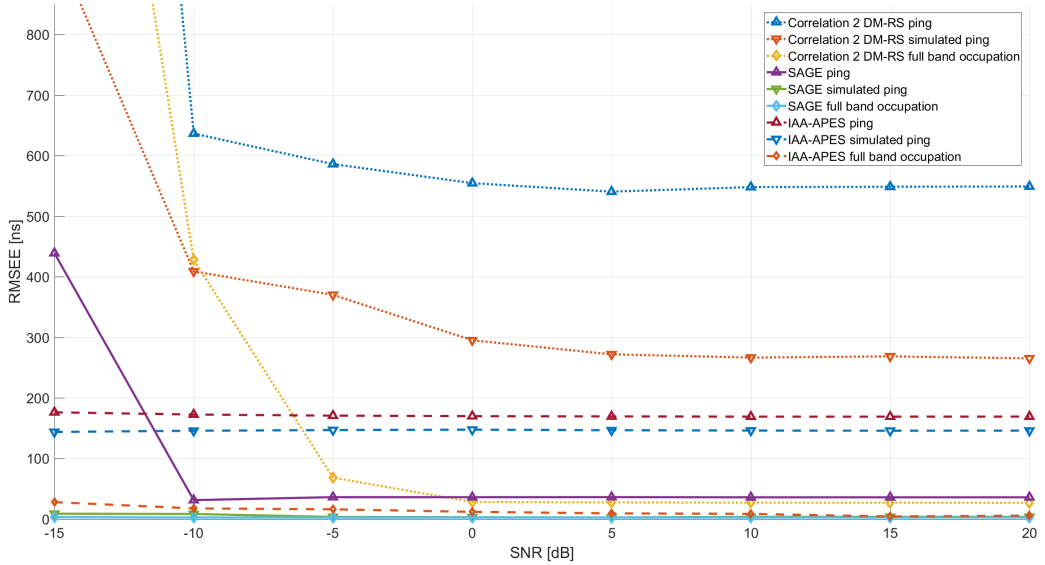

Fig. 5.58 RMSEE of the first path delay. Comparison between SAGE, IAA-APES and the correlator peak detector, considering the ETU channel model in the three different scenarios with fixed Doppler.

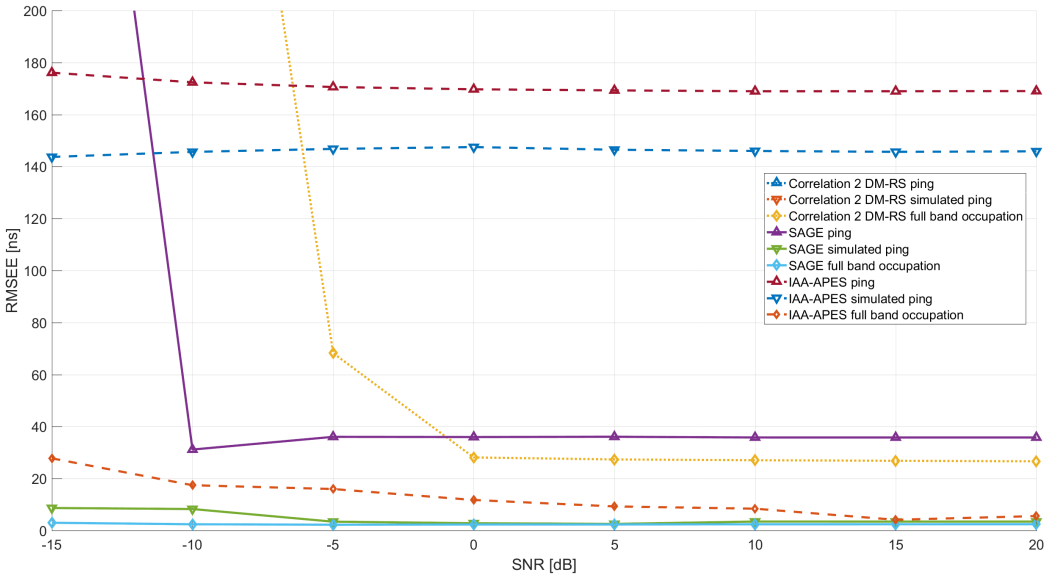

Fig. 5.59 RMSEE of the first path delay. Inset of the comparison between SAGE, IAA-APES and the correlator peak detector, considering the ETU channel model in the three different scenarios with fixed Doppler.

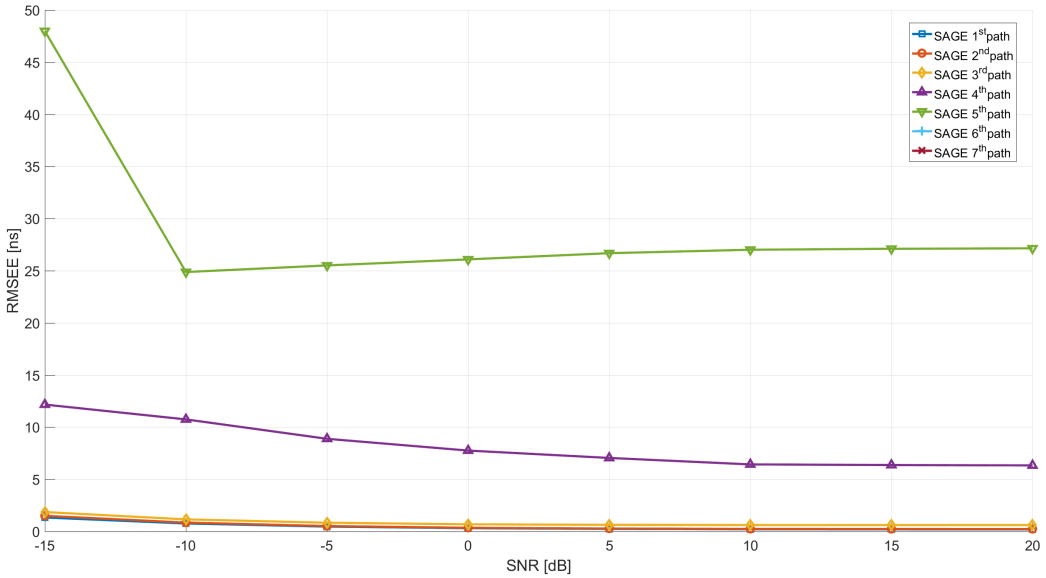

Fig. 5.60 RMSEE of the delays. Comparison between different paths estimation obtained with SAGE, considering the ETU channel model in the full band scenario with random Doppler.

ETU Random Doppler Results

Figure 5.60 and Figure 5.61 show, respectively, the RMSEE of the delays and of the Doppler obtained with SAGE, considering the ETU channel model in the full band scenario with random Doppler. In this case, the RMSEE of the delay relative to the first three paths is below 5 ns. The fourth and the fifth path have an RMSEE around 7 ns and 25 ns, respectively, at high SNR. Also, the Doppler is estimated well, and the error is always below 5 Hz for the first four paths. The other paths have higher RMSEE that exceeds 250 ns for the delay and 180 Hz for the Doppler. The RMSEE of the delay of the first path is below 2 ns, which corresponds to an error in pseudorange below 1 m. In this case, the better estimation performance is due to the high separation of the Doppler frequencies, due to the random generation and to the high value of $\nu_{l,MAX}$. With the considered number of snapshots, the algorithm can distinguish properly the different paths in the Doppler domain.

Figure 5.62 shows the RMSEE of the delays obtained with IAA-APES, considering the ETU channel model in the full band scenario with random Doppler. This algorithm is able to estimate only three paths, with a small RMSEE that is slightly higher than the RMSEE of the first three path estimates obtained with SAGE. The RMSEE of the first path is around 16 ns at low SNR and below 2 ns at high SNR. The second and

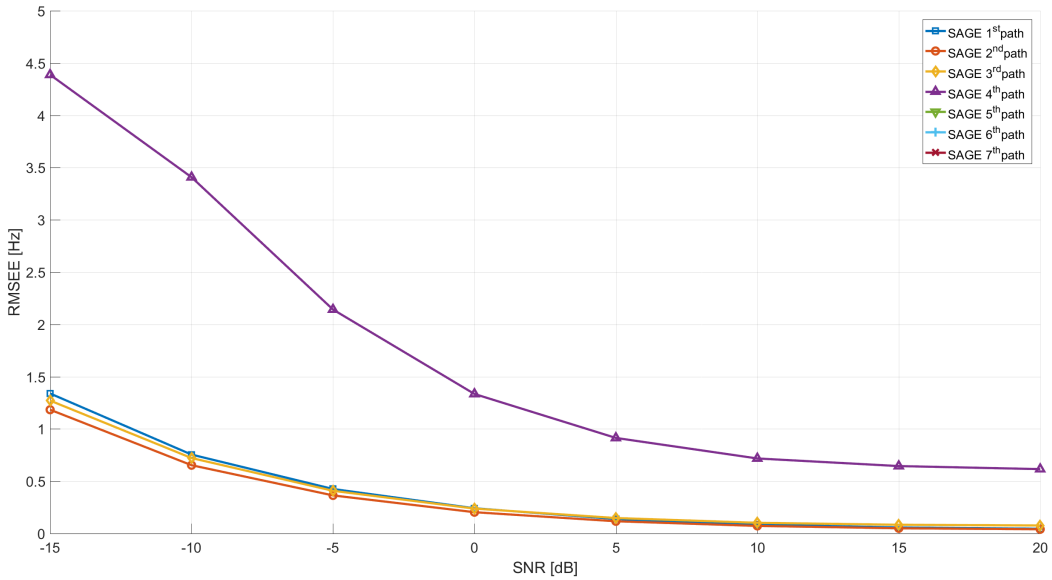

Fig. 5.61 RMSEE of the Doppler. Comparison between different paths estimation obtained with SAGE, considering the ETU channel model in the full band scenario with random Doppler.

third path have an RMSEE approximately between 28 and 2 ns and between 40 ns and 6 ns, respectively, in the considered SNR range.

Figure 5.63 and Figure 5.64 show, respectively, the RMSEE of the delays and of the Doppler obtained with SAGE, considering the ETU channel model in the simulated ping scenario with random Doppler. We can notice that the RMSEE of the delay relative to the first and second path is similar to the full band scenario, and in particular it is about 2 ns. For the third, fourth and fifth path, the RMSEE is below 25 ns. The first path delay RMSEE is high only at low SNR. The RMSEE of the Doppler is in general similar to the full band scenario for the first two paths, with a higher error only at low SNR. The third and fourth paths have estimation errors around 15 Hz and 25 Hz, respectively, whereas the other paths have an error around 150 Hz.

As before, the first path delay RMSEEs of IAA-APES for the two ping scenarios will be shown later.

Figure 5.65 and Figure 5.66 show, respectively, the RMSEE of the delays and of the Doppler obtained with SAGE, considering the ETU channel model in the real ping scenario with random Doppler. The RMSEE of the delays in this case is higher compared to the simulated ping scenarios, and in general the first five paths RMSEE is approximately between 28 and 80 ns in the considered SNR range. This relatively high error is related to the small overall band and little snapshot number available for

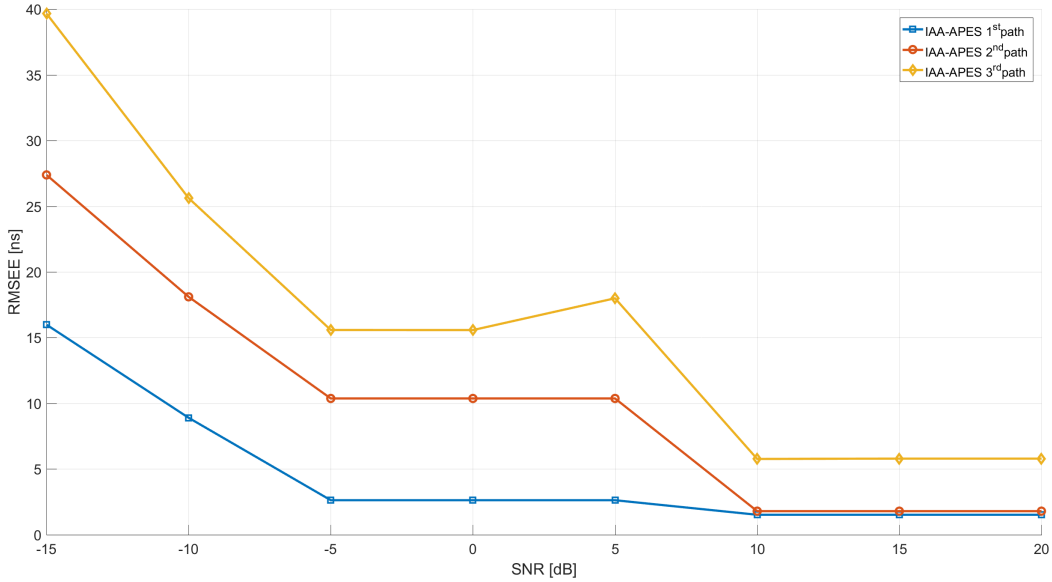

Fig. 5.62 RMSEE of the delays. Comparison between different paths estimation obtained with IAA-APES, considering the ETU channel model in the full band scenario with random Doppler.

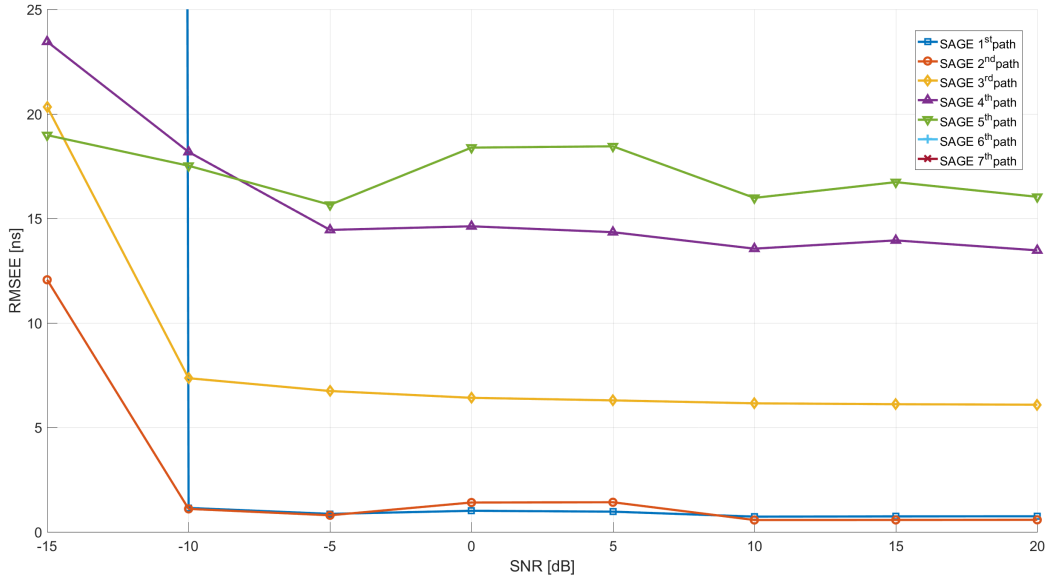

Fig. 5.63 RMSEE of the delays. Comparison between different paths estimation obtained with SAGE, considering the ETU channel model in the simulated ping scenario with random Doppler.

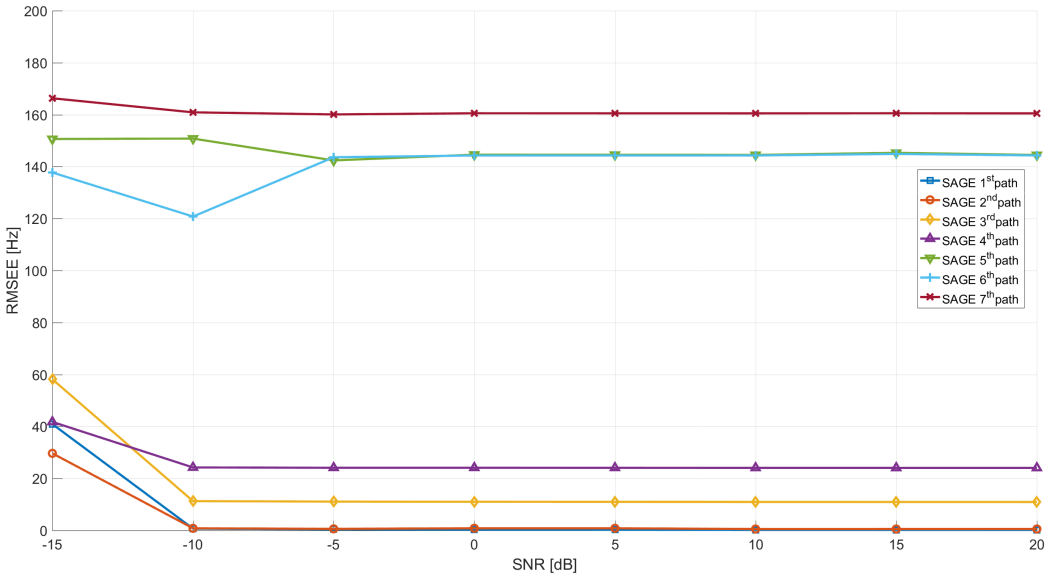

Fig. 5.64 RMSEE of the Doppler. Comparison between different paths estimation obtained with SAGE, considering the ETU channel model in the simulated ping scenario with random Doppler.

the estimation. The RMSEE of the Doppler has values between 80 and 200 Hz. The RMSEE of the delay relative to the first path is around 60 ns at low SNR and reaches 28 ns at high SNR, which are respectively 18 m and 8.5 m in pseudorange.

Figure 5.67 and 5.68 show the RMSEE of the first path delay. In particular, we compare the results obtained with SAGE, IAA-APES and the correlation peak detector, considering the ETU channel model in the three different scenarios with random Doppler. Figure 5.67 shows a detail of Figure 5.68. From this figures, we can observe that the correlation based estimation has a high error at low SNR and in the two ping scenarios. In the full band scenario, the correlation RMSEE is comparable with the other methods. However, IAA-APES performs better then the correlation method in the full band scenario. IAA-APES also performs better than SAGE when the SNR is below -10 dB in the simulated ping scenario. In the full band scenario, IAA-APES has an error in pseudorange approximately between 4.8 m and below 1 m at low and high SNR, respectively. The SAGE algorithm in this case outperforms the other algorithms, in particular in the two ping scenarios and the SNR is above -10 dB. Indeed, the performance of SAGE in the simulated ping scenario is close to the performance of SAGE in the full band scenario and the RMSEE of the first path in pseudorange is below 1 m.

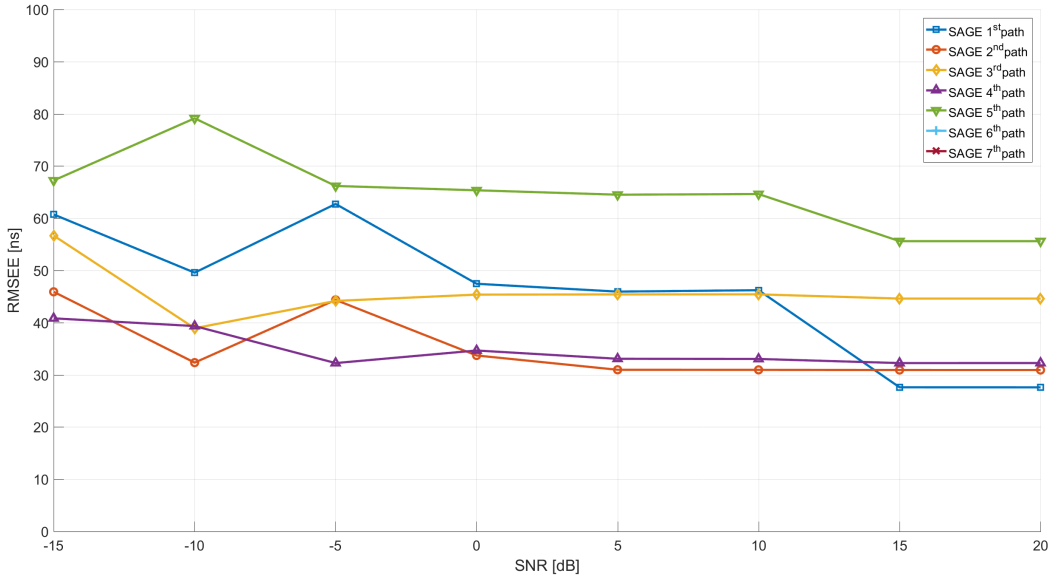

Fig. 5.65 RMSEE of the delays. Comparison between different paths estimation obtained with SAGE, considering the ETU channel model in the real ping scenario with random Doppler.

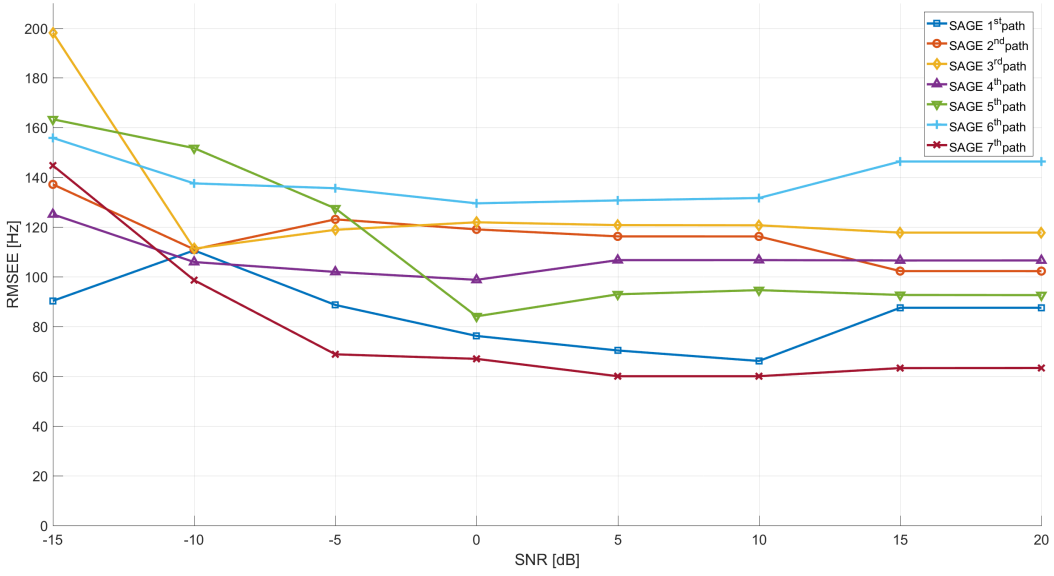

Fig. 5.66 RMSEE of the Doppler. Comparison between different paths estimation obtained with SAGE, considering the ETU channel model in the real ping scenario with random Doppler.

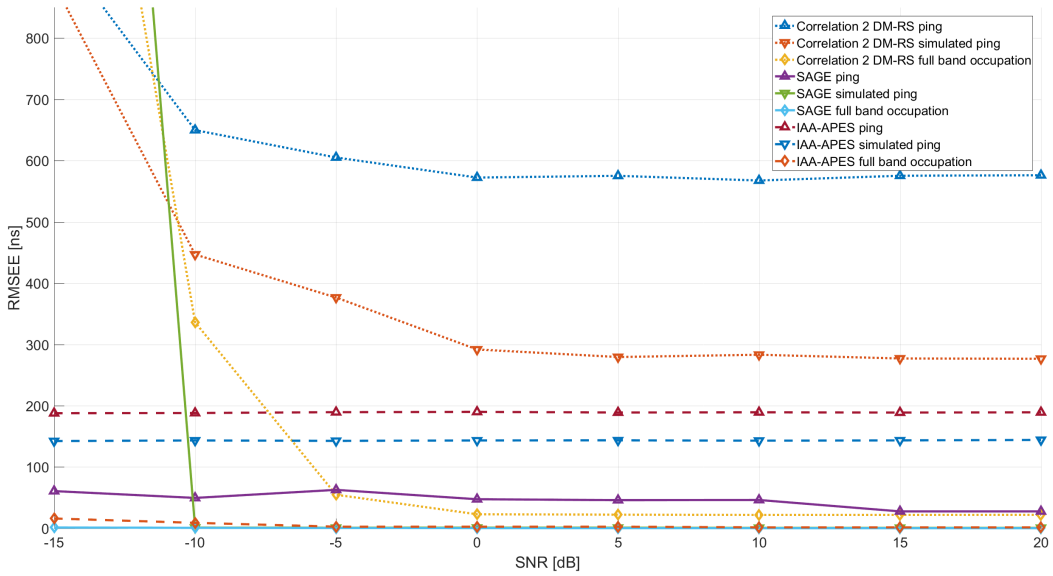

Fig. 5.67 RMSEE of the first path delay. Comparison between SAGE, IAA-APES and the correlator peak detector, considering the ETU channel model in the three different scenarios with random Doppler.

In the real ping scenario SAGE has an RMSEE in pseudorange between 18 and 8.5 m. These values are considerably smaller compared to the RMSEE of the first path obtained with IAA-APES in the real ping scenario, which is around 57 m.

Summarizing the results obtained with the ETU channel, IAA-APES shows good performance in the full band scenario for both random and fixed Doppler simulations. With the ETU channel, IAA-APES outperforms SAGE only in the simulated ping scenario with SNR below -10 dB. SAGE has the best performance in the full band scenario with RMSEE in pseudorange below 1 m. SAGE has also the best performance in the simulated ping scenario when the SNR is higher than -10 dB. In the real ping scenarios, the RMSEE of the first path obtained with SAGE in the worst case is about 10 m, in the fixed Doppler simulations, and about 18 m in the random Doppler simulations. These errors are strongly better than the errors obtained with the other algorithms.

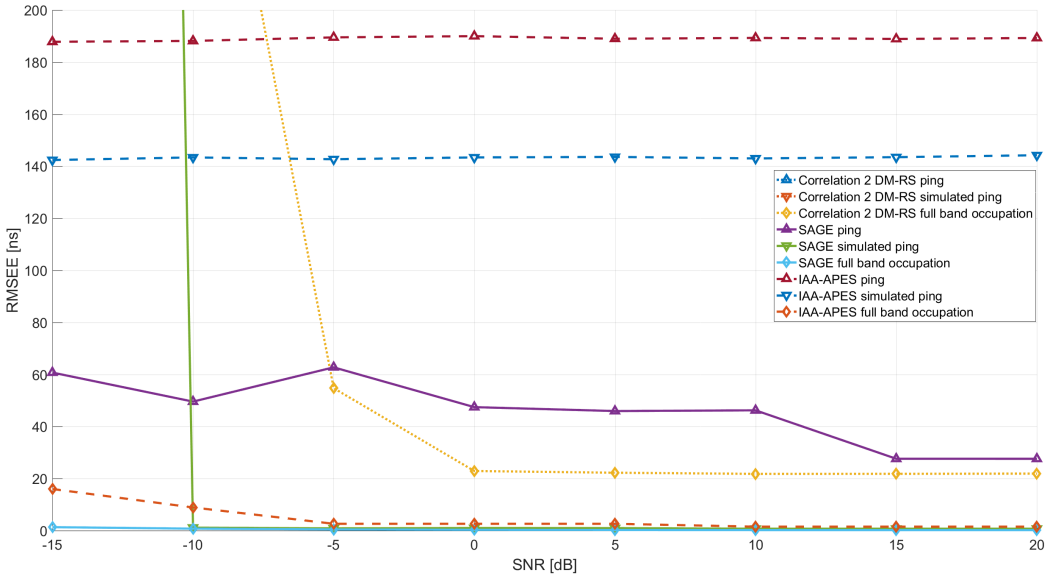

Fig. 5.68 RMSEE of the first path delay. Inset of the comparison between SAGE, IAA-APES and the correlator peak detector, considering the ETU channel model in the three different scenarios with random Doppler.

The results obtained from the simulations of the EPA, EVA and ETU channels with random and fixed Doppler, are encouraging. We saw that, in a full band scenario, the IAA-APES and the SAGE algorithm have similar performance in all the different channel realizations. The RMSEE in this scenario is generally small and in some cases the pseudorange error is below one meter. This scenario represents a reference lower bound. Indeed, considering the CRLB described in Section 4.5, the delay estimation is proportional to the occupied bandwidth. However, this scenario is not realistic, because, in an LTE uplink transmission, UE data do not occupy the whole bandwidth. In general, IAA-APES appears to be more reliable when the SNR is below -10 dB. This is because IAA-APES uses the time snapshots to average the results, whereas SAGE uses all the time snapshots in order to estimate the Doppler frequency. When a data transmission is simulated at an SNR larger than -10 dB, SAGE outperforms all the other methods and provides estimate with a smaller RMSEE then the other algorithms. In the simulated ping scenario, where the occupation bandwidth is random and between 4 to 18 RBs, SAGE has a performance almost equal to the full band case. This means that SAGE is not affected by the decrease of the bandwidth. When we consider a real ping transmission pattern, which has a lower overall band occupation compared to the simulated ping scenario, SAGE performance degrades but still remains much better than that of the other algorithms. Considering the Doppler RMSEE, SAGE shows good performance when the full band scenario is considered. However, we see a general low degradation in the simulated ping scenario and a high degradation in the real ping scenario, which is probably due to limited number of snapshot used in this case. Indeed, with a low number of snapshots and a low number of occupied subcarriers, it can happen that some subcarriers f_k, are filled with zeros in all the snapshots (see for example Figure 5.2). These subcarriers obviously do not contribute to the Doppler estimation, and inevitably make the estimate less precise.

5.7 Experimental Results in a Real Scenario

5.7.1 Set-up

In this section, we present some experimental results obtained by measuring the TDOA exploiting the uplink DM-RS. In particular, we try to determine the distance between two antennas using DM-RS signals and the SAGE algorithm with 2D initialization. The SAGE algorithm is selected because, as seen above, it appears to be the best

choice when there are missing bins in the CFR, which is exactly the situation that we face during uplink transmissions.

In general, to measure a TOA using the DM-RS, knowledge of some parameters is necessary, otherwise it is impossible to reconstruct the correct reference signals at the receiver used to estimate the CFR. These parameters are listed in Table 5.2. In particular, Cell ID represents the physical cell ID, SubNumber is the subframe

Name	**Range**
Cell ID	0-503
SubNumber	0-19
NTxAnts	1,2 or 4
CycPref	normal or extended
Hopping	Off, Sequence or Group
SeqGroup	0-29
CycShift	0-7
NPUSCHID	0-509
NDMRSID	0-509
PRBSet	maximum range is 0 to (N_{RB}-1)
NLayers	1,2,3,4
DynCycShift	0-7
OrthCover	On-Off
PMI	0-23

Table 5.2 Parameters that has to be known in order to estimate the TOA using the DM-RS.

number, NTxAnts is the number of transmission antennas, CycPref is the length of the cyclic prefix, Hopping is the frequency hopping mode, SeqGroup is the sequence group assignment, CycShift is the cyclic shift equal to $n^{(1)}_{DMRS}$ in [15], NPUSCHID is the PUSCH virtual cell identity, NDMRSID is the DM-RS identity for cyclic shift hopping, PRBSet is the set of physical resource blocks used for the uplink transmission, NLayers is the number of transmission layers, DynCycShift represents the cyclic shift field related to the DCI format, which is equal to $n^{(2)}_{DMRS,\lambda}$ in [15], OrthCover indicates if the orthogonal cover sequence is applied to the reference sequence and PMI is the precoder matrix indication. More detail about these parameters and about their influence on the DM-RS can be found in [15].

The experiment was carried out inside a building of the University of Udine. As one can see in Fig. 5.69, the two antennas are connected to two different inputs of the same USRP. The connection cables have the same length, in order to guarantee, as first approximation, that we do not have to compensate the delay introduced by the cables.

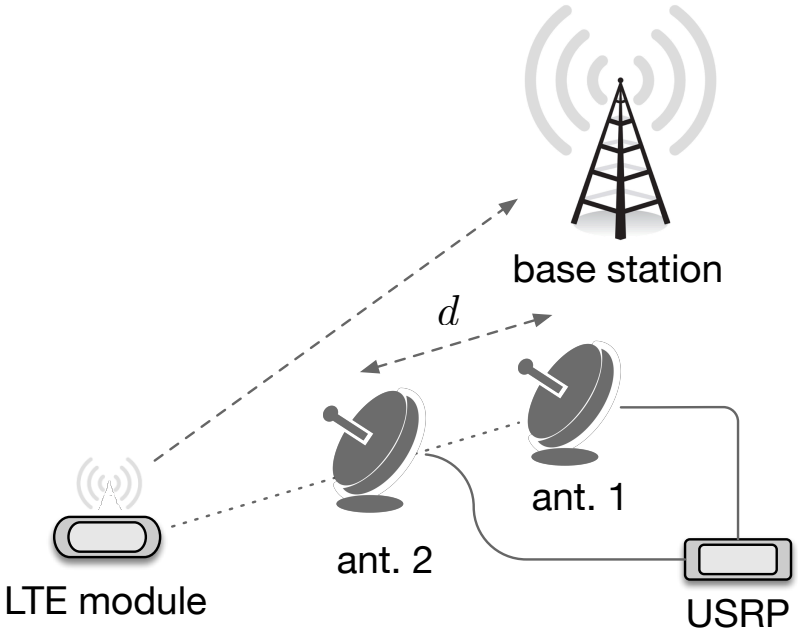

Fig. 5.69 Arrangement of the experimental setup.

Furthermore, in order to allow synchronised acquisition of the signals coming from the LTE module, the two acquisition channels of the USRP share the same reference clock. The two antennas are positioned at a distance d and are aligned with the LTE module, then we can estimate d by measuring the TDOA between the two antennas and multiplying the result by the speed of light. In this way, we do not need to know the transmission time, thus making the setup simpler. A good estimate of d implies that the proposed system can provide good TDOA measurements, which are the basis of hyperbolic positioning systems as shown in Chapter 2.

The DM-RS is always associated with a data transmission. In our experiment, we force the LTE module Toby L2 [54] to transmit a "ping". After receiving the signal from the two antennas at the USRP, we find the arrival time of the first DM-RS signal inside the received signals by correlating them with the known transmitted DM-RS. This estimate is rather coarse, since it does not take into account the effect of the multipath channel, as it is possible to see in the results showed in Section 5.5 and Section 5.6. We denote this coarse TOA as $t_{m,TOA}$ where m indicates the m-th antenna. Considering that the LTE standard ensures a fixed time $\Delta t = 0.5$ ms between a DM-RS and the one transmitted in the next slot, knowledge of $t_{m,TOA}$ allows the estimation of the time position of successive DM-RSs in a given number of consecutive slots. Knowing the

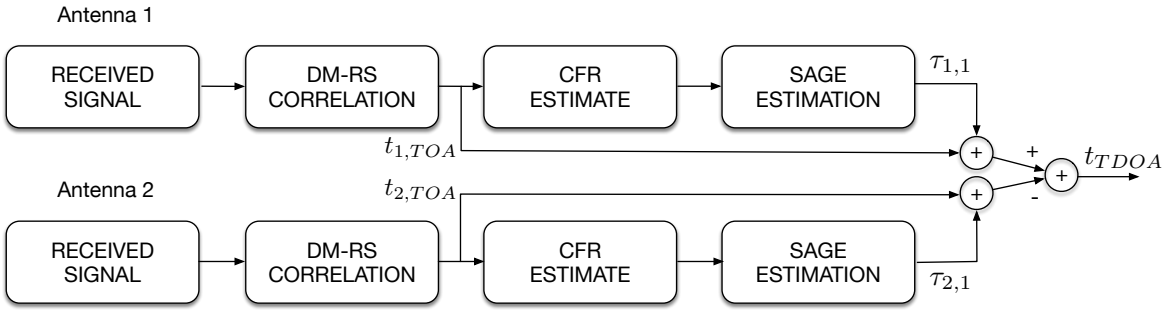

Fig. 5.70 Block diagram of the proposed system.

positions in time and the bandwidth occupied by the DM-RSs, we can estimate the CFRs for each DM-RS discarding the cyclic prefix and using the deconvolution method in frequency, to obtain the estimates $\hat{H}(t_n; f_k)$ as defined in Section 4.4. The values $\hat{H}(t_n; f_k)$ for frequencies outside the DM-RS band occupation at each t_n are set to zero, as shown in Section 5.3. Using the SAGE algorithm, we can then process the full observation matrix $\hat{\boldsymbol{H}}(\boldsymbol{t}; \boldsymbol{f})$ to estimate the delay. The most important path for TOA estimation is the first arrival path $\tau_{m,1}$, where m denotes the m-th antenna, which is represented by the minimum $\tau_{m,l}$ estimated. Indeed, there is no certainty that the first path is the path with the larger amplitude $|\alpha_1|$. Notice that the "ping" signal occupies a relatively small number of subframes, around 25-35 subframes, and that we can indeed assume that the channel parameters $\boldsymbol{\theta}$ remain constant during its transmission. After estimating the coarse TOA and the delay with SAGE for the two antennas, we can finally calculate the TDOA as $t_{TDOA} = (t_{1,TOA} + \tau_{1,1}) - (t_{2,TOA} + \tau_{2,1})$ and estimate the distance between the two antennas as $d = t_{TDOA}\, c$, where c is the speed of light, and we have assumed that the first antenna is further from the LTE module. Fig. 5.70 shows a block diagram of the main steps involved in the procedure.

5.7.2 Results

In this section, we describe the parameters of the experiment and present the results. The LTE module was connected to a base station that uses the LTE band 3 (further details on LTE band definitions can be found in [52]), which used an uplink central frequency of 1.775 GHz, and configured with the 100 RBs bandwidth described in Table 3.1. Thus, the available bandwidth is 18 MHz (which corresponds to 1200 subcarriers). The time and frequency scheduling is managed by the BS. Typically, a ping transmission occupies around 25-35 subframes in time and from 2 to 50 RBs

in frequency. The USRP was set to have a sample rate of 35 MHz which is then downconverted to 30.72 MHz in post processing. The measurements were made in three different scenarios varying the distance between antennas with $d = 40$ m, $d = 35$ m and $d = 30$ m.

The estimation of the number of paths L may not be a trivial task and is important for a successful use of the algorithm. In our experiments, to estimate L we use a procedure based on the amplitude α_l of the different paths and to the MDL described in Section 4.4.2. In particular, the procedure based on the amplitude α_l stops the algorithm when a path with an amplitude $|\alpha_l|$ 20 dB below the value $|\alpha_{MAX}|$ of the path with maximum amplitude is found. So, we run the algorithm for $L = 1, 2, ...$ and stop the procedure when, in correspondence to the current value $L = L_s$, we find a path that has amplitude 20 dB lower than the maximum amplitude, or when the MDL criteria is reached (i.e., when the L_s paths have an MDL metric higher than the $L_s - 1$ MDL metric). Then, we keep the channel parameters calculated for $L = L_s - 1$. Indeed, when a path has amplitude 20 dB lower than the maximum amplitude, then probably the estimated L_s path is negligible. This threshold choice is justified by the fact that the delay profiles described in [52] (i.e., the EPA, EVA and ETU delay profile in Table 5.1) have a minimum relative power of -20.8 dB. In order to safely stop the procedure if both the described criteria are not reached, in any case, we limit the search to a maximum number of paths $L_{MAX} = 10$.

Note that the transmission power may vary in different subframes [52], so we normalize the received signals by taking it into account, otherwise this would affect the estimated CFRs. The antennas were placed in a line of sight condition. In the experiment with $d = 40$ m, the furthest antenna was placed behind an open door, which could contribute to increased multipath. Distances between antennas were measured with a laser distance-meter, so that we can compare the value obtained with the distance-meter and the estimates obtained using the setup described above. For each value of d, we measure the distance obtained in 15 "ping" transmissions. We show the mean distance obtained with the correlation peak detector and the mean distance obtained with SAGE. The results of distance estimation with SAGE are compared with the average distance calculated as $(t_{1,TOA} - t_{2,TOA})\, c$, with $t_{1,TOA}$ and $t_{2,TOA}$ obtained with the correlation method.

Fig. 5.71 shows the distance estimates corresponding to the 15 "ping" transmissions when the two antennas were at a distance of 40 m. As we can see, using SAGE we have only one estimate with an error greater than 15 m, while the error is always below 10 m in the other cases. The average distance estimate error is about 2 m. With the

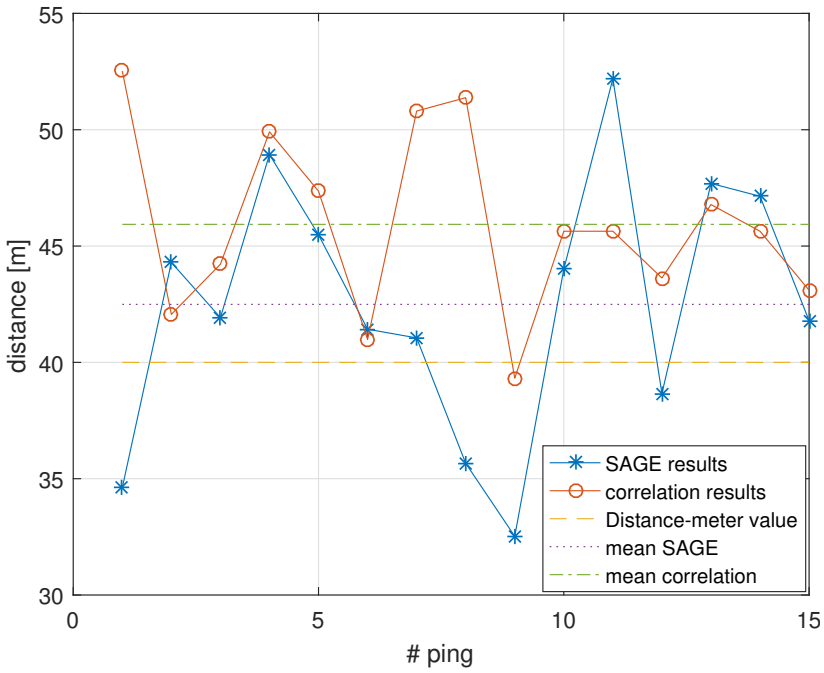

Fig. 5.71 Distance estimates using SAGE and the correlator, for a 40 m distance between the two antennas.

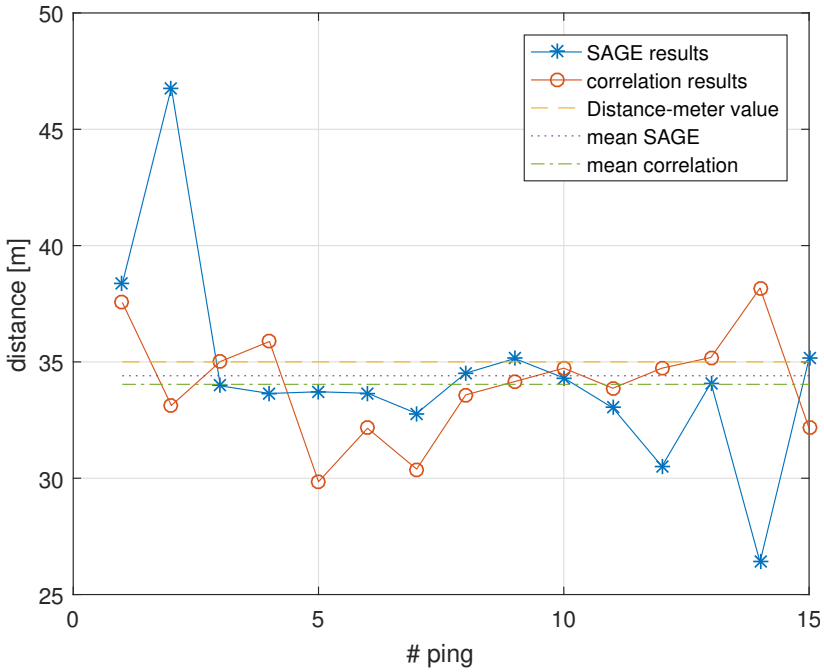

Fig. 5.72 Distance estimates using SAGE and the correlator, for a 35 m distance between the two antennas.

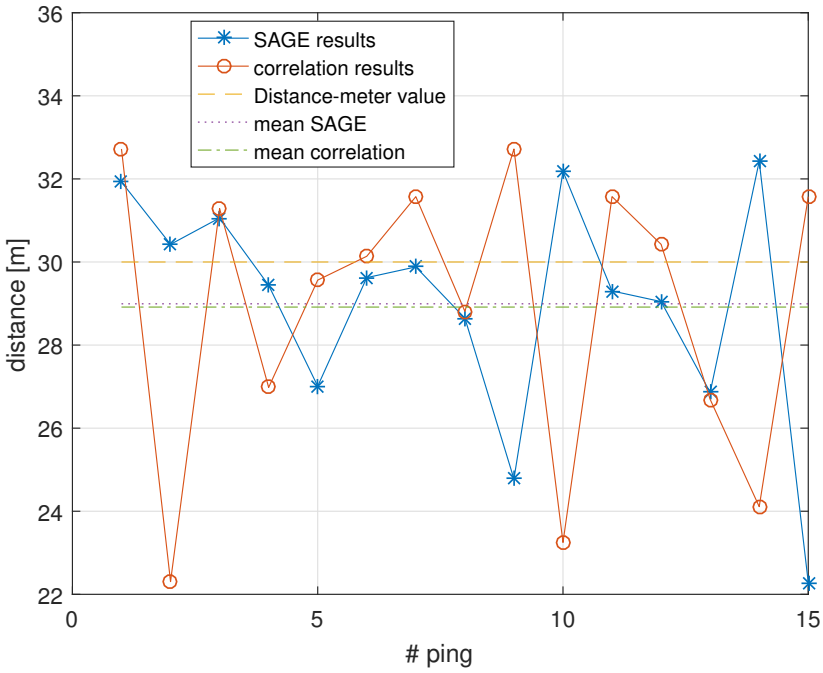

Fig. 5.73 Distance estimates using SAGE and the correlator, for a 30 m distance between the two antennas.

correlation estimate, instead, the error exceeds 10 m in three measures and the average error is about 6 m.

Fig. 5.72 shows the estimation corresponding to the "ping" transmissions when the two antennas were at distance of 35 m. The SAGE algorithm gives an error greater than 10 m in one case, but the other estimates are close to the correct distance 35 m. Also, the estimate average value is very close to 35 m and the error is below 1 m. The correlation estimate error never exceeds 5 m, but the mean value is slightly worse than the one obtained with SAGE. The improved precision of the correlation method in this case is probably due to the strong line of sight component.

Fig. 5.73 shows the distance estimation corresponding to the "ping" transmissions when the two antennas were at a distance of 30 m. In this case, the error with the SAGE algorithm is always below 8 m, and the average error is around 1 m. The same happens for the correlation estimation, and in particular the average error is close to that one obtained with SAGE. Also in this case, we can assume that the strong line of sight component probably increases the accuracy of the correlation method.

Comparing these experimental results with the simulation results, we can say that simulations and experiments give consistent results. Indeed, the experimental errors are compatible with the errors obtained in simulations.

5.8 Conclusions

A new method for the estimation of TOA using the uplink DM-RS instead of the SRS is proposed. In particular, the idea is to use a simple ping uplink transmission to estimate the TOA, since this occupies a small portion of the bandwidth. This method can easily extend to any data transmission in uplink, giving the opportunity to estimate UE position each time some data is transmitted. To demonstrate the feasibility of the method we have compared different algorithms for TOA estimation. Initially, we propose a novel initialization method for the SAGE algorithm. We demonstrate by means of extensive simulations that the proposed initialization method provides better performance compared to the non-coherent accumulation method proposed in [7], when uplink data transmissions is considered. Then we show, by means of extensive simulations, that, when more sophisticated channel models like EPA, EVA and ETU models are considered in uplink transmission, the SAGE algorithm with our initialization method performs better then the correlation based method and the IAA-APES algorithm. We have to mention, however, that IAA-APES seems to be more reliable then SAGE when low SNR is considered. From these extensive simulations we can conclude that the SAGE algorithm with our proposed initialization outperforms the other algorithm when a real DM-RS transmission pattern is used. In particular the results are similar to those obtained with a large bandwidth occupation. Then, we have demonstrated by means of experimental results that, using a simple "ping" uplink transmission, it is possible to obtain a good TOA estimations. Indeed we estimate the distance between two antennas through TDOA estimation exploiting real LTE uplink DM-RS signals and the SAGE algorithm. We obtain average errors between 1 m and 2 m in different experiment. The benefit of the proposed method is that position can be estimated each time any data is transmitted, without relying on the SRS signal, which in most cases is never transmitted or is transmitted rarely. In this chapter we point out that a reliable positioning opportunistic system, with the support of the eNodeB, can be implemented using the DM-RS instead of the SRS and that the results are comparable to the one obtained in full band transmission scenario, which can be seen as a bound for delay estimation performance.

Chapter 6

AOA and TOA estimation using LTE signals.

6.1 Introduction

The estimation of the angle of arrival (AOA) that we will analyze in the following continues what has been shown in Chapter 5. Indeed, we can assume a similar scenario where multiple eNodeBs, or alternatively multiple LMUs instructed by the reference eNodeB, can measure the DM-RS and estimate both the angle of arrival and the time of arrival (TOA). Then, hybrid positioning techniques that exploit AOA and TOA can be used to detect the UE position. In this chapter, we also consider a dual scenario where the AOA and TDOA measurements are made at the UE, using downlink reference signals coming from multiple eNodeB. In particular, the downlink cell specific reference signal (CRS) can be exploited for this purpose. Indeed, as we will see in the following sections, AOA estimation has a weak dependence on the type of transmission used, whatever it is downlink or uplink. We can therefore assume that the same performance obtained with downlink transmissions can be also obtained with uplink transmissions, which we have focused on so far. We note that this is not the case of TOA, since TOA estimation performance is strictly related to the occupied bandwidth, which is typically different for downlink and uplink transmissions.

This chapter focuses on AOA estimation. In particular, AOA estimates obtained with the IAA-APES algorithm are compared with SAGE AOA estimates, where SAGE is set for joint AOA, TOA and Doppler estimation. As mentioned before, IAA-APES

can not be used for joint AOA and TOA estimation, because of the problems related to the high memory consumption.

In the first part of this Chapter we present simulations comparing the AOA performance with SAGE and IAA-APES in the three different scenarios defined in the previous chapter. Moreover, we verify that the AOA estimation is not really influenced by the particular type of transmission used, downlink or uplink. Once established that the estimation performance does not depend on the type of transmission, in the second part we perform real world experimental results using downlink signals. In particular, we made experiments inside an anechoic chamber and the choice of using downlink signal was due to the limitations of the available instrumentation. Indeed, we did not have any possibility to transmit LTE uplink signals with an LTE module inside the chamber. This is because, in order to force the LTE module to transmit an uplink signal, we need a connection with the eNodeB, which is not reachable from the anechoic chamber. On the other hand, the use of the chamber was necessary to properly set-up an environment with correct AOA and TDOA references.

6.2 Simulation set-up

This section presents the simulation set-up used to evaluate the AOA estimation performance of SAGE with 3D initialization (see Section 5.4) and the IAA-APES algorithm in different scenarios. Since SAGE in this case is set to estimate the delay, the Doppler and the angle, for completeness we show the SAGE performance also in delay and Doppler estimation. The same SAGE settings are used in the experiment in the anechoic chamber, described in in Section 6.4.

The simulations use the same set-up described in Section 5.5, and the block diagram of the setup is the same showed in Figure 5.3. In the simulations, only four antennas are considered ($M = 4$), to match the uniform linear array (ULA) with 4 antennas that we had available for the anechoic chamber experiment (Section 6.4). We evaluate the root mean square error (RMSEE) performance in the three scenarios described in Section 5.5, namely, the full band scenario, the simulated ping scenario and the real ping scenario.

The simulation objective is to test the ability of SAGE and IAA-APES to separate close paths in the angle domain. So, similarly to what we did in Section 5.5, for each scenario we set the SNR to 10 dB and we simulate three paths, where the delays are set to $\tau_1 = 15$ ns, $\tau_2 = 65$ ns and $\tau_3 = 115$ ns, the Doppler are generated randomly

Parameters	τ_l [ns]	$\nu_{l,max}$ [Hz]	ϕ_l [°]	$\lvert\alpha_l\rvert^2$ [dB]
Paths				
1	15	70	0	0
2	65	70	$\Delta\phi$	0
3	115	70	$-\Delta\phi$	0

Table 6.1 Parameter used in simulations for AOA estimation

with uniform values between -70 Hz and 70 Hz, and the angles are set to

$$\begin{aligned} \phi_1 &= 0° \\ \phi_2 &= \phi_1 + \Delta\phi \\ \phi_3 &= \phi_1 - \Delta\phi \end{aligned} \tag{6.1}$$

The modulus of the complex gain α_l is equal for all the three paths, while the phase for each path is generated randomly, i.e., $\alpha_l = |\alpha_l| e^{j\varphi}$ with φ uniform in $[0, 2\pi]$. We simulate the transmission of 25 consecutive subframes, which are approximately the number of subframes occupied by a ping. For each scenario, we vary $\Delta\phi$ from 1° to 35° with step 1°, and we perform 100 different channel realizations, changing the seed of the random number generator. Table 6.1 summarizes the adopted parameters. We also assume that the number of paths is known, in order to have a better perspective on the algorithms performance in AOA and TOA estimations.

The first scenario, in particular, represents a transmission that occupies the entire bandwidth: this can mimic the case of a downlink transmission. Indeed, the only difference between a downlink CRS transmission and an uplink transmission in the full band scenario, is represented by the subcarrier spacing Δf_k. In particular, Δf_k is 15 kHz for the uplink transmission, while in downlink, using one antenna port, it is 90 kHz. Moreover, with two antenna ports, we can aggregate the estimated CFRs and obtain Δf_k equal to 45 kHz.

6.3 Simulation Results

Figure 6.1 shows the RMSEE, in logarithmic scale, of the three path delays obtained with SAGE, in the three considered scenarios. We can notice that the RMSEE of the delays for all the paths in all scenarios is always below 20 ns. In particular, when the distance in angle domain between paths exceeds 5°, the RMSEE for all the paths in all scenarios is below 1 ns, i.e., it is below one meter accuracy. The results obtained

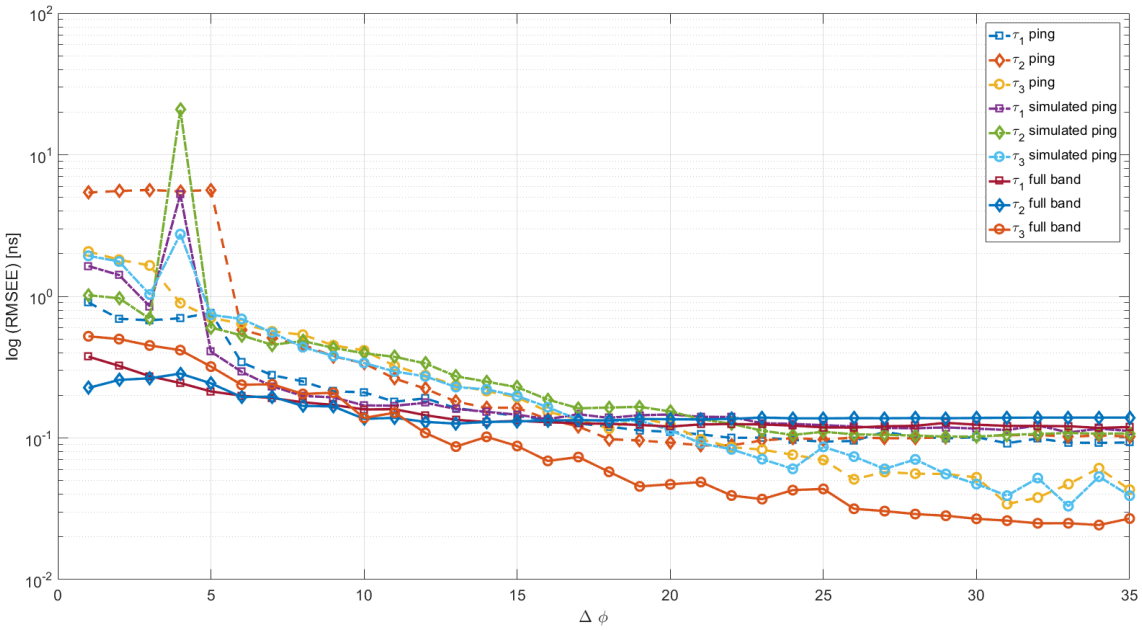

Fig. 6.1 RMSEE of the three path delays considering the full band, simulated ping and real ping scenarios, using SAGE with 3D initial conditions.

in this case are much better that the results obtained in Chapter 5, because in this case we are performing a joint estimation in three domains (delay, angle, and Doppler). Indeed, if two paths are not separable in two domains, they can be separable in the third, and the additional information can be exploited by SAGE in order to separate and properly estimate the two paths.

Figure 6.2 shows the RMSEE of the Doppler relative to all the three paths in logarithmic scale obtained with SAGE, in the three considered scenarios. We can notice that the RMSEE of the Doppler for all the paths in all scenarios is always below 20 Hz. In particular, when the angle separation between paths exceeds 11° approximately, the RMSEE for all the paths in all scenarios is below 1 Hz. Also in this case, the high accuracy can be attributed to the addition of a further dimension.

Figure 6.3 shows the RMSEE of the three paths angle of arrival in logarithmic scale obtained with SAGE and IAA-APES, in the full band scenario. Considering first the results for IAA-APES, we do not show the first path angle RMSEE between 1° and 6° because the error is zero. This is due to the fact that the first path angle (ϕ_1) is equal to zero, and zero is also a point of the grid used in the algorithm. Between 1° and 13°, only one path is estimated and the error increases with $\Delta\phi$. For greater $\Delta\phi$, IAA-APES starts to estimate a second path and the error stabilize. Starting at $\Delta\phi = 26°$, also the third path could be estimated. Around this point, the second path

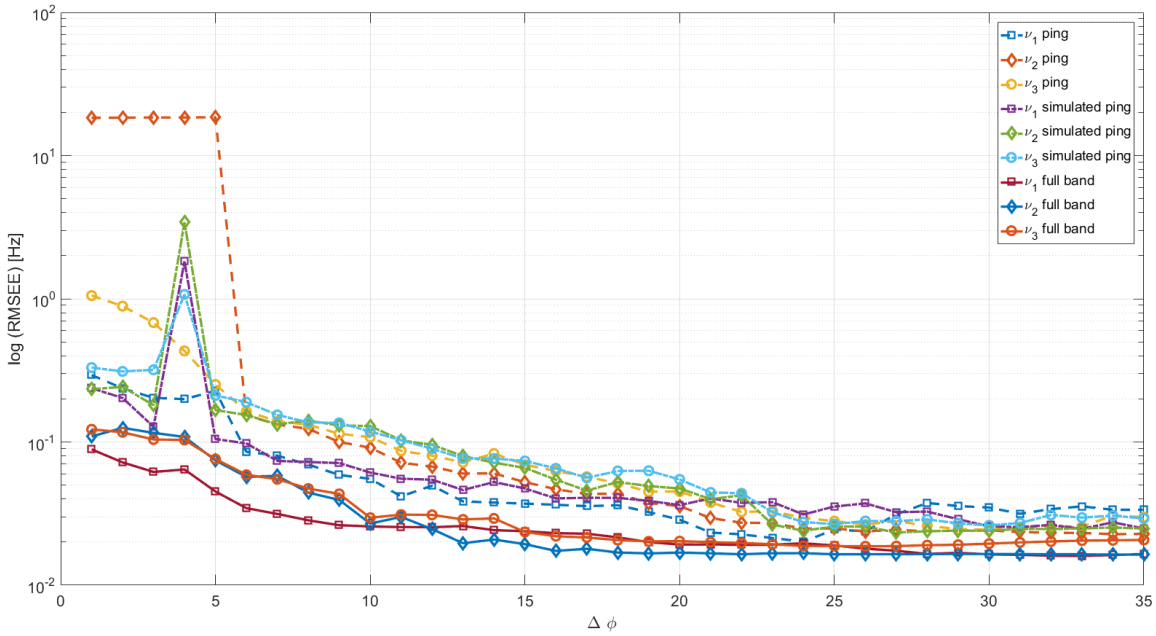

Fig. 6.2 RMSEE of the three path Doppler considering the full band, simulated ping and real ping scenarios, using SAGE with 3D initial conditions.

RMSEE decreases while the third path RMSEE has a relatively higher value. Note that, when the third path starts to be detected, it is not always estimated in all the 100 different channel realizations. When we calculate the RMSEE for the third path, we do not consider the realizations where the third path is not estimated. Furthermore, the error is higher because in this scenario ($\Delta\phi = 26°$) represent the point where the algorithm sometimes is able to distinguish three paths and sometimes is able to distinguish only two paths. Above an angle separation of 28°, the three paths are always estimated and the error is consistently below 0.3°. While the RMSEE obtained with IAA-APES is between 0.01° and 0.1°, we can see that with SAGE the error is always below 0.001° for all the three paths, which is a very precise estimation.

Figure 6.4 shows the RMSEE of the three paths angle of arrival in logarithmic scale obtained with SAGE and IAA-APES, in the simulated ping scenario. Considering the IAA-APES results, we can notice that the curves have a behavior similar to the one seen in the full band scenario (Figure 6.3), and that the behaviour obtained around $\Delta\phi = 21°$, is due to the same reasons explained before. In this scenario, the IAA-APES angle RMSEE is always contained below 1° for all the paths and for the entire $\Delta\phi$ range. SAGE in this case presents a slightly higher RMSEE compared to the full band scenario, and the RMSEE is always below 0.01° when $\Delta\phi$ is low, and reaches values below 0.001° when $\Delta\phi$ is greater than approximately 23°.

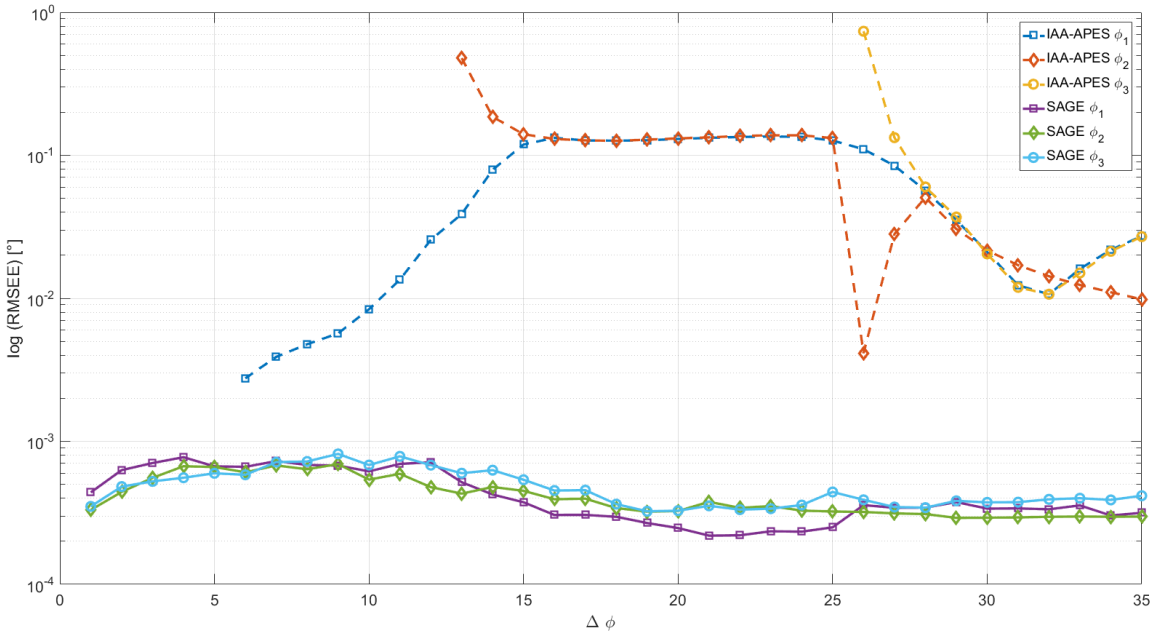

Fig. 6.3 RMSEE of the angle. Comparison between SAGE and IAA-APES in the full band scenario.

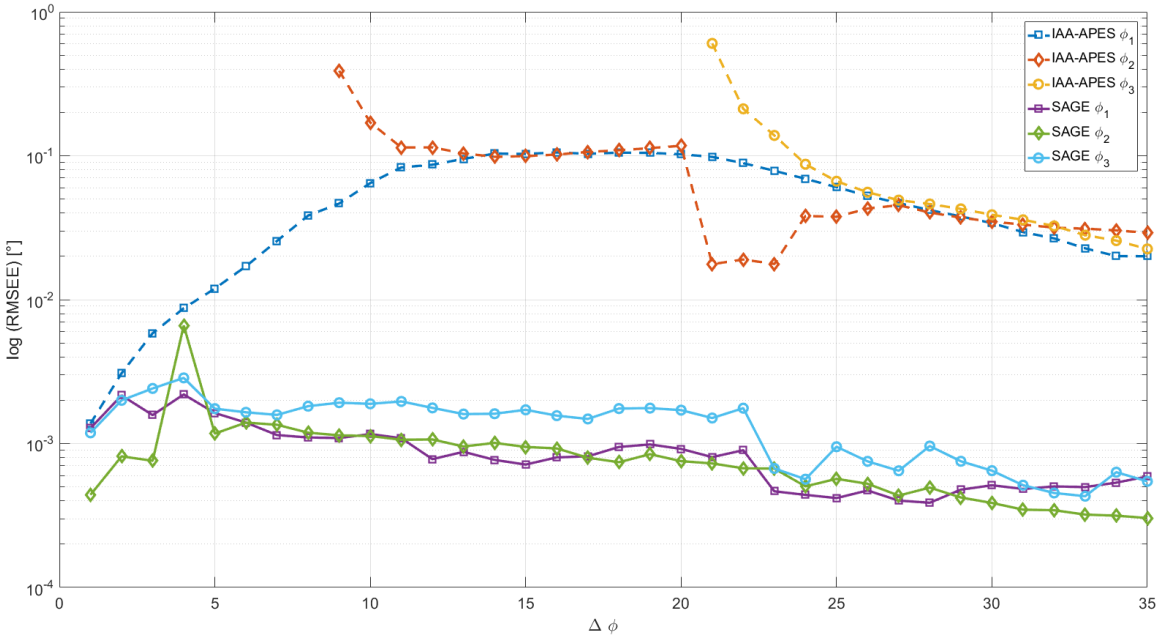

Fig. 6.4 RMSEE of the angle. Comparison between SAGE and IAA-APES in the simulated ping scenario

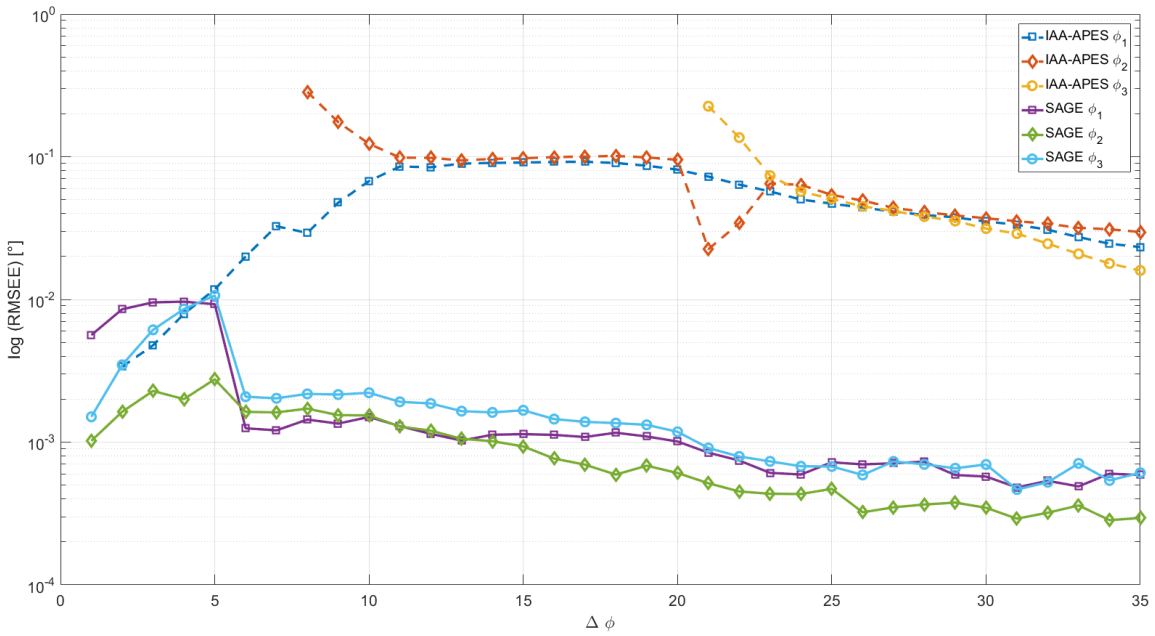

Fig. 6.5 RMSEE of the angle. Comparison between SAGE and IAA-APES in the real ping scenario

Figure 6.5 shows the RMSEE of the three paths AOA in logarithmic scale obtained with SAGE and IAA-APES, in the real ping scenario. The behaviour of the IAA-APES curves can be explained as before. We obtain an RMSEEs always below 1°, while with SAGE the error is approximately below 0.01° for low values of $\Delta\phi$ and below 0.001° when $\Delta\phi$ exceeds 23°.

The results obtained in this simulations are interesting because they show that the angle estimation is in general very precise, with a weak dependence on the particular scenario used. This probably can be explained considering Equation 4.89. Indeed, we can notice that the estimation of the angle ϕ does not depend on either the bandwidth or the time window considered. The CRLB relative to the angle estimation has a dependence on the AOA and on the number of antenna elements M, which are equal in all the scenarios. Moreover, the CRLB depends also on the number of observations available, due to its dependence from $\gamma_0 = N_t N_{sc} M \gamma_m$. So, in AOA estimation, the full band scenario represent a performance lower bound, only because the number of observations is higher compared to the other scenarios, and not because there is a higher occupation of the bandwidth. This explains why in this scenario the angle RMSEE is just slightly better compared with the RMSEE of the other scenarios.

Based on these observations, if we consider a downlink AOA estimation (based for example on the CRS, which occupies the overall bandwidth), we can expect an

estimation performance similar to that obtainable with an uplink AOA transmission based on DM-RS.

In the following section, due to our set-up, we will describe the experimental results obtained inside the anechoic chamber and using downlink transmission. We can expect that the following downlink AOA estimation performance can also be obtained in uplink exploiting the DM-RS.

6.4 Experimental set up for the Anechoic Chamber

In this section, we present the set up used during the experiments made in the anechoic chamber of the University of Udine. Experimental results are obtained by measuring the TOA and AOA exploiting the downlink CRS (see Section 3.5.1). In particular, using the available equipment, we try to simulate some real multipath inside the anechoic chamber. The idea is to use an LTE downlink signal generator connected to different antennas through a splitter and cables with different length. In this way, the different lengths of the cables produce different delays for the signals transmitted by the different antennas. Moreover, the different cable length and the splitter provide different transmission power at the antennas. Finally, the different antenna positions inside the anechoic chamber correspond to different angles of arrival. This set-up can be seen as a multipath scenario with different τ_l, ϕ_l and complex gains α_l.

In the experiment, we use a ULA consisting of four antennas ($M = 4$), with the distance between antenna elements set to $\lambda/2$. Before starting the experiments, we align the first antenna perpendicularly to the antenna array, i.e., with an AOA equal to 0°. This antenna corresponds to the first path. We do not add a delay to this antenna, using cables, so it can be considered as a reference antenna that corresponds to the LOS component. In the following, we refer to the angle between the reference antenna and the ULA as ϕ_1 and as τ_1 to the TOA. Then we evaluate three different scenarios with different number of antennas. Figure 6.6 shows a sketch of the first scenario, where two antennas are used and the second antenna is connected to a cable having length 50 m. Measuring the distances a, b, and c in the figure using a laser distance-meter, with simple trigonometric formulas we can calculate the relative angle ϕ_2. Since we previously aligned the first antenna at 0°, the angle ϕ_2 represents also the angle of arrival of the second path that the ULA sees. Figure 6.7 shows a sketch of the second scenario, where three antennas are used. In this case the antenna representing the second path is connected to a cable having length 50 m, while the antenna representing the third path is connected to a cable with length 100 m. Using the same procedure explained for the first scenario, we can calculate the angles that the ULA sees, measuring the sides of the two triangles formed by the two antennas with the reference antenna. In the third scenario, showed in Figure 6.7, we used four antennas. In particular, the antennas named in the figure as Tx_3 and Tx_4 were connected to a cable with length 50 m, while the antenna named Tx_2 was connected to a cable with length 100 m. In this scenario, we wanted to simulate a situation where two paths arriving at the ULA are close in the delay domain but can be separated in angle domain because they arrive at the ULA with different AOAs. Since we know from the

Parameters	ϕ_1 [°]	$\Delta\tau_{1,2}$ [ns]	ϕ_2 [°]	$\Delta\tau_{1,3}$ [ns]	ϕ_3 [°]	$\Delta\tau_{1,4}$ [ns]	ϕ_4 [°]
First Scenario	0	193	-33	/	/	/	/
Second Scenario	0	193	-33	387	44	/	/
Third Scenario	0	388	-43	191	44	195	-12

Table 6.2 Table of the parameters used in the anechoic chamber scenarios.

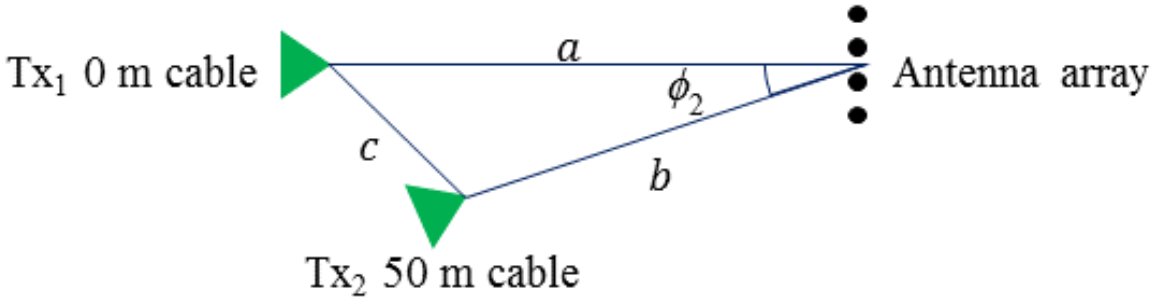

Fig. 6.6 Sketch representing the set up of the first scenario in the anechoic chamber

data-sheet of the cables [55] the introduced delays, we can calculate the difference in delay between the reference antenna and the other antennas. All the parameters used in the three scenarios are summarized in Table 6.2, where $\Delta\tau_{i,j}$ is the difference in TOA calculated as $\tau_j - \tau_i$ (we also have considered the propagation time in the air to calculate this difference).

To acquire the signal, the ULA was connected to a USRP with four receiving channels. We use an external rubidium clock in order to have a better time reference. Then, the local oscillator of one channel is shared with the other channels. In this way, the phase between channels remains constant during the measurements. In order to know the phase misalignment among the channels, we did some calibration. The LTE downlink signal generator was set to transmit a radio frame, i.e., 10 subframes of 1 ms duration. This radio frame (10 ms) was repeated in loop and the USRP used to acquire 100 ms of the downlink transmission. as part of the downlink transmission, the generator transmits also the CRS. Knowing the CRS specifications, we can perform the estimation of the CFR bins, which follow the pattern showed in Figure 3.6. Then, the estimated CFR is used as input of the SAGE and IAA-APES algorithms. In particular, the LTE signal generator used a carrier frequency $f_c = 1.85$ GHz and was set to use a bandwidth of $N_{sc} = 1200$ subcarriers with two antenna ports. This means that for each CRS symbol, 400 bins of the CFR with a spacing of 45 kHz were available. This

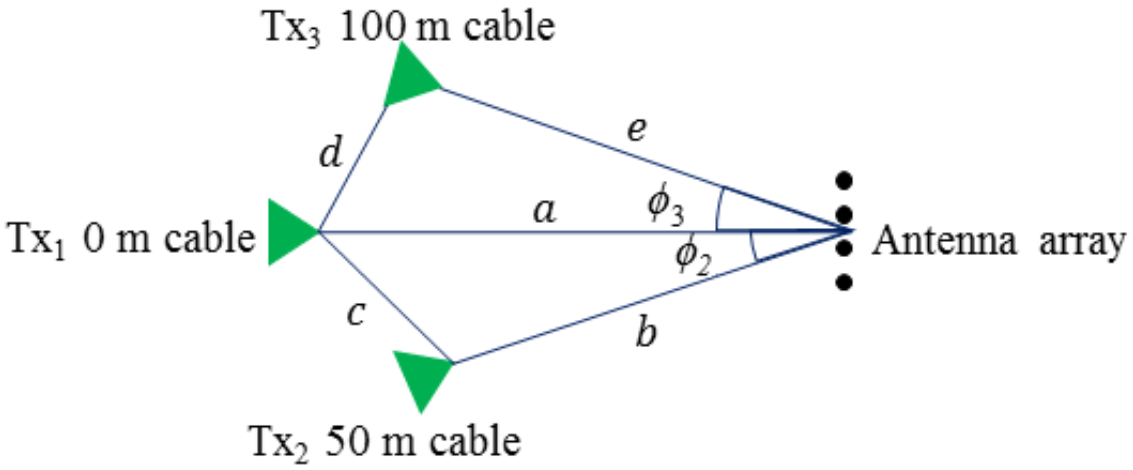

Fig. 6.7 Sketch representing the set up of the second scenario in the anechoic chamber

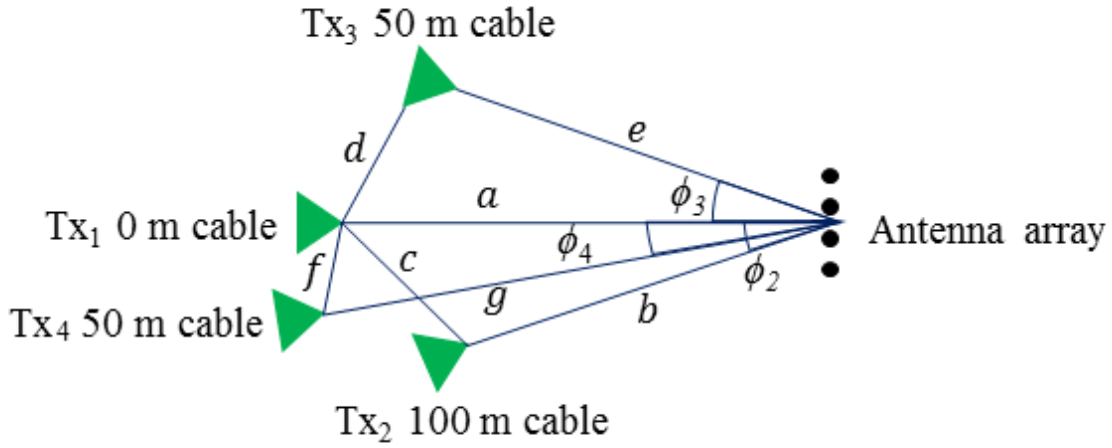

Fig. 6.8 Sketch representing the set up of the third scenario in the anechoic chamber

Fig. 6.9 Picture representing the set up of the second scenario in the Anechoic chamber

is because we can exploit the two antenna ports CRSs, which are shifted by 45 kHz in frequency.

Figure 6.9 shows the actual measurement set up used in the anechoic chamber in the second scenario.

6.5 Results for the Anechoic Chamber Experiments

In this section we present the results obtained in real experiments made in the anechoic chamber. In particular, the ULA was placed on the top of a rotating platform. This allows to evaluate the performance for different angles of arrival in each scenario. The platform was rotated with angles ϑ between -45° to 45° with step $\Delta\vartheta = 15°$. With this choice, all paths in the experiments have an AOA inside the $[-90° \ +90°]$ range.

For each scenario and for each value of ϑ, we performed two 100 ms acquisitions and we calculate the CFR estimates. In this way, we obtain a time-frequency grid with $N_{sc} = 1200$ subcarriers and $N_t = 1400$ snapshots. This is because the CRS is repeated at the first and fifth symbol of each slot (Figure 3.6), so we construct a regular grid filled with zeros where no information about the CFR is available. Then, we subdivide the 100 ms duration in subsets of 5 ms duration and we perform the parameter estimation for each subset using SAGE and IAA-APES. In other words, we had in total 40 estimates for each value of ϑ in each scenario. The RMSEE of the AOA is calculated as a function of the rotation of the platform, considering the reference values in Table 6.2.

Since SAGE was set to estimate also the delay and the Doppler, we also show the SAGE RMSEE of the difference in delays between paths, using as reference the values in Table 6.2. Since we do not have any reference for the Doppler (the values ν_l include also the frequency offset between transmitter and receiver) we omit the results. Furthermore, since we know the number of antennas inside the anechoic chamber and we can assume that inside the chamber there is no external interference, we assume to know the number of path L in order to perform the estimation. This means that each antenna inside the chamber represents a path. Figure 6.10 shows the RMSEE of the two paths angle of arrival obtained with SAGE and IAA-APES, in the first scenario. The RMSEE of the AOAs considering IAA-APES is always below 5°. In particular, when the platform is rotated up to -45°, IAA-APES is not able to recognise the second AOA. This is because the value of ϕ_2 is -78° in this case and, as explained in Section 4.3.3, when the angle approaches -90° or 90°, the beam pattern becomes larger: this probably causes IAA-APES not to resolve the second path. SAGE has an RMSEE always below 2.2° and in most of the cases the RMSEE is about 1°.

Figure 6.11 shows the RMSEE of the delay difference obtained with SAGE, in the first scenario. In this case, the RMSEE of the difference of the two paths is between 8.6 ns and 10 ns, which corresponds to an error in pseudorange of about 3 m.

Figure 6.12 and Figure 6.13 show the RMSEE of the three paths angle of arrival obtained with SAGE and IAA-APES, in the second scenario. In particular Figure 6.13

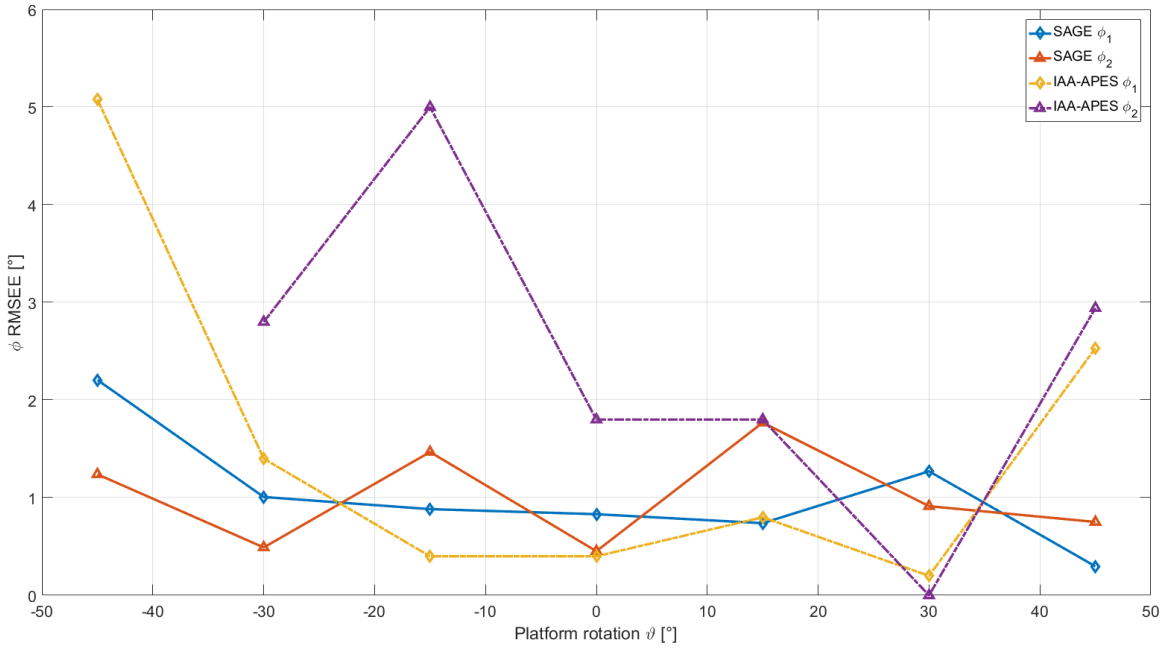

Fig. 6.10 RMSEE of the angle of arrival. Comparison of the results obtained with SAGE and IAA-APES in the first scenario used in the anechoic chamber.

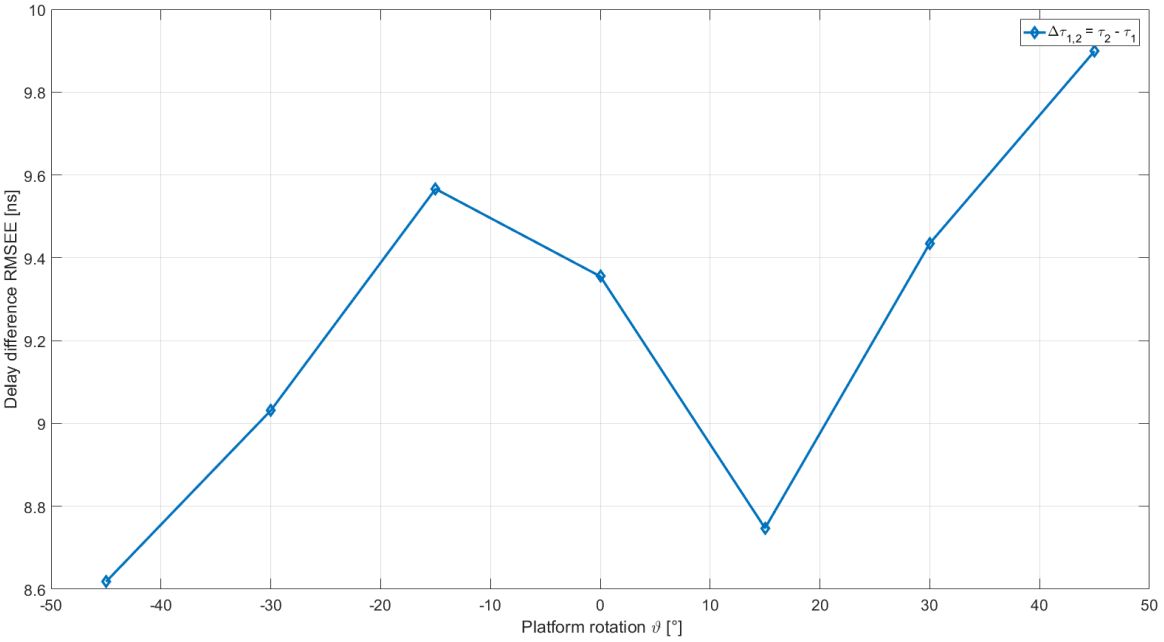

Fig. 6.11 RMSEE of the delays difference. Results obtained with SAGE in the first scenario used in the anechoic chamber.

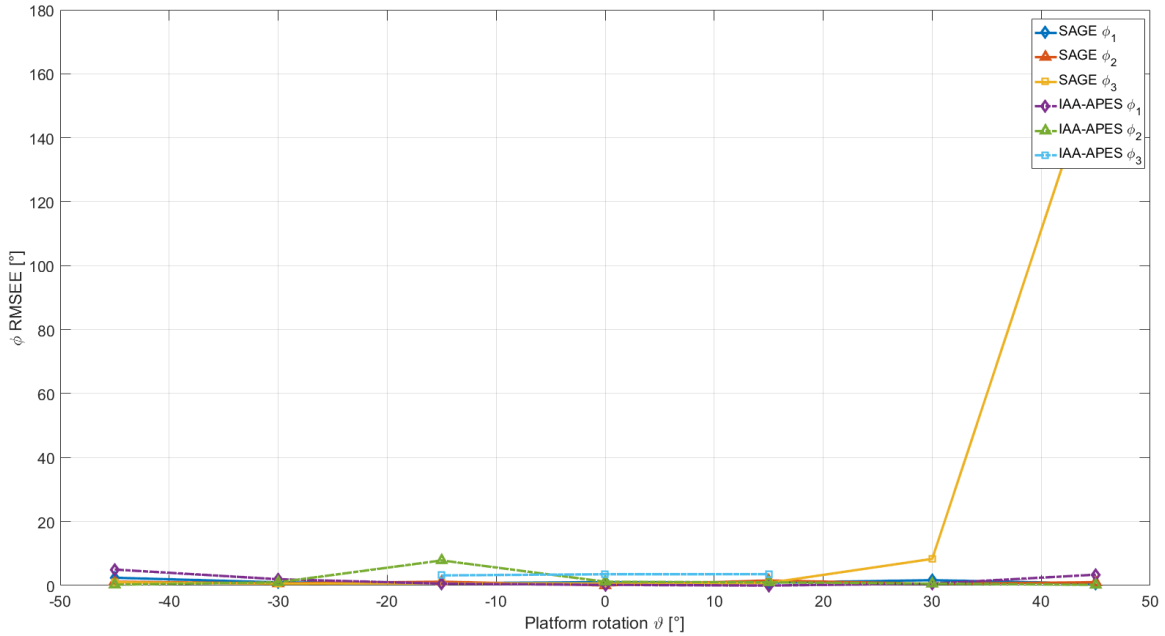

Fig. 6.12 RMSEE of the angle of arrival. Comparison of the results obtained with SAGE and IAA-APES in the second scenario used in the anechoic chamber.

shows a detail of Figure 6.12. The RMSEE of IAA-APES for the first AOA is similar to the AOA RMSEE obtained in the first scenario. The RMSEE is also similar for the second AOA estimation, with an error of about 8° only for a 15° rotation ϑ. IAA-APES is able to distinguish the third AOA only when ϑ is between -15° and 15°. The first thing one notices watching the SAGE performance is the extremely large RMSEE obtained for the third AOA. The large error at 45° is due to the fact that for this ϑ the third AOA is $\phi_3 = 89°$. This error is due by the combination of two factors, the symmetry of the beam pattern (Section 4.3.3) and the high variance of AOA estimation when the angle approaches -90° or 90° (Equation (4.89). In the other cases SAGE shows RMSEE always below 2.5° for the three AOA.

Figure 6.14 shows the RMSEE of the delays differences obtained with SAGE, in the second scenario. In this case two delays differences can be calculated and, similarly to the first scenario, the error is always below 10 ns. In particular the difference between the second and the first delay is about 9 ns, while the delay difference between the third and first delay starts approximately at 2 ns for $\vartheta = -45°$, approaches 5 ns for $\vartheta = 0°$ and falls below 1 ns for $\vartheta = 45°$. Generally the error in pseudorange for the first difference is around 2.7 m and for the second difference is on average around 1 m.

Figure 6.15 and Figure 6.16 show the RMSEE of the four paths angle of arrival obtained with SAGE and IAA-APES, in the third scenario. In particular Figure 6.13 is

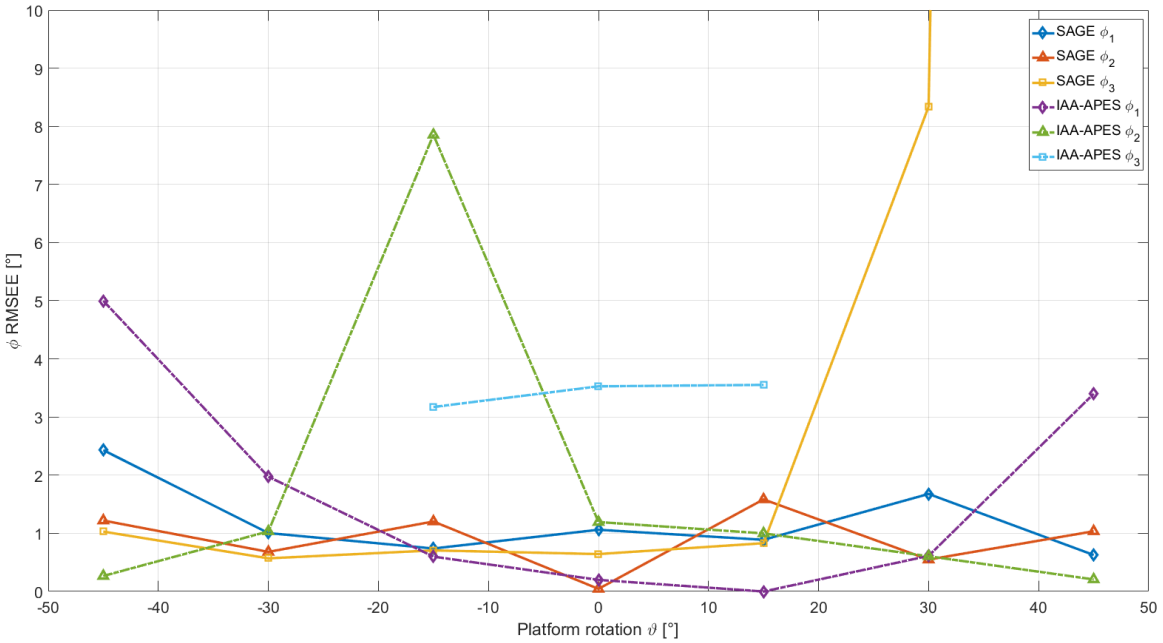

Fig. 6.13 RMSEE of the angle of arrival. Inset of the comparison between SAGE and IAA-APES in the second scenario used in the anechoic chamber.

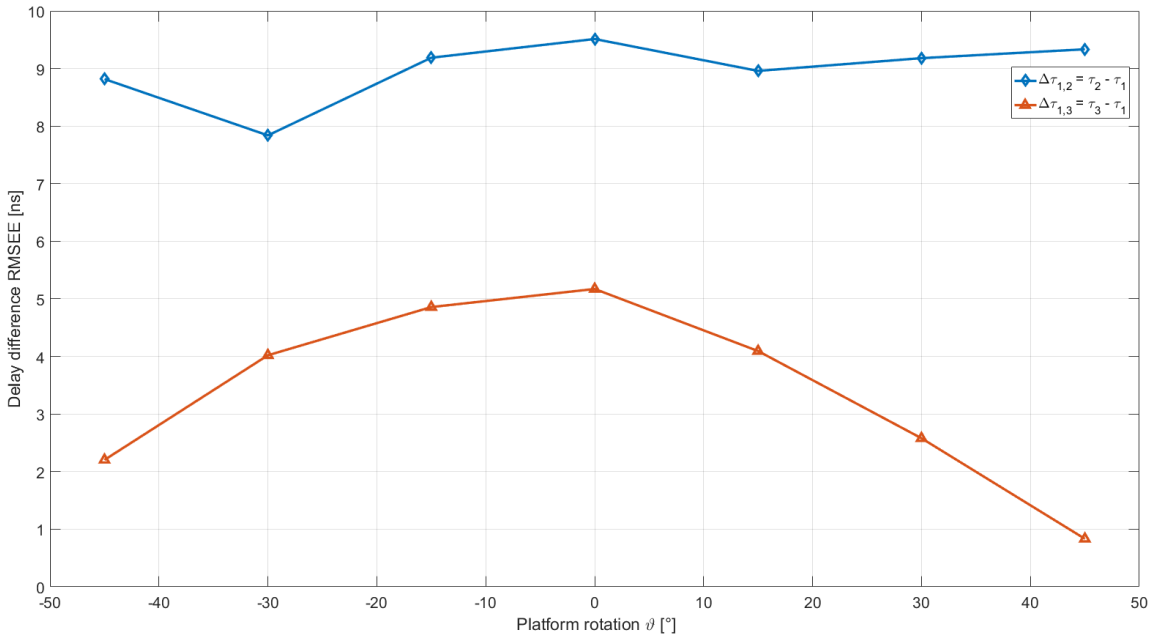

Fig. 6.14 RMSEE of the delays difference. Results obtained with SAGE in the second scenario used in the anechoic chamber.

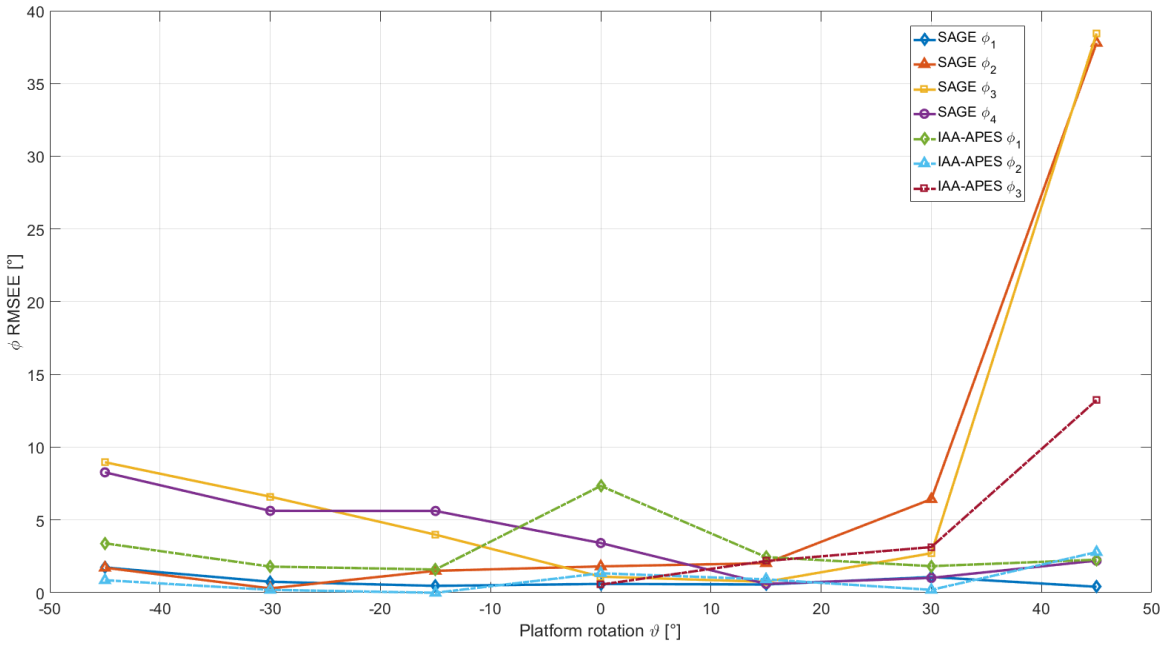

Fig. 6.15 RMSEE of the angle of arrival. Comparison of the results obtained with SAGE and IAA-APES in the third scenario used in the anechoic chamber.

an inset of Figure 6.12. The RMSEE of IAA-APES for the first AOA is approximately between 2° and 7.5°. This relatively high error is probably due to the proximity with the fourth AOA (the difference in angle is only 12°), which is never estimated. Furthermore, with IAA-APES the second AOA has an RMSEE always below 2°, while the third AOA is estimated only for ϑ greater than 0°. The RMSEE of ϕ_3 reaches 14° when ϕ_3 approaches 90°. SAGE shows a high RMSEE when ϕ_3 approaches 90°, but in this scenario also the RMSEE of ϕ_2 is influenced by ϕ_3, when it approaches 90°. This is probably due to the incorrect cancellation that SAGE performs during the E-step, which influences the estimation of the second path (this phenomenon was explained also in Section 5.4). In general, the RMSEE of the first AOA obtained with SAGE is always below 2°, while the other three AOAs (apart from the previous particular case) are always below 9°. In general, the relatively high RMSEE in this scenario can be explained by the fact that with only four antennas the beam pattern presents relatively large main lobes and sidelobes. The effect is particularly enhanced when the lobes relative to AOA with higher power approaches the values -90° or 90°.

Figure 6.17 shows the RMSEE of the delays differences obtained with SAGE, in the third scenario. In this case three delays differences can be calculates and the error is always below 20 ns. In particular, the RMSEE of the difference between the second and the first delay is about 12 ns for ϑ between -45° and 30°, while for $\vartheta = 45°$ the

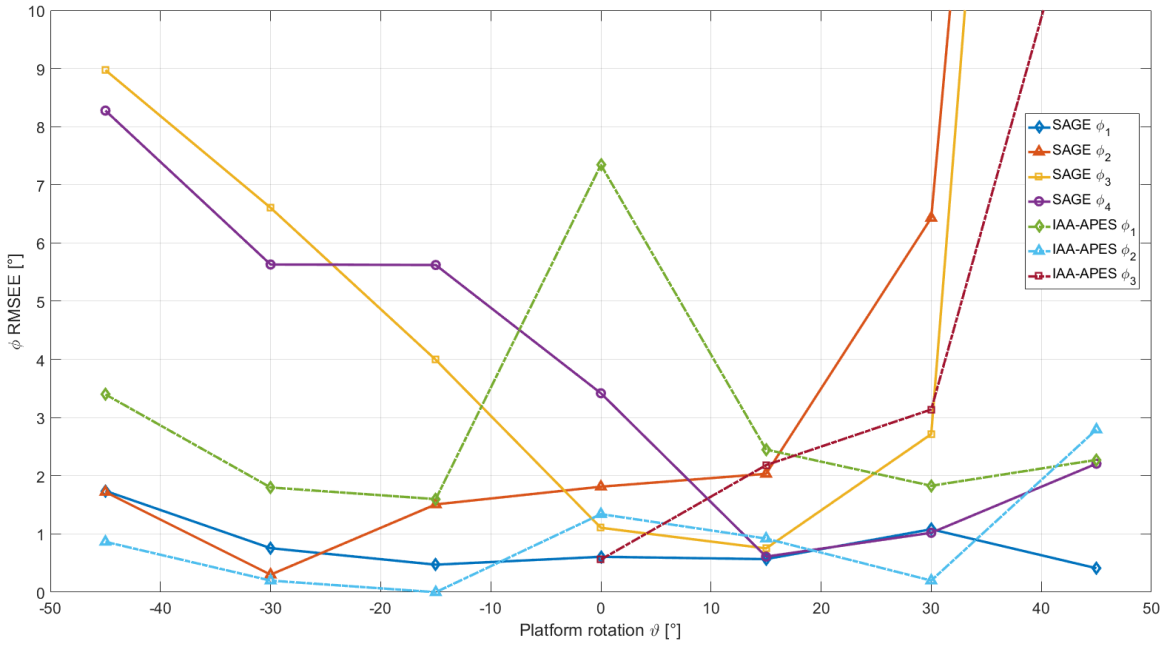

Fig. 6.16 RMSEE of the angle of arrival. Inset of the comparison between SAGE and IAA-APES in the second scenario used in the anechoic chamber.

RMSEE is about 20 ns. Therefore, the first delay difference has a maximum RMSEE in pseudorange of about 6 m. The RMSEE of the difference between the third and the first delay is approximately 2 ns for $\vartheta = -45°$, it approaches 10 ns for ϑ around 15°-30° and falls around 8 ns for $\vartheta = 45°$. This delay difference shows a maximum RMSEE of about 3 m in pseudorange. The RMSEE of the difference between the fourth and the first delay start is below 2.5 ns for all values of ϑ, apart when $\vartheta = 45$ where the RMSEE is about 6 ns. The corresponding maximum RMSEE is around 1.8 m in pseudorange.

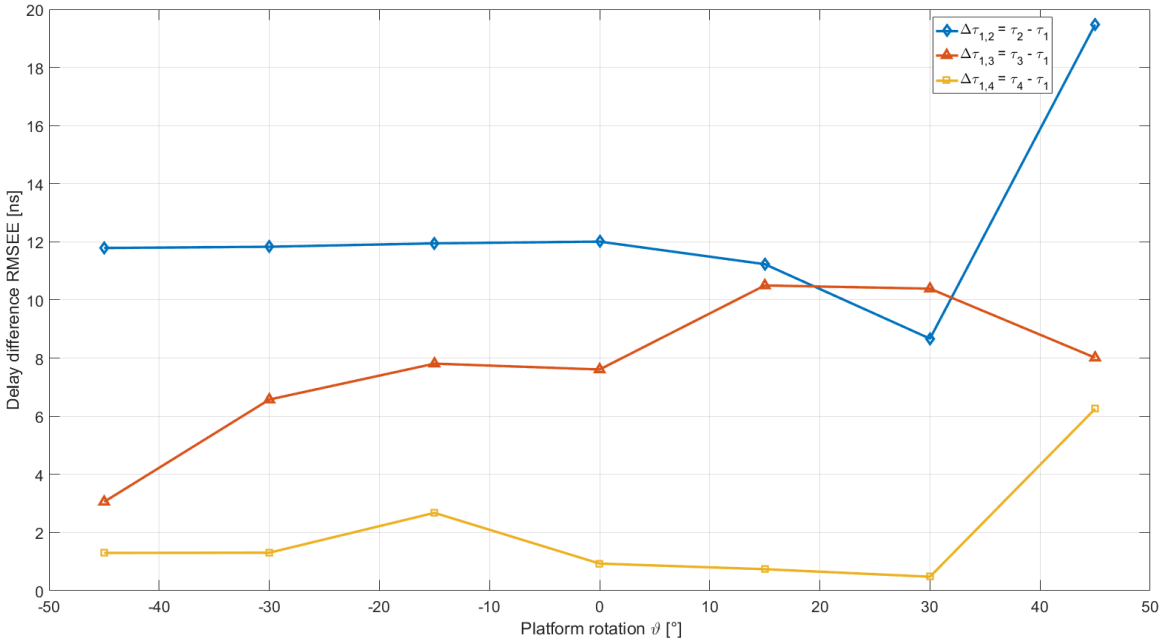

Fig. 6.17 RMSEE of the delays difference. Results obtained with SAGE in the second scenario used in the anechoic chamber.

6.6 Conclusion

In the first part of the chapter we demonstrate by means of simulations that the AOA estimation does not depend on the particular transmission used, whatever it is downlink or uplink. Indeed, we saw that missing data in the time frequency pattern do not have a real impact on the AOA estimation. Note that this is not true when TOA estimation is considered, as showed in Chapter 5.

In the simulations, we considered one scenario that can be seen similar to a downlink scenario and two scenarios that simulate uplink transmissions. The RMSEE obtained in the simulation is very low, IAA-APES shows a RMSEE of the AOA always below 1°, while SAGE has RMSEE values always below 0.01°. For SAGE, we evaluate also the delay and the Doppler estimates and we obtain respectively an RMSEE below 1 ns and an RMSEE below 1 Hz, when the paths was well separated in angle domain. From these results we can conclude that the AOA estimation does not depend on uplink or downlink transmission. Thus, for simplicity of implementation we have considered downlink transmission in a real experiment in the anechoic chamber.

In the anechoic chamber experiment, we use a method similar to the one proposed in Chapter 5 for uplink transmission to perform some estimations of the parameters. This method consists in using the CRS to estimate the CFR and subsequently use the CFR bins as input for the SAGE and IAA-APES algorithms. In particular, SAGE was set to estimate also the delay.

The experimental results show good performance in TOA estimations with SAGE, and indeed the error in pseudorange is always below 6 m in all the experimental scenarios, and in most cases it is around 2-3 m. The IAA-APES AOA estimations show a general difficulty with three or four paths but, in general the error in the estimated paths is always below 10°, apart in one case with four paths where the error is about 12°. This inability of IAA-APES to distinguish more paths is mainly due to the relatively small number of antennas used in the experiment. Note that the number of sources is indeed comparable with the number of antenna elements. The SAGE AOA estimation shows good performance in the two scenarios with two and three paths and the estimation error is always below 2.5°, apart when the AOAs approach 90°. In the four paths scenario, the AOA RMSEE of the first path is always below 2°, while the other three paths have in general errors always below 9°, apart when AOAs approach 90°.

The higher error obtained in the experimental results compared with the simulation results can be due to different reasons. The effect of AOA that are close to -90° or 90° is a known effect, see Section 5.1. Other sources of errors can be due to our equipment,

and in particular the ULA, which is actually a "*homemade*" antenna array, constructed with some commercial cheap omnidirectional antennas. Moreover, the distance between antennas, $\lambda/2$, was determined approximately. Therefore, there may be some mismatch between the model used in the algorithms and the real world situation.

We can conclude that the results are encouraging. In particular using SAGE we can perform a joint AOA, TOA estimation that can be used with hybrid positioning algorithms in order estimate the position of the UE.

Chapter 7

Conclusion

This thesis describes my research work on the estimation of the time of arrival (TOA) and of the angle of arrival (AOA) using 3GPP LTE signals, for both downlink and uplink transmissions, with more focus on uplink signals. The main original contributions are presented in the following.

A new method for the estimation of TOA using the uplink DM-RS instead of the SRS is proposed. In particular, the idea is to use a simple ping uplink transmission to estimate the TOA, since this occupies a small portion of the bandwidth. This method can be easily extended to any data transmission in uplink, giving the opportunity to estimate the UE position each time some data is transmitted. To demonstrate the feasibility of the method, we compared different algorithms for TOA estimation. In order to perform uplink TOA estimation with SAGE, we propose a novel initialization method for the algorithm. We demonstrate by means of extensive simulations that the proposed initialization method provides better performance compared to the non-coherent accumulation method proposed in [7]. Moreover, we performed extensive simulations with more sophisticated channel models in order to prove that the uplink DM-RS can indeed be used for TOA estimation purposes. From the simulations results, we conclude that SAGE outperforms the other algorithms for TOA estimation and uplink transmissions, while it gives similar results in simulations mimicking downlink transmissions. In particular, we observed that SAGE performance is less influenced by the bandwidth occupation of the signals. Then, we demonstrated by means of experimental results that, using a simple "ping" uplink transmission, it is possible to obtain a reasonable TOA estimate, with average errors between 1 m and 2 m in different experiments. The benefit of the proposed method is that position can be estimated each time any data is transmitted, without relying on the SRS signal, which in most cases is never transmitted or is transmitted rarely. The conclusion is that

a reliable positioning opportunistic system, can be implemented using the DM-RS instead of the SRS.

Our second contribution consists of a method to evaluate the AOA of uplink and downlink transmissions. By means of simulations, we demonstrate that the AOA estimate quality is not much influenced by the type of transmission, uplink or downlink. In simulations, we see that SAGE performance is much better than that of IAA-APES. This is because SAGE can jointly exploit different domains, i.e., delay and Doppler.

In the final part of the thesis, we performed some real-world experiments in an anechoic chamber. The results reveal that SAGE provides better performance than IAA-APES for AOA estimation. Moreover, SAGE also provides good TOA estimates. Based on this, we conclude that the proposed SAGE implementation makes it suitable for AOA estimation in uplink and downlink transmissions, and that it can provide joint AOA, TOA estimates to exploit hybrid positioning techniques.

Future work requires, at least, an intensive campaign of measurements in a real-world environment, in order to evaluate all the possible limitations of the proposed approach. A further future topic should be the implementation of an actual position tracking system, based on the estimates provided by the proposed method.

References

[1] E. D. Kaplan and C. J. Hegarty, *Understanding GPS, Principles and Applications*. Artech House, 2006.

[2] S. A. Reza Zekavat and R. Michael Buehrer, *Handbook of Position Location Theory, Practice, and Advances*. Wiley-IEEE Press, 2011.

[3] N. Patwari, J. N. Ash, S. Kyperountas, R. L. Hero III, Alfred O.and Moses, and N. S. Correa, "Locating The Nodes: Cooperative localization in wireless sensor networks," *IEEE Signal Processing Magazine*, vol. 22, pp. 54–69, 2005.

[4] Figueiras, J. and Frattasi, S. , *Mobile Positioning and Tracking. From Conventional to Cooperative Techniques*. Whiley, 2010.

[5] Dardari, D. and Falletti, E. and Luise, M., *Satellite and Terrestrial Radio Positioning Techniques*. Elsevier, 2012.

[6] D. Schneider, "You are here," *IEEE Spectrum*, vol. 50, no. 12, pp. 34–39, December 2013.

[7] B. H. Fleury, M. Tschudin, R. Heddergott, D. Dahlhaus, and K. I. Pedersen, "Channel parameter estimation in mobile radio environments using the SAGE algorithm," *IEEE Journal on Selected Areas in Communications*, vol. 17, pp. 434 – 450, 1999.

[8] 3GPP. https://www.3gpp.org/. [Online Accessed Oct. 31 2019].

[9] S. Frattasi and F. Della Rosa, *Mobile Positioning and Tracking: From Conventional to Cooperative Techniques*. John Wiley & Sons Ltd, 2017.

[10] N. Facchi, F. Gringoli, F. Ricciato, and A. Toma, "Emitter localisation from reception timestamps in asynchronous networks," *Computer Networks*, vol. 88, pp. 202–217, 2015.

[11] S. Fischer, "Observed Time Difference Of Arrival (OTDOA) Positioning in 3GPP LTE." http://www.qualcomm.com/media/documents/files/otdoa-positioning-in-3gpp-lte.pdf, 2014, [Online; accessed 22-August-2019].

[12] K. Ranta-aho and Z. Shen, *LTE - The UMTS Long Term Evolution*. John Wiley & Sons Ltd, 2009, ch. User Equipment Positioning.

[13] *Evolved Universal Terrestrial Radio Access (E-UTRA); LTE Positioning Protocol (LPP)*, https://www.etsi.org/deliver/etsi_ts/136300_136399/136355/15.04.00_60/ts_136355v150400p.pdf, 3GPP Std. TS 36.355, Rev. 15.4.0, 2019, [Online Accessed Oct. 31 2019].

[14] *Evolved Universal Terrestrial Radio Access (E-UTRA); LTE Positioning Protocol A (LPPa)*, https://www.etsi.org/deliver/etsi_ts/136400_136499/136455/15.02.01_60/ts_136455v150201p.pdf, 3GPP Std. TS 36.455, Rev. 15.2.1, 2019, [Online Accessed Oct. 31 2019].

[15] *Evolved Universal Terrestrial Radio Access (E-UTRA); Physical channels and modulation*, https://www.etsi.org/deliver/etsi_ts/136200_136299/136211/15.06.00_60/ts_136211v150600p.pdf, 3GPP Std. TS 36.211, Rev. 15.6.0, 2019, [Online Accessed Oct. 31 2019].

[16] A. Goldsmith, *Wireless communications*. Cambridge University Press, 2005.

[17] Y. Hu and G. Leus, "Robust Differential Received Signal Strength-Based Localization," *IEEE Transactions on Signal Processing*, vol. 65, pp. 3261–3276, 2017.

[18] P. J. Teunissen and O. Montenbruck, *Springer Handbook of Global Navigation Satellite Systems*. Springer, 2017.

[19] J. Khalife, S. Bhattacharya, and Z. Kassas, "Centimeter-Accurate UAV Navigation with Cellular Signals," in *Proceedings of the 31st International Technical Meeting of the Satellite Division of The Institute of Navigation (ION GNSS+ 2018)*, September 2018, pp. 2321–2331.

[20] A. Bensky, *Wireless Positioning Technologies and Applications*. Artech House, 2016.

[21] K. Yu, I. Sharp, and Y. Jay Guo, *Ground-Based Wireless Positioning*. Wiley-IEEE Press, 2009.

[22] C. Mensing, S. Sand, and A. Dammann, *Positioning in Wireless Communications Systems*. John Wiley & Sons Ltd, 2014.

[23] S. Sesia, M. Baker, and I. Toufik, *LTE: The UMTS Long Term Evolution: from Theory to Practice*. John Wiley & Sons Ltd, 2011.

[24] Stüber, G. L., *Principles of Mobile Communications*. Springer Publishing Company, third ed., 2011.

[25] M. Driusso, F. Babich, F. Knutti, M. Sabathy, and C. Marshall, "Vehicular Position Tracking Using LTE Signals," *IEEE Transactions on Vehicular Technology*, vol. 66, pp. 3376–3391, 2017.

[26] M. Driusso, "Time of arrival estimation of LTE signals for positioning bounds and algorithms," Ph.D. dissertation, Università Degli Studi di Trieste, 2015.

[27] Ahmadi, Sassan, *LTE-Advanced 1st Edition, A Practical Systems Approach to Understanding 3GPP LTE Releases 10 and 11 Radio Access Technologies.* Academic Press, 2013.

[28] Van Trees, Harry L., *Optimum Array Processing, Part IV of Detection, Estimation, and Modulation Theory.* John Wiley & Sons Ltd, 2002.

[29] C. Knapp and G. Carter, "The generalized correlation method for estimation of time delay," *IEEE Transactions on Acoustics, Speech, and Signal Processing*, vol. 24, pp. 320–327, 1976.

[30] X. Li and K. Pahlavan, "Super-resolution TOA estimation with diversity for indoor geolocation," *IEEE Transactions on Wireless Communications*, vol. 3, pp. 224–234, 2004.

[31] N. Alsindi, X. Li, and K. Pahlavan, "Analysis of Time of Arrival Estimation Using Wideband Measurements of Indoor Radio Propagations," *IEEE Transactions on Instrumentation and Measurements*, vol. 56, pp. 1537–1545, 2007.

[32] Y. Liu, Z. Tan, H. Hu, L. Cimini, and G. Li, "Channel Estimation for OFDM," *IEEE Communications Surveys and Tutorials*, vol. 16, pp. 1891–1908, 2014.

[33] B. Yangm, K. Letaief, R. Cheng, and Z. Cao, "Channel estimation for OFDM transmission in multipath fading channels based on parametric channel modeling," *IEEE Transactions on Communications*, vol. 49, pp. 467–476, 2001.

[34] V. Prabhu and D. Jalihal, "An Improved ESPRIT Based Time-of-Arrival Estimation Algorithm for Vehicular OFDM Systems," *IEEE 69th Vehicular Technology Conference (VTC Spring),*, pp. 1–4, 2009.

[35] Manolakis, D. G. and Ingle, V. K. and Kogon,S. M., *Statistical and Adaptive Signal Processing: Spectral Estimation, Signal Modeling, Adaptive Filtering, and Array Processing.* Artech House, 2005.

[36] H. Krim and M. Viberg, "Two decades of array signal processing research: the parametric approach," *IEEE Signal Processing Magazine*, vol. 13, pp. 67–94, 1996.

[37] B. Van Veen and K. Buckley, "Beamforming: a versatile approach to spatial filtering," *IEEE Acoustic Speech Signal Processing Magazine*, pp. 1361–1375, 1986.

[38] Theodoridis,Sergios and Chellappa, Rama , *Academic Press Library in Signal Processing, Volume 3 Array and Statistical Signal Processing.* Academic Press, 2013.

[39] Stoica,Petre and Moses, Randolph , *Spectral Analysis of Signals.* Academic Press, 2013.

[40] Anderson, T.W. , *An Introduction to Multivariate Statistical Analysis.* Wiley, 2003.

[41] J. Capon, "High-resolution frequency-wavenumber spectrum analysis," *Proceedings of the IEEE*, vol. 57, pp. 1408 – 1418, 1969.

[42] Li, Jian and Stoica, Petre, *Robust Adaptive Beamforming.* John Wiley & Sons Ltd, 2006.

[43] T. Yardibi, J. Li, P. Stoica, M. Xue, and A. B. Baggeroer, "Source Localization and Sensing: A Nonparametric Iterative Adaptive Approach Based on Weighted Least Squares," *IEEE Transactions on Aerospace and Electronic Systems*, vol. 46, pp. 425 – 443, 2010.

[44] L. Du, T. Yardibi, J. Li, and P. Stoica, "Review of user parameters-free robust adaptive beamforming algorithms," *Digital Signal Processing*, vol. 19, pp. 567–582, 2009.

[45] J. Fessler and A. Hero, "Space-alternating generalized expectation-maximization algorithm," *IEEE Transactions on Signal Processing*, vol. 42, pp. 2664 – 2677, 1994.

[46] K. I. Pedersen, B. H. Fleury, and P. Mogensen, "High resolution of electromagnetic waves in time-varying radio channels," *Proceedings of 8th International Symposium on Personal, Indoor and Mobile Radio Communications - PIMRC '97*, pp. 650–654, 1997.

[47] B. H. Fleury, D. Dahlhaus, R. Heddergott, and M. Tschudin, "Wideband angle of arrival estimation using the SAGE algorithm," *Proceedings of ISSSTA'95 International Symposium on Spread Spectrum Techniques and Applications*, pp. 79–85, 1996.

[48] P. Stoica and Y. Selen, "Model-order selection: a review of information criterion rules," *IEEE Signal Processing Magazine*, vol. 21, no. 4, pp. 36–47, 2004.

[49] P. Djuric, "Asymptotic MAP criteria for model selection," *IEEE Transactions on Signal Processing*, vol. 46, no. 10, pp. 2726–2735, 1998.

[50] Lehmann, E.L. and Casella, George, *Theory of Point Estimation,Second Edition.* Springer, 1998.

[51] Poor, H.V. , *An Introduction to Signal Detection and Estimation.* Springer-Verlag, 1988.

[52] *Evolved Universal Terrestrial Radio Access (E-UTRA); User Equipment (UE) radio transmission and reception*, https://www.etsi.org/deliver/etsi_ts/136100_136199/136101/15.06.00_60/ts_136101v150600p.pdf, 3GPP Std. TS 36.101, Rev. 15.6.0, 2018, [Online Accessed Oct. 31 2019].

[53] *Evolved Universal Terrestrial Radio Access (E-UTRA); Base Station (BS) Radio Transmission and Reception.*, https://www.etsi.org/deliver/etsi_ts/136100_136199/136104/15.06.00_60/ts_136104v150600p.pdf, 3GPP Std. TS 36.104, Rev. 15.6.0, 2018, [Online Accessed Oct. 31 2019].

[54] u-blox TOBY-L2 series. www.u-blox.com/en/product/toby-l2-series. [Online Accessed Oct. 31 2019].

[55] Coaxial cable LLF400 data-sheet. https://www.rf-microwave.com/resources/products_attachments/5aec0d1a4cd75.pdf. [Online Accessed Oct. 31 2019].